On understanding the dynamics of energetic electrons in the inner magnetosphere

by

Leng Ying Khoo

B.S., University of Michigan, 2016

M.S., University of Colorado, 2020

A thesis submitted to the

Faculty of the Graduate School of the

University of Colorado in partial fulfillment

of the requirements for the degree of

Doctor of Philosophy

Department of Aerospace Engineering Sciences

2022

Committee Members:

Xinlin Li, Chair

Prof. Mary Hudson

Prof. David Malaspina

Prof. Robert Marshall

Prof. Howard Singer

Khoo, Leng Ying (Ph.D., Aerospace Engineering Sciences)

On understanding the dynamics of energetic electrons in the inner magnetosphere

Thesis directed by Prof. Xinlin Li

Earth's inner magnetosphere is a highly dynamic region with different particle populations overlapping with each other. Energetic electrons (tens of keV to > 1-MeV) in the inner magnetosphere are nominally trapped in the inner and outer electron radiation belts. However, the physical processes that contribute to the dynamic variations of energetic electrons are not fully understood. Therefore, the goal of this work is to improve the understanding of energetic electron dynamics in the inner magnetosphere. First, we investigate the dynamics of energetic electrons in the outer belt, specifically the sudden enhancements of energetic electrons. By exploring the relationship between the inner edge of energetic electron enhancements and the boundary of the cold plasmasphere, we identified a persistent observation where the innermost plasmapause location remains as the innermost limit of the sudden enhancement of energetic electrons regardless of storm drivers and storm magnitudes. Unlike its relationship with the simulated innermost plasmapause, a comparison between sudden enhancements and in-situ plasmapause locations reveals a local-time dependent relationship where sudden enhancements can sometimes be inside or outside the in-situ plasmapause locations, depending on the spacecraft location. On the other hand, energetic electron (especially the relativistic electron) dynamics in the inner belt is harder to identify largely due to background contamination that overwhelms electron measurements and instrument electronics. In the second part of this work, we explore ways to improve inner belt measurements and introduce a new energetic particle telescope that aims to overcome the challenge of measuring energetic electrons in the inner belt. A detailed description of the design and performance of this instrument is provided. In addition, we have conducted tests to study the limitation of two flux determination methods under different flux spectra; such an analysis is crucial to improving data quality. Together, our studies lead to a better understanding of energetic electron dynamics in the inner magnetosphere.

Dedicated to my parents.

Acknowledgements

First and foremost, I would like to thank my advisor, Prof. Xinlin Li. I am lucky to have an advisor who has as much faith and patience in me as he does, opening the research door when I had minimal background in Space Physics and giving me sufficient space and guidance to explore, learn, and grow. His insightful feedback has helped me overcome obstacles in research and grow professionally. More importantly, he taught me to think critically and deliver thoughts with clarity; these skills will prove valuable not just in research but also in life. Thanks to him, I have also had the wonderful opportunity to work in the CIRBE mission, which is instrumental in my graduate experience. It has been a joy to know the team members and work with them. Through the CIRBE mission, I have the honor to work alongside mentors like Dr. Richard Selesnick. In one of our early conversations, I asked him to "nudge me" if I am ever on the wrong path. He has been true to his words and stopped me multiple times from going down the rabbit hole by showing me a more elegant way to solve the problem and kindly (and very patiently) guiding me through the learning process. His meticulous attitude toward research has left a strong impact on me. I hope I will grow to be someone as helpful as he is to me.

I would also like to thank my committee members: Prof. Mary Hudson, Prof. David Malaspina, Prof. Robert Marshall, and Prof. Howard Singer for their generosity and warm support. Their valuable feedback has helped shape this dissertation. In the final stretch of my graduate studies, I am blessed with the opportunity to work with Dr. Greg Cunningham, to whom I owe a debt of gratitude for his kindness and unselfish sharing. I am also thankful to have colleagues like Dr. Hong Zhao, Dr. Kun Zhang, Dr. Zheng Xiang, Dr. Wenxun Zhang, Ben Hogan, Dr. Theodore

Sarris, Dr. Scott Thaller, Dr. Xiangning Chu, Dr. Quintin Schiller, Dr. Lauren Blum, Dr. Allison Jaynes, Guillem Megias i Homar, Yang Mei, and Declan O'Brien for discussion, support, and advice. I owe a special debt to Prof. Mark Moldwin, who introduced space physics to me. Finally, I would not make it this far without my family and friends. Their love, understanding, and support have been essential to this work.

Contents

Chapter

1 Introduction **1**

2 Background **5**

2.1 Earth's magnetosphere 5

2.1.1 Particle populations in Earth's inner magnetosphere 6

2.1.2 Motion of charged particles and the adiabatic invariants 8

2.1.3 Magnetospheric waves and wave-particle interactions 12

2.2 Earth's electron radiation belts 15

2.2.1 Acceleration mechanisms 17

2.2.2 Loss mechanisms 18

2.3 Plasmasphere 19

2.3.1 Drift paths of cold and hot plasma 19

2.3.2 Plasmasphere dynamics 23

2.3.3 Relation to radiation belt electron dynamics 24

2.4 Challenges of measuring energetic particles 26

2.4.1 Interaction of particles with matter 27

2.4.2 Deadtime, pileup, and chance coincidence 29

2.4.3 Challenge to convert measured count rates to flux 33

3 On the Initial Enhancement of Energetic Electrons and the Innermost Plasmapause Location: CME-Driven Storm Periods **35**

3.1 Introduction . . . 35

3.2 Methodology . . . 38

3.2.1 Plasmapause models . . . 38

3.2.2 Overview of observations from January 2013 to July 2015 . . . 40

3.3 Results . . . 42

3.3.1 Initial enhancement definition and observations during the five storm periods 42

3.3.2 Energy dependence of the spatial and temporal relationship between L_{IE} and innermost L_{pp} . . . 45

3.3.3 Energy spectrum inside and outside of the plasmasphere . . . 51

3.4 Conclusion . . . 51

4 On the Initial Enhancement of Energetic Electrons and the Innermost Plasmapause Location: CME vs CIR-Driven Storm Periods and Non-Storm Periods **53**

4.1 Introduction . . . 53

4.2 Data and method . . . 54

4.3 Initial enhancement events during CME- and CIR-driven storm periods . . . 56

4.4 Non-stormtime enhancement events . . . 63

4.5 Discussion and summary . . . 66

5 Multi-Event Studies of Sudden Energetic Electron Enhancements in the Inner Magnetosphere and Its Association with Plasmapause Positions **68**

5.1 Introduction . . . 68

5.2 Data and Analysis . . . 71

5.2.1 Energetic electron measurements and phase space density calculation . . . 71

5.2.2 Plasmapause: Definition, determination, and simulations . . . 72

5.3 Event overviews . . . 74

5.3.1 The 14 October 2014 Event . . . 74
5.3.2 The 25 July 2013 Event . . . 78
5.3.3 Summary of the outlier events . . . 83
5.4 Phase space density analysis . . . 85
5.5 Discussion and conclusion . . . 88

6 Overcoming the Challenges of Measuring Energetic Particles in the Inner Belt: A Geant4-based Performance of an Energetic Particle Detector Instrument, REPTile-2 **90**
6.1 Introduction . . . 90
6.2 REPTile-2 design . . . 92
6.3 Geant4 simulations . . . 95
6.4 Instrument characterization . . . 96
6.4.1 Passive shielding . . . 96
6.4.2 Monoenergetic simulation results . . . 98
6.4.3 Anticoincidence detectors - the guard rings . . . 99
6.4.4 Logic and binning equations . . . 100
6.4.5 Instrument characterization . . . 104
6.4.6 Pileup . . . 112
6.5 Final remarks . . . 115

7 Flux determination using Bowtie analysis and generalized least-square method **118**
7.1 Introduction . . . 118
7.2 Bowtie method . . . 119
7.3 Generalized least square method . . . 120
7.3.1 Linear problem . . . 121
7.3.2 Generalized least square method - nonlinear problem . . . 124
7.4 Instrument validation: Sr-90 radioactive source test . . . 126
7.5 Performances under extreme scenarios . . . 129

7.6 Summary and discussion 131

8 Summary and Suggestions for Future Work **132**

8.1 Summary 132

8.2 Future Work 135

8.2.1 Role of plasmasphere on the evolution of energetic electrons after initial enhancements 135

8.2.2 Role of large-scale electric fields on energetic particles 136

8.2.3 REPTile-2 measurements and the implication of the Geant4 analysis 136

Bibliography **139**

Appendix

A Additional information for Chapter 4, "On the Initial Enhancement of Energetic Electrons and the Innermost Plasmapause Locations: CME vs CIR-Driven Storm Periods and Non-Storm Periods" **156**

B Additional information on REPTile-2 **159**

B.1 Estimated count rate per energy using AE9 and AP9 159

B.2 Angular response function 160

C Review for Chapter 7: solving inverse problem using the length method **164**

C.1 Derivation of matrix 164

C.2 Simple least square solution 165

C.3 Minimum length solution 166

C.4 Derivation of different forms of the generalized least square solution for linear problems 168

C.5 Covariance for posterior model 169

Tables

Table

3.1 Geometric indices and solar wind velocity for the five geomagnetic storm periods. . . 42

5.1 Summary of the outlier events. 85

6.1 Logic equation for REPTile-2 101

6.2 Logic and binning equations for RNGp channels. 105

6.3 Logic and binning equations for RNGe channels. 106

6.4 Logic and binning equations for PENp and PENe channels. 107

6.5 Differences between REPTile and REPTile-2. 117

A.1 List of CME- and CIR-driven storm events. 156

A.2 List of non-storm periods. 157

Figures

Figure

2.1 Schematic of Earth's magnetosphere 6

2.2 Motion of a charged particle in Earth's magnetic field 9

2.3 Gyration, bounce, and drift frequency of electrons as a function of L and energy . . 11

2.4 Waves in the magnetosphere 13

2.5 Energy-dependent dynamic of the outer radiation belt electrons 16

2.6 Loss and acceleration mechanisms of outer radiation belt electrons 17

2.7 Drift path of cold plasma 21

2.8 Drift path of cold plasma in a time-dependent convection electric field 22

2.9 Drift path of positive hot plasma under the influence of both time-independent convection electric field and gradient-B drift 23

2.10 Dynamics of the plasmapause 25

2.11 The relationship between the inner edge of outer belt electrons and the plasmapause 26

2.12 Mean energy loss rate in different materials. 29

3.1 Innermost Lpp 39

3.2 Flux measurements 44

3.3 How to identify initial enhancement event 45

3.4 Initial enhancement locations vs innermost Lpp 46

3.5 Quantification of the distance between initial enhancement locations and the innermost Lpp 47

3.6 Energy spectrum inside and outside of the innermost Lpp 52

4.1 The total number of initial enhancement events identified during CME-driven and CIR-driven storms. 56
4.2 Comparison of the innermost location of the initial enhancement events, L_{IE}, and the innermost L_{pp} during CME-driven and CIR-driven storms. 58
4.3 Quantification of the median (50th percentiles) and average distance between L_{IE} and L_{pp} for both CME-driven and CIR-driven storms. 59
4.4 Time lag between the initial enhancements of more energetic electrons (t_{IE}) and the initial enhancements of the lowest available energy electrons (t_{IE} min)for both CME-driven and CIR-driven storms. 60
4.5 Comparison of the innermost location of the initial enhancement events, L_{IE}, and the innermost L_{pp} during non-storm periods. 63
4.6 Quantification of the median (50th percentiles) and average distance between L_{IE} and L_{pp} during non-storm periods. 64

5.1 Overview of an outlier event where initial enhancements were found inside the innermost plasmapause location during the 14 October 2013 event. 75
5.2 Variation of the energy spectrum during the 14 October 2013 enhancement event. . . 77
5.3 Location of Van Allen Probes and GOES 13 and 15 during the 14 October 2013 enhancement event. 79
5.4 Overview of an outlier event where initial enhancements were found inside the in-situ plasmapause location during the 25 July 2013 event. 80
5.5 Variation of the energy spectrum during the 25 July 2013 enhancement event. 81
5.6 Location of Van Allen Probes and GOES 13 and 15 during the 25 July 2013 enhancement event. 82
5.7 Summary of all outlier events. 84

5.8 Phase space density evolution between two successive outbound passes by Van Allen Probes on October 14, 2014. 87
5.9 Phase space density evolution between two successive outbound passes by Van Allen Probes on July 25, 2013. 88

6.1 Illustration of REPTile-2 design with key features labelled. 93
6.2 Simulations of the trajectories of electrons and protons through the REPTile-2. . . . 97
6.3 Histogram of total energy deposited by boresight-shooting, monoenergetic electrons and protons. 98
6.4 The efficiency of anticoincidence detectors at removing contaminated particles. . . . 100
6.5 The effect of the logic equations 103
6.6 Energy response function for incident electrons that originate from the boresight. . . 107
6.7 Energy response function for RNG channels. 108
6.8 Energy response function for RNG channels. 109
6.9 Energy response function for PEN channels. 110
6.10 Energy response function for incident electrons and protons that originate from the spherical surface and are binned into the wrong RNG channels. 112
6.11 AE9 and AP9 spectra for the pileup analysis in a 'worst-case' scenario. 113
6.12 Count rates with and without two-event pileup on Detector 1 and guard detector. . 114
6.13 AE9 and AP9 spectra for the pileup analysis in a 'nominal' scenario. 115
6.14 Count rates with and without two-event pileup on Detector 1 and guard detector under a nominal flux condition 116

7.1 Example of bowtie analysis. 121
7.2 Strontium-90 radioactive test result. 127
7.3 Strontium-90 radioactive test result. 128
7.4 Comparison of bowtie and least square solution under a spiky flux spectrum. 130
7.5 Comparisons of bowtie and least square solution under a flat flux spectrum. 130

A.1 Quantification of the median (50th percentiles) and average distance between L_{IE} and L_{pp} for both CME-driven and CIR-driven storms using background-corrected data. 157

A.2 Time lag between the initial enhancements of more energetic electrons (t_{IE}) and the initial enhancements of the lowest available energy electrons (t_{IE} min)for both CME-driven and CIR-driven storms for background-corrected data. 158

A.3 Quantification of the median (50th percentiles) and average distance between L_{IE} and L_{pp} during non-storm period using background-corrected data. 158

B.1 Estimated count rates for RNG channels from AE9 and AP9 models. 160

B.2 Estimated count rates for RNG channels from AE9 and AP9 models. 161

B.3 Estimated count rates for RNGe channels by incident proton based on AP9 model. . 161

B.4 Angular response function for RNGe channels by incident electrons that originate from the spherical surface. 162

B.5 Angular response function for RNGp channels by incident protons that originate from the spherical surface. 163

Chapter 1

Introduction

Earth's magnetosphere is a complex region where charged particles are controlled by Earth's magnetic and electric fields. These charged particles primarily originate from the solar wind and the ionosphere. Residing in the inner magnetosphere are three distinct populations [Ebihara and Miyoshi, 2011]: the plasmasphere, the ring current, and the radiation belts. As our society is increasingly dependent on space-based assets, our understanding of this dynamic region becomes instrumental to mitigating the threat of these charged particles on spacecraft and humans in space. For instance, energetic electrons between tens of keV to a few MeV in the magnetosphere can cause surface charging or internal charging of spacecraft and may lead to subsequent discharges, damaging spacecraft components [e.g., Baker et al., 2018]. These energetic electrons are often characterized by dynamic variations on spatial and temporal scales, and the underlying mechanism that controls particle dynamics is still not well understood.

The work in this dissertation addresses two main topics, both related to understanding the dynamics of energetic electrons in the inner magnetosphere. The first half of the work focuses on the frequently observed, sudden enhancements of energetic electrons in the radiation belts (mostly in the outer belt and the slot region). To address unanswered questions such as the spatial extent of the sudden enhancement of energetic electrons, we offer a new perspective by examining how sudden enhancement locations relate to the plasmapause location. In the latter half of this dissertation, we address a crucial element in energetic electron studies: how to improve the quality of energetic electron measurements. The dynamics of energetic electrons are difficult to characterize in the inner

belt due to background contamination and electronics limitations. We introduce a new energetic particle detector instrument onboard an upcoming CubeSat mission, the Colorado Inner Radiation Belt Experiment (CIRBE), and describe ways to improve the current instrumentation and the flux extraction technique to produce cleaner and more refined measurements. Such measurements are necessary to advance our current understanding of energetic electrons.

Chapter 2 begins with a brief overview of Earth's magnetosphere. It includes discussions on different particle populations in the inner magnetosphere, motions of charged particles and the associated adiabatic invariants, magnetospheric waves, and wave-particle interactions. More details related to the electron radiation belts and the plasmasphere, such as dynamics and relevant physical processes, are provided. Finally, I present the basic principles of energetic charged particle detection and measurement, specifically on the particle's interaction with matter and electronic limitations, including deadtime, pileup, and chance coincidence.

After establishing the background in Chapter 2, Chapter 3 addresses questions regarding sudden enhancements of energetic electrons: 1) what is the underlying mechanism that leads to these sudden flux enhancements? 2) over what spatial extent can these enhancement events reach? Many studies have examined the dynamics of energetic electrons as a standalone entity. However, in reality, they coexist with other populations in the inner magnetosphere, such as the plasmasphere. It is still unclear how the dynamics of energetic electrons in the radiation belts relate to the plasmasphere, which is the focus of this chapter. Chapter 3 investigates the relationship between the initial enhancement of energetic electrons (30 keV to 3 MeV) and the innermost plasmapause locations. Findings on sudden flux enhancements of energetic electrons during the five largest geomagnetic storms between January 2013 and June 2015 are provided. These storms are coronal mass ejection (CME)-driven storms, and we compare the inner boundary of sudden flux enhancements with the innermost plasmapause locations derived from plasmapause models. Our analysis determined a persistent relationship between sudden energetic electron enhancements and the innermost plasmapause location during the five largest geomagnetic storms in the early Van Allen Probes era.

Chapter 4 investigates the influence of different storm drivers and geomagnetic activity on the relationship between sudden energetic electron enhancements and the innermost plasmapause locations. Previous studies have indicated that different storm drivers can affect energetic electron dynamics differently. In addition, radiation belt electrons are thought to be less dynamic during the non-stormtime periods. Chapter 4 examines these notions by studying storm-time and non-stormtime enhancements events between January 2013 to June 2015. The storm-time enhancement events are categorized according to their storm drivers (CME- or corotating interaction region [CIR]). I then quantified the distance between sudden energetic electron enhancements and the innermost plasmapause location and the time difference between the initial enhancements and the time at minimum Dst for storm-time and non-stormtime enhancement events.

Finally, Chapter 5 examines the outlier events in previous studies where sudden enhancement events were reported inside the innermost plasmapause locations or in-situ plasmapause location. The cause of these outlier events remains unclear. To investigate this, I utilized multiple spacecraft measurements and studied the enhancement location with respect to the in-situ plasmapause and the simulated innermost plasmapause. Chapter 5 reveals that sudden enhancements are often found inside the in-situ plasmapause near the dusk sector and outside the in-situ plasmapause near the midnight or dawn sector. Our analysis concludes that the innermost plasmapause location remains the limit of the initial sudden enhancements of energetic electrons.

On the other hand, to better understand the variation of energetic electrons in the inner belt and the energy extent of a sudden enhancement event, we need measurements with better-resolved energy resolution and minimal background contamination. In the second part of this thesis, I investigate ways to improve energetic particle measurements. With the end of the Van Allen Probes mission, the task of providing fine resolution and clean, energetic electron measurements has now fallen upon small satellites. Our predecessor instrument, the Relativistic Electron Proton Telescope integrated little experiment (REPTile), has proven the ability to achieve quality science using a miniaturized instrument onboard a CubeSat. In Chapter 6, I introduce REPTile-2 that pushes the limit of energetic particle measurements (particularly in/near the inner belt) and aims

to provide one of the cleanest and most well-resolved energetic electron and proton measurements ever available. I assisted Dr. Richard Selesnick in deriving the logic and binning equations and under his guidance, I have characterized the instrument performance by analyzing the Geant4 simulation results and the Sr-90/Y-90 test results. Using pulse-height analysis and active shielding like guard rings, REPTile-2 is designed to measure 300 keV to ∼4 MeV electrons with fine energy resolution ($\Delta E/E \sim 7 - 38\%$), with secondary proton measurements (6.7 - 35 MeV). Chapter 6 also includes a comprehensive description of how to utilize Geant4 simulation to inform the design and performance of the instrument. The Geant4 simulation results are validated through a Sr-90 radioactive source test.

The flux extraction from a count rate is also a critical process that could bias the final data quality. The conversion of count rate to flux, however, is not a trivial task. Therefore, it is essential to understand how flux is derived using different flux determination methods and considering the limitation of each approach. Chapter 7 uses three different flux spectra to test the performance of two flux extraction techniques: a bowtie method that is widely used for radiation belt particle measurements and a generalized least square method that is commonly used in geophysics. Discussions on the limitation of these methods are discussed. This analysis is an integral part of a rigorous process to provide good measurements that are essential for radiation belt studies.

Finally, I conclude the thesis by summarizing the major findings of this work in Chapter 8. I will discuss the work needed to complete current studies and present ideas on the potential extension of the work in this thesis.

Chapter 2

Background

2.1 Earth's magnetosphere

Earth's magnetosphere is a comet-shaped region where Earth's magnetic field dominates [Gold, 1959]. Its shape and size vary as a result of the interaction between the solar wind and Earth's magnetic field [e.g., Kivelson and Russell, 1995]. The boundary that separates Earth's magnetosphere and the interplanetary magnetic field is known as the magnetopause. Its location is primarily a balance between the dynamic pressure of the solar wind and the magnetic pressure of Earth's magnetic field [Chapman and Ferraro, 1930]. Typically, the magnetopause is located ∼10 Earth radii ($R_E = 6371$ km) on the dayside, but under extreme solar wind conditions, it can reach below the geosynchronous orbit, $< 6.6R_E$ [Shue et al., 1998]. On the other hand, the tail of the magnetosphere on the nightside can be stretched out to 100s of R_E [e.g., Sibeck and Lin, 2014]. Figure 2.1 illustrates numerous particle populations and current systems in the magnetosphere [Kivelson and Russell, 1995].

Earth's inner magnetosphere is a region closer (within $\sim 10R_E$) to Earth where the geomagnetic field resembles a dipole field [Ebihara and Miyoshi, 2011; Wolf et al., 2007]. It consists of three distinct particle populations that overlap each other in space: the plasmasphere, the ring current, and the radiation belts. The characteristics of each population are summarized in Section 2.1.1, with a more detailed discussion about the plasmasphere and the radiation belt in Sections 2.2 and 2.3.

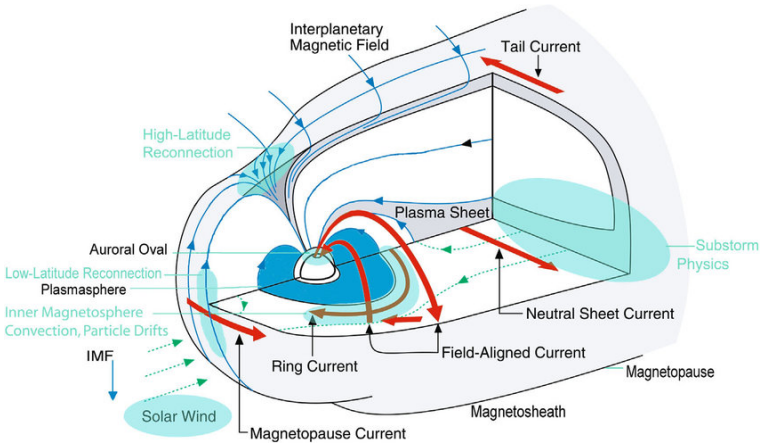

Figure 2.1: Schematic of Earth's magnetosphere. Modified from Kivelson and Russell [1995]. From Frey [2007].

2.1.1 Particle populations in Earth's inner magnetosphere

The plasmasphere is a cold (∼eV), dense (10 - $10^3 cm^{-3}$) plasma that corotates with Earth [Goldstein, 2006, and references therein]. It mainly consists of H^+, He^+, O^+ and electrons[Lemaire and Gringauz, 1998]. The source of the cold plasma in the plasmasphere is of ionospheric origin where the sunlit-driven outflow of cold plasma from the dayside ionosphere and the eastward rotation of Earth's magnetic field lead to a torus of cold ionospheric plasma drifting around Earth. The outer boundary of the plasmasphere is called the plasmapause, where the plasma density drops drastically [Carpenter, 1963]. The plasmasphere is highly dynamic; during prolonged quiet solar wind conditions, it can reach beyond geosynchronous orbit and has no sharp density gradient near the outer boundary, while during disturbed periods, it can shrink and reach as low as 2 R_E [e.g., Goldstein et al., 2003].

Often overlapping with the plasmasphere is the ring current, a near-equatorial electric current that flows westward around Earth and is located at geocentric distances between ∼2 R_E and 9 R_E [Daglis et al., 1999, and references therein]. It comprises mostly ions with energies of a few keV to hundreds of keV, with a relatively small contribution from electrons [Baumjohann and Treumann, 1996; Ebihara and Miyoshi, 2011; Zhao et al., 2016]. The source of the ring current

particles is of ionospheric and solar wind origin [Daglis et al., 1999, and references therein]. The strength of the ring current and its composition varies, depending on geomagnetic conditions. During geomagnetically active periods, charged particles are transported radially inward from the tail of the magnetosphere. As they come closer to the inner magnetosphere where the magnetic field strength is stronger, the particles undergo a charge-dependent drift around Earth due to magnetic field gradient; electrons drift eastward while ions drift westward. This leads to the formation of a westward electric current that is also known as the ring current. The ring current can induce magnetic fields that are in opposition to Earth's magnetic field. Therefore, the variation in the horizontal component of the geomagnetic equatorial surface field as measured by ground magnetometers, also known as the Dst index [Sugiura, 1991], is frequently used as a proxy for geomagnetic activity.

Finally, the radiation belts consist of trapped energetic electrons and protons that drift around Earth. They are also known as the Van Allen radiation belts as a tribute to Dr. James Van Allen, who discovered this region in 1958 [Van Allen et al., 1958]. The electron radiation belts are separated into inner and outer belts. The inner belt is often centered near 1.5 R_E as measured from the center of Earth in the equatorial plane, while the outer belt is most intense around 4-5 R_E. There is a low-flux region called the 'slot' region between the inner and outer belt. However, this description is merely a simple reference. In reality, the outer radiation belt is a highly dynamic region that is populated by relativistic electrons and varies with geomagnetic activities. During intense geomagnetic storms, the electrons can fill the 'slot' region and reach the inner belt, a relatively stable region that is characterized by occasional injection from the outer belt and slow decay of the electrons [e.g., Reeves et al., 2016; Turner et al., 2017]. On the other hand, the proton radiation belt generally refers to the inner zone proton belt and often overlaps (spatially) with the inner electron belt. The source of energetic protons in the proton belt includes those generated from the decay of energetic neutron (also known as Cosmic Ray Albedo Neutron Decay, CRAND) and solar energetic protons in Earth's magnetic field [e.g., Selesnick et al., 2014]. Recent studies have demonstrated that a solar proton source is a major contributor of the inner belt

protons ($< 100MeV$) at L > 1.5, while a CRAND source mostly dominates otherwise [Selesnick et al., 2016; Li et al., 2021].

2.1.2 Motion of charged particles and the adiabatic invariants

In the inner magnetosphere, the trapped charged particles perform three periodic motions: gyro-motion around a magnetic field line, bounce motion along the magnetic field between magnetic mirror points, and azimuthal drift motion around Earth (Figure 2.2). These three periodic motions are also associated with three adiabatic invariants that are conserved when the spatial and temporal changes in an electric and magnetic field are small compared to the timescales of the gyration, bounce, and drift motion.

The first periodic motion of a charged particle is gyration. A charged particle with mass m and charge q gyrates around the magnetic field line with a gyroradius of $\frac{\gamma m v_\perp}{qB}$ and a gyrofrequency of $\frac{qB}{\gamma m}$, where B is the local magnetic field, γ is the Lorentz factor, and $v_\perp$ is the particle's velocity component that is perpendicular to the local magnetic field. Note that the gyrofrequency is independent of $v_\perp$. In other words, the gyrofrequency of, say, electrons with varying $v_\perp$ at one location is the same, and this remains true for all non-relativistic particles since the only term that is dependent on $v_\perp$ in the gyrofrequency equation is γ, which is ~ 1 for non-relativisitc particles (See Figure 2.3. Also see Schulz and Lanzerotti [2012] for related discussion). The instantaneous center of the gyration is known as the guiding center. The adiabatic invariant associated with the gyration motion is the magnetic moment,

$$\mu = \frac{p_\perp^2}{2m_0 B} \tag{2.1}$$

where $p_\perp$ is the relativistic momentum component perpendicular to the local magnetic vector ($\gamma m_0 v_\perp$). In conserving the first adiabatic invariant (i.e., the electric field and/or magnetic field fluctuations are slow relative to the gyroperiod), μ describes how the perpendicular velocity of particles changes with respect to the variations in the local magnetic field.

In Earth's dipole-like magnetic field, the magnetic field strength is weakest near the

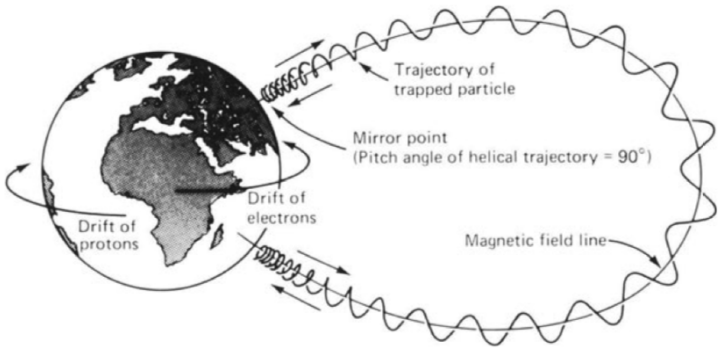

Figure 2.2: Motion of a charged particle in Earth's magnetic field. From Lyons and Williams [2013]

geomagnetic equator and increases as it approaches the poles. Due to the gradient of magnetic field strength along the field line, the charged particle with a nonzero parallel component of velocity, $v_{||}$, experiences another periodic motion, the bounce motion. The pitch angle of a charged particle is the angle between the particle's velocity vector and the local magnetic field vector, $\alpha(s) = cos^{-1}(\frac{v_{||}(s)}{v(s)}) = sin^{-1}(\frac{v_{\perp}(s)}{v(s)})$, where s is the field line arc length. In other words, particles with a pitch angle of 0° have no local perpendicular velocity component. As derived in Roederer [1970], particles with an initial pitch angle of α_i at local magnetic field, B_i, spiral along the field line with a parallel velocity of

$$v_{||}(s) = v\cos(\alpha(s)) = v[1 - \frac{B(s)}{B_i}\sin^2\alpha_i]^{\frac{1}{2}} \tag{2.2}$$

The gradient of magnetic field strength along a curved field line also causes the particles to experience a field-aligned Lorentz force, $\boldsymbol{f}_{||} = -\frac{1}{2}qv_{\perp}\rho_c\nabla_{||}B$ that is derived from the Lorentz equation $f_{||} = q\boldsymbol{v}_{\perp} \times \boldsymbol{b_r}$ where $\boldsymbol{b_r}$ is obtained from the Maxwell's equation ($\nabla \cdot \boldsymbol{B} = 0$). As the particle proceeds toward a region of higher field intensity, its $v_{||}$(s) decreases until it reaches a mirror point where the corresponding field strength is

$$B_m = \frac{B_i}{\sin^2\alpha_i} \tag{2.3}$$

and its parallel velocity becomes zero. At the mirror point, the field-aligned Lorentz force drives the particles away from regions of increasing field intensity along the field line and back to a lower

field intensity region. In a dipole-like magnetic field where the magnetic field strength increases as it goes from the equator to the pole, the particles will experience a bounce motion between two mirror points. The second adiabatic invariant that is associated with the bounce motion along a field line is known as the longitudinal invariant, J, defined as

$$J = 2\sqrt{2m_0\mu}\int_{S_m}^{S'_m}\sqrt{B_m - B(s)}\,ds \tag{2.4}$$

where S_m and S'_m are the location of mirror points at the northern/southern hemispheres, B_m and $B(s)$ are the field strengths at mirror point m and point s, m_0 is the rest mass of the particle, μ is the magnetic moment, and ds is the distance along the field line.

The last periodic motion involves the drift motion of particles that is represented by the term,

$$v_d = \frac{\boldsymbol{F}\times\boldsymbol{B}}{qB^2} \tag{2.5}$$

where $\boldsymbol{F}$ is the external force such as electric force, $\boldsymbol{B}$ is the local magnetic field and q is the charge of particle. The drift motion of charged particles is mainly caused by magnetic drift and electric drift. Magnetic drift is due to the combined effect of the magnetic field gradient and the curvature of magnetic field lines. The resultant drift velocity can be written as,

$$v_d = (\frac{1}{2}v_\perp^2 + v_{||}^2)\frac{\boldsymbol{B}\times\boldsymbol{\nabla}B}{\omega_g B^2} \tag{2.6}$$

where ω_g is the gyrofrequency. On the other hand, the electric drift is a drift motion caused by electric force, defined as

$$v_d = \frac{\boldsymbol{E}\times\boldsymbol{B}}{B^2} = \frac{E}{B} \tag{2.7}$$

where E is the electric field and B is the local magnetic field. Note that the electric drift is independent of the particle charge. Therefore, unlike the magnetic drift that can cause electrons to drift eastward and protons to drift westward, the electric drift will make the electrons and ions move in the same direction. The azimuthal drift motion of charged particles around Earth forms a surface, known as a drift shell, and is associated with the third adiabatic invariant where the magnetic flux enclosed by the particle's drift path remains constant as long as the variations in the

electric/magnetic field are slower than the particle's drift period. The third adiabatic invariant can be calculated as

$$\Phi = \oint \boldsymbol{A}_{\boldsymbol{\phi}} dl \tag{2.8}$$

where $\boldsymbol{A}$ is the magnetic vector potential and dl is the curve where the particle's drift shell lies. It is often written in the form of

$$L^* = \frac{2\pi M}{|\Phi| R_E} \tag{2.9}$$

where L^* is the Roederer L and is defined as the radial distance to the equatorial location where an electron crosses if only an internal dipole field remains and all external magnetic fields were slowly turned off, M is Earth's dipole magnetic moment, and R_E is Earth's radius. Figure 2.3 illustrates contour plots of the gyration, bounce, and drift frequency as a function of energy and L for electrons that mirror at the equator in a geomagnetic dipole field.

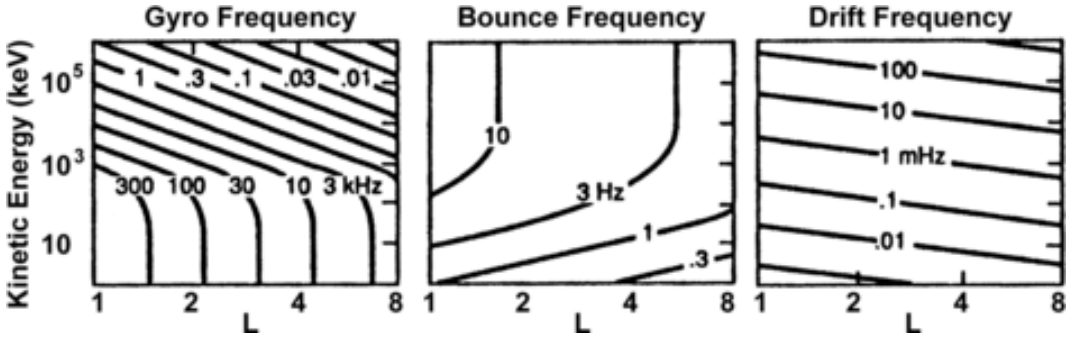

Figure 2.3: Gyration, bounce, and drift frequency as a function of energy for electrons that mirror at the equator of a geomagnetic dipole field. Adapted from Schulz and Lanzerotti [2012]. From Ukhorskiy and Sitnov [2012].

Phase space density (PSD) is a distribution function of particles in six-dimension phase space that involves three components of position and three components of momentum, f(x, y, z, p_x, p_y, p_z). It is also commonly presented in term of the phase of each periodic motion, f(μ, K, L^*,ϕ_1, ϕ_2, ϕ_3), where ϕ_1, ϕ_2, and ϕ_3 are corresponding phases of the three periodic motions of a charged particle. Due to limited observations in space, and for all practical purposes, the PSD is often represented by the phase-averaged PSD, f(μ, K, L^*), in radiation belt studies. Interested readers

are referred to Schulz and Lanzerotti [2012], Ukhorskiy and Sitnov [2012], and Lyons and Williams [2013] for more discussion.

The evolution of phase space density follows the Liouville theorem that states that the density of particles in phase space, f, is constant along the particle trajectory in the absence of source or loss. Therefore, the study of PSD evolution can help identify the underlying source and loss mechanisms and distinguish a non-adiabatic process from the adiabatic. The phase-averaging of the PSD also introduces randomness where the particle distribution subjected to non-adiabatic forces appears to walk randomly with respect to the violated invariant. This permits the violation of the adiabatic invariants to be represented by a diffusion process. The diffusion approximation holds as long as the magnetic and electric field perturbations are small or slowly-varying, such that the nonlinear phase-dependent effect is negligible [e.g., Ukhorskiy and Sitnov, 2012]. Important diffusion processes in radiation belt studies are: 1) radial diffusion that involves the violation of the third adiabatic invariant and can cause particles to transport radially across field lines; 2) pitch angle diffusion and energy diffusion that are caused by the violation of the first and second adiabatic invariant and can change the particle' pitch angle and energy.

2.1.3 Magnetospheric waves and wave-particle interactions

Particularly, wave-particle interactions can lead to violation of one or more of the adiabatic invariants and cause diffusion of charged particles [e.g., Chen et al., 1984; Tsurutani and Lakhina, 1997; Thorne, 2010; Schulz and Lanzerotti, 2012]. Figure 2.4 illustrates important plasma waves in the magnetosphere and their general location with respect to the plasmasphere and the ring current. Generally, the interaction between the waves and charged particles becomes strong when they are resonant with the cyclotron frequency, bounce frequency, and/or drift frequency. The cyclotron resonance occurs when the particle senses the Doppler-shifted wave at its cyclotron frequency or its harmonics. It can be written as:

$$\omega - \boldsymbol{k} \cdot \boldsymbol{v} = \frac{n\Omega}{\gamma} \tag{2.10}$$

where ω is the wave frequency, $\boldsymbol{k}$ is the wave vector, $\boldsymbol{v}$ is the velocity vector of the charged particles, n is an integer equal to 0, ±1, ±2, $\cdots$. In the case of n = 0, it refers to Landau resonance. On the other hand, the charged particles also experience drift resonance with the wave under the drift resonant condition: $\omega = m\Omega_d$, where ω is the wave frequency, Ω_d is the drift frequency of the charged particles, and m is the azimuthal wave number. The properties of these waves and their interactions with charged particles are summarized as below.

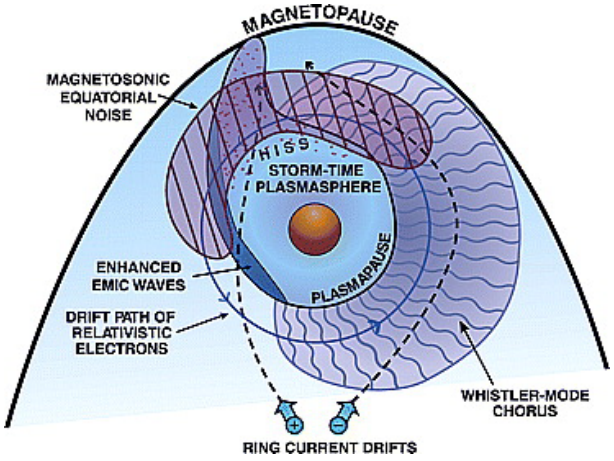

Figure 2.4: Schematic illustrations of the spatial distributions of magnetospheric waves, in relation to the plasmasphere. From Thorne [2010].

Whistler-mode waves generally refer to low-frequency electromagnetic waves with right-hand polarization in which the electric field vector rotates clockwise with respect to the wave propagation direction. Plasmaspheric hiss waves are incoherent whistler-mode waves with a typical frequency between ~100 Hz to 2000 Hz (although recent studies like Chen et al. [2014] reported the presence of low-frequency hiss, extending down to $\sim$ 20 Hz) and are mostly confined within the plasmasphere and dayside plasmaspheric plumes [e.g., Bortnik et al., 2009, and references therein]. Hiss waves can scatter energetic electrons via electron cyclotron resonance and are likely responsible for the formation of a slot region during quiet periods [e.g., Lyons and Thorne, 1973; Meredith et al., 2007]. Outside the plasmasphere, discrete, coherent whistler-mode chorus waves are mostly found near the dawn and dayside sectors. Chorus waves occur in two distinct bands:

a lower band (0.1-0.5 of electron cyclotron frequency, f_ce) and a upper band (0.5-0.8 f_ce) [e.g., Burtis and Helliwell, 1969; Tsurutani and Smith, 1974; Li et al., 2019] . Chorus waves are formed from instability caused by temperature anisotropies of the injected plasmasheet electrons during enhanced convection [e.g., Tsurutani and Smith, 1974; Santolík et al., 2010; Schriver et al., 2010; Li et al., 2019]. Chorus waves can cause a violation of the first adiabatic invariant and lead to pitch-angle scattering of energetic electrons near the loss cone [e.g., Thorne, 2010; Kasahara et al., 2018] as well as a local acceleration of hundreds of keV electrons to relativistic electrons [e.g., Reeves et al., 2013; Thorne et al., 2013; Jaynes et al., 2015]. Recent studies like Artemyev et al. [2020] have also indicated the possibility of nonlinear wave-particle resonance in whistler waves, even though the relative importance of nonlinear wave-particle resonance remains an active investigation [Ripoll et al., 2020, and references therein]. Although not shown in Figure 2.4, an ultra-low-frequency (ULF) wave is generally described as a broadband electromagnetic wave in the mHz range. It can cause radial transport of energetic electrons through drift resonance [e.g., Hudson et al., 2000, 2004; Mann et al., 2016] on a time scale of hours to several days [e.g., Baker et al., 1998].

On the other hand, equatorial magnetosonic waves are generally confined within 2-3 degree of the geomagnetic equator near the plasmasphere. The waves are excited by a cyclotron resonant instability with the injected ring current ions [e.g., Chen et al., 2011] and have a frequency range between the proton gyrofrequency and the lower hybrid frequency. Magnetosonic waves can undergo Landau resonance with radiation belt electrons (hundreds of keV to MeV), leading to pitch angle diffusion and energy diffusion of these electrons [e.g., Horne et al., 2007; Lei et al., 2017]. Finally, electromagnetic ion cyclotron (EMIC) waves are discrete electromagnetic waves in distinct frequency bands that range between 0.1-5 Hz. Generally found near the dusk sector, EMIC waves can cause pitch-angle scattering of ring current protons as well as rapid loss (as fast as a few minutes) of relativistic electrons [e.g., Daglis et al., 1999; Summers and Thorne, 2003; Usanova et al., 2010, 2014; Blum et al., 2015; Cao et al., 2019].

2.2 Earth's electron radiation belts

The radiation belts consist of trapped energetic particles that perform all three particle motions (gyration, bounce motion, and drift motion). Before the launch of Van Allen Probes, Earth's radiation belts were known to be a two-belt structure [Li and Hudson, 2019]: an inner belt and an outer belt separated by a slot region. The inner belt is a relatively stable region with occasional transport of electrons from the outer belt to the inner belt [Baker et al., 2004; Turner et al., 2017]. Recent findings from the Van Allen Probes mission indicate that > 1-MeV electrons in the inner belt are extremely low during the Van Allen Probes era and can be detected only after a thorough background correction because they are mostly below the background noise [Li et al., 2015; Claudepierre et al., 2017, 2019]. In addition, flux enhancements of few MeV electrons are restricted to higher L (L >∼2) during the Van Allen Probes era, and this feature was also interpreted as an 'impenetrable barrier' where the relativistic electrons cannot reach below a certain L [Baker et al., 2014].

Compared to the inner belt, the outer belt is a more dynamic region with flux variations over a timescale of minutes to days. Van Allen Probes discovered that the radiation belts are not always a two-belt structure. Under certain conditions, a second, new outer belt could form at a higher L, outside of the existing outer belt, also known as the remnant belt or storage ring in this scenario [e.g., Baker et al., 2013]. On the other hand, the slot region is a low-flux region that separates the inner and outer belts during quiet periods. Occasionally, a slot-filling event could happen where energetic electrons fill the slot region and reach the inner belt. Studies have suggested that the slot-filling event could be a significant source of the inner belt [e.g., Turner et al., 2017]. The slot-filling events generally occur more frequently for lower energy. Even if an enhancement event does not fill the slot region, enhancement of lower energy electrons still reaches lower L than higher-energy electrons [e.g., Reeves et al., 2016]. As shown in Figure 2.5, the spatial extent of the inner belt, slot region, and outer belt is also energy-dependent. However, the spatial and energy extent of these enhancements that could occur under given geomagnetic conditions remain unclear;

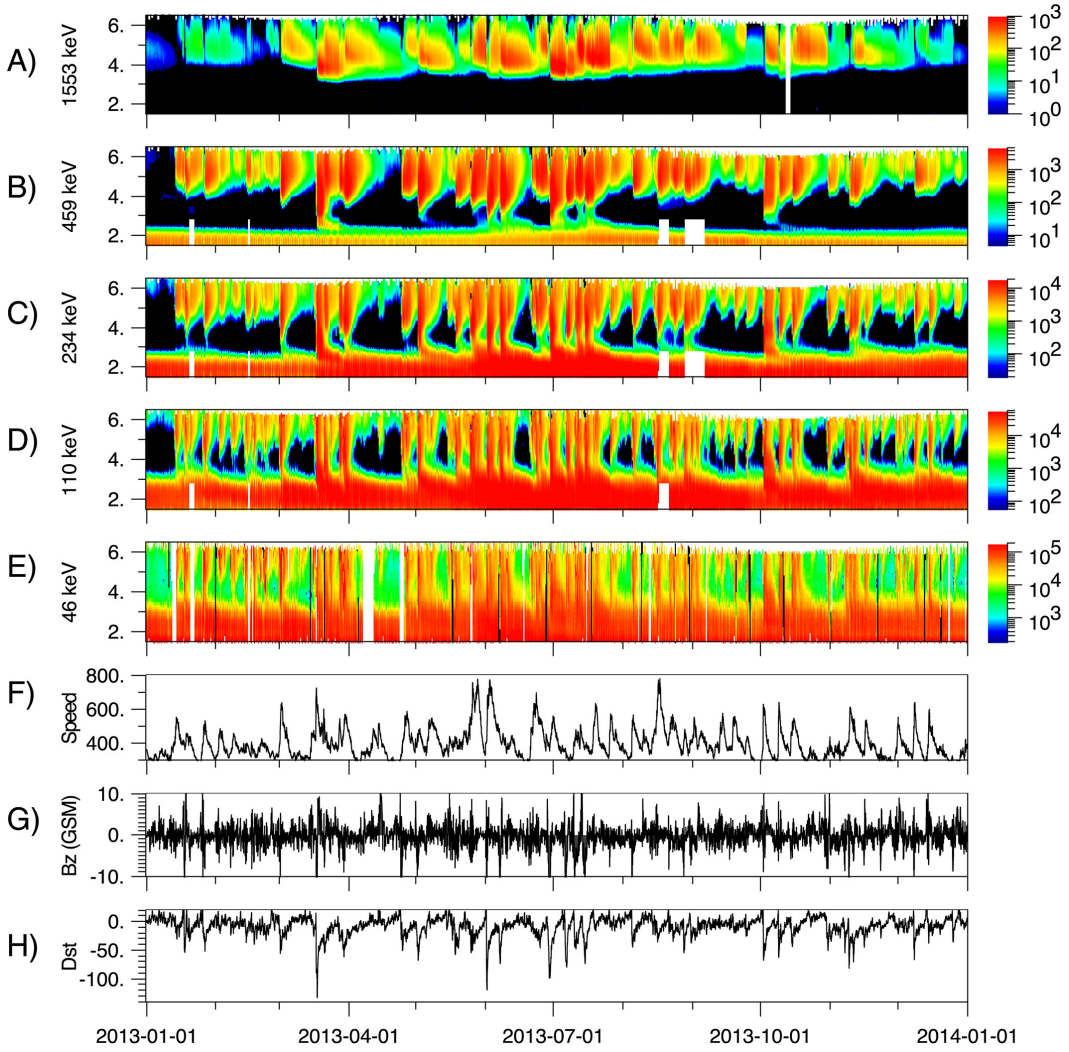

Figure 2.5: (a-e) Background-corrected fluxes of 1553 keV, 459 keV, 234 keV, 110 keV, 46 keV electrons as a function of L-shell and time from the Van Allen Probes measurements. (f-h) Variation of solar wind speed, IMF Bz, and Dst index in the year of 2013. From Reeves et al. [2016].

this is also one of the focuses in this thesis.

Since the state of the radiation belts is determined by a balance between transport, acceleration, and loss mechanisms, it is important to understand different physical mechanisms that can influence the radiation belts [Li and Hudson, 2019; Ripoll et al., 2020, and references therein]. Various acceleration and loss mechanisms are discussed in the following subsections, 2.2.1 and 2.2.2.

2.2.1 Acceleration mechanisms

There are two major acceleration mechanisms of radiation belt electrons: inward radial transport and local acceleration. Inward radial transport can accelerate radiation belt electrons in the violation of the third adiabatic invariant while conserving the first two adiabatic invariants. When the fluctuation of an electric and/or magnetic field is on a timescale comparable to the drift period of radiation belt electrons (mHz), the third adiabatic invariant can be violated, and energetic electrons can experience a random walk in its radial location; this is also known as radial diffusion. The net radial diffusion direction depends on the radial gradient: a positive radial gradient leads to an inward diffusion and vice versa (See Figure 2.6). As the first invariant is conserved, an inward transport of electrons moves them to a stronger magnetic field region and thus increases the electron momentum/energy. Therefore, inward radial transport of radiation belt electrons can lead to electron acceleration.

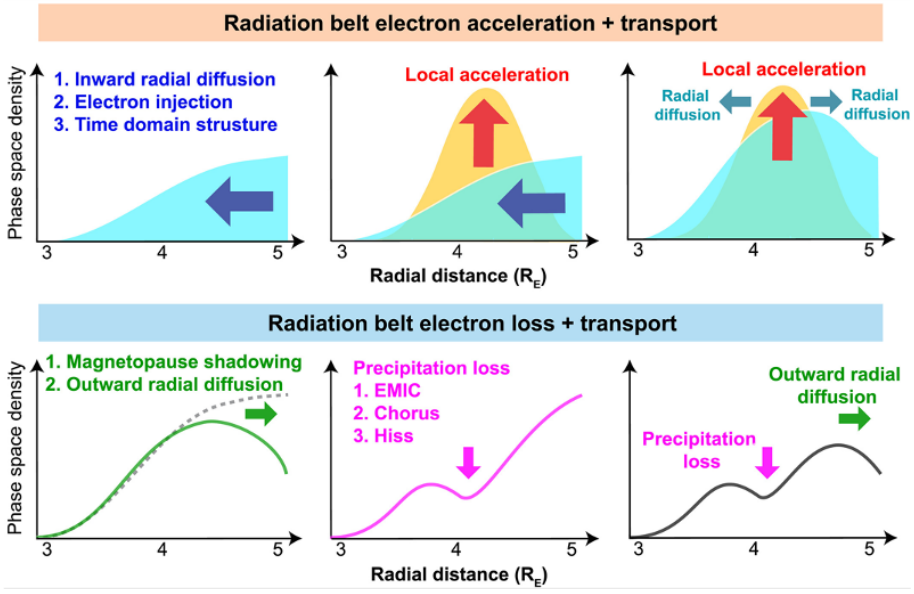

Figure 2.6: (top) Physical processes that can cause acceleration and transport of radiation belt electrons. (bottom) Loss mechanisms of the radiation belt electrons. Adapted from Li and Hudson [2019].

On the other hand, the local acceleration can happen through a Doppler-shifted cyclotron

resonance between energetic electrons and waves. As described in the previous section, this type of wave-particle interaction violates the first adiabatic invariant and can cause pitch angle diffusion and energy diffusion. Since the local acceleration occurs on a much shorter timescale (within multiple cyclotron periods), the local acceleration usually creates a PSD profile that has a peak near the heart of the radiation belts. Waves such as whistler-mode chorus waves that reside outside the plasmasphere can efficiently interact with hundreds of keV electrons and energize them to MeV electrons [e.g., Reeves et al., 2013]. Studies also showed that magnetosonic waves can locally accelerate energetic (100 keV to few MeV) electrons [e.g., Horne et al., 2007; Thorne, 2010].

2.2.2 Loss mechanisms

The trapped radiation belt electrons can be lost via two major loss mechanisms: precipitation loss into the atmosphere and magnetopause shadowing. Precipitation losses are often associated with the pitch angle diffusion of trapped energetic electrons into the loss cone through wave-particle interactions. Various waves can resonantly interact with radiation belt electrons and cause pitch-angle scattering. For instance, plasmaspheric hiss waves are a loss mechanism for energetic electrons by scattering energetic electrons to the loss cone, which contributes to the formation of the slot region [e.g., Lyons and Thorne, 1973; Meredith et al., 2007]. Whistler chorus waves outside the plasmasphere have a dual role in both the acceleration and loss of radiation belt electrons. The pitch angle scattering of energetic electrons by chorus waves is believed to cause microbursts, a short-duration (<1 sec) bursts of enhanced electron precipitation in the loss cone [e.g., Nakamura et al., 2000; Thorne et al., 2005; Breneman et al., 2017; Mozer et al., 2018]. Electromagnetic ion cyclotron (EMIC) waves can also cause pitch angle diffusion of radiation belt electrons and is an efficient loss mechanism for relativistic electrons [Usanova et al., 2010, 2014; Blum et al., 2015]. In addition, very low frequency (VLF) waves emitted by ground-based transmitters and lightning-generated waves (in the 10-60 kHz) can cause loss energetic (hundreds of keV) electrons in the inner belt ($L < 2$) [e.g., Inan et al., 1985; Abel and Thorne, 1998; Bortnik et al., 2002, 2006; Cohen, 2013].

In addition to the atmosphere, the magnetopause is another ultimate sink of radiation belt electrons. Magnetopause shadowing refers to the loss of energetic electrons into the magnetopause. It is a major loss process during storm times when the solar wind compresses the magnetopause to a lower L. The magnetopause compression forms a sharp negative gradient in the electron distribution, leading to an outward radial diffusion of electrons. As the magnetopause location moves to lower L, energetic electrons whose drift path intersects with the magnetopause will be lost. A combination of a magnetopause shadowing and outward radial diffusion leads to a rapid loss of radiation belt electron [e.g., Ukhorskiy et al., 2006; Loto'Aniu et al., 2010; Turner et al., 2012]. Figure 2.6 illustrates the competitive influence of different acceleration and loss mechanisms on radiation belt electrons and indicates the challenge to determine the relative contribution of each mechanism.

2.3 Plasmasphere

The plasmasphere is a cold (∼eV) and dense (10 - 1000 cm^{-3}), torus-shaped plasma region that corotates with Earth and often overlaps with the radiation belts. The boundary of the plasmasphere is determined by a balance between the corotation electric field and the convection electric field [Kivelson and Russell, 1995; Kavanagh et al., 1968]. This section first discusses the adiabatic drift of charged particles under the influence of the corotation and convection electric fields as well as the gradient-B drift before introducing the evolution of the plasmapause during enhanced convection. It also describes the relationship between the plasmasphere and the radiation belt electrons at the end of the section.

2.3.1 Drift paths of cold and hot plasma

The rotation of Earth's magnetic field produces a corotation electric field that dominates the near-Earth region with its direction pointing radially inward toward Earth [Alfvén, 1963; Kivelson and Russell, 1995]. Representing Earth's magnetic field as a dipole magnetic field, the

corotation electric field and the corotation potential can be written as

$$\boldsymbol{E_{corotation}} = -\boldsymbol{\nabla}\Phi_{corotation} \tag{2.11}$$

$$\boldsymbol{E_{corotation}} = -(\boldsymbol{\omega_E} \times \boldsymbol{r}) \times \boldsymbol{B} \tag{2.12}$$

$$E_{corotation} = -\frac{\omega_E B_0 R_E^3}{r^2} \tag{2.13}$$

$$\Phi_{corotation} = \frac{-\omega_E B_0 R_E^3}{r} \tag{2.14}$$

where ω_E is the angular velocity of Earth, B_0 is the magnetic field strength at Earth's surface at the equator, R_E is Earth's radius, and r is the distance from the center of Earth in the equatorial plane.

In addition, the interaction of solar winds with Earth's magnetosphere generates a convection electric field that can be approximated as a uniform dawn-to-dusk electric field [Baumjohann and Treumann, 1996], which can lead to a sunward ExB drift of charged particles. The potential representing the uniform dawn-to-dusk electric field in the equatorial plane is

$$\Phi_{convection} = -E_0 r sin\phi \tag{2.15}$$

where E_0 is the electric field strength and ϕ is the coordinate angle that is zero at local noon, $\pi/2$ at local dusk, π at local midnight, and $3\pi/2$ at local dawn.

Combining the effects of gradient B drift, convection and corotation electric field drift, the total drift velocity can be written in this form,

$$v_D = \frac{\boldsymbol{B} \times \nabla\Phi_{eff}}{B^2} \tag{2.16}$$

where B is the local magnetic field strength, $\Phi_{eff} = -E_0 r sin\phi + \frac{\mu B_0 R_E^3}{qr^3} - \frac{\omega_E B_0 R_E^3}{r}$ and $\frac{\mu B_0 R_E^3}{qr^3}$ is the potential due to gradient B drift. The particles drift along paths of constant Φ_{eff}. In the case of cold plasma like those in the plasmasphere ($\mu \sim 0$), $\Phi_{cold} = -E_0 r sin\phi - \frac{\omega_E B_0 R_E^3}{r}$. Note that the $\Phi_{corotation}$ is inversely proportional to r while $\Phi_{convection}$ is proportional to r. In other words, the corotation electric field dominates near Earth, while the convection electric field takes over further from Earth.

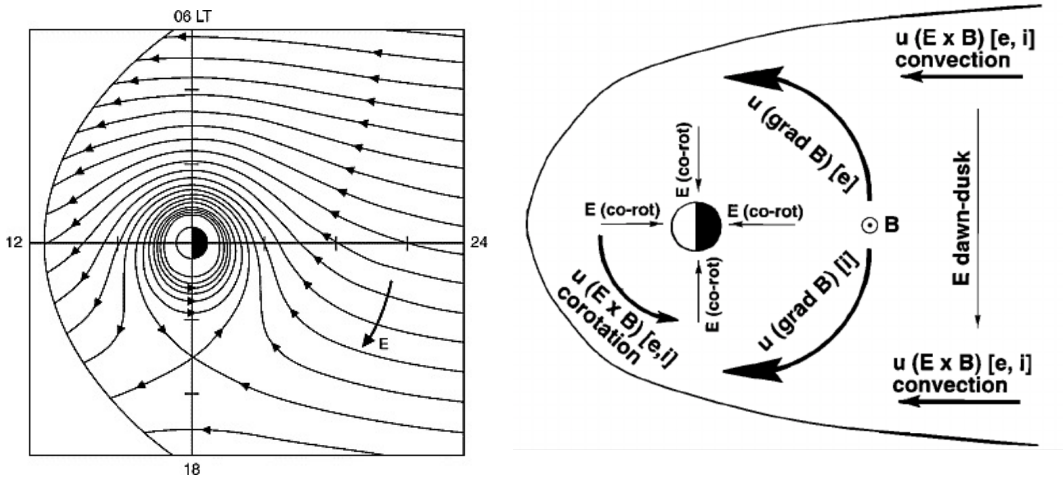

Figure 2.7: (left) Drift path of cold plasma in the equatorial plane as a superposition of a uniform convection electric field and the corotation electric field. From Russell [2003]. (right) An illustration of different components of particle drifts and the corresponding electric fields in the magnetosphere. From Friedel et al. [2001].

Figure 2.7 presents the drift paths of a cold particle, $\mu \sim 0$, in the equatorial plane under the influence of time-independent convection and corotation electric fields [Russell, 2003]. The outermost closed trajectory indicates the position of the magnetopause and the separatrix between the closed trajectories that circle Earth and those with open drift paths. Near the dawn sector, both corotation and convection electric fields act in the same direction, making the particles drift sunward; in the dusk sector, the competition between the corotation and convection electric field eventually contributes to the formation of a plasmaspheric bulge [Chappell, 1972]. In reality, the strength of the convection electric field varies with time. During geomagnetic active periods, the convection electric field enhances, and the separatrix that separates open and closed drift paths (also known as the Alfvén layer) moves inward. The slowly-rotating plasmaspheric particles that were in the closed trajectory region could find themselves in the open trajectory region as they rotate around Earth [Grebowsky, 1970]. This leads to the formation of the plasmaspheric plume, also known as the drainage plume, that extends to the dayside magnetopause, as shown in Figure 2.8 [Ebihara and Miyoshi, 2011, and references therein]. The cold plasma in the plasmaspheric plume are then 'drained' or lost to the dayside magnetopause, although the fate of the drained

plasma on or outside the magnetopause is not well-known [e.g., Elphic et al., 1997; Borovsky and Denton, 2008].

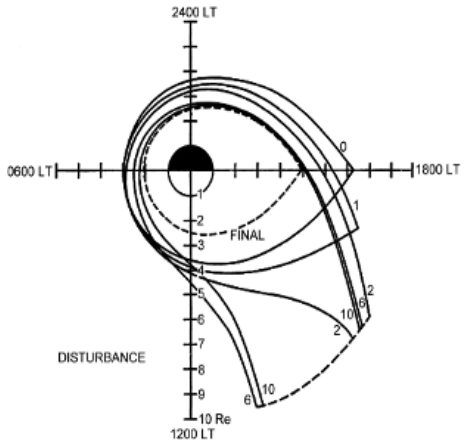

Figure 2.8: The evolution of the cold plasma drift path in a time-dependent convection electric field. The numbers (0 to 10) near the edge of plasmaspheric bulge indicates the time in hours (i.e., 0 to 10 hours). From Grebowsky [1970]

To complete the discussion, let's look at the case of hot plasma, such as plasmasheet particles, whose drifts are mainly under the influence of the convection electric field and gradient-B drift [e.g., Friedel et al., 2001, and references therein] (here I only consider the case of 90 degree equatorial particles; for particles with $<$ 90 degree equatorial pitch angles, the curvature drift will also contribute to the particles' azimuthal drift). For simplicity, we assume the contribution of the corotation electric field to the drift of hot plasma is small compared to the gradient-B drift and convection electric field (which is true for most plasmasheet particles, as noted in Kivelson and Russell [1995]) and represent the effective potential as $\Phi_{hot} = \frac{\mu B_0 R_E^3}{qr^3} - \frac{\omega_E B_0 R_E^3}{r}$. Since the electric drift is independent of particle charge, the convection electric field moves both electrons and ions sunward. As the particle comes closer to Earth, the magnetic field strength it experiences increases, and the gradient-B drift dominates over the sunward ExB drift. Unlike ExB drift, the gradient-B drift is charge-dependent and causes electrons to drift eastward and ions to drift westward. The separatrix between the open and closed drift path is also known as the Alfvén layer, which is often approximated as the boundary of the plasmasheet (See Figure 2.9) [Kavanagh et al., 1968; Korth

et al., 1999; Friedel et al., 2001]. The more energetic particles will experience a stronger gradient-B drift and start the azimuthal drift at a distance further from Earth. Therefore, more energetic particles will have an Alfvén layer further from Earth.

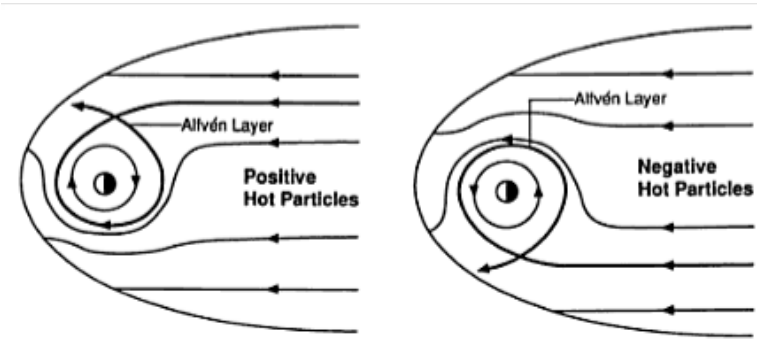

Figure 2.9: Drift path of 90-degree equatorial pitch angle, hot plasma under the influence of both time-independent convection electric field and gradient-B drift. From Kivelson and Russell [1995]

2.3.2 Plasmasphere dynamics

As shown in Figure 2.8, the plasmasphere is a dynamic region that varies with time as determined by a balanced between corotation and (time-dependent) convection electric fields. Figure 2.10 presents the evolution of the observed and simulated plasmasphere during a storm period. During the enhanced convection period, the erosion of the plasmasphere occurs, and the plasmapause near the midnight sector began moving inward, forming an indentation. This indentation will widen in magnetic local time (MLT) as the plasmaspheric particles slowly rotate eastward (an average time for cold plasma in the plasmasphere to conduct a full corotation is ~ 30 hours [Sandel et al., 2003]). In the meantime, the enhanced convections lead to the formation of a plasmaspheric bulge that gradually evolves into a broad dayside plasmaspheric plume as a result of the time-varying convective electric field [e.g., Grebowsky, 1970], as shown in Figure 2.10 (a-f) and (g-h). As the erosion progresses during enhanced convection, the plasma is steadily removed from the plasmasphere to the dayside magnetopause, which lead to the narrowing of the dayside plasmaspheric plume [e.g., Borovsky and Denton, 2006; Goldstein et al., 2004]. Meanwhile, a shoulder-like

structure, where the predawn plasmapause moves outward while the postdawn plasmapause moved inward, is also observed as the main plasmasphere rotates eastward [Goldstein et al., 2005]. Although the actual cause of the plasmaspheric shoulder is still under active investigation, theoretical studies have suggested that over-shielding of the inner magnetosphere (which generally refers to when the inductive or shielding electric field - a result of ring-current-ionosphere coupling during enhanced convection - with a dusk-to-dawn direction remains while the dawn-to-dusk convection electric field strength decreases, see Goldstein [2006] and references therein to learn more) could contribute to such a feature. As the convection strength decreases, the plume slowly rotates and wraps around the main plasmasphere.

More generally, the evolution of the plasmasphere is divided into four phases [e.g., Goldstein et al., 2019]: the initial phase where the plasmasphere expands to a high L shell after a prolonged quiet period, the sunward surge that marks by the erosion of the plasmasphere and the formation of the broad dayside plasmaspheric plume and often occurs during the main phase of the geomagnetic storm [Carpenter and Lemaire, 1997; Goldstein et al., 2005], the plume narrowing phase that occurs near the minimum Dst during a storm period [Goldstein et al., 2005, 2019], and the plume rotating phase as the convection strength decreases during the recovery storm phase [Goldstein and Sandel, 2005; Goldstein et al., 2014].

2.3.3 Relation to radiation belt electron dynamics

As discussed in the previous section, the plasmapause location is closely related to the favored regions of different magnetospheric waves. For instance, plasmaspheric hiss waves reside mostly inside the plasmasphere [e.g., Malaspina et al., 2016, and references therein] and can scatter radiation belt electrons. On the other hand, chorus waves can cause local acceleration of radiation belt electrons and are mainly found outside of the plasmapause location. It suggests an intimate role played by the plasmasphere in shaping the dynamics of radiation belt electrons.

Many previous studies have examined the relationship between radiation belt electrons and the plasmapause [e.g., Goldstein et al., 2005; Li et al., 2006; Goldstein et al., 2016]. Li et al.

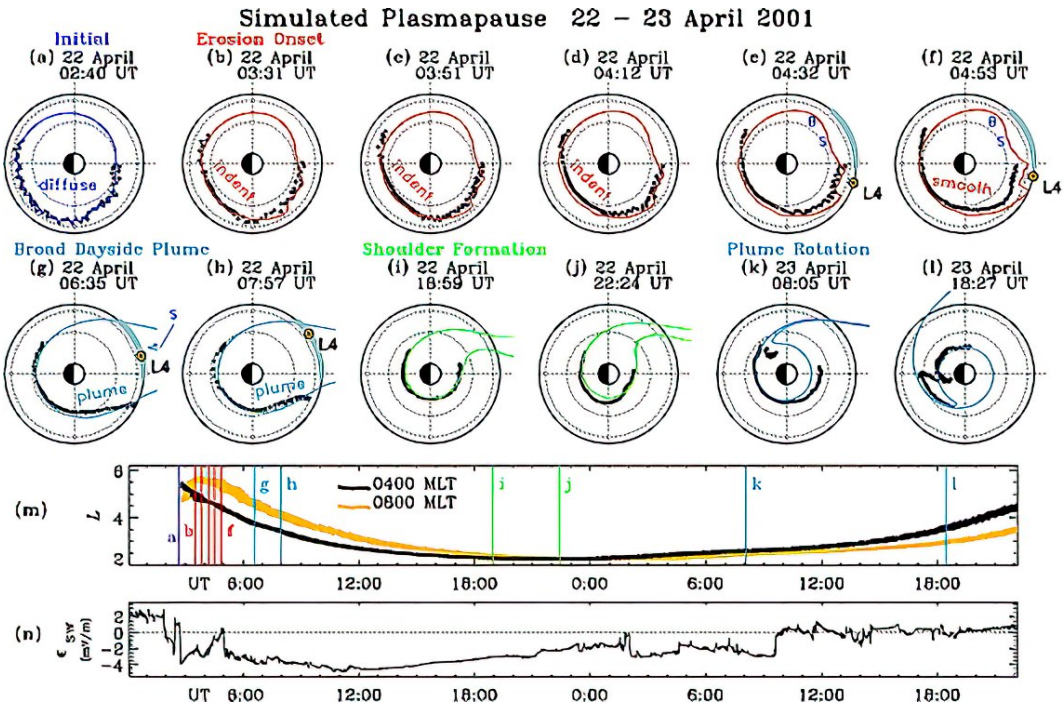

Figure 2.10: The evolution of the plasmapause between 22-23 April 2001. The plasmapause observations were from the IMAGE EUV imager and indicated by the black dots, while the solid lines show the simulated plasmapause that was driven by a time-varying convection E-field with contributions from the solar wind and the subauroral polarization stream (SAPS). It is plotted in the SM-coordinate magnetic equatorial plane. From Goldstein et al. [2005]

[2006], for instance, used Solar, Anomalous, Magnetospheric Particle Explorer (SAMPEX) measurements to study the relationship between the inner edge of the relativistic electrons in the outer belt and the innermost plasmapause locations. Figure 2.11 shows the long-term flux variation of 2-6 MeV electrons between 1993 to 2004 and how this variation corresponds to the minimum plasmapause location (L_{pp}). Since the shape of the plasmapause is local-time dependent, the minimum plasmapause location refers to the distance of the plasmapause that is closest to Earth among all local time. Their analysis suggests that the minimum L_{pp} is the innermost limit of the initial enhancement of relativistic electrons in the outer belt. On a related note, studies also suggest a close relationship between the remnant belt and the minimum plasmapause location [Thorne et al., 2013; Pinto et al., 2018, 2020; Li et al., 2021]. According to Thorne et al. [2013], the long term stability of the remnant belt is likely because the plasmasphere shields these relativistic electrons

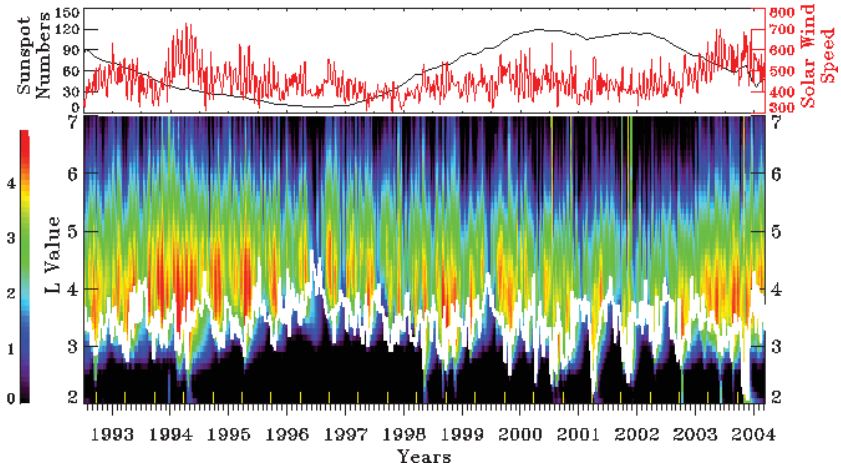

Figure 2.11: (Top) Variations of yearly window averaged sunspot numbers (black curve) and the solar wind speed (km/s, red curve) between 1993 to 2004. (bottom) Monthly window-averaged electron fluxes of 2-6 MeV electrons. The white curve represents every 10-day minimum Lpp from an empirical model [O'Brien and Moldwin, 2003]. From Li et al. [2006]

from the dynamic process such as local acceleration by chorus waves, and thus these populations are only subjected to the slow decay from its interactions with hiss waves. Most studies, however, focus on the relationship between relativistic electrons (> 1-MeV) in the radiation belts and the plasmapause. Therefore, one of the goals in this thesis is to improve our understanding of energetic electrons (tens of keV to few MeV) in the inner magnetosphere by examining the relationship of energetic electron dynamics with the plasmapause location. Details of our related work can be found in Chapters 3-5.

2.4 Challenges of measuring energetic particles

In-situ measurements have contributed to our understanding of energetic particles in the inner magnetosphere. High-quality measurements are often required for detailed analysis, but measuring energetic particles is not an easy task. It requires an understanding of how particles interact with matter and potential electronics errors when capturing these particles. The challenges lie in not just measuring the particles, but also extracting flux from a count rate reliably. This section provides a brief discussion on these topics that serves as useful background for our work in

Chapters 6 and 7.

2.4.1 Interaction of particles with matter

The fundamental aspect of measuring energetic particles is the understanding of how the particles interact and lose energy in matter. The amount of energy loss during these stochastic microscopic interactions depends on the types/energies of the particles and the material that the particles interact with. Stopping power is defined as the differential energy loss of a particle within the material divided by the corresponding differential path length, dE/dx [Knoll, 2010]. This is also known as the linear stopping power with units like MeV/mm. For better comparison between materials of different density, it is also expressed in mass stopping power ($MeV/(g/cm^2)$), where the linear stopping power is divided by the density of the material. Range is also a useful quantity that describes the maximum path length a particle can penetrate before losing all of its energy in the material.

The mean stopping power of moderately relativistic ($0.1 < \beta\gamma <$1000) particles is well described by the Bethe formula [Zyla et al., 2020, and references therein],

$$< \frac{-dE}{dx} >= Kz^2 \frac{Z}{A\beta^2}[\frac{1}{2} ln \frac{2m_e c^2 \beta^2 \gamma^2 W_{max}}{I^2} - \beta^2 - \frac{\delta(\beta\gamma)}{2}] \tag{2.17}$$

where $K = 4\pi N_A r_e^2 m_e c^2$, N_A is the Avogadro′s number, r_e is the electron radius, z is the charge number of incident particles, Z is the atomic number of the absorber, A is the atomic mass of the absorber, β is the ratio of the particle′s velocity to speed of light ($\frac{v}{c}$), $m_e c^2$ is the electron mass energy (0.511 MeV), γ is the Lorentz factor, W_{max} is the maximum possible energy transfer to an electron in a single collision [MeV], I is the mean excitation energy [eV], and $\delta(\beta\gamma)$ is the density effect correction to ionization energy loss. Notably, the mean stopping power function is a function of $\beta\gamma$, which means that it is independent of particle types and only depends on the momentum (GeV/c) of the particles. Multiple x-axes in Figure 2.12 show examples of how $\beta\gamma$ can be translated to a particle′s momentum by multiplying $\beta\gamma$ with M, which is the incident particle mass in MeV/c^2. The mean stopping function also exhibits similar qualitative trends

under different materials: the stopping power of particles decreases as the particle's momentum and energy increases until it reaches the minimum, which is also known as the minimum ionization point [Knoll, 2010; Zyla et al., 2020]. After the minimum ionization point, the stopping power increases slightly and remains relatively constant for more relativistic particles.

The Bethe equation is useful but limited to describe the average energy loss behavior of particles while in reality, we are likely to observe a wide range of responses, depending on the particle′s type. Here we focus on protons and electrons [Vampola, 1998; Zyla et al., 2020], which exhibit very different behaviors when interacting with matter. Protons generally lose energy in a medium through ion-electron interactions that transfer a small amount of energy in a single interaction due to the large mass ratio between the proton and electron. For the same reason, the angular scattering of protons is negligible and thus the interactions and the energy loss of protons in a medium is generally well-defined as compared to electrons. However, the same cannot be said for electrons. When electrons interact with matter, they lose energy in ways such as excitation and ionization of the atoms and are often associated with large angular scattering due to the comparable mass between the incident electrons and orbital electrons in the medium. This results in fluctuations in path length and energy losses for individual electrons, also known as range and energy straggling. Therefore, electrons are known to have a wider energy loss distribution, rather than a well-defined distribution like protons.

As detailed in Vampola [1998], measuring energetic particles, particularly the electrons, is a challenging task. The key challenge is to make an accurate inference of what the incident energies are, given the mere information of the energy deposit on the detectors. By knowing how much particles lose energy when passing through the detector, dE/dx, one can develop keen insights on the most probable energy of the incident particle. A careful characterization of the instrument response function with good statistics is also necessary, especially with electrons which involve straggling and scattering that makes it harder to infer incident energy from the deposited energy.

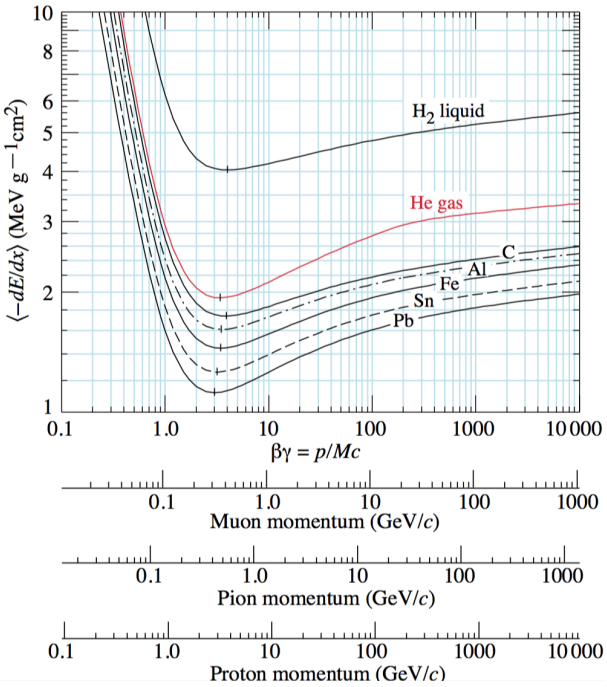

Figure 2.12: Mean energy loss rate in liquid hydrogen, gaseous He, carbon, aluminum, iron, tin and lead. Radioactive effects are not included, which will become significant for muons in iron for $\beta\gamma \gtrapprox 1000$. From Zyla et al. [2020]

2.4.2 Deadtime, pileup, and chance coincidence

A count is a pulse that is registered by the detector system. An ideal detector system can capture all incident particles that hit on the detector as counts. But in reality, the limitation of an electronic system could result in detection errors such as mistaking two pulses as a single pulse or miscounting some true events. The challenge is, therefore, to estimate these errors and obtain the 'error-free' counts. This subsection discusses errors caused by dead time, pileup and chance coincidence and how they can be estimated using statistical analysis [Knoll, 2010].

Almost all detector system requires a minimum time to separate two pulses, and this minimum time separation is called the deadtime of the system, τ. During the deadtime, any new event that occurs will not be registered by the detector system. However, there is always some probability that a true event occurs too quickly after a preceding event, especially when

high counting rates are encountered. Therefore, these 'dead time' losses need to be corrected from measurements. Two common models of deadtime behavior in a detector system are paralyzable and nonparalyzable models [Knoll, 2010]. In a paralyzable detector, a true event that happens during the deadtime will not just be lost, but will extend the deadtime by another period τ, paralyzing the system for a longer period. A non-paralyzable system is one that an event that occurs during the deadtime will simply be missed, without extending the deadtime.

Due to the difference in the paralyzable and non-paralyzable models, the deadtime corrections are different for each model. In the non-paralyzable case, the fraction of time when the detector is dead is given by $m\tau$, where m is the recorded count rate and τ is the system dead time. The rate at which true events are lost is $n - m = nm\tau$, where n is the actual count rate. We can rewrite the equation to get the actual count rate, n:

$$n = \frac{m}{1 - m\tau} \tag{2.18}$$

In the paralyzable system, the dead period is not always a fixed length. Instead, we note that the measured count rate, m, is the same as the rate of event occurrences with a time interval between true events exceeding τ. The distribution function for intervals between adjacent random events, $I(t)dt$, can be obtained by realizing that it is a product of the probability of no events during time from 0 to t, $P(0)$, and the occurrence probability of an event during dt, rdt, i.e., $I(t)dt = P(0) \times rdt$. Any random process where the average time between events is known can be characterized by a Poisson random process. Therefore, the probability of no events between time= 0 to t, $P(0)$ can be determined using the poisson distribution,

$$P(x) = \frac{(\bar{x})^x e^{-\bar{x}}}{x!} \tag{2.19}$$

where $\bar{x}$ is the average number of recorded events and x is the number of occurrence. $P(0)$ and

$I(t)dt$ can be represented as follows:

$$P(0) = \frac{(rt)^0 e^{-rt}}{0!} \tag{2.20}$$

$$P(0) = e^{-rt} \tag{2.21}$$

$$I(t)dt = re^{-rt}dt \tag{2.22}$$

where r is the count rate and t is the total time when the count rate is recorded. In our case, the distribution function for intervals between random events occurring at a true rate of n can be written as

$$P(T)dT = ne^{-nT}dT \tag{2.23}$$

and the probability of event occurrences at a time interval larger than τ is found by integrating this distribution between τ and ∞,

$$P(\tau) = \int_{\tau}^{\infty} P(T)dT = e^{-n\tau} \tag{2.24}$$

The rate of events that occur at t $> \tau$ is then a product between this probability and the true rate, n. This gives us the deadtime estimate for a paralyzable system:

$$m = ne^{-n\tau} \tag{2.25}$$

Unlike the non-paralyzable model, the true rate, n, for a paralyzable model cannot be solved explicitly [Knoll, 2010]. Instead, it must be solved iteratively when computing n from m and τ.

A pile up is the superposition of two or more pulses within the charge collection window that is mistaken by the detector as a single pulse at a higher amplitude. The consequence is that the detector will measure a higher count of more energetic particles and a lower count of less energetic particles. Like deadtime, we can estimate the pileup effect through statistical analysis by assuming that the events that are detected by the system can be represented as poisson distributed random processes, which is true for energetic particles in the inner magnetosphere. The two-event pileup correction is a correction with the assumption that the superposition only involves two pulses that occur within the resolution time of the detector, τ (see also Knoll [2010]; Selesnick and Stone

[1991]). The probability of no events occurring in channel j within τ is $P(0) = e^{-r_j\tau}$, where r_j is the rate of events in channel j. A two-event pile up occurs when: a true event at $t = 0$, following by a second event that occurs between $0 < t < \tau$ and no other events occur between t and $t + \tau$. The probability of such events can be represented as

$$P(1) = \int_0^\tau \underbrace{\text{probability of no event in channel j}}_{\text{0-t}} \underbrace{\text{probability of event in channel j dt}}_{} \underbrace{\text{probability of no event in all channels}}_{\text{between t } +\tau} \quad (2.26)$$

$$P(1) = \int_0^\tau e^{-r_j t} r_j dt e^{-R\tau} \quad (2.27)$$

$$= e^{-r_j\tau}(1 - e^{-r_j\tau}) \quad (2.28)$$

where r_j is the true count rate of channel j and R is the integral rate. To obtain the count rate of such pileup events that occur in, say, channel i, we can simply multiply the count rate in channel i with this probability. The count rate in channel k with a two-event pile up is then

$$r_k^{p2} = \underbrace{\text{pile-up free count rate in channel k}}_{} + \underbrace{\text{events that would be lower channels but pile up into k}}_{} - \underbrace{\text{events that would be in channel k but pile up into higher channel}}_{} \quad (2.29)$$

$$= r_k + e^{-\tau R}\Big[\sum_{i=1}^{k-1} r_i(1 - e^{-r_{k-i}\tau}) - \sum_{i-1}^{N}\big[r_i(1 - e^{-r_k\tau} + r_k(1 - e^{-r_i\tau})\big]\Big] \quad (2.30)$$

Naturally, we can extend this analysis to three-event pileup, etc. An interested reader is referred to Knoll [2010, Eq. 17.37] for more detailed discussion on multiple-event pile up.

In a detector system where multiple detectors are involved, coincidence counting is commonly used to measure high energy particles by regarding detection from multiple detectors within the resolution time, τ to be a single event. Chance coincidence can occur when, instead of a single particle that triggers multiple detectors, two or more particles reach different detectors within the resolution time and are registered as a single particle. This could result in a higher count in the high-energy channel. A two-fold chance coincidence is the sum of probability of a particle reaching detector 2 within time τ after the detector 1 is triggered and the probability of a particle reaching detector 1 within time τ after the detector 2 is triggered. We can expand e^{rt} using Taylor's expansion. Typically, the resolving time is much smaller than the average rates in detector 1 and detector

2, and thus we can ignore the high-order terms and express e^{rt} as $e^{rt} = 1 - rt$. The two-fold chance coincidence is eventually given by

$$r_{ch} = 2\tau r_1 r_2 \tag{2.31}$$

where r_1 and r_2 are the count rates at detector 1 and 2, respectively.

Chapter 6 utilizes the equations provided in this subsection to estimate the pileup effect in a new instrument, REPTile-2. It is noted that the effect of pileup, deadtime, and chance coincidence on actual measurements varies for different instruments and depends on the satellite's orbit. In the case of REPTile-2, deadtime and chance coincidence effects are not studied in the current study, but that will be done as part of the future data calibration.

2.4.3 Challenge to convert measured count rates to flux

Finally, the conversion of an observed count rate to flux is an important process that requires careful treatment to ensure data quality. The relationship between the count rate and the flux is described by

$$r_i = \int G_i(E) j(E) dE \tag{2.32}$$

where r_i is the count rate in channel i, $G_i(E)$ is the instrument response (of channel i, with a unit of $cm^2 sr$) to a particle's incident energy, E, and $j(E)$ is the differential flux spectrum as a function of energy. A detector system typically accumulates counts within a certain time period, and this gives us the count rate. However, depending on the instrument design, the instrument has a varying degree of efficiency at measuring different particle types and energies. Therefore, a count rate generally does not directly translate to flux.

To compute a count rate, given the instrument response function and the flux spectrum, is a rather simple forward problem. On the other hand, to extract flux from a count rate is an inverse problem that is not as straightforward to solve. An inverse problem can be further divided into underdetermined, overdetermined and mixed determined. An underdetermined problem is one when the number of binned channels, N, is less than the number of incident energy whose fluxes we

are trying to estimate, M. An overdetermined problem is when N is more than M. A problem that is simultaneously underdetermined in some channels but overdetermined in other channels is known as a mixed determined problem, which is often the case for radiation belt particle measurements. Chapter 7 will discuss two approaches that can be used to solve this type of inverse problems and the limitation of each method.

Chapter 3

On the Initial Enhancement of Energetic Electrons and the Innermost Plasmapause Location: CME-Driven Storm Periods

This chapter is based on the published work of Khoo et al. [2018], On the initial enhancement of energetic electrons and the innermost plasmapause locations: CME-driven storm periods, Journal of Geophysical Research: Space Physics, 123, 9252-9264, doi:10.1029/2018JA026074.

3.1 Introduction

In the inner magnetosphere, energetic electrons (tens keV to >MeV) are nominally trapped in the inner and outer electron radiation belts. The inner electron radiation belt is centered near 1.5 Earth radii (R_E), as measured from the center of the Earth in the equatorial plane, whereas the outer electron belt is most intense around 4-5 R_E [e.g., Baker et al., 2013; Li et al., 2001]. Between the inner and the outer electron radiation belts lies the "slot" region that has the lowest electron fluxes during geomagnetic quiet periods [e.g., Lyons and Thorne, 1973]. However, in reality, the electron belts are often waning and waxing, merging with each other. The observed state of the radiation belts is a complex balance between acceleration, transport, and loss mechanisms [Reeves et al., 2003]. In the present study, we focus on electron flux enhancement events and the underlying mechanisms of the observed electron dynamics associated with the plasmapause location.

The plasmasphere is a dense, cold (∼1eV) plasma region that co-rotates with the Earth. Like radiation belt electron populations, it also exhibits a dynamic response to the changes in the

magnetospheric environment [Goldstein, 2006, and references therein]. Its dynamics are largely controlled by the balance between corotation and convection electric fields. During times of strong convection, the plasmasphere is eroded, and its outer boundary, the plasmapause (L_{pp}), can occasionally move to L<2 [e.g., Baker et al., 2004; Foster et al., 2016]. As the enhanced convection recedes, the plasmapause can extend outwards beyond L=6 [e.g., Moldwin et al., 2002; O'Brien and Moldwin, 2003]. The drastic density difference inside and outside of the plasmasphere affects various waves, their growth, and their interactions with radiation belt electrons. Wave-particle interactions [Thorne, 2010, and references therein] can lead to violations of the adiabatic invariants, which may result in energy diffusion, radial diffusion, or pitch angle scattering. For instance, due to the low plasma density and thus higher phase velocity outside of the plasmasphere, chorus whistler waves, which reside mostly outside of the plasmapause, have been proven to be capable of accelerating hundreds of keV electrons to >1 MeV [e.g., Horne et al., 2005a,b; Summers et al., 1998; Thorne et al., 2013]. Meanwhile, electromagnetic ion cyclotron (EMIC) plasma waves, prominently existing near the plasmapause, serve as an efficient loss mechanism that precipitates relativistic electrons to the atmosphere [e.g., Miyoshi et al., 2008; Summers and Thorne, 2003; Xiang et al., 2017]. Plasmaspheric hiss, which is highly associated with higher electron density regions and mainly found within the plasmasphere, is efficient in scattering electrons over a broad range of energies from tens to hundreds of keV that leads to the precipitation loss [Thorne, 2010; Li et al., 2015]. Although the generation mechanisms and the characteristics of these waves can be greatly different, they all share a close connection with the plasmapause location [e.g., Malaspina et al., 2016; Tetrick et al., 2017].

In the past decades, there have been several studies on the relationship between electron enhancements and plasmapause locations. For instance, Baker et al. [2004] compared the electron flux measurements from the Solar, Anomalous, and Magnetospheric Particle Explorer (SAMPEX) with L_{pp} locations derived from Imager for Magnetopause-to-Aurora Global Exploration (IMAGE) observations and found that the L_{pp} locations tracked the inner edge of the outer radiation belt for relativistic electrons very well during the 2013 Halloween storm. Subsequent studies [e.g., Goldstein

et al., 2005; Li et al., 2006] examined the correlation between the electron enhancement and the plasmapause location over a prolonged period and demonstrated the same correlation. Particularly, Li et al. [2006], through studying 12-year >MeV electron flux measurements from SAMPEX and the Combined Release and Radiation Effects Satellite (CRRES), determined that the initial penetration of >MeV electrons was found consistently outside of the innermost L_{pp} (innermost of the average L_{pp} values derived from the O'Brien and Moldwin [2003] empirical plasmapause model). In contrast, the correlation between electron enhancements and the innermost plasmapause location for tens and hundreds of keV electrons is not well-studied. With the launch of Van Allen Probes, high energy- and temporal-resolution measurements of electrons from eV to MeV have become available; this offers an unprecedented opportunity to explore the relationship between initial electron enhancements and the innermost plasmapause location for tens and hundreds of keV electrons, which is the main goal of this study.

In this chapter, we establish an energy-dependence relationship between the initial electron enhancement and the innermost L_{pp} for ∼30 keV to ∼2MeV electrons. For the first time, we determine a remarkably consistent relationship between electron enhancements and the innermost plasmapause location over a wide range of electron energies (∼30 keV to ∼2MeV): the innermost location for the initial enhancement (L_{IE}) of energetic electrons in the above energy range is always observed to be outside of the innermost L_{pp} derived from established L_{pp} models [Goldstein et al., 2014; Liu et al., 2015]. We further quantify the relationship between the initial electron enhancements and the innermost L_{pp}, spatially and temporally, to shed light on the physical mechanisms behind the initial enhancements of radiation belt electrons. A drastic difference of the energy spectrum evolution inside and outside of the plasmasphere during storm periods is also reported in this study.

3.2 Methodology

3.2.1 Plasmapause models

In this study, the model-derived L_{pp} is preferred over the observational L_{pp} because the L_{pp} model can offer higher time-resolution L_{pp} for all magnetic local time (MLT) sectors, unlike the observational L_{pp} that is constrained by the orbit/period of the active spacecraft. Often, these spacecraft only encounter the plasmapause twice in each orbit. For instance, if measurements from Van Allen Probes, which are in a geostationary-transfer orbit with a ∼9-hour orbital period, were employed to determine the plasmapause locations, then the observational L_{pp} can only be identified at a specific MLT sector in each pass and measurements are separated by an interval of ∼2 to 6 hours. However, the L_{pp} dynamics varies within a timescale of an hour or less under strong convection conditions. Thus, the observational L_{pp} is not sufficient to identify the innermost L_{pp} among all MLT sectors, especially during active periods. Consequently, the model-derived L_{pp} location becomes a more desirable choice in the present study.

Two L_{pp} models are used in this study: the Liu et al. [2015] and the Plasmapause Test Particle simulation [Goldstein et al., 2014]. The Liu et al. model is a multivariate plasmapause empirical model based on observations from the Time History of Events and Macroscale Interaction during Substorms (THEMIS) mission. Using five years of THEMIS measurements (from 2009 to 2013), Liu et al. determined 5878 plasmapause crossings and used these crossings to establish the empirical model. In their study, a plasmapause crossing was identified by a factor-of-five change in plasma density within $\Delta L \leq 0.5$, which is a criterion commonly used in plasmapause studies [e.g., Carpenter and Anderson, 1992; Moldwin et al., 2002; O'Brien and Moldwin, 2003]. This empirical model uses five-minute averaged Sym-H, AL, AU indices and hourly averaged AE and Kp indices as inputs and provides L_{pp} outputs for all MLT sectors on a timescale as short as 5 minutes. Overall, the Liu et al. model demonstrated a good agreement with observations, particularly before and after the storm (e.g. See Figure 7 and 9 in Liu et al., 2015b). During the storm period, the model-derived L_{pp} can reproduce the IMAGE observational L_{pp} locations very well on the dawnside,

which is often associated with the innermost L_{pp} location during active periods [e.g., Liu et al., 2015; O'Brien and Moldwin, 2003], with differences less than 0.5 R_E. The model performance during the refilling/recovery phase is not as good, and the predicted L_{pp} is often 1.5 to 2 R_E higher than the observations. An additional caveat in this model is that it does not reproduce the plasmaspheric plume structure and the plasmaspheric boundary layer structure. Nonetheless, this does not affect the result of our analysis since our focus is the innermost L_{pp}.

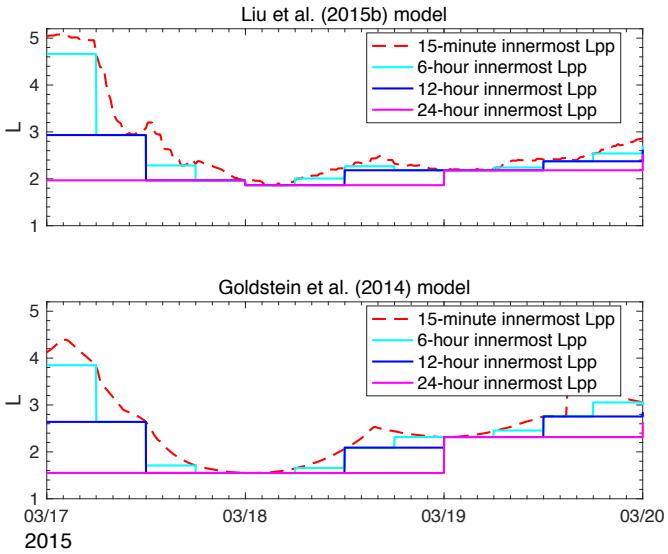

Figure 3.1: Comparison of 15-minute, 6-hour, 12-hour and 24-hour binned innermost L_{pp} derived from the Liu et al. [2015] model (top panel) and the Goldstein et al. [2014] model (bottom panel) during the March 17-20, 2015 storm period.

Another plasmapause model used in this study is the plasmapause test particle simulation [Goldstein et al., 2014]. The plasmapause in this model is represented as an ensemble of cold test particles under the influence of the $E \times B$ drift. The simulation is driven by the Volland-Stern convection electric field model [Stern, 1975; Volland, 1973] and an analytical electric field model [Goldstein et al., 2005] of the subauroral polarization stream (SAPS). Inputs to the model are the solar wind electric field, the solar wind-driven magnetospheric electric field, and the Kp index. Despite its simple setup, the Goldstein et al. [2014] model has successfully simulated 92% of the virtual plasmapause encounters by Van Allen Probes from 15-20 January 2013 (See Figure 5 in

Goldstein et al. [2014]). Generally, the plasmapause from the Goldstein et al. model performs better during storm periods where the convection is stronger than the recovery and quiet periods. The model uncertainty is taken into account when analyzing the findings in this study.

In the present study, we emphasize the need to identify the innermost L_{pp} in order to uncover the correlation between electron enhancements and the plasmapause. Accordingly, we first determined the innermost L_{pp} among all MLT sectors for each time step (15-minute resolution) as the innermost L_{pp}. To capture the actual innermost L_{pp} locations that are not easily reproduced through the plasmapause models, especially during the recovery phase where the strong convection recedes, we identified the innermost L_{pp} within 6-hour, 12-hour, and 24-hour periods (Figure 3.1). In general, 6-hour and 12-hour innermost L_{pp} capture the overall pattern of the innermost L_{pp} well, in contrast to the 24-hour innermost L_{pp}. At certain instances (e.g., 00:00 to 12:00 UT on March 17, 2013 in Figure 3.1), 6-hour innermost L_{pp} does a better job in tracing the innermost L_{pp} variations, as shown in Figure 3.1. However, unlike the 12-hour innermost L_{pp}, the 6-hour innermost L_{pp} is also more likely to be subjected to the slight dynamic variation of the L_{pp} locations as illustrated from 12:00 to 20:00 UT on March 18, 2013 (the cyan lines) in Figure 3.1. To determine the optimal choice of the innermost L_{pp}, we have performed the analysis using 6-hour and 12-hour innermost L_{pp} and verified that both yield very similar results. Nonetheless, since the 12-hour innermost L_{pp} produces a more consistent (with slightly lower uncertainties) outcome, the analysis results using 12-hour L_{pp} are reported in this study.

3.2.2 Overview of observations from January 2013 to July 2015

In the present study, we use high temporal and energy resolution electron flux data from Magnetic Electron Ion Spectrometer (MagEIS) aboard the Van Allen Probe A and B [Blake et al., 2013]. There are four MagEIS spectrometers on each spacecraft: one low-energy unit (20-240 keV), two medium-energy units (80-1200 keV), and one high-energy unit (800-4800 keV). We focused on MagEIS spin-averaged electron flux data from 30 keV to 2 MeV in this study.

The MagEIS electron flux data are commonly subjected to two major background con-

tamination sources [Claudepierre et al., 2015]: inner belt energetic protons and bremsstrahlung X-ray radiation by multi-MeV electrons. Generally, the trapped > tens of MeV protons in the inner belt that reside at L< 2.5 can contaminate/affect all energetic electron measurements [e.g., Li et al., 2015]. However, lower energy electrons, particularly tens of keV electrons, at L<2.5 are mostly unaffected by the background correction algorithms [Claudepierre et al., 2015] because their high flux level at L<2.5 dominates over the contamination caused by inner belt energetic protons. As expected, the contamination of energetic inner belt protons is more apparent for >500 keV electrons due to the relatively low fluxes of >500 keV electrons in the inner zone [e.g., Reeves et al., 2016]. On the other hand, the bremsstrahlung effect caused by >MeV electrons is mostly responsible for the contamination of ∼30-500 keV electron flux measurements near the heart of the outer radiation belt (L∼4). Even though the background-corrected MagEIS electron data are valuable for analysis, it is not always available. As stated in Claudepierre et al. [2015], the background correction is not possible when the low and medium-energy units of the MagEIS instrument are in the high-rate mode or sample mode, which has a higher temporal resolution than the normal science mode [Blake et al., 2013]. In addition, the background correction for three out of the nine low- and medium-energy channels is not available, as discussed in Claudepierre et al. [2015] . Therefore, background-corrected electron flux measurements are used in this study only to validate and support the observations made using the non-background-corrected MagEIS electron flux data.

An overview of the Van Allen Probe-A MagEIS spin-averaged electron fluxes from January 2013 to July 2015 is exhibited in Figure 3.2. In the first three panels, the color-coded electron fluxes are plotted as a function of time and L, where L is the radial distance in R_E at which the dipole magnetic field line crosses the magnetic equatorial plane. For a qualitative comparison, we superimpose the 10-day innermost L_{pp} on the electron fluxes plots and observe that electron enhancements for 1016 keV electron energy channel (Figure 3.2c) occurred mostly outside of the 10-day binned innermost L_{pp} locations in both L_{pp} models at all time. This relationship is also evident in the 183 keV electron energy channel, primarily during quiet periods (Figure 3.2b). However, the relationship between electron enhancements and the innermost L_{pp} is not easy to identify during

Table 3.1: Statistical values of the geomagnetic indices (Dst, AE) and solar wind velocity (V_sw) for the five storm periods under investigation. [a] the storm number corresponds to that indicated in Figure 3.2d.

Storm periods/Parameters		Storm 1[a]	Storm 2	Storm 3	Storm 4	Storm 5
Dst (nT)	Minimum	-132.0	-119.0	-116.0	-223.0	-204.0
	Mean	-46.9	-35.0	-43.8	-73.9	-55.0
	Median	-39.0	-26.0	-45.0	-66.0	-56.0
	Standard dev.	28.0	26.3	25.3	49.3	60.4
AE (nT)	Maximum	1822.0	1217.0	1236.0	1570.0	1636.0
	Mean	251.0	347.7	361.2	467.0	383.2
	Median	71.0	315.0	317.0	408.0	230.0
	Standard dev.	350.8	238.2	283.0	319.3	371.9
V_{sw} (km/s)	Maximum	725.0	774.0	691.0	683.0	742.0
	Mean	522.1	632.6	487.9	574.9	499.8
	Median	499.5	639.0	504.5	576.0	555.5
	Standard dev.	79.2	92.1	79.1	50.0	148.8

geomagnetically active periods (e.g., the time periods indicated by red boxes in Figure 3.2b).

To further investigate the correlation between the electron enhancement and the innermost L_{pp} during geomagnetically active periods, we draw attention to five intense storm periods with minimum Dst index below -110 nT (see the highlighted blue boxes in Figure 3.5d and Table 3.1) and study the enhancement events that occurred during these periods in detail. An overview of the statistical values of the Dst and AE indices as well as the solar wind velocity over these five periods can be found in Table 3.1. Common characteristics of the studied periods are that: 1) they are mainly driven by coronal mass ejections (CME) and are associated with strong interplanetary shocks [e.g., Baker et al., 2014, 2016; Ghamry et al., 2016]; 2) they have a $\geq$ 5-day quiet period (with Dst $>$ -50 nT) prior to the onset of the magnetic storms.

3.3 Results

3.3.1 Initial enhancement definition and observations during the five storm periods

In the following, we address how initial electron enhancements vary with respect to the innermost L_{pp} during geomagnetic storm periods. We first identify enhancement events using the

following criteria: 1) an order of magnitude or more increase of electron flux must be observed by the same spacecraft in two consecutive passes (an average of $\sim$ 4.5 hours) at the same L ($\pm$0.01); 2) these enhancements must also be seen over a larger L range ($\Delta L > 1$) with an L bin size of $\pm$0.1, in order to avoid discrepancies that might be introduced by the magnetic latitude variation of the satellite observations due to the tilted offset of the Earth's dipole. If two enhancement events are identified in the same pass (but at different L shells), only the enhancement event at the lower L shell is kept since our aim is to study the inner extent of the enhancement event. The first enhancement event observed by both spacecraft for the same energy channel in each storm is identified as the initial enhancement (IE) event, and the inner extent (lowest L-shell) of the IE event is known as L_{IE}. In other words, there is only one IE event (and hence one L_{IE}) for a given electron energy during a storm period.

Figure 3.3 illustrates how the L_{IE} (highlighted as the yellow triangles) are identified and how they are compared to the innermost L_{pp} locations during the March 17-20, 2015 storm period. From Figure 3.3, several features are noted: 1) L_{IE} for $\sim$30 keV to 2 MeV electrons is often located outside of the innermost L_{pp}; 2) L_{IE} for tens/hundred keV electrons happens more promptly after the onset of the geomagnetic storm, as compared to >1 MeV electrons; 3) L_{pp} derived from the Goldstein et al. [2014] model (marked by a dashed blue line in Figure 3.3) is often located at lower L shells than the L_{pp} derived from the Liu et al. [2015] model, particularly during times of strong convection that can be inferred from the steep Dst gradient in Figure 3.3d. It is also worth noting that the definition of L shell during strong convection periods is less certain, particularly for tens of keV electrons. However, it does not qualitatively affect the general observations we made.

To further quantify the correlation between L_{IE} and L_{pp}, we plot L_{IE} from the five studied storm periods against the innermost L_{pp} in Figure 3.4. Based on our initial enhancement definition, we identified a total of 64 IE events (and 64 corresponding L_{IE}) for 30 keV to 2 MeV electrons over the five periods studied. Overall, all L_{IE} were located outside the 12-hour binned innermost L_{pp} locations with only one exception for the initial enhancement of 54 keV electron during June 21-24, 2015 storm period. More specifically, the outlier is found at 0.02 and 0.09 R_E

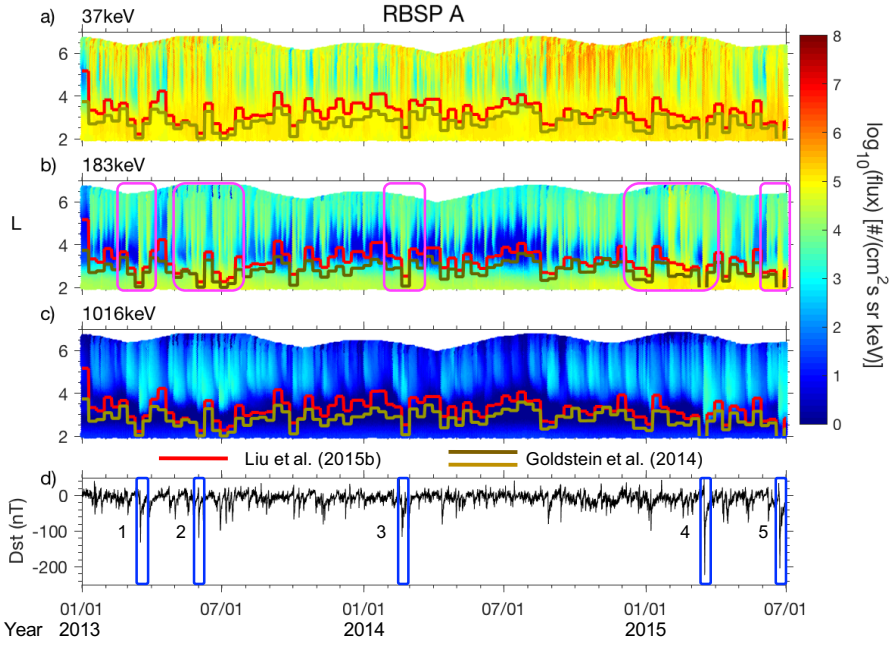

Figure 3.2: (a-c) Spin-averaged electron fluxes for the 37 keV, 183 keV, and 1016 keV energy channels obtained from MagEIS aboard the Van Allen Probe A, from January 2013 to July 2015. The gold (and dark gold) and solid red lines are the 10-day binned minimum plasmapause locations from the Goldstein et al. [2014] model and the Liu et al. [2015] model, respectively. The magenta boxes in the second panel show examples of periods when the spatial relationship between the plasmapause location and electron enhancements is hard to discern. (d) Dst index for the above period where blue boxes and the corresponding numbering indicate five storm-time periods that are studied herein.

inside of the 12-hour innermost L_{pp} location from the Liu et al. [2015] model and the Goldstein et al. [2014] model, respectively. The relationship between electron enhancements and the innermost L_{pp} in Figure 3.4 is not a mere coincidence but a suggestion that plasmaspheric structures (and the underlying mechanisms for their formation) are important at controlling the dynamics of energetic electrons. Since different electron populations are subjected to different acceleration mechanisms, it is necessary to understand the energy dependency of the relationship between the initial electron enhancement and the innermost L_{pp}.

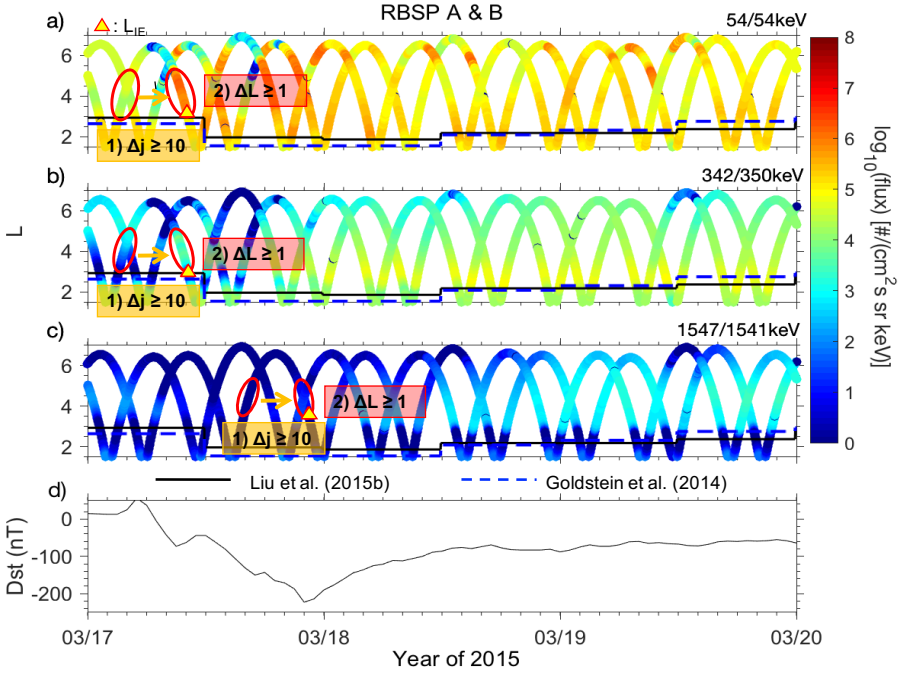

Figure 3.3: a-c) Spin-averaged electron fluxes data from MagEIS onboard the Van Allen Probes A and B for March 17 - 20, 2015 with the superimposed 12-hour innermost plasmapause locations. An enhancement event is characterized by two criteria: 1) an order of magnitude or more flux increase is observed between two subsequent passes of the same spacecraft ($\Delta j \geq 10$), as indicated by the orange arrows; 2) these enhancements must be seen over a larger L range, $\Delta L \geq 1$ (highlighted by the red circled regions. The yellow triangles represent the inner edge of the initial enhancement events (L_{IE}). The solid black line refers to the 12-hour innermost L_{pp} from the Liu et al. [2015]model and the dashed blue line indicates the 12-hour innermost L_{pp} from the PTP simulation [Goldstein et al., 2014]. d) Corresponding Dst values for the March 17-20, 2015 storm period.

3.3.2 Energy dependence of the spatial and temporal relationship between L_{IE} and innermost L_{pp}

We next investigate how the relationship between the L_{IE} and the innermost L_{pp} varies with electron energy, both spatially and temporally. First, we compute the spatial displacement between the L_{IE} and the model-derived 12-hour innermost L_{pp} as ΔL_{min}, and we average the computed ΔL_{min} across all five storms for each energy channel. The results are plotted in Figures 3.5a (based on the Liu et al. [2015] model) and 3.5b (Goldstein et al. [2014] model), where positive (negative) ΔL_{min} refers to the distance outside (inside) of the plasmapause. We also investigate how the occurrence time of L_{IE} varies with electron energy (Figure 3.5c). Δt_{min} is defined as the

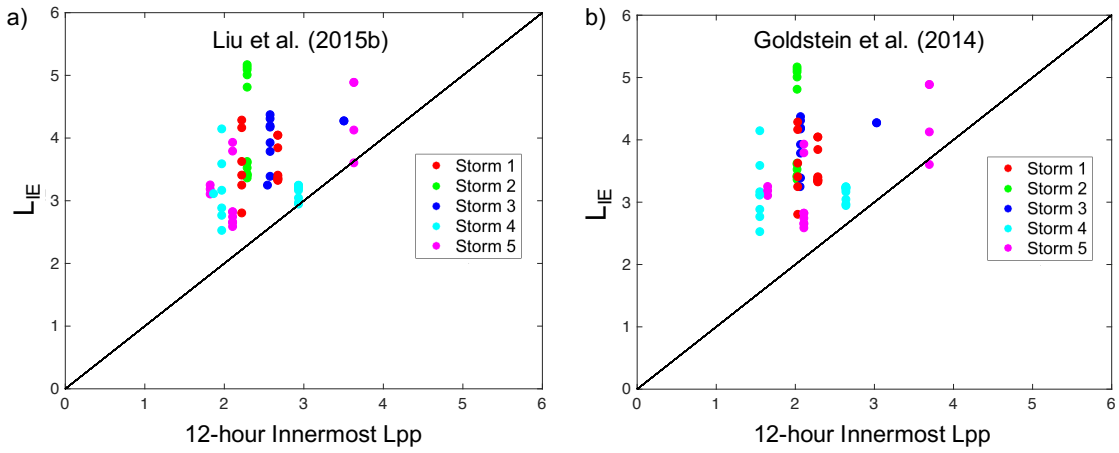

Figure 3.4: Comparison of the inner extent of the electron enhancement events (L_{IE}) and the 12-hour innermost Lpp using the Liu et al. [2015] model (the left panel) and the Goldstein et al. [2014] model (the right panel). The five colors here represent the five different storm periods (also refer to Table 3.1).

temporal difference between the time when the earliest L_{IE} among all energy electrons occurs (t_0) and the time when the L_{IE} is identified for each energy population (t). After computing Δt_{min} (t-t_0) for each storm period, we determine the average Δt_{min} for each energy population over five storm periods, as shown in Figure 3.5c.

A 95% confidence interval of the averaged quantities for non-background-corrected MagEIS electron flux data is determined and illustrated as the shaded area in Figure 3.5. It is computed by multiplying the standard error (SE) of the mean with a constant, 1.96. The value of 1.96 is based on the fact that the Z-score (the number of standard deviations away from the mean) for 95% of the area of a normal distribution is 1.96. SE is calculated using the equation, SE $= \frac{SD_i}{\sqrt{n_i}} = \frac{S_{pooled}}{\sqrt{k}}$. The pooled standard deviation, $S_{pooled} = \sqrt{\frac{\sum_{i=1}^{k} n_{i-1} SD_i^2}{\Sigma_{i=1}^{k} n_i - k}}$, derived from Cohen [2013], is to determine the weighted average of the standard deviation for two or more electron energy/populations, where SD_i represents the standard deviation of a certain electron population, n_i refers to the number of samples for each electron population, and k is the total number of electron populations. The superimposed dashed lines and error bars in Figure 3.5 represent average ΔL_{min} or Δt_{min} and the corresponding 95% confidence interval computed using background-corrected electron fluxes.

There is a data gap in the superimposed blue dashed line (Figure 3.5) because the background fit for 1MeV electron range cannot be determined due to instrument design limitations [Claudepierre et al., 2015]. Despite the slight discrepancies, the overall trends in Figure 3.5 for background-corrected (blue dashed lines) and non-background-corrected (black solid lines) electron flux data agrees with each other; this indicates that the correlations found in Figure 3.5 are likely attributed to some physical mechanisms, as discussed below.

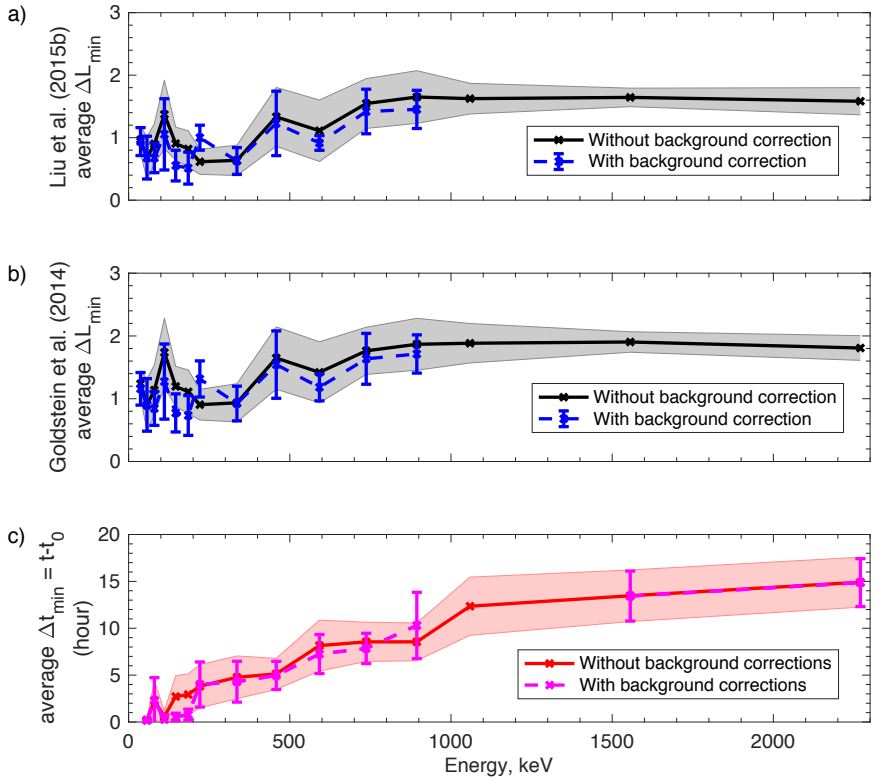

Figure 3.5: a) Average ΔL_{min} in the Liu et al. [2015] model, b) Average ΔL_{min} in the Goldstein et al. [2014] model, c) Average Δt_{min} among the five storm periods against electron energies using uncorrected (solid line) and corrected (dashed line) MagEIS electron fluxes data, where Δt_{min} represents the temporal difference between the time when the inner edge of L_{IE} is identified (t) and the time when the earliest IE event occurs among all energy electrons (t_0). The shaded areas (for uncorrected MagEIS data) and error bars (for corrected MagEIS data) in all three panels represent the 95% confidence interval of the computed average values.

When comparing Figure 3.5a and 3.5b, we noted that ΔL_{min} derived from the Liu et al. [2015] model (Figure 3.5a) is smaller (L_{IE} is closer to the plasmapause location) than ΔL_{min} obtained from the Goldstein et al. [2014] model (Figure 3.5b). This is consistent with our observation

in Figure 3.3 that the Goldstein et al. [2014] model often estimates L_{pp} to be at a lower L shell than the Liu et al. [2015] model during strong convection periods. Since most of the IE events occurred during the storm main phase with strong convection, the L_{IE} is often further from the L_{pp} locations derived from the Goldstein et al. [2014] model than the L_{pp} locations derived from the Liu et al. [2015] model. Nevertheless, both cases (Figures 3.5a and 3.5b) exhibit a very similar and interesting trend: the average ΔL_{min} varies for lower energy electrons (<200 keV) before transitioning to a relatively stable average ΔL_{min} for >800 keV electrons. The L_{IE} for <800 keV electrons often lies closer to the 12-hour innermost L_{pp} than that for >800 keV electrons. Among all electron populations, ∼200-300 keV electron have the lowest average ΔL_{min}, 0.70 ± 0.18 R_E and 0.99 ± 0.22 R_E away from 12-hour innermost L_{pp} from the Liu et al. [2015] and the Goldstein et al. [2014] models, respectively. The average ΔL_{min} for < 800 keV is associated with more variability and with a wider 95% confidence interval, or in other words, with a higher uncertainty of the computed average ΔL_{min}. This is partly due to the small sample size (the maximum sample size for each energy channel in this study is five, which corresponds to the five storm periods). Besides, various mechanisms like convective transport, substorm injections, and chorus wave activity might act on <800 keV electrons, and the complicated, combined effect of these mechanisms could contribute to the higher variations of ΔL_{min} for < 800 keV.

Since the plasmapause location results from the balance between the corotational ExB drift and the sunward ExB drift that is closely associated with enhanced convection [Goldstein, 2006, and references therein], our observations suggest that the same enhanced convection responsible for plasmasphere erosion could account for the flux enhancements of lower energy electrons. Simulations from previous studies [Korth et al., 1999; Liu et al., 2003; Thorne et al., 2007; Zhao et al., 2017] suggested that <200 keV electrons are likely to be radially transported inward by enhanced convective electric fields in the slot region, around 3 < L < 5. Using test particle simulations, Califf et al. [2016] showed that convective transport by large scale of electric fields on the order of 1 to 2 mV/m can explain the flux enhancement of 100s keV electrons at L∼3 during the February 2014 storm that is also examined in this study. During the June 1st, 2013 storm

event, another event that is studied in this paper, Thaller et al. [2015] reported the appearance of a large duskward electric field on the order of 1 to 2 mV/m. They determined that this enhanced convection electric field can contribute to the erosion of the plasmasphere and the formation of the ring current by radially transporting few keV ions inward from the plasma sheet to lower L shells. Although Thaller et al. [2015] did not provide direct evidence that relates enhanced convection electric fields to electron flux enhancements in the slot region, we can infer from the simulation conducted by Califf et al. [2016] that the observed 1 to 2 mV/m electric field enhancement is also capable of transporting <200 keV electrons inward. Combined with results from previous studies, our observations indicate that the same convective electric field responsible for the erosion of the plasmasphere also plays an important role in the dynamics of <200 keV electrons, potentially transporting tens and a few hundred of keV electrons radially inwards during strong convection periods.

Another interesting feature is the relatively stable average ΔL_{min} that is observed for relativistic (>800 keV) electrons (Figures 3.5a and 3.5b). On average, L_{IE} for >800 keV electrons, from both corrected and uncorrected flux data, are found to be 1.56 ± 0.22 RE and 1.81 ± 0.22 RE from the innermost L_{pp} locations derived from the Liu et al. [2015] model and the Goldstein et al. [2014] model. The L_{IE} for >800 keV electrons were identified, on average, 12.6 ± 2.3 hours after the earliest L_{IE} identified in the lower energy electron channel. The late occurrence of relativistic electron flux enhancements and the constant spatial difference between L_{IE}-L_{pp} for relativistic electrons are consistent with the proposed mechanism of local acceleration of the seed population (tens to a few hundred keV electrons) by chorus waves, as discussed in previous studies such as Horne et al. [2005a], Reeves et al. [2013], and Jaynes et al. [2015].

According to studies like Horne et al. [2005a], Summers et al. [2007], and Thorne et al. [2013], chorus waves that reside outside the plasmapause are most efficient in locally accelerating hundreds-keV electrons to relativistic (> MeV) energies with acceleration timescales ≤ 1 day. Several past studies [e.g., Foster et al., 2014, 2016; Li et al., 2014; Liu et al., 2015; Xiao et al., 2014] analyzed the relativistic electron dynamics over the five intense storm periods that we ex-

amined in this paper using observations/simulations; they concurrently attributed chorus wave as an important contributor to the relativistic electron enhancements. For instance, Li et al. [2014] and Xiao et al. [2014] conducted two independent studies of the March 2013 storm period using a simulation driven by chorus waves only and chorus waves/radial diffusion, respectively. Both papers highlighted the importance of chorus-driven acceleration in reproducing > 1-MeV electron flux enhancements at L∼4 that occurred ∼12-15 hours after the onset of the storm. Likewise, Boyd et al. [2018] examined 80 outer belt enhancement events from October 2012 to April 2017 using Van Allen Probes and THEMIS data. They found that local acceleration is the dominant acceleration mechanism for equatorially mirroring electrons with μ= 700 MeV/G, which translates to ∼1 MeV electrons at L = 5. In addition, they determined that the locations of the growing phase space density peak, which is a signature of local acceleration, are outside of the plasmapause locations. These results are in agreement with our observations for > 800 keV electron enhancements as described in Figure 3.5. Since local acceleration is most effective outside of the plasmapause location [e.g., Horne et al., 2005b], our observations, along with the previous literature, suggests local acceleration as the dominant acceleration mechanism that contributes to the initial enhancement of > 800 keV electrons.

When studying the flux enhancement of energetic (> 30keV) electrons, it is also necessary to consider the effect of ULF waves on these electrons. Previous studies showed that an increase in energetic electron flux is often observed in association with enhanced ULF wave activity [Elkington et al., 2003, and references therein]. It is noteworthy that the five storm periods studied in this paper are all CME-driven storms and are associated with strong interplanetary shocks. Since the strong interplanetary shock is an important driver for the generation of ULF waves, the latter is expected to play a role in the observed electron dynamics in this study. Previous studies have discussed how ULF wave-driven radial diffusion can transport hundreds of keV electrons into lower L-shells [e.g., Pokhotelov et al., 2016; Shprits et al., 2008]. It is conceivable that the enhancements of the energetic (hundreds of keV to > MeV) electrons are due to inward radial transport associated with ULF waves.

3.3.3 Energy spectrum inside and outside of the plasmasphere

A statistical analysis was conducted to understand the overall energy spectrum evolution inside and outside of the plasmasphere during the five storm periods. In Figure 3.6a, we plot electron energy spectra at L = 1.5 ± 0.01 at $t_{min(Dst)}$ and t_{bef}, where $t_{min(Dst)}$ represents the time when the Dst value reaches its minimum during the storm period and t_{bef} refers to 24 hr before $t_{min(Dst)}$. At both time instances, these spectra (at L=1.5) are located inside of L_{pp}. We observe little variation of 30 keV to 2 MeV electron flux at L = 1.5 before and during the storm. In Figure 3.6b, the measured spectra at L = 3 ± 0.01 are located within the plasmasphere at t_{bef}, but outside of the plasmasphere at $t_{min(Dst)}$ (this is true for all five storms that are studied in this study.). An increase in electron flux is observed across all electron energies up to ∼2 MeV, with larger flux enhancements occurring in the electron range from ∼300 to ∼500 keV.

A similar analysis using background-corrected data (not shown here) was also conducted. Even though the observed energy spectrum using background-corrected measurements are relatively sparse (due to data gap), we still observe a similar drastic flux increase outside of the plasmasphere during storm time, in contrast to little change in the energy spectrum inside the Lpp; this further validates our observations in Figure 3.6. In addition to the statistical analysis, we also analyze how the energy spectrum varies from L = 1.5 to L = 3.5 for the five storm periods and observe the same pattern as noted in the statistical analysis (Figure 3.6). In short, the striking difference of the energy spectrum evolution between inside and outside of the plasmasphere during storm periods serves as another piece of supporting evidence to illustrate the important role of the plasmasphere in shaping the dynamics of energetic electrons from ∼30 keV to ∼2MeV.

3.4 Conclusion

This chapter investigates the relationship between the initial enhancement of ∼30 keV to ∼2MeV electrons and the innermost plasmapause locations. Over the five CME-driven geomagnetic storm periods, we presented strong evidence that the initial enhancement of 30 keV to 2 MeV

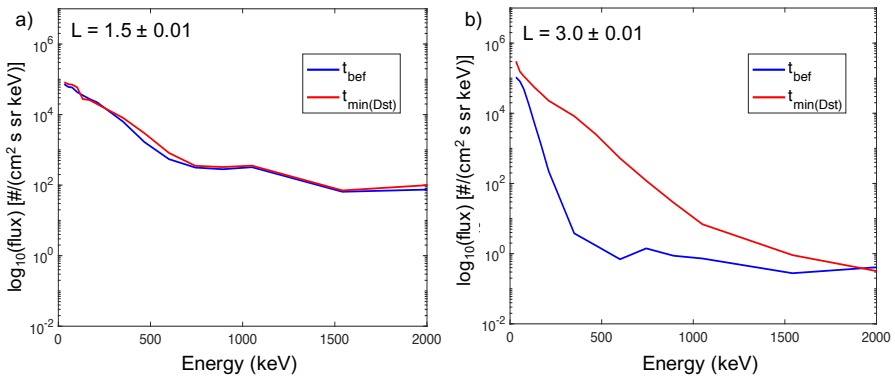

Figure 3.6: Statistical analysis of the energy spectrum before and during the five intense storm periods at L = 1.5 (left) and 3 (right). The blue solid line represents the energy spectrum before the storm periods (t_{bef}) and the red line depicts the energy spectrum during the storm periods ($t_{min(Dst)}$).

electrons is persistently outside the innermost plasmapause locations. Our findings suggest that enhanced convection is the dominant mechanism at transporting <200 keV electrons into lower L shells while local acceleration due to chorus waves predominantly controls the relativistic (>800 keV) electron enhancements, which always occur ∼12.6 hours later (than the earliest IE events) at ∼1.56 R_E and ∼1.81 R_E away from the innermost Lpp locations derived from the Liu et al. [2015] model and the Goldstein et al. [2014] model, respectively. A drastic difference of the energy spectrum evolution inside and outside of the plasmasphere further attests to the significant role of the plasmasphere in affecting the dynamics of energetic electrons over a wide energy range, ∼30 keV to ∼2MeV, during intense storm periods. Lastly, it is also important to note that this study focuses only on active periods driven by CME events. Therefore, it would be interesting to investigate the storms driven by corotating interaction region (CIR) in the next chapter; this will provide a more comprehensive understanding of the relationship between electron enhancements and the plasmapause location under various solar wind conditions.

Chapter 4

On the Initial Enhancement of Energetic Electrons and the Innermost Plasmapause Location: CME vs CIR-Driven Storm Periods and Non-Storm Periods

This chapter is edited based on the published work of Khoo et al. [2019], How sudden, intense energetic electron enhancements correlate with the innermost plasmapause locations under various solar wind drivers and geomagnetic conditions, Journal of Geophysical Research: Space Physics, 124, 8992-9002. https://doi.org/10.1029/2019JA027412.

4.1 Introduction

To understand the dynamics of outer belt electrons, many statistical studies [Kataoka and Miyoshi, 2006; Yuan and Zong, 2013; Kilpua et al., 2015; Turner et al., 2019] found it helpful to study the behavior of energetic electrons under the influence of different solar wind drivers, such as coronal mass ejections (CMEs) and corotating interaction regions (CIRs). Differences in the structure and morphology of these drivers can have different effects on the radiation belt electrons. For instance, Shen et al. [2017] and Turner et al. [2019] found that CME-driven storms, which are often associated with interplanetary shocks and intense magnetic disturbances [Borovsky and Denton, 2006], are more effective in energetic (hundreds keV to >1-MeV) electron enhancement at lower L shells than CIR-driven storms, which are of longer duration and thus allow extended enhanced convection [Borovsky and Denton, 2006; Denton et al., 2006]. Here L can be viewed as the radial distance in Earth radii from the center of the Earth at which the dipole magnetic field

line crosses the magnetic equatorial plane.

Besides the storm time periods, the energetic electron enhancements also occur during non-storm periods. Schiller et al. [2014] have reported observations of sudden relativistic (>500 keV) electron enhancement during non-storm times. Anderson et al. [2015] and Boyd et al. [2018] further conducted statistical studies of the relativistic electron enhancements during small geomagnetic/non-storm periods (minimum Dst > -50nT). They determined that small storm/non-stormtime enhancements are indeed significant and the radiation belt responses are not strictly scaled with the size of the storms.

The relationship between electron enhancements and the plasmasphere has long been a subject of study [Baker et al., 2004; Goldstein et al., 2005, 2016; Li et al., 2006]. In the past decade, multiple studies [Baker et al., 2004; Goldstein et al., 2005; Li et al., 2006] have observed that the inner edge of the outer electron belt generally follows the L_{pp} well. The previous chapter examined five intense (Dst < -110 nT) geomagnetic storm periods and determined that this relationship is not exclusive to >1-MeV electrons but also valid for electrons with energies as low as 30 keV. This chapter aims to provide a comprehensive quantification of this relationship by examining energetic electron (∼30 keV to ∼2.5 MeV) enhancements that occurred between January 2013 and June 2015. These enhancements are categorized into stormtime or non-stormtime enhancements and compared with the innermost L_{pp} to investigate how this correlation varies during different type of storms (CME vs CIR) and non-storm periods.

4.2 Data and method

In this study, we followed the same enhancement definitions as the previous chapter (from Khoo et al. [2018]). Electron measurements are from the Magnetic Electron Ion Spectrometer (MagEIS) [Blake et al., 2013; Claudepierre et al., 2015] onboard Van Allen Probes (also known as Radiation Belt Storm Probes, RBSP), a pair of geostationary-transfer orbit satellites with a ∼9-hour orbital period. All electron measurements are binned in 0.02 L-shell bins. An enhancement event is defined as an order of magnitude or more increase in electron flux over an L range greater

than 1 within two consecutive orbital passes. The first enhancement event (between both Van Allen Probes A and B) during each storm period is identified as the initial enhancement (IE) event of a given electron energy. During non-stormtime periods, it is difficult to discern the initial enhancement events. Therefore, all enhancement events are included when analyzing non-stormtime enhancements. The storm and non-stormtime periods identified in this study are listed in Tables A.1 and A.2 in the Appendix A, respectively.

The lowest L value of the initial enhancement and (general or non-stormtime) enhancement event are identified as L_{IE} and L_{enh} (where the initial enhancement is hard to identify during non-stormtime periods), respectively. The L values for L_{IE} and L_{enh} refer to the centered dipole L obtained from the RBSP spacecraft magnetic ephemeris data and are linearly interpolated so that the time resolution of the L value is consistent with the time resolution of the MagEIS data. Since the plasmapause models in this study also used dipole L-shell to define the plasmapause location, this approach ensures the consistency of the L definition when comparing the identified L_{IE} and L_{enh} to the innermost L_{pp}, derived from two different plasmapause models [Liu et al., 2015; Goldstein et al., 2014]. The Liu et al. [2015] model is an empirical plasmapause model that is established based on the plasmapause crossings from the 5-year Time History of Events and Macroscale Interaction during Substorms (THEMIS) measurements. The plasmapause location in Liu et al. [2015] is defined as a factor of 5 (or more) change in plasma density within $\Delta L \leq 0.5$. Meanwhile, the Goldstein et al. [2014] plasmapause model is a convective model, which uses the Kp index and solar wind electric field as inputs, to simulate the plasmapause that is represented by cold test particles subjected to the ExB drift. In this study, the innermost L_{pp} refers to the minimum plasmapause location among all MLT sectors, which is also consistent with the minimum plasmapause definition used in previous studies like Goldstein et al. (2016). The innermost L_{pp} obtained from both models have a 15-minute resolution, which is the time resolution of the Goldstein et al. [2014] plasmapause model.

4.3 Initial enhancement events during CME- and CIR-driven storm periods

We selected 21 CME- and 13 CIR-driven storms between January 2013 to June 2015, following the event list from Shen et al. [2017]. Note that the five intense storm periods in the prior study [Khoo et al., 2018] are included in the 21 CME-driven storms. Among the 13 CIR-driven storms, there is only one storm period (12-15 May 2015) with no electron enhancements that fulfill our enhancement criteria. Likewise, over the 21 CME-driven storm periods, there are three storm periods (9-12 July 2013, 22-25 August 2013, and 7-10 January 2015) with no sudden, intense energetic electron enhancements identified. The number of initial enhancement events identified in each energy channel is shown in Figure 4.1. Since the electron energies measured on RBSP A and B are slightly different [e.g., Blake et al., 2013], the electron energy was binned to ±10% of the listed energy values on the x-axis of Figure 4.1. For CIR-driven storms, there is no sudden, intense enhancement event identified for >2-MeV electrons. Generally, more storm-time initial enhancements are identified for lower energy (<400-keV) electrons than higher energy electrons. This is expected and consistent with what was previously reported in Reeves et al. [2016]. It is also important to note that the sample size of >700keV electron enhancements during CIR-driven storm periods are generally small, and thus the result for >700keV electron enhancements should be interpreted with caution.

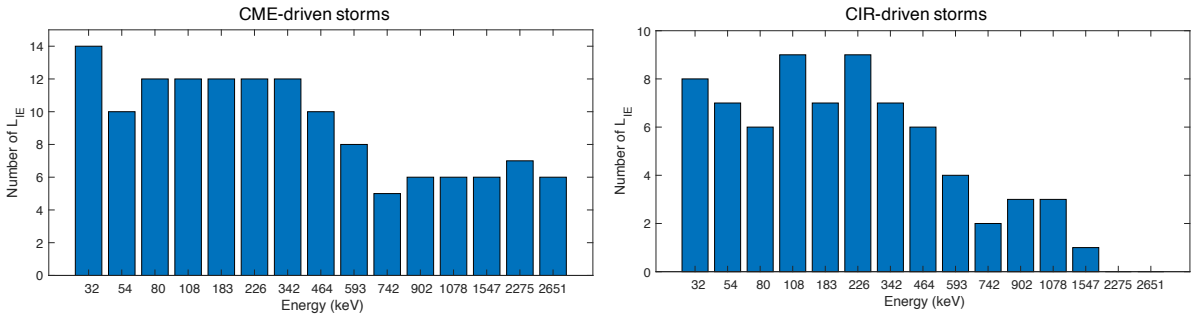

Figure 4.1: The number of initial enhancement events identified at each energy channel during both CME-driven (left) and CIR-driven (right) storms.

We identified a total of 147 and 84 IE events over the 18 electron channels (∼30 keV to

$\sim$2.5 MeV) during CME- and CIR-driven periods, respectively. Figure 4.2 displays the comparison of the L_{IE} and the innermost L_{pp} during both CME- and CIR-driven storm periods. The blue and red colors in Figure 4.2 indicate the initial enhancements of <500keV and >500keV electrons, respectively. It is interesting to note that the initial enhancements of high-energy (>500-keV) electrons seem to only occur when the innermost L_{pp} is low (L $\leq$ 3), whereas initial enhancements of <500keV corresponds to a wider innermost L_{pp} range. Since the plasmapause model is closely related to the storm activity (both plasmapause models use the Kp index as input), this might suggest that the sudden, intense energetic (>500keV) electron enhancements are associated with more intense geomagnetic activity, which agrees with previous reports [e.g., Reeves et al., 2016; Zhao et al., 2016]. In addition, we noted that >500keV electron enhancements during CIR-driven storms are only found at higher L (L>3), unlike CME-driven storms where these electron enhancements are occasionally seen at L as low as 2.8. This observation also confirms what was previously reported by Shen et al. [2017] and Turner et al. [2019], as discussed in the introduction section.

Only one(two) out of 147 (84) initial enhancement events during CME- (CIR-) driven storms is found inside of the minimum L_{pp} from the Goldstein et al. [2014] model. When comparing L_{IE} with the innermost L_{pp} from the Liu et al. [2015] model, 14 of the IE events are inside of the minimum L_{pp} during both CME- and CIR- driven storms. All IE events that fell inside the innermost L_{pp} are associated with lower energy electrons (<500 keV). These outliers are generally found within $\sim$1 R_E inside the innermost L_{pp} derived from the Goldstein et al. [2014] or the Liu et al. [2015] model. We also repeated the analysis using the background-corrected electron fluxes and obtained very similar results (not shown here). Qualitatively, we conclude from Figure 4.2 that regardless of whether the storm is driven by CMEs or CIRs, the location of the IE events are generally outside but close to the innermost L_{pp} and this correlation seems to hold regardless of the electron energies, as well.

One apparent difference between CIR- and CME-driven storms is that innermost L_{pp} for CIR-driven storms seems to be confined to a narrower L range such that no corresponding innermost L_{pp} are found at L < $\sim$2.5 for CIR-driven storms. This 'restricted' L_{pp} range is likely

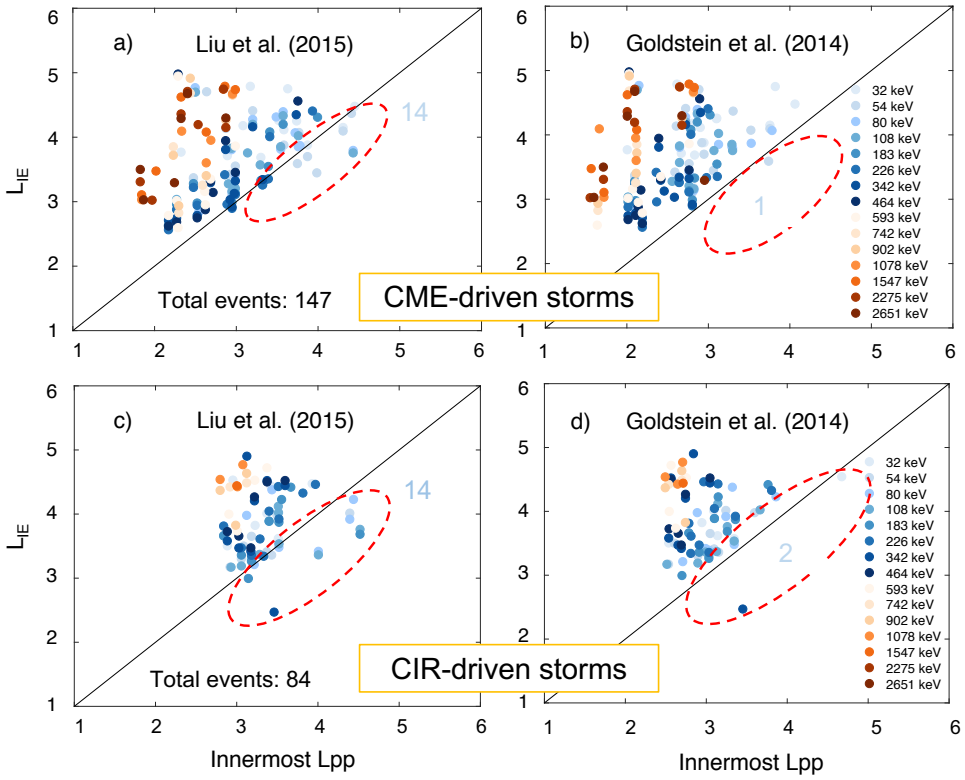

Figure 4.2: Comparison of the innermost location of the initial enhancement events, L_{IE}, and the innermost L_{pp} using Liu et al. [2015] (panels a and c) and Goldstein et al. [2014] models (panels b and d). The top (bottom) panels refer to the comparison of the initial enhancement events during CME- (CIR-) driven events.

due to the narrower intensity range of the CIR storms included in this study (See Table A.1). Interestingly, not all IE events with the innermost $L_{pp} < 2.5$ are associated with intense storm periods (minimum Dst <-100nT). Instead, several of these events have minimum Dst values of ∼-70 nT that is comparable to some CIR-driven storms. It is worth noting that CME storms tend to have a lower innermost L_{pp} than CIR storms, even if their minimum Dst index is similar. We also observed that the CME-driven storms in this study are associated with stronger solar wind electric field (and in turn stronger convective electric field), when compared to CIR-driven storms with comparable minimum Dst values. Since the plasmasphere is generally more eroded when the convective electric field is stronger, it is thus reasonable to observe stronger erosion or lower innermost L_{pp} during CME-driven storms.

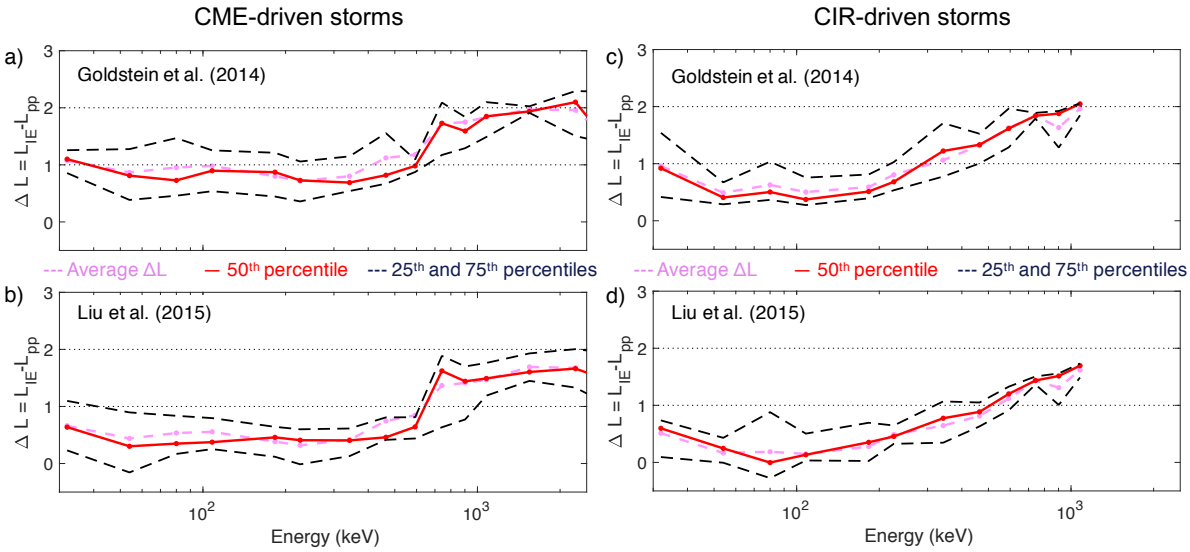

Figure 4.3: Quantification of the median (50th percentiles) and average distance between L_{IE} and L_{pp} are indicated by solid red and pink lines, respectively. The top panels are ΔL using Goldstein et al. [2014] model and the bottom panels are ΔL using Liu et al. [2015] model. The left (and right) panel is the results obtained for CME- (and CIR-) driven storms. The dashed black lines indicate the 25th and 50th percentiles of ΔL.

The distance between L_{IE} and the corresponding innermost L_{pp} is determined for each energy channel using non-background-corrected data as shown in Figure 4.3. Only results that have at least 2 or more IE events per energy channel (See Figure 4.1) are plotted in Figure 4.3; hence, no ΔL (derived from non-background-corrected data) is plotted for >1.5-MeV electrons during CIR-driven storm periods. Positive (negative) ΔL means that L_{IE} is located outside (inside) of the innermost L_{pp}. The dashed pink line shows the average ΔL, while the solid red line and the dashed black lines represent the 50th percentile (median) and 25th/ 75th percentiles of ΔL. The difference between the median and average values provide hints on how 'skewed' the dataset is. For instance, in Figure 4.3, when the average value is higher than the median, this means that there are extremely high values of ΔL in the dataset where most values have smaller ΔL. Generally, the average and the median values in Figure 4.3 are very close to each other, often with average values only slightly higher than the median values. In other words, ΔL values for these energy channels are generally symmetrically distributed. The 25th and 75th percentiles of ΔL together

provide additional information on how the ΔL values are distributed for each electron energy channel. Due to the caveat of background-corrected data availability [Claudepierre et al., 2015], we have included results from background-corrected data in the Appendix A (Figures A.1, A.2 and A.3), mainly to support and complement the non-background-corrected results (Figure 4.3, 4.4 and 4.6). One notable observation in Figure 4.3 is that the observed trend is consistent across different plasmapause models (the top and bottom panels of Figure 4.3), even though the ΔL derived from Goldstein et al. [2014] is slightly higher than the ΔL obtained from Liu et al. [2015]. For instance, during CME-driven storms, the median of the L_{IE} of <500keV is ~1 R_E from the innermost L_{pp} derived from Goldstein et al. [2014], but is ~0.5 R_E from the innermost L_{pp} using Liu et al. [2015]. Similar trends are also seen across different flux types (background- and non-background-corrected fluxes as shown in Figure A.1 and Figure 4.3 in the text, respectively).

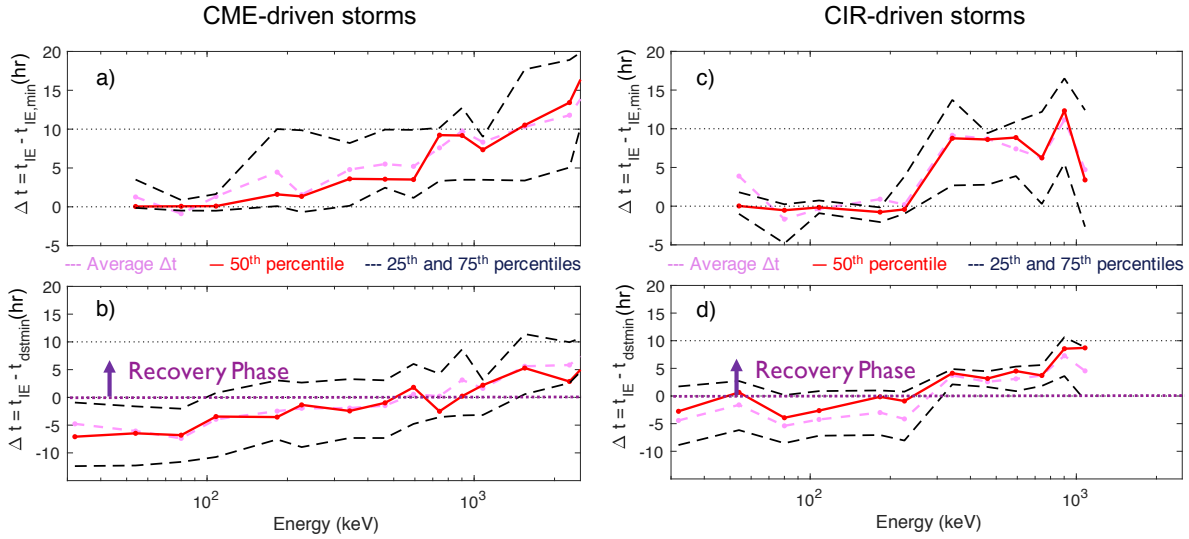

Figure 4.4: Quantification of the median (50th percentile) and average temporal difference for two different references across different energy channels are indicated by solid red lines and dashed pink lines, respectively. The top panels are the time-lag of initial enhancements of higher energy electrons as compared to the initial enhancements of the lowest available energy electrons. The bottom panels are the time difference between the initial electron enhancements and the time where the minimum Dst value occurs. The left (and right) panel is the results obtained for CME- (and CIR-) driven storms. The dashed black lines indicate the 25th and 75th percentiles of Δt from non-background-corrected data. The unit of the Δt is hour. The two horizontal dashed lines mark Δt = 0 and Δt = 10-hour, respectively.

In addition, the overall trend between CME-driven and CIR-driven storms is also comparable: L_{IE} of tens and low hundreds of keV electrons stay at a relatively constant distance from the innermost L_{pp} and beyond a certain electron energy, ΔL starts increasing with the electron energy. This $'$turning-point$'$ energy is lower for CIR-driven ($\sim$200keV) than for CME-driven storm ($\sim$500keV) periods.

Figure 4.4a and 4.4c display the time lag between the initial enhancements of more energetic electrons (t_{IE}) and the initial enhancements of the lowest available energy electrons (t_{IEmin}). In most cases ($>\sim$70% of the storm periods), $\sim$30 keV electrons are the lowest available electron energy where an enhancement is detected. In the few cases where the 30keV electron enhancement does not fulfill our enhancement criteria and hence is not available, 80keV or 108keV electrons are used as the lowest (available) electron energy. In addition, Figure 4.4b and 4.4d present the temporal difference between the initial enhancements of energetic electrons and the time when the Dst value of the specific storm event reaches its minimum, where positive (negative) Δt means that initial enhancements occur during the recovery (main) phase. Together, they offer important information of when the initial energetic electron enhancements occur with respect to energetic (tens of keV) electron enhancements and with respect to the different storm phases. Similar to Figure 4.3, the average, median, and 25th/75th percentiles of Δt in Figure 4.4 are expressed in dashed pink, solid red, and dashed black lines, respectively.

Like Figure 4.3, the overall trends observed during CME-driven and CIR-driven storms in Figure 4.4 are comparable: higher electron enhancements occur later as compared to the lower energy electron enhancements and generally happen during the recovery phase. Combined with the observations made in Figure 4.3 where the initial enhancements of higher energy electrons are further away from the innermost L_{pp}, this energy-dependent dynamic supports the observations described in Reeves et al. [2016]. This picture is also consistent with the stepwise acceleration as described in Boyd et al. [2014] and Jaynes et al. [2015]. Tens to hundreds of keV electrons are often brought in by substorm injection or enhanced global convection [e.g., Smith and Hoffman, 1974; Korth et al., 1999; Obara et al., 2000; Califf et al., 2016; Zhao et al., 2017], and based on adiabatic

drift theory, they are likely found closer to (but not inside) the innermost L_{pp}. The temperature anisotropy of tens of keV electrons, also known as the source population, can effectively produce chorus waves [e.g., Thorne et al., 2013]. Chorus waves, which exist outside of the plasmapause, can then efficiently accelerate hundreds of keV to >MeV electrons within a timescale of 12-24 hours [e.g., Li et al., 2007; Thorne et al., 2013]. By examining 25 CME- and 35 CIR-driven storm periods, Bingham et al. [2018] have previously reported that the chorus wave power in both CIR- and CME storms is comparable spatially, temporally and in intensity. These results are consistent with our results that during both CME- and CIR- storms, the initial enhancements of tens and few hundreds of keV electrons occur close (within 1 RE) to the innermost L_{pp}, while the IE events of >1-MeV electrons occur at $\sim$2 R_E away from innermost L_{pp} with a longer (>10hr, as compared to <$\sim$100keV electron enhancements) time lag during the recovery phase of the storms.

Despite the similarity of the general trend in both storm types, CIR and CME storms still pose some distinct differences. For instance, 50% of the initial enhancements of <$\sim$500 keV electron occurred during the main phase of CME-driven storms and occurred less than 5 hours after the initial enhancements of the lowest electron energy. The same is also observed during CIR-driven storms but for lower energy (<$\sim$250keV) electrons. On the other hand, the initial enhancements for >$\sim$250keV electrons during CIR-driven storms happened during the recovery phase of the storms, and 50% of these events occurred $\sim$10 hours after the initial enhancements of the lowest electron energy were observed (Please note, again, that due to the small number of >700keV electron enhancement events during CIR-driven storms, it is best to interpret the corresponding results with caution). However, for CME-driven storms, this is true only for >$\sim$500keV electrons. A closer look at the data shows that the occurrence of more energetic electron enhancements during the main phase of the CME-driven storms is likely related to the double-dip main phase features seen in multiple CME-driven storms in this study. However, exactly how the double-dip storms are related to this observation requires more analysis, which is out of the scope for this study, and is likely varied depending on the solar wind structures and geomagnetic conditions that lead to these storms. It is also worth mentioning that the $'$turning-point$'$ energy in time lag, beyond

which the Δt starts increasing, in Figures 4.4a and 4.4c for both CME-driven($\sim$500keV) and CIR-driven($\sim$200keV) storms are comparable to those in Figure 4.3. However, it is still unclear what causes the distinction of the $'$turning-point$'$ energy under different solar wind drivers.

4.4 Non-stormtime enhancement events

The common understanding is that the radiation belt electrons are less dynamic during non-storm times and thus experience less intense non-stormtime enhancements. To investigate this, we first identify the enhancement events during non-storm periods. In this study, a non-storm time refers to a period where the Dst value is greater than -30nT for at least 5 days and the Dst value at the time when enhancements occur must be between 0 and -30nT to exclude the adiabatic effect or Dst effect [e.g., Li et al., 1997]. Enhancement events that occur during storm development or recovery phase are omitted from this study.

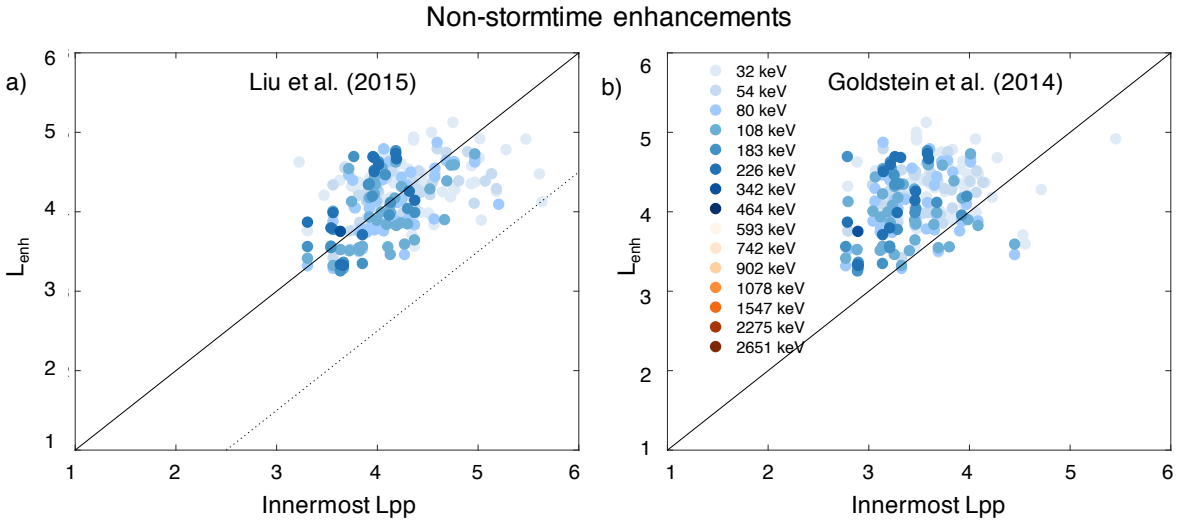

Figure 4.5: Similar figure as Figure 4.1 but for all enhancement events during non-storm times. Enhancements were only observed for electrons with energies <400 keV based on the same enhancement criteria.

Figure 4.5 shows the inner extent of all (not just the initial) enhancement events observed by both the Van Allen Probes spacecraft and the corresponding innermost L_{pp} during non-storm times. There are a total of 246 non-stormtime enhancement events for $<$ 342 keV electrons. Note

that like Figure 4.2, the color in Figure 4.5 represents enhancements of different electron energies. Qualitatively, most of the enhancement events are outside of the minimum L_{pp} derived from Goldstein et al. [2014] as shown in Figure 4.5b. The outliers are generally found within 0.23 R_E from the innermost L_{pp}. However, when compared to Liu et al. [2015] L_{pp} in Figure 4.5a, we observed a higher number of L_{enh} inside the innermost L_{pp}. That is because the estimated L_{pp} using Liu et al. [2015] during recovery or quiet periods is generally 1.5-2 R_E higher than the observed L_{pp} (as discussed and noted in their paper). Therefore, we compare the L_{enh} to the dashed line in Figure 4.5a, which indicates the location of innermost L_{pp} after being shifted by -1.5R_E. This new comparison yields a similar conclusion as before: electron enhancements are still outside of the innermost L_{pp} during non-storm times.

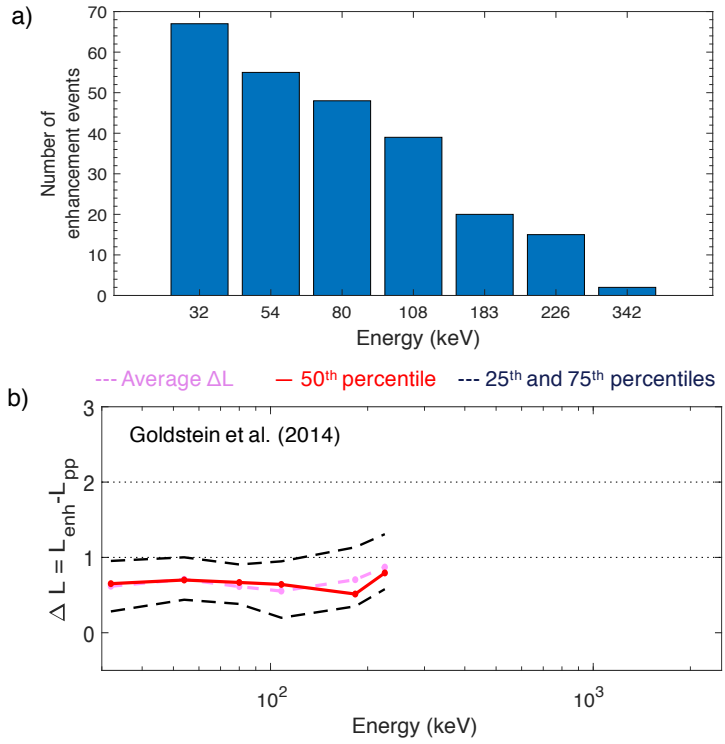

Figure 4.6: (a) Total number of enhancement events identified at each energy channel during quiet periods. (b) Similar to Figure 4.3 but for non-stormtime enhancements using Goldstein et al. [2014] plasmapause model.

Figure 4.5 also demonstrates that even during quiet periods where Dst is >-30nT, we

can still observe drastic electron enhancements that occur within a short duration (between two consecutive passes). As expected, there are more enhancement events identified for lower energies (See also Figure 4.6a). Figure 4.6a summarizes the total non-stormtime enhancement events identified using non-background-corrected fluxes. Due to the strict criteria used to identify the sudden enhancement, it is reasonable that no >400 keV electron enhancement during non-storm times is observed as seen in Figures 4.5 and 4.6. However, if the enhancement criteria are loosened such as comparing fluxes over a longer timescale, more enhancement events for more energetic electrons will be identified as reported in previous studies [Anderson et al., 2015; Schiller et al., 2014; Su et al., 2014]. Our frequent observations of <400 keV electron sudden enhancements support the conclusion that geomagnetic storms are not required to cause dramatic enhancements of the outer belt electrons [Schiller et al., 2014].

Quantitatively, these electron enhancements are generally found less than 1 R_E away from the innermost L_{pp}, as shown in Figure 4.6b. Particularly, ΔL between the L_{IE} and the innermost L_{pp} from Goldstein et al. [2014] (Figure 6b) is quantitatively comparable to ΔL during stormtime enhancements as shown in Figure 4.3. On the other hand, it is noted in Figure 4.5 that the corresponding innermost L_{pp} is within a comparable range between non-stormtime and stormtime (particularly to CIR-driven storms) enhancements. Occasionally, the innermost L_{pp} during non-stormtime enhancements can reach as low as L<3. Since the plasmapause models in this study are functions of parameters such as AL index and solar wind electric field that are closely related to the substorm activity [Baker et al., 1996], these imply that the sudden <400 keV electron enhancements during quiet geomagnetic storm periods are likely a result of substorm injection [e.g., Kamide et al., 1998]. However, more works, such as detailed event studies to examine the influence of substorms on these enhancement events, are needed to verify this, which is beyond the scope of this study.

4.5 Discussion and summary

We have examined the relationship between the sudden energetic electron enhancements and the innermost plasmapause locations over 2.5 years. Throughout our study, we found one coherent characteristic: the initial electron enhancements are mostly outside of the innermost L_{pp} during both geomagnetically active (regardless of the solar wind drivers) and quiet periods. It was previously known that the initial enhancement of the relativistic (>1 MeV) electrons are always outside of the minimum plasmapause locations (Li et al., 2006). This chapter demonstrates that the same relationship is applied to energetic electrons as low as 30 keV and holds regardless of the geomagnetic conditions as well as solar wind drivers. Such findings provide the insight and constraints for modeling efforts to forecast the dynamics of energetic electrons in the inner magnetosphere.

This coherent relationship is, in fact, physically reasonable and fits into the current understanding of acceleration/loss of the energetic electrons: the efficient acceleration mechanisms like chorus waves are outside of the plasmapause while inside the plasmasphere, the loss mechanism lead by hiss or EMIC waves dominates [Xiang et al., 2017, 2018; Zhao et al., 2019]. The lack of an efficient acceleration mechanism inside the plasmasphere could explain our observation where the innermost L_{pp} appears to be the innermost limit of the sudden electron ($\sim$30-keV to $\sim$2.5 MeV) enhancements, even during non-storm periods.

Also intriguing is that this correlation is valid only if we compare the initial enhancement events with the innermost L_{pp} (minimum L_{pp} among all MLT sectors) instead of the instantaneous L_{pp}. The plasmapause contracts due to strong convection, which is likely associated with strong enhancement at low L shells. Since the plasmapause varies in a relatively short timescale, the electron enhancement still stays at lower L (than L_{pp}) and drifts to the spacecraft locations where the instantaneous plasmapause has recovered to higher L shells. Therefore, it is likely to observe no clear correlation when comparing the initial electron enhancements to the instantaneous L_{pp} from the in-situ measurements.

In summary, we have quantified how the sudden enhancements of energetic electrons correlate to the innermost plasmapause locations, as a function of energy. For the first time, this correlation is studied in detail under both geomagnetic active and quiet times. The main findings are as follows:

(1) There is a coherent relationship between the sudden, intense electron enhancements and the innermost L_{pp}. Regardless of the geomagnetic conditions and solar wind drivers, the initial enhancements of energetic electrons ($\sim$30 keV to $\sim$2.5 MeV) are almost always outside of the innermost L_{pp}.

(2) The overall trend of the quantified relationship between the initial enhancement locations and the innermost L_{pp} for both CME and CIR storms is similar: lower energy electrons occur close (within 1 R_E) to the innermost L_{pp} with a shorter time lag (<5 hr). Beyond the $'$turning-point$'$ energy, the ΔL starts increasing with electron energies until >1-MeV, where the initial enhancements are found consistently at $\sim$2 R_E away from innermost L_{pp} with a longer (>10hr) time lag during the recovery phase of the storms.

(3) However, the turning-point energy is different for CIR-driven ($\sim$200keV) and CME-driven ($\sim$500keV) storms. It is still unclear what causes this distinction between CIR-driven and CME-driven storms.

(4) Frequent sudden flux enhancements of $\sim$30-400 keV electrons are observed during non-storm times and are generally less than 1 R_E away from the innermost L_{pp} (from Goldstein et al. [2014]), which is quantitatively comparable to the ΔL for storm-time enhancements.

Chapter 5

Multi-Event Studies of Sudden Energetic Electron Enhancements in the Inner Magnetosphere and Its Association with Plasmapause Positions

This chapter is based on the recent published work of Khoo et al. [2021], 'Multi-Event Studies of Sudden Energetic Electron Enhancements in the Inner Magnetosphere and Its Association with Plasmapause Positions', Journal of Geophysical Research: Space Physics, 126 (11), e2021JA029769.

5.1 Introduction

With the launch of Van Allen Probes in late 2012, the twin probes have provided flux measurements near the equatorial region with fine energy and temporal resolution. Many have utilized these detailed observations to study the energy-dependent dynamics of energetic electron (tens to hundreds of keV) populations [e.g., Turner et al., 2015; Reeves et al., 2016; Zhao et al., 2017]. One frequent observation is the sudden enhancement of energetic electrons to low L-shells, which is a significant source of the inner radiation belt [Turner et al., 2017]. What contributes to such rapid enhancements of energetic electrons at low L remains obscure. While this topic is still under active investigation, the proposed mechanisms can be generalized into two major processes. One is the effect of large-scale electric fields such as convection electric fields [Liu et al., 2003; Su et al., 2016; Califf et al., 2017] and subauroral polarization streams (SAPS) [Califf et al., 2016; Lejosne et al., 2018]. The large-scale westward electric field can open drift paths and bring energetic particles deep into the inner magnetosphere. The second is the localized resonance with electric

field pulses generated by interplanetary shocks [e.g., Li et al., 1993; Hudson et al., 1995; Schiller et al., 2016] or by the braking of dipolarization front bundles [Sergeev et al., 1998; Turner et al., 2015].

The effect of large-scale electric fields is commonly inferred by examining the electron enhancement locations with respect to the measured plasmapause position as well as the proton enhancement locations. The plasmasphere is a cold and dense plasma region that corotates with the Earth and is influenced by electric fields, as demonstrated by Goldstein et al. [2005]. Under adiabatic drift theory, the energetic particles are generally subjected to the ExB drift and the gradient-B/curvature drift, whereas the cold plasma is influenced by the ExB drift only [Roederer, 1970; Kivelson and Russell, 1995]. Since the ExB drift is independent of particle energy and charge, the same large-scale electric field that transports energetic particles inward is also capable of eroding the plasmasphere [See Chapter 2.3 for more discussion. Also refer to Kivelson and Russell [1995]; Califf et al. [2017]; Thaller et al. [2015]. Additionally, the less energetic a charged particle is, the more earthward its Alfvén layer (i.e., the boundary between the open and closed trajectories of particles) is. Under this premise, the Alfvén layer of the cold plasma should be the most earthward boundary layer as compared to that of energetic electrons. Therefore, the appearance of energetic electron enhancements inside the measured plasmapause location and the lack of observations of low-L shell enhancement of protons at the same energy are often used to argue against the role of large-scale electric fields on sudden electron enhancement events [Reeves et al., 2016; Turner et al., 2015, 2017]. Lejosne et al. [2018] have recently provided a viable explanation for the absence of the same-energy protons at low L shells by examining the distinct influence of SAPS on different charged populations. They proposed that SAPS can transport energetic electrons inward while moving energetic ions outward. Their study, however, did not explain how sudden enhancements of energetic electrons occur within in-situ plasmapause locations.

The plasmapause location is also related to different favorable growth locations for various waves. For instance, efficient acceleration mechanisms for energetic electrons like chorus waves and ultra-low-frequency (ULF) waves are generally found outside of the dense plasmasphere [e.g.,

Thorne, 2010]. Meanwhile, hiss waves that are efficient in scattering energetic electrons are predominantly found inside the plasmasphere [e.g., Malaspina et al., 2016]. The energy-dependent wave-particle interaction also contributes to the formation of the prevalent bump-on-tail flux spectra inside the plasmasphere [Zhao et al., 2019; Ni et al., 2019]. In short, the cold and dense plasmasphere shares an intimate relationship with energetic electrons in the inner magnetosphere [Wang et al., 2020].

Many observational studies have indeed determined an excellent association between electron enhancements, particularly relativistic electrons (>1-MeV), and the plasmapause [Frank, 1971; Goldstein et al., 2005; Li et al., 2006; Foster et al., 2014; Goldstein et al., 2016]. For instance, Li et al. [2006] studied long-term 2-6 MeV electron measurements from SAMPEX and identified that the initial enhancement locations of relativistic electrons are consistently found beyond the minimum plasmapause locations. The observational evidence of the dynamic linkage between tens and hundreds of keV electrons and the plasmasphere, however, is still not fully understood. Previous chapters expanded such studies to energetic (>30keV) electrons using Van Allen Probes data. For instance, Chapter 4 demonstrated, statistically, that the same correlation also applies to >30keV electrons and holds regardless of the solar and/or geomagnetic conditions [Khoo et al., 2018, 2019]. Nevertheless, there are also reports of enhancements found inside the in-situ plasmapause locations [e.g., Turner et al., 2017] as well as a small set of events that were found inside the innermost L_{pp} [Khoo et al., 2019], which warrants a closer look at this subject. This study, therefore, seeks to investigate the cause of the observations inside the L_{pp} by examining these outlier events in depth.

The remainder of this chapter includes a description of energetic electron measurements and the plasmapause used in this study. Section 5.3 presents observations of two distinct ′outlier′ events in detail to examine the observed enhancement locations with respect to the in-situ L_{pp} and the innermost L_{pp}, as well as a summary of all nine outlier events we examined in this study. An investigation of the phase space density evolution before and during the initial enhancement pass is presented in Section 5.3.3. The final section summarizes our findings, along with their implications on the inner magnetosphere dynamics.

5.2 Data and Analysis

5.2.1 Energetic electron measurements and phase space density calculation

This study uses data from Van Allen Probes [Mauk et al., 2012]. The twin Van Allen Probes (also referred to as RBSP-A and RBSP-B) are identically instrumented spacecraft in a geostationary-transfer orbit with an inclination of 10 degrees and an orbital period of ∼9 hours. The Magnetic Electron Ion Spectrometer (MagEIS) instrument [Blake et al., 2013] onboard Van Allen Probes offers finely resolved flux measurements for a wide range of electrons (∼30 keV to ∼4 MeV with an energy resolution of $\Delta E/E \sim 30\%$). In this study, we employ spin-averaged measurements of 30 keV to ∼2 MeV electrons from MagEIS to identify the inner boundary of the sudden enhancement events.

To complement the electron flux measurements from Van Allen Probes, we use energetic electron measurements from Geostationary Operational Environmental Satellites, GOES 13 and GOES 15, that provide information of energetic electrons at geostationary orbit. Energetic Particle Sensor MAGnetospheric Electron Detector (EPS-MAGED) onboard GOES 13 and GOES 15 supplies the electron fluxes in five channels (30-50 keV, 50-100 keV, 100-200 keV, 200-350 keV, and 350-600 keV). This study uses one-minute averaged flux measurements that were corrected for deadtime errors and other contamination sources [Hanser, 2011]. There are nine MAGED telescopes pointing at different directions on the GOES spacecraft and only the data from the telescope pointing closest to the equatorial plane (i.e., perpendicular to the local magnetic field) is used in this study.

For a complete radial coverage in our phase space density analysis, we utilize flux measurements from Helium, Oxygen, Proton, and Electron Mass Spectrometer (HOPE) in addition to the MagEIS observations and we average the flux measurements for the overlapped energy channels between MagEIS and HOPE. Electron fluxes are then converted to phase space density using the method described in Chen et al. [2006]. The PSD results shown in this manuscript use the T89D external magnetic field model [Tsyganenko, 1989] and IGRF internal magnetic field [Finlay et al.,

2010] that were provided in the Van Allen Probes magnetic ephemeris file. Although not shown here, we also conduct the same phase space density analysis using different magnetic field models like TS04 [Tsyganenko and Sitnov, 2005] and Olson-Pfitzer quiet-time field model (OP77Q) [Olson and Pfitzer, 1979] and obtain comparable results.

5.2.2 Plasmapause: Definition, determination, and simulations

This study uses two different plasmapause values (L_{pp}): measured in-situ L_{pp} and simulated L_{pp} to provide a global context of the plasmasphere. The in-situ L_{pp} is commonly identified from the measured plasma density gradient, which is defined as a factor of 5 drop in density within a distance of 0.5 L [Carpenter and Anderson, 1992]. However, this definition is not easy to implement. As pointed out by Moldwin et al. [2002], even though the plasmapause can be identified in $\sim$ 73% of the passes in their study, only $\sim$16% of the identified plasmapause locations have the clean and sharp $'$classic$'$ plasmapause. An alternative to this L_{pp} definition is to use a density threshold (ne) of 100 cm^{-3} to infer the plasmapause. Many studies have utilized the density threshold as a proxy of the plasmapause position [Chappell et al., 1970; Malaspina et al., 2016; Thaller et al., 2019]. In Thaller et al. [2019], they derived the plasmapause using both the plasma density gradient and density threshold methods and demonstrated that these two quantities are comparable. They further noted that the plasmapause derived from the density threshold has fewer gaps, thanks to its simplicity of implementation. The good agreement between these two approaches was explained by Malaspina et al. [2016] through their statistical study; they found that the steepest plasma density gradient often occurs near a plasma density of 100 - 200 ($\sim$50) cm^{-3} at L<4 (L>4). Therefore, this study uses the plasma density threshold of 100 cm^{-3} to determine if the enhancements happen inside (ne $>$ 100 cm^{-3}) or outside (ne $\leq$ 100 cm^{-3}) the plasmasphere.

The plasma density was derived from the spacecraft potential measurements using the Electric Field and Waves (EFW) instrument [Wygant et al., 2013; Escoubet et al., 1997] and from upper hybrid resonance measurements using the Electric and Magnetic Field Instrument Suite and Integrated Science (EMFISIS) instrument [Kletzing et al., 2013; Kurth et al., 2015]. Both

approaches have their pros and cons; the former is more accessible even during geomagnetic active periods but only serves as a proxy for the plasma density, while the latter is a more robust approach, but the measurements can be difficult to interpret during geomagnetic active periods. Interested readers may refer to Jahn et al. [2020] for a more comprehensive discussion. This study presents the plasma density profiles from both instruments (EFW and EMFISIS). The plasma density measurement from EMFISIS is primarily used in the case where the plasma density measurements are available from both instruments.

In this study, we also obtain the global evolution of the plasmapause using the Plasmapause Test Particle (PTP) simulations. The plasmapause in the PTP simulation is represented as the boundary of a cold test particle ensemble [Goldstein et al., 2005] that is subjected to ExB drift. The simulation is driven by an empirical model of the convection electric field [Volland, 1973; Stern, 1975] and an analytical representation of subauroral polarization stream (SAPS). The time resolution of the PTP simulation is 15 minutes. Goldstein et al. [2014] have previously simulated the plasmapause crossing events using the PTP simulations and obtained a good agreement (a mean uncertainty of 0.40 $\pm$ 0.05 R_E) with the observed plasmapause locations by Van Allen Probes. The simulated plasmapause location is represented in dipole L value, which is defined as the radial distance in the magnetic equator in Earth radii, R_E. In the subsequent comparison, the simulated L_{pp} is transformed to the GSM coordinates by rotating about the y-axis for the dipole tilt angle, which is the angle between the Earth′s north dipole axis and the GSM-Z axis. The dipole tilt angle was obtained from the magnetic ephemeris file provided by the Van Allen Probes. The minimum L_{pp} in this study refers to the most earthward plasmapause location of all local times at a specific time instant, and the innermost L_{pp} generally refers to the lowest of all minimum L_{pp} between the starting time of the substorm and the time when the inner boundary of the initial enhancements of energetic electrons was identified.

5.3 Event overviews

We studied nine enhancement events that were previously reported inside the in-situ plasmapause locations [Turner et al., 2015, 2017] or inside the simulated innermost plasmapause locations [Khoo et al., 2019]. The definition of enhancements used in this study is the same as that used in our previous studies [Khoo et al., 2018, 2019]: an order of magnitude or more increase in flux between two subsequent passes of the same probes across an arbitrarily determined L range, $\Delta L \geq 1$. For the outlier events reported inside the in-situ L_{pp}, we decrease the L range criteria from ≥ 1 to ≥ 0.5 to ensure we capture the enhancement events that were observed by other studies [Turner et al., 2015, 2017]. The initial sudden enhancement is the earliest enhancement that was first observed between the two probes. The L values used in this study are derived using the OP77Q magnetic field model. In this section, we examine two different enhancement events in detail and present a summary of our results for all nine outlier events at the end of this section.

5.3.1 The 14 October 2014 Event

The 14 October 2014 event is a relatively weak geomagnetic storm with Dst > -50nT that was driven by corotating interaction regions (CIR) [Shen et al., 2017]. Figure 5.1 shows flux measurements from the Van Allen Probes and GOES 13 and GOES 15 between October 13 to October 15, 2014. The dashed black line indicates the onset of substorms at 13 UT on October 14, 2015. The apogee of the Van Allen Probes in this event was near the post-midnight sector as shown in Figure 5.3. This enhancement event was previously reported inside the minimum L_{pp} that were inferred from both Liu et al. [2015] plasmapause and PTP simulation models [Khoo et al., 2019].

Figure 5.1 shows that flux enhancements of 40-150 keV electrons were first observed by both GOES 15 and GOES 13 around 14:20 UT (5.6 MLT) and 14:30 UT (9.8 MLT), respectively. The inner boundary of 30 keV electron enhancements was subsequently observed by RBSP-A a few minutes after, ∼14:37 UT, at L = 4.71 (2.1 MLT) during its outbound pass. It is therefore likely that RBSP-A observed the same enhancement event that was measured by the GOES spacecraft

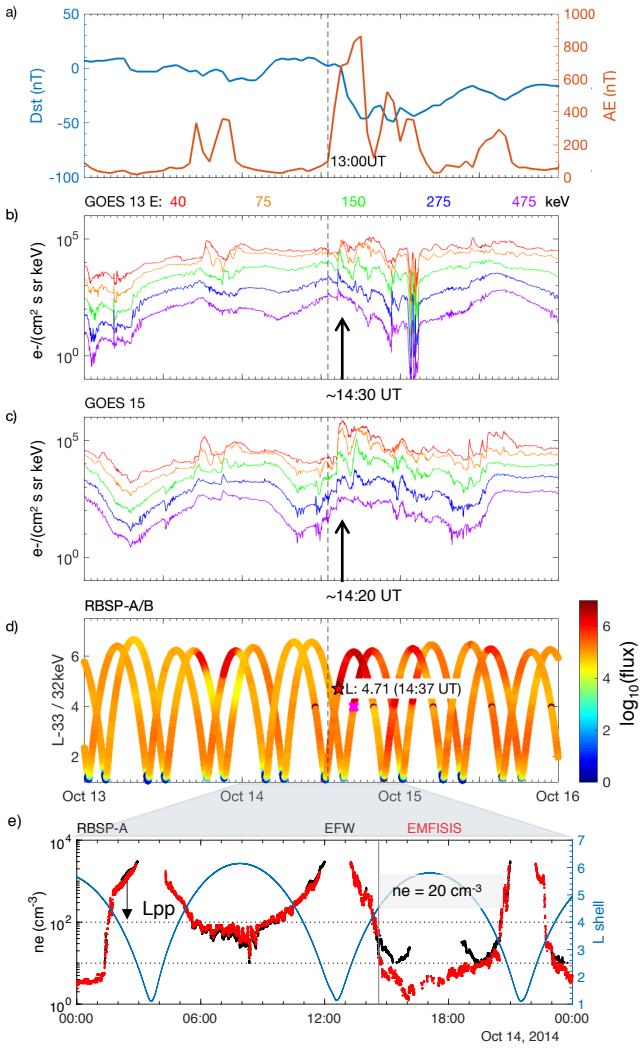

Figure 5.1: (a) Dst (blue) and AE (red) indices between October 13-15, 2014. The dashed black line shows the onset time of the substorm (13 UT) on October 14, 2014. (b-c) Flux variations of the five energy channels from GOES 13 and GOES 15. The median energies of each energy channel are 40keV (red), 75keV (orange), 150 keV (green), 275 keV (blue), and 475 keV (purple), respectively. The corresponding flux enhancement time is marked using the black arrow and listed accordingly. (d) Flux measurements of 33/32 keV energetic electrons from Van Allen Probes between October 13-15, 2014. The y-axis lists the plotted electron energies from RBSP-A and RBSP-B, respectively. The inner boundary of the initial enhancement is indicated by the black-edge star with the corresponding enhancement time and L-values listed in the inserted white box. The unit of flux is $cm^{-2}sr^{-1}s^{-1}keV^{-1}$). (e) Plasma density from RBSP-A on October 14, 2014. The red and black lines show plasma density results from EFW and EMFISIS, respectively. The highlighted vertical gray bar indicates the time when the inner boundary of the initial enhancement occurs, and the corresponding plasma density is listed in the inserted gray box. The blue line indicates the L-shell. Two horizontal dotted black lines highlight two plasma densities, ne = 10 cm^{-3} and 100 cm^{-3}.

earlier and is near the actual enhancement locations when it observed the initial enhancements. Note that the initial enhancements of higher energy like 54 keV and 120 keV electrons were also observed during this storm event but those enhancement events were outside of the innermost plasmapause location. Therefore, there is only one outlier event during this storm period, and we only show observations for 30 keV electrons in Figure 5.1. The in-situ plasma density measured by EMFISIS and EFW instruments onboard the Van Allen Probes are shown in Figure 5.1e. We determined that the inner boundary of the initial enhancement was outside the in-situ plasmapause based on its plasma density, ne $\sim$ 20 cm^{-3}. Here we focus only on the initial enhancement of 32 keV electrons. However, we note that during this storm period, the initial enhancement of 346 keV electrons was also found inside the innermost L_{pp}. This particular initial enhancement event was identified approximately one day after the initial enhancements of tens of keV electrons. That is because even though significant flux enhancements were observed at an earlier pass, they did not fulfill the L range criteria ($\Delta L \geq 1$, while it has $\Delta L \sim 0.8$) for our initial enhancement definition. When we decrease our L range criteria to $\Delta L \geq 0.5$, we find that the initial enhancement of 346 keV electrons remains outside of the in-situ L_{pp}, like what we observed with the initial enhancement of 32 keV electrons.

Figure 5.2 illustrates in detail how the flux varies between two consecutive passes for 10 keV to 2.5 MeV electrons. Particularly, Figures 5.2a and 5.2b provide the flux evolution of 10 keV to 2.5 MeV electrons measured by RBSP-A at two different L values: 1) L = 4.26, the in-situ L_{pp} that was defined as the lowest L shell with the plasma density closest to 100 cm^{-3}; 2) L = 4.71, the inner boundary of the initial enhancement for 32 keV electrons. Even though we also observe an increase in flux for 54 keV electrons in Figure 5.2b, the flux enhancement for 54 keV electrons does not sustain over a wide L range (in this case, ΔL $<$ 0.5), and therefore we only identify sudden flux enhancements of 32 keV electrons during this outbound pass. When comparing the energy spectrum evolution at and outside the in-situ L_{pp} (Figures 5.2a and 5.2b, respectively), it is notable that no drastic flux variation is observed for 10 keV - 2.5 MeV electrons at the in-situ L_{pp}. This energy spectrum evolution is also consistent with our previous report that the energy spectrum inside the

innermost L_{pp} remains unchanged before and during the initial enhancement event [Khoo et al., 2018]. Trailing behind RBSP-A, RBSP-B also observes at least an order of magnitude increase in fluxes at the subsequent outbound pass, but for 30 keV-132 keV electron (Figure 5.2c). This supports the earlier observations by GOES that a flux enhancement was observed for 40 - 150 keV electrons. The contrast between RBSP-A and RBSP-B energy spectra also highlights the importance of the timing and spacecraft locations in understanding energetic electron dynamics. Since the plasma density profile from RBSP-B is incomplete during this outbound pass, we only provide the plasma density at L = 4.26. Like RBSP-A, the plasma density measurement indicates that RBSP-B remains outside of the in-situ L_{pp} during its outbound pass when it observes flux enhancements for 30 - 132 keV electrons.

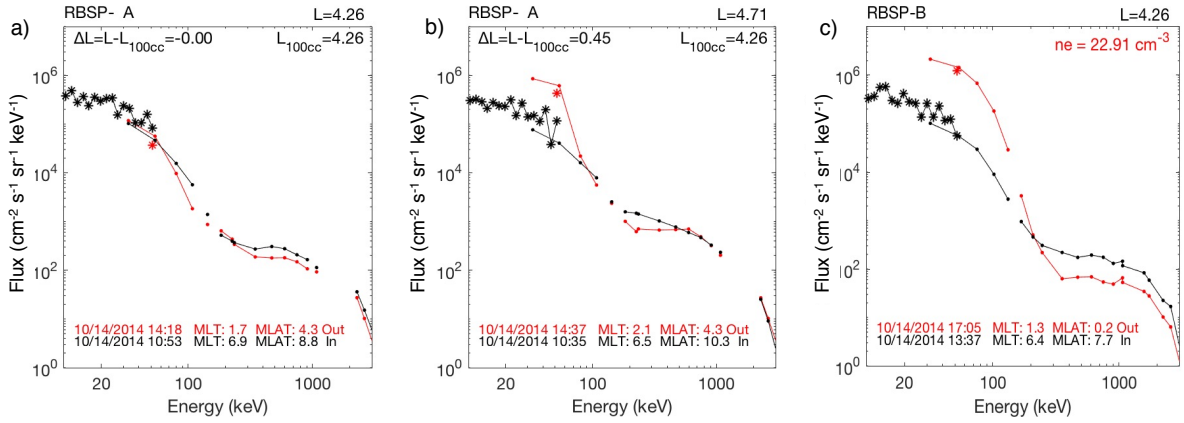

Figure 5.2: (a-b) Energy spectra of electrons measured by RBSP-A between two subsequent passes as indicated by the black (inbound pass) and red (outbound pass) lines. They present energy spectra at two different L values: at the in-situ L_{pp} and the inner boundary of enhancements. The identified in-situ L_{pp} on the outbound pass where the initial enhancement event was observed is listed on the top right of each plot and is defined as the lowest L shell at which the plasma density is the closest to 100 cm^{-3}. The distance between the in-situ L_{pp} and the corresponding L value (listed on the top right) is also presented, where the positive (negative) value indicates that the inner boundary of the initial sudden enhancement is outside (inside) the in-situ L_{pp}. The data with asterisks are from the HOPE instrument and the dotted data are from the MagEIS instrument. c) Energy spectra of electrons measured by the following RBSP-B during its inbound (black) and subsequent outbound (red) passes. The plasma density measured by RBSP-B during the outbound pass is also listed on the top right of the plot.

We next examine where the initial enhancement observed by RBSP-A occurs with respect

to the simulated plasmapause location in the Geocentric Solar Magnetospheric (GSM) coordinates at three different timestamps: when the substorm begins (13 UT), when flux enhancements were first observed by the GOES spacecraft (14:20 UT), and when the inner boundary of the initial sudden enhancement was observed by RBSP-A (14:37 UT). The simulated plasmapause locations from the PTP simulation for all local times at the specific timestamp are plotted in Figure 5.3 as solid tangerine yellow lines. The innermost L_{pp} between the beginning of the substorms and the specific timestamp were outlined as dotted black lines. The simulated plasmapause in Figure 5.3 suggests that a residual plume rotates eastward and wraps around the main plasmasphere at the time when the initial enhancement was observed around 14:37 UT. The multiple layers of the plasmaspheric plume in Figure 5.3 indicate the wrapping of the plasmaspheric plumes during this event; this feature was previously discussed in Goldstein et al. [2014]. Due to the eastward rotation of the plasmaspheric plume, the plasmapause near the midnight sector was located at higher L values. The innermost L_{pp}, in this case, was found near the dawn sector and incidentally, RBSP-A was near the local time of the simulated innermost L_{pp} when it observed the inner boundary of the initial enhancement event. Based on the simulated plasmapause, the inner boundary of the initial enhancement was just inside the simulated innermost L_{pp}. However, the measured plasma density profile indicates otherwise, suggesting that RBSP-A was just outside of the in-situ L_{pp}. This discrepancy between model and observation is understandable since the PTP simulation (mean uncertainty of 0.4 ± 0.015) does not include quiet-time processes like neutral wind coupling [Burch et al., 2004] or interchange instability [Lemaire and Gringauz, 1998] and thus has a higher uncertainty during the recovery/quiet period, as noted by Goldstein et al. [2014]. Despite that, the proximity between the innermost L_{pp} and the inner boundary of the initial enhancements suggests that the innermost L_{pp} remains a good proxy of the inner boundary of the initial enhancements.

5.3.2 The 25 July 2013 Event

The 25 July 2013 event is considered a non-storm event with Dst > -20 nT but is associated with substorm activity (AEmax = 749 nT, starting at 15 UT on July 25, 2013). Figure

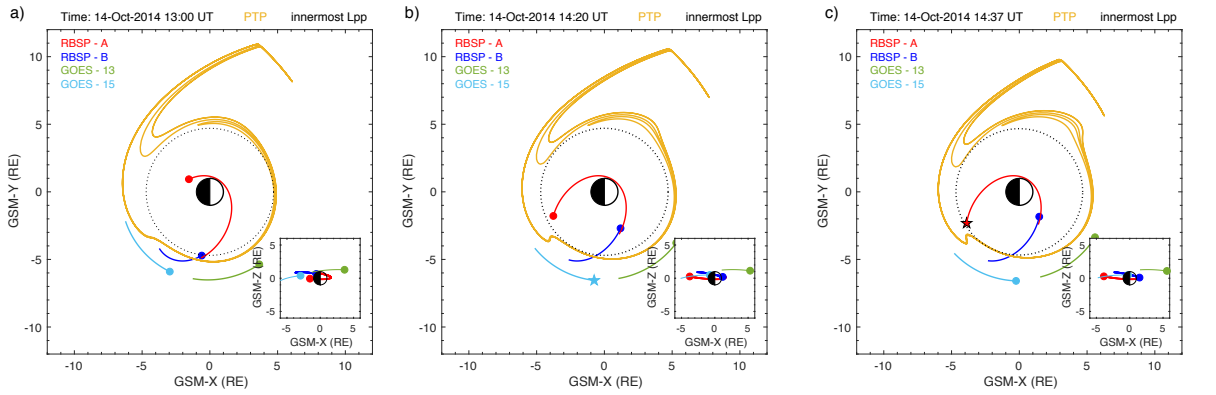

Figure 5.3: Location of Van Allen Probes and GOES 13 and 15 as well as the plasmapause locations from the PTP simulations at three different timestamps: (a) The onset time of the substorm (b) the time when flux enhancements were observed by the GOES spacecraft (c) the time when the inner boundary of initial enhancement was first observed by RBSP-A. Both the solid circle and the star symbol represent the location of the spacecraft at the time indicated on the top left of the plot, with the star symbol highlights the spacecraft that observes flux enhancements at the specific timestamp. The solid lines trailing the solid/star symbols show the trajectory of the spacecraft three hours prior to the specific timestamp. The dotted black lines indicate the innermost L_{pp} between the start time of the substorm to the specified timestamp. The small insert on the bottom right of each plot illustrates the spacecraft locations in GSM-Z and GSM-X coordinates.

5.4 showcases the flux enhancements of ∼33 keV, ∼75 keV, and ∼143 keV electrons from the Van Allen Probes since the sudden enhancements observed in this event were limited to E $\leq$ 145 keV (see also Figure 5.5). The corresponding L-shell and the time near the observed inner boundary of the initial enhancement event (specified as black-edged red stars) are also listed. As shown in Figures 5.4 and 5.6, GOES 13 was heading toward the noon sector during the onset of the substorm and did not observe any obvious flux enhancements. GOES 15, on the other hand, only has equatorial flux measurements for >150 keV electrons during that period and hence we can only verify the flux increase of the 150 keV electron channel around 21 UT. The apogee of the Van Allen Probes during this event was near the duskside. The inner boundary of the initial enhancement of 32 - 132 keV electrons was first observed by RBSP-B between 22:46 UT to 23:13 UT during its outbound pass, at L = 3.88 - 4.75. Based on the plasma density profile for this outbound pass, we identified the in-situ L_{pp} to be L = 4.99. The comparison of the in-situ L_{pp} and the inner boundary location verifies that the initial sudden enhancements for 32 - 132 keV electrons were within in-situ

plasmapause positions; thus, it is counted as one of our outlier events.

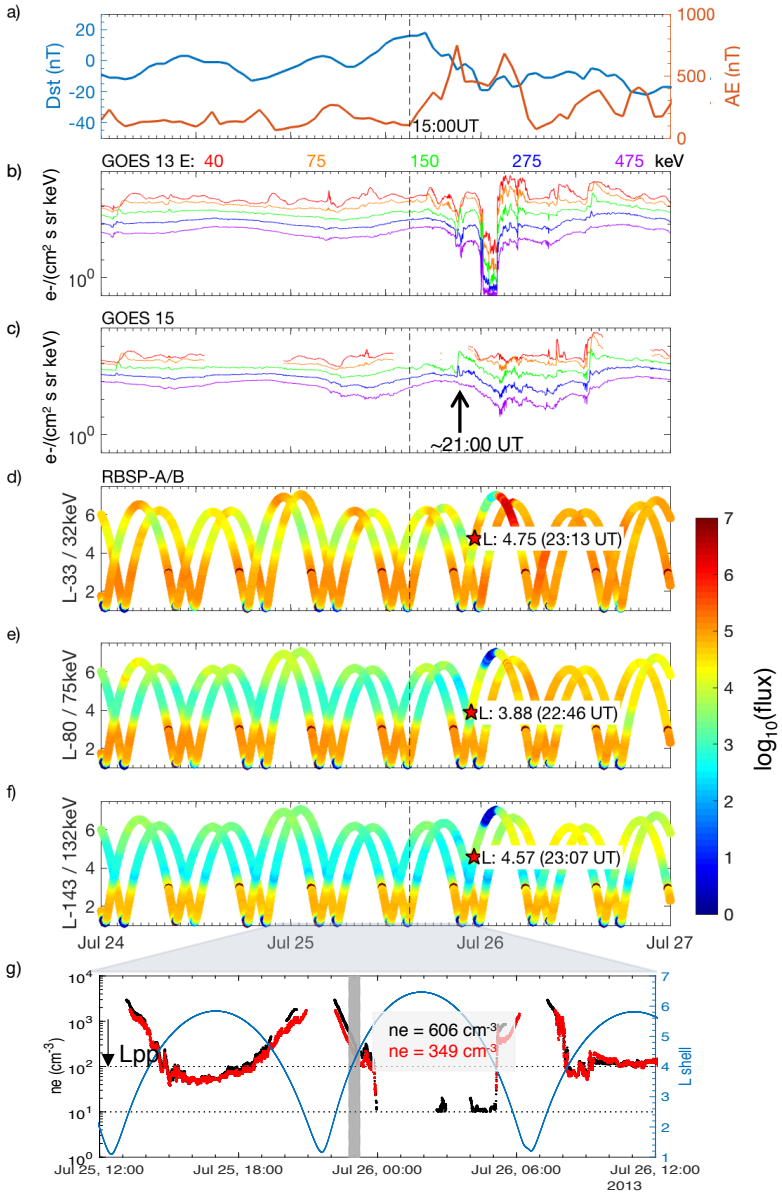

Figure 5.4: Like Figure 5.1, but for the July 25, 2013 event with the flux measurements from three different electron channels: 33/32 keV, 80/75 keV, and 143/132 keV for RBSP-A and RBSP-B, respectively; (g) The highlighted vertical gray bar covers the corresponding time where the inner boundary of the initial sudden enhancements of ∼30 keV to ∼145 keV electrons were identified.

Figure 5.5 describes the energy spectrum evolution between the inbound and outbound passes before and during the initial enhancements of energetic electrons. As seen in Figure 5.5a, 75 keV electrons is the only energy channel that observed a large magnitude of flux increase at L

~3.88, which was the inner boundary of the initial sudden enhancement for this particular energy during this event and was ~1 L inside the in-situ L_{pp}. Flux enhancements over a wide range of energies from 20 keV to 143 keV are identified at the in-situ L_{pp} (Figure 5.5b). We also observe a very different energy spectra evolution in Figure 5.5 than in Figure 5.2: flux enhancements were observed for different electron energies at and inside the in-situ L_{pp} in Figure 5.5. This discrepancy suggests that sorting/comparing flux enhancements with the in-situ L_{pp} is likely to yield an inconclusive result due to the local-time dependency of the plasmasphere and the localized nature of the spacecraft observations. In this event, the spacecraft was unfortunately located far from the local time of the actual initial enhancement (see the following for more related discussion) and was near the dusk side when observing the initial enhancement events. For such events, the innermost L_{pp} could serve as a good proxy for the plasmapause location near the actual initial enhancement locations and thus a better estimate for the inner boundary of initial enhancements, as shown in Figure 5.6 and previous statistical studies [Khoo et al., 2018, 2019].

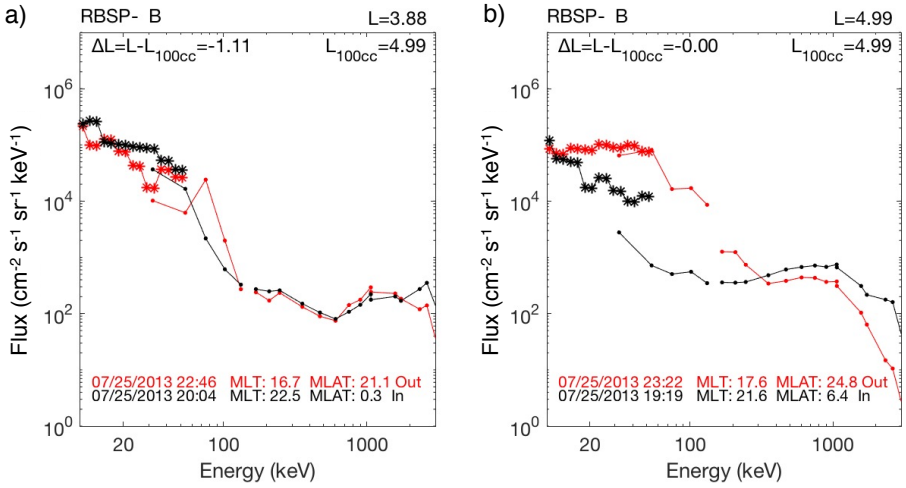

Figure 5.5: Same as Figure 5.2, but for the 25 July 2013 event.

This event was also studied in depth by Turner et al. [2015] using 13 different spacecraft. Therefore, we refer to Turner et al. [2015] to provide information on energetic electrons at other locations. According to their study, two injections were observed below geosynchronous orbit during this event. The first enhancements were observed by LANL-04A and LANL-02A around 20:46 UT

(∼3 MLT) and 20:48 UT (∼5 MLT), and the local time distance between the two spacecraft marks the local time limit of the first enhancement/injection. The second deep injection was observed first by LANL-04A at 21:25 UT. Due to the difference in our enhancement definition, we identified a slightly higher inner boundary of the initial sudden enhancement than Turner et al. [2015]. We, however, have verified that in both scenarios, the initial sudden enhancements coincide or stay beyond the innermost L_{pp} (Figure 5.6c).

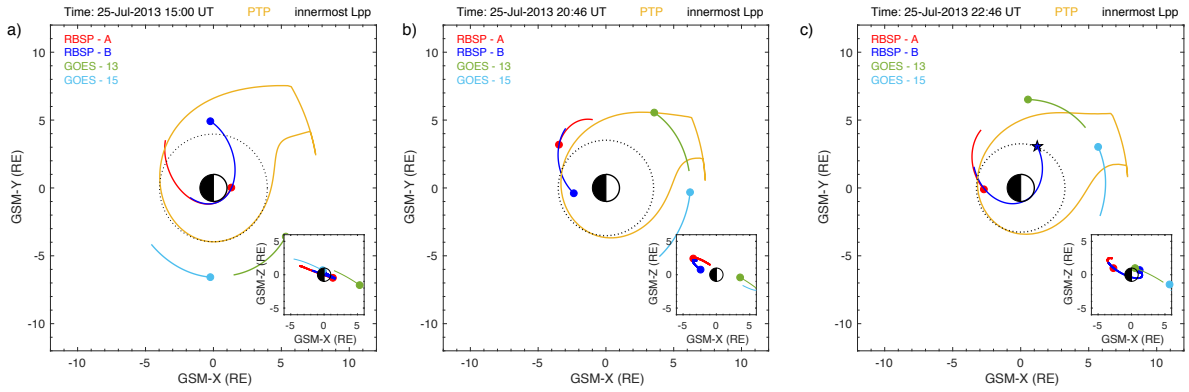

Figure 5.6: Like Figure 5.3, but for July 25, 2013 event. (b) the location of the Van Allen Probes and GOES spacecraft when flux enhancements were first observed by LANL-04A at 20:46 UT.

The simulated innermost L_{pp} refers to the lowest plasmapause position of all local times between 15 UT to 22:46 UT. In this case, it represents the plasmapause position near the post-midnight sector, which is consistent with the local time of the LANL-02A and LANL-04A when they observed flux enhancements. In other words, the innermost L_{pp} is likely associated with the plasmapause location near the actual enhancement region. The initial sudden enhancements were determined inside the in-situ L_{pp} (near the dusk sector) but beyond the innermost L_{pp} (near the postmidnight sector), as seen in Figure 5.6. This result can be explained by the combined effect of ExB and gradient-B/curvature drift. Once the energetic electrons are transported to such low L, the gradient-B/curvature drift is likely to dominate and forces them to drift eastward. As noted by Turner et al. [2015], the enhancements detected by Van Allen Probes are likely related to the enhancements observed first by the geosynchronous satellites. They also determined that one of

the THEMIS spacecrafts, TH-A, passed through the plasmapause around 21:02 UT, at L = 3.7 and 05:10 MLT. Based on the PTP simulation, TH-A was likely measuring the minimum plasmapause location. Assuming a simple dipole magnetic model, a 75 keV electron at L = 3.88 can complete its drift in ∼2.4 hours. Because of their orbit, Van Allen Probes only detect a significant flux enhancement an hour or two after at ∼17 MLT (22:46 UT) and were inside the plasmaspheric bulge/plume during that time, according to the projected global plasmapause locations by the PTP simulation [Goldstein et al., 2005]. This is thus supportive of our observations that the initial flux enhancements were observed inside in-situ L_{pp} but remain outside the innermost L_{pp}. This event also demonstrates that the innermost L_{pp} is a good proxy for the plasmapause location near the actual initial enhancement event, and it is particularly useful in the case when the spacecraft is located far from the actual initial enhancement such as this event.

5.3.3 Summary of the outlier events

This section provides a summary of the relationship between the ′outlier′ enhancement events and the in-situ plasma density as well as the innermost L_{pp}. Table 5.1 lists nine outlier events with the minimum Dst and maximum AE index, the distance between the innermost L_{pp} and the inner boundary of the initial enhancements (among all energy channels) during a specific event, the corresponding plasma density, the magnetic local time (MLT) of the observed initial enhancements by the Van Allen Probes as well as the MLT of the innermost L_{pp} during the initial enhancements. Note that the events in Table 5.1 are arranged according to the MLT of the observed initial enhancement events. The MLT are further categorized into four different sectors: post-midnight (0-6 MLT), pre-noon (6-12 MLT), post-noon (12-18 MLT), and pre-midnight (18-0 MLT). In this section, we only study the ′innermost′ of all the initial enhancements from different energy channels during a specific event, and these ′innermost′ initial enhancements are from 32-80 keV electrons. This is relevant to the energy-dependent dynamics of energetic electrons discussed in previous studies like Khoo et al. [2019] and Reeves et al. [2016] that enhancements of lower-energy electrons often occur earlier than higher-energy electrons.

To complement Table 5.1, Figure 5.7 presents the location of these initial enhancements for all outlier events in Geocentric Solar Magnetospheric (GSM) coordinates. The colors in Figures 5.7a represent the distance of the inner boundary of initial enhancements from the innermost L_{pp}. The negative (positive) ΔL means the inner boundary is inside (outside) the innermost L_{pp}. Based on Table 5.1 and Figure 5.7a, five out of nine events were found outside the innermost L_{pp}, while the other four events were <0.45 L inside the innermost L_{pp}. Our earlier statistical studies [Khoo et al., 2018, 2019] examined CME- and CIR-driven storms that occurred between January 2013 to June 2015 and identified 231 initial enhancement events across different electron energies. Only three out of 231 initial enhancement events were found inside the simulated innermost L_{pp}. As detailed in Goldstein et al. [2014], the PTP simulation is generally in agreement with the Van Allen Probes′ observations but there still exist discrepancies between model and observations especially during quiet or weakly disturbed conditions. Our investigation of these outlier events suggests that even for those that are inside the innermost L_{pp}, they are still within the range of the model uncertainty (0.40±0.05).

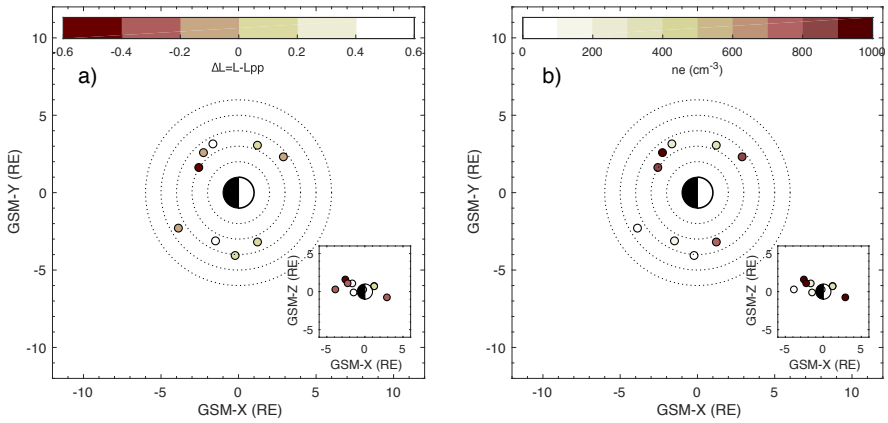

Figure 5.7: Initial enhancement events in GSM coordinates. The colors in (a) and (b) represent the distance between the inner boundary of initial enhancement events and the simulated innermost L_{pp} (ΔL) and the corresponding plasma density, respectively.

The colors in Figure 5.7b, on the other hand, represent the corresponding plasma density at the inner boundary of initial enhancement events. A plasma density less than 100 cm^{-3} suggests

Table 5.1: Geomagnetic indices (Dst and AE index), the distance between the inner boundary of initial enhancement events and the simulated innermost L_{pp} (ΔL), the corresponding plasma density (ne), the magnetic local time (MLT) for the outlier events examined in this study that are measured by RBSP, and the MLT of the innermost L_{pp} during the initial enhancements.

Event	Dst_{min} (nT)	AE_{max} (nT)	ΔL	ne (cm^{-3})	MLT of the observed initial enhancements	MLT of the innermost L_{pp}
10/14/14	-49	864	-0.19	51.46	Post-midnight (2)	Pre-noon (8.6)
3/1/13	-55	935	0.44	161.02	Post-midnight (4.1)	Post-midnight (2.9)
11/4/14	-44	856	0.07	41.82	Post-midnight (5.8)	Pre-noon (6.4)
12/17/12	-11	589	0.09	763.59	Pre-noon (7.4)	Post-midnight (2.7)
7/23/15	-63	1162	-0.11	841.87	Post-noon (14.6)	Pre-noon (7.0)
7/25/13	-19	749	0.12	349.14	Post-noon (16.5)	Post-midnight (2.8)
5/18/13	-61	1009	0.55	239.64	Pre-midnight (19.8)	Post-midnight (4.7)
6/22/15	-204	1636	-0.15	926.05	Pre-midnight (20.9)	Post-midnight (2.5)
6/8/15	-73	957	-0.43	838.81	Pre-midnight (21.7)	Post-midnight (2.8)

that the spacecraft is outside of the in-situ L_{pp} and vice versa. We note that the $'$outlier$'$ initial enhancement events near the post-midnight sector are found outside the in-situ L_{pp}, while those near the duskside are inside the in-situ L_{pp}. The MLT of the innermost L_{pp} in Table 5.1 also indicates that the innermost L_{pp} for these nine events were identified near the post-midnight and pre-noon sectors between 2.5 to 8.6. These observations are consistent with the common understanding of the local-time-dependent plasmapause positions. The plasmapause near the post-midnight and pre-noon sector is generally the most earthward especially during the geomagnetic active period, while the plasmapause near the dusk side is often further away from the Earth. The observed initial enhancements near duskside thus are more likely to be found inside the in-situ L_{pp} than those near the midnight sectors, as shown in Table 5.1 and Figure 5.7b. Therefore, it warrants caution when using the location of the enhancements with respect to the in-situ L_{pp} to infer the effect of convective electric field on the energetic electrons.

5.4 Phase space density analysis

The in-situ nature of the spacecraft measurements and the uncertainty associated with the plasmapause simulation make it hard to fully capture the relationship between the plasmapause

locations and these outlier enhancement events. To further investigate these outlier events, we conduct a phase space density analysis. The idea behind this is that if it is the large-scale electric field that transports energetic electrons inward and erodes the plasmasphere, we will likely observe an inward shift of the phase space density gradient, rather than a local peak in the phase space density. We converted flux to phase space density as a function of the three adiabatic invariants, μ, K, and L^*, and examined the phase space density profile during the enhancement events (dashed lines in Figures 5.8 and Figures 5.9) as well as the closest prior pass (solid lines in Figures 5.8 and 5.9) for both the October 14, 2014 event and the July 25, 2013 event.

The phase space density evolution between the outbound pass where the initial enhancement of 32keV electrons was identified by RBSP-A and the prior outbound pass observed by RBSP-B during the October 14, 2014 event is presented in Figure 5.8. We selected μ values of 6, 9, and 15 MeV/G for this event, which translates to 73 keV, 117 keV, and 151 keV at $L^* = 4$ during this storm period. For this event, we choose K= 0.12 $G^{0.5}R_E$, which corresponds to electrons with equatorial pitch angles of 38 - 52° for L^*= 3 - 5.5 to ensure sufficient statistics for this analysis. RBSP-B passed L^*=4 at 07:41 UT during its outbound pass, and in the subsequent outbound pass where the initial enhancement event was observed, RBSP-A passed L^*=4 at 14:24 UT. Due to the orbit of the spacecraft and the variations in the geomagnetic latitude that they cover, the prior outbound pass observed a wider range of L and L^*, as shown in Figures 5.8 and 5.1d. The relatively weak geomagnetic activity a few weeks before the event could explain the rather flat phase space density profile we observed at the pass before the initial enhancements (the solid line in Figure 5.8). With the lack of local peaks in the phase space density profile during the initial enhancement pass, radial transport of electrons is favored as the underlying mechanism for this initial enhancement event.

To study the initial sudden enhancements of <145 keV electrons during the July 25, 2013 event, we look at three distinct μ values: 9, 15, and 20 MeV/G, which translates to 38keV, 57 keV, and 92 keV at $L^* = 4$, respectively. We choose K= 0.2 $G^{0.5}R_E$, which corresponds to electrons with equatorial pitch angles of 30 - 45° for L^* = 3 - 5.5 to provide sufficient statistics for this analysis.

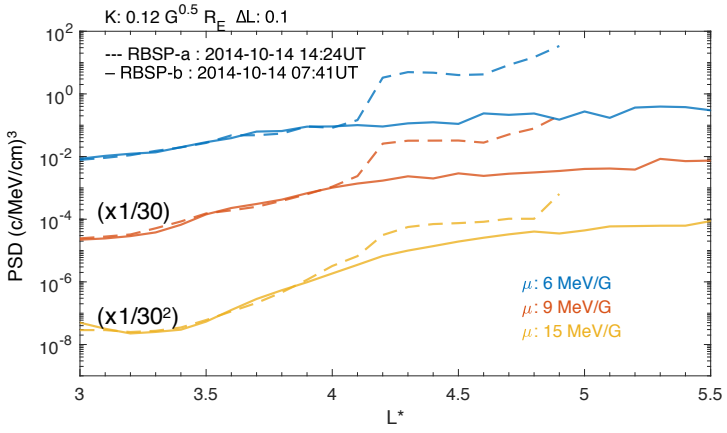

Figure 5.8: Phase space density evolution between two successive outbound passes by Van Allen Probes on October 14, 2014 at three μ values of 6, 9, 15 MeV/G, and K of 0.12 $G^{0.5}R_E$. The time on the top left indicates the time when the RBSP-A/B passed L^*=4 during their corresponding outbound pass.

From Figure 5.9, it is clear that the radial gradient of the PSD moves radially inward between two consecutive outbound passes. This suggests that the flux enhancement described in Section 5.3.2 is also likely due to inward radial transport. The same type of phase space density evolution was observed by Califf et al. [2017]. Using a simple large-scale convection electric field model, they successfully reproduced a similar PSD evolution. Their study emphasizes the importance of time-varying electric fields to produce a net inward radial transport of energetic electrons. It is noted that the time-varying enhanced electric field is also responsible for the erosion of the main plasmasphere and the formation of the plasmaspheric bulge and/or plume near the duskside. This is in agreement with our observations in Section 5.3.2 that the inner boundary of the initial enhancement near duskside is outside of the simulated innermost L_{pp} but inside the in-situ L_{pp}. In short, the phase space density analysis for these two events points to inward radial transport as the underlying mechanism for the initial sudden flux enhancements. This is pertinent to the effect of enhanced electric field on the energetic electrons and the plasmasphere, and it is consistent with our findings in Section 5.3 where most of the initial enhancements remains outside the innermost L_{pp}.

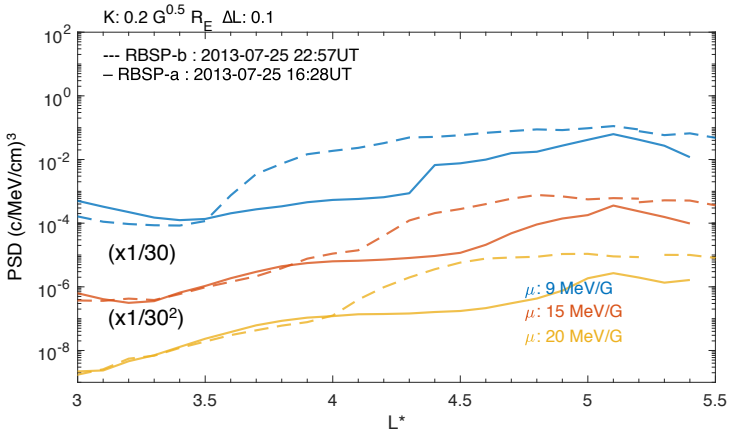

Figure 5.9: Phase space density evolution between two successive outbound passes by Van Allen Probes on July 25, 2013 at three μ values of 9, 15, 20 MeV/G and K of 0.2 $G^{0.5}R_E$. The time on the top left indicates the time when the RBSP-A/B passed L*=4 during their corresponding outbound pass.

5.5 Discussion and conclusion

This study examined multiple events where enhancements were previously reported inside the in-situ L_{pp} or the simulated innermost L_{pp}. A close inspection of these nine $'$outlier$'$ events reveals a local-time dependency of the relationship between the observed initial enhancements and the in-situ L_{pp} that is inferred using the density threshold of ne =100 cm^{-3}. In this study, two out of the three initial enhancement events detected near the postmidnight sector are found outside the in-situ L_{pp}. In the meantime, the initial sudden enhancement events detected near noon/dusk sectors are found inside the in-situ L_{pp} but remain outside of the innermost L_{pp} (within the plasmapause uncertainty), as demonstrated in six out of nine outlier events that we studied here (see Table 5.1 and Figure 5.7). The satellite observations are limited by their localized nature and hence lack the global contextual information of the plasma population. Meanwhile, the inner magnetosphere dynamic is temporal and local time dependent. The distinction between the in-situ L_{pp} and the innermost L_{pp} is thus an important one to make.

After taking uncertainties of the plasmapause model into account, our study suggests that the innermost L_{pp} remains the innermost limit for the initial sudden enhancements of energetic

electrons. This correlation has been observed by previous studies [Li et al., 2006; Khoo et al., 2018, 2019], and this study shows that this relation persists even in events that were previously regarded as ′outliers′. Thaller et al. [2015] have demonstrated a clear coincidence between the electric field enhancement and the plasmaspheric erosion using Van Allen Probes data. Note that plasmasphere dynamics are subjected to both convection electric field and SAPS [Goldstein et al., 2003], as were the PTP simulations used in this study. Our findings thus suggest that the large-scale duskward electric field that is responsible for the plasmaspheric erosion can also transport the energetic electrons to low L-shells. These large-scale electric fields could be a result of enhanced global convection and/or localized electric field structure like SAPS [Goldstein et al., 2003]. It is thus important to note that our findings bespeak the role of the large-scale electric fields in these sudden enhancement events without isolating the source of these fields.

In summary, we have shown that due to the localized nature of satellite measurements and the spatiotemporal dependency of the inner magnetosphere dynamics, the initial sudden enhancement locations are more commonly found inside the in-situ L_{pp} when the observations were made near the noon/dusk sectors where the local L_{pp} is usually at a larger L value. Unlike the comparison of the measured enhanced energetic electrons with the in-situ L_{pp}, our study suggests that the innermost L_{pp} presents the limit of the inner boundary of the initial enhancements of energetic electrons regardless. The phase space density analysis further implies that inward radial transport is responsible for these initial enhancement events. These observations fit the understanding of the role of large-scale electric fields on energetic electrons and the plasmasphere. This study also inherently implores caution when using the comparison between the measured particle enhancement locations and the in-situ L_{pp} to imply the effect of large-scale electric fields on energetic electrons. Finally, insights from this study will allow us to leverage advances in the modeling of plasmapause/plasma density to infer the initial enhancement location of energetic electrons and improve predictive simulations of energetic electron dynamics.

Chapter 6

Overcoming the Challenges of Measuring Energetic Particles in the Inner Belt: A Geant4-based Performance of an Energetic Particle Detector Instrument, REPTile-2

This chapter is based on parts of the work that is submitted to Journal of Geophysical Research: Space Physics, titled 'On the Challenges of Measuring Energetic Particles in the Inner Belt: A Geant4-based Simulation of an Energetic Particle Detector Instrument, REPTile-2', Journal of Geophysical Research: Space Physics.

6.1 Introduction

High quality measurements of energetic particles can shed light on old, lingering questions and sometimes provide a new perspective on our prior understanding of the radiation belts. For instance, one of the perplexing findings from the Van Allen Probes mission is the absence of MeV electrons in the inner belt [Li et al., 2015; Fennell et al., 2015; Li et al., 2017]. This observation contrasts with previous findings such as those of Baker et al. [2004], Zheng et al. [2006], and Li et al. [2009], where significant >MeV fluxes from previous missions were observed in the inner belt during the early 2000s. Inspired by Van Allen Probes measurements, Selesnick [2015b] reexamined earlier observations of relativistic electrons in the inner belt and determined that equatorial trapping electrons measured by SAMPEX (a low-Earth orbit satellite) near/at the South Atlantic Anomaly (SAA) were contaminated by lower energy electrons or high-energy proton, leaving observations such as the missing MeV electrons for future verification [Selesnick, 2015b]. On the

other hand, the theoretical prediction of the CRAND contribution to high-energy inner radiation belt electrons (>800 keV) has not been verified by observation due to the lack of high-sensitivity detectors [Selesnick, 2015a]. To address these questions requires fine-energy resolution and clean (i.e., low contamination) energetic particle measurements.

Measuring energetic particles, especially electrons, can be a daunting task as explained by Vampola [1998]. It requires an understanding of how particles of interest and background populations interact with the instrument. In addition to contamination from background particle sources, electronic limitations such as saturation add additional complexity to identifying the energy and species of incident particles correctly. In an ideal system, the electronics can handle and resolve every single pulse triggered by incident particles. In reality, they cannot distinguish pulses that occur within the resolution time (pileup) and require some time to recover after recording a pulse (deadtime). A coincidence system might also be tricked by two different particles that hit almost simultaneously on two different detectors and interpret them as a single particle (chance coincidence). Previous instruments have suffered from these detrimental effects in the inner belt region, where actual measurements are sometimes overwhelmed [Selesnick, 2015b; Selesnick et al., 2019]. To ensure the quality of energetic particle measurements, it is thus necessary to consider and understand the effect of these potential problems early in the instrument design phase.

The Relativistic Electron Proton Telescope integrated little experiment-2 (REPTile-2) is a miniaturized solid-state telescope that aims to undertake this difficult task. The goal is to provide fine energy resolution measurements with minimal contamination, including background contamination sources and electronics limitations. REPTile-2 has the flight heritage from REPT [Baker et al., 2012] onboard Van Allen Probes and REPTile onboard the Colorado Student Space Weather Experiment (CSSWE) CubeSat [Li et al., 2012, 2013a,b; Schiller and Mahendrakumar, 2010]. With the addition of guard rings and detailed pulse-height analysis, REPTile-2 has improved upon its previous design; through Geant4 simulations and calibration results, it shows promising capability in providing 300 keV - 3 MeV electron measurements with energy resolution as low as 40 keV ($\Delta E/E < 16\%$ for 300 keV - 3 MeV) and in minimizing unwanted background contamination.

REPTile-2 is the sole payload onboard Colorado Inner Radiation Belt Experiment (CIRBE), a low-Earth orbit (LEO) CubeSat mission supported by NASA. The primary objective of the CIRBE mission is to improve our understanding on the formation of the inner belt (L < 2) electrons (100s of keV to multiple MeV), and to determine the source, the intensity, and dynamic variations of these electrons. To study the detailed variations of these electrons, the instrument is required to provide measurements for 0.3 - 3 MeV electrons with $\Delta E/E < 20$ % and a secondary measurements of 6.7 - 30 MeV protons with $\Delta E/E < 25$ %. REPTile-2 is designed to constantly point at directions perpendicular to the local magnetic field lines. The mission is currently scheduled for launch no earlier than the fourth quarter of 2022.

The purpose of this chapter is to provide a description of REPTile-2 design and a detailed discussion of instrument performance that is characterized using the Geant4 simulations. Specifically, sections 6.2 and 6.3 describe the REPTile-2 design and Geant4 setup for this instrument. Section 6.4 includes the instrument characterization and a study of the pileup effect on the instrument. Section 6.5 concludes this chapter with some final remarks. As an instrument scientist for the CIRBE mission, I directly involved in the decision-making for the Be-window thickness, the simulations of charged particles interacting with the instrument using Geant4, and the characterization of instrument performance to ensure the design meets the requirements using both simulated and actual test results. I only indirectly involved in the derivation of logic and binning equations, which was mainly done by Dr. Richard Selesnick; my contribution was limited to providing the Geant4 simulation results that are necessary to derive those equations.

6.2 REPTile-2 design

REPTile-2 is a 1.5 U (10 cm x 10 cm x 15 cm, with electronics) energetic particle telescope, as illustrated in Figure 1. It includes four 1.5 mm thick silicon detectors separated into inner areas (radius of 10mm) and outer rings (inner radius: 10 mm; outer radius: 20 mm), which are also known as guard rings. The silicon detectors are obtained from Micron Semiconductors, UK. Each silicon detector is held in the center of a detector holder with a separation of 4 mm between two

detectors.

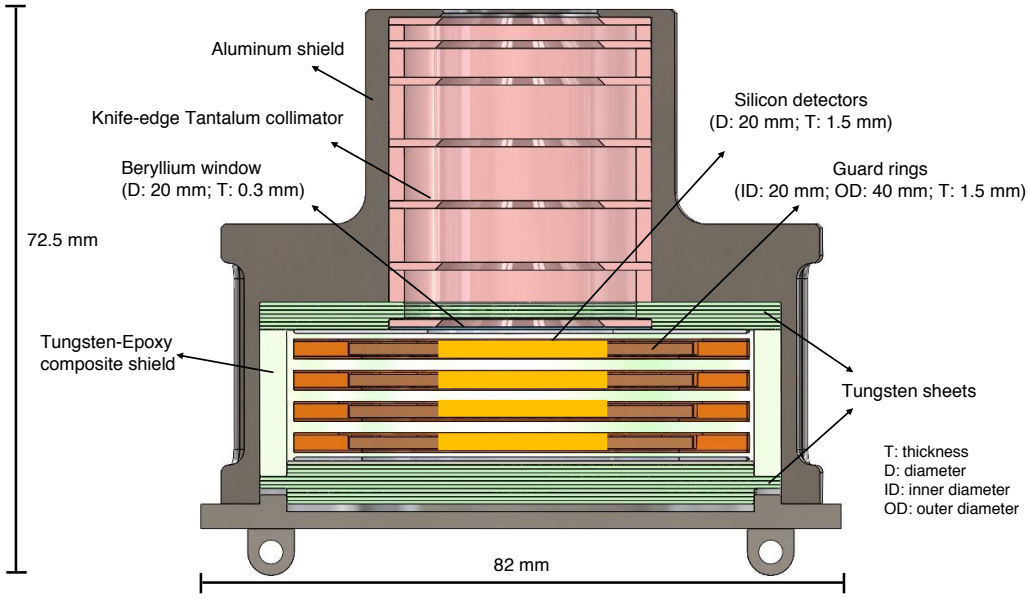

Figure 6.1: Illustration of REPTile-2 design with labelled key features.

In front of the silicon detectors, there is a beryllium (Be) window with a diameter of 20 mm and a thickness of 0.3 mm that can block <200 keV electrons and <6 MeV protons from reaching the silicon detectors. In front of the Be window, a collimator with a length of 36.5 mm and seven optimally spaced, knife-edge baffles is used to prevent electrons outside of the field of view (FOV) from scattering off the collimator walls into the detectors. The collimator has an inner radius of 10 mm and is made of Tantalum (Ta), a high atomic number (Z) material. Under this configuration, REPTile-2 has a ∼50 degree FOV. The spacing of the baffle is designed to maintain the 50-degree FOV angle such that an out-of-field electron cannot directly reach the detector stack [Schiller and Mahendrakumar, 2010].

The entire instrument is shielded by aluminum (Al) with additional inner shield made of mostly Tungsten (W) that surrounds the silicon detectors. This layered shield stops electrons with energy less than 10 MeV and protons with energy less than 60 MeV from reaching the detector stack. Although not modeled in Figure 1, Tungsten sheets with 0.5 mm thickness each are used on the top and bottom of the detector stack, while the inner Tungsten shield ring around the detector stack

is made of Tungsten-epoxy composite (64% Tungsten and 36% epoxy). These changes are made to meet the orbital debris requirement during atmospheric reentry for spacecraft de-orbit. The overall mechanical design is inherited from REPTile with some changes such as the use of guard rings for all four detectors and a thinner Be window to decrease the lower limit of measurable particles.

The REPTile-2 design is inherited from REPTile. Most changes were performed by the engineers to meet the mass and debris requirement. The only design component that I was actively involved in is the thickness of Be window, which benefits from the assistance of Guillem Megias i Homar (whose senior project revolves on this subject). There are several key physical differences between REPTile and REPTile-2 as listed:

(1) The thickness of Be window changes from 0.5 mm in REPTile to 0.3 mm in REPTile-2. A Be window with 0.5 mm thickness can stop < 400 keV electrons from reaching the detector. Changing the thickness of Be window from 0.5 mm to 0.3 mm allows us to measure lower energy electrons (> 200 keV electrons).

(2) In REPTile-2, all four active silicon detectors are separated into inner and outer detectors: the inner detector is the active detector with the same diameter as the aperture and the outer detector is the anti-coincidence guard detector that vetoes counts that trigger it.

(3) The gap between the detectors is bigger in REPTile-2 (~ 2.5 mm) than REPTile (~ 1.0 mm). This change is unintentional and due to an oversight during the purchase of the silicon detectors. We have verified that this change have little influence on the instrument performance (see Section 6.4.5.2 for more discussion).

(4) The tungsten shielding also changes from pure tungsten solid to tungsten powder-epoxy composite with a ratio of 64 % W to 36 % Epoxy to ensure there is no debris that reaches the ground during the atmospheric reentry. The density of Tungsten-epoxy composite is estimated to be $\sim 11\ g/cm^3$ ($0.64 \times \rho_W + 0.36 \times \rho_{Epoxy} = 0.64 \times 16.7\ g/cm^3 + 0.36 \times 1.3\ g/cm^3 = 11\ g/cm^3$).

(5) The aluminum shield in REPTile-2 was also updated and was reduced in thickness to ensure the entire spacecraft is below the mass requirement.

6.3 Geant4 simulations

Geant4 (abbreviation for Geometry And Tracking, version 4) is an object-oriented toolkit that uses a Monte-Carlo approach to simulate the passage of particles through matter [Agostinelli et al., 2003; Allison et al., 2006, 2016]. Geant4 is robust because it considers all known particle′s interactions and uses reference data from experimental particle reactions. This toolkit allows users to make changes in all typical domains of detector simulations such as geometry modeling, physics models, run and event management, tracking, and visualization, enabling the users to tailor the simulations to their specific needs. With its improved functionality and usability, Geant4 has been widely used in areas such as space applications, high energy physics experiments, instrument design, medicine, and more.

In this study, all simulations were performed using Geant4.10.3. source code. The more precise standard Geant4 electromagnetic physics list G4EmStandardPhysics-option4 ($'EMZ'$) is selected for this study. Prior to the simulations, it is required to specify the initial particle source, particle types, number of particles, and incident energy in each simulated event. We conducted two types of simulations: the boresight-shooting simulation and the ′spherical simulation′ where a particle with a randomized incident energy shoots from an inner spherical surface around the instrument. The former tells us the likely responses from field-of-view (FOV) particles, while the latter allows us to explore the detector′s responses of particles from and outside the FOV. G4General Particle Source package available in Geant4 is utilized for the spherical simulations. The radius of the source sphere is 50 mm, centered to cover the entire instrument. To generate isotropic flux inside the sphere, the angular distribution of the incident particles is prescribed a cosine-law distribution [e.g., Zhao et al., 2013].

Incident electrons and protons that range from 100 keV to 10 MeV electrons and 1 to 200 MeV protons are simulated in this analysis. Tens of billions of spherical simulation events were

stimulated to ensure sufficient statistics. The energy deposited on all four detectors and guard rings for each event were recorded and analyzed under logic/binning equations. The simulation results are analyzed using MATLAB 2017b software, and the analysis results are described in detail in the following section.

6.4 Instrument characterization

6.4.1 Passive shielding

Figure 6.2 shows sample paths of incident electrons and protons through the REPTile-2 instrument model that is reconstructed in Geant4 at four distinct incident energy. For illustration purposes, the trajectories are randomly chosen at the plane of the figure, whereas the actual simulations utilize a full three-dimensional distribution. The thickness of the Al shield on REPTile-2 ranges between 0.1-10 mm, while the thickness of the W shield ranges from 3.5 mm on the side to 5 mm on the back.

On the top panel of Figure 6.2, the 300 keV incident electrons entering from FOV can barely pass through the Beryllium (Be) window. In comparison, 1.5 MeV incident electrons from the FOV can readily reach the detector stacks. 3.5 MeV electrons from the FOV can penetrate the entire detector stack, whereas the 'off-axis' 3.5 MeV electrons can reach deeper into the passive shields but are still far away from the detector stack. Photons (indicated as green lines) are generated as byproducts of the interactions between the instrument and these energetic electrons. Non-FOV 10 MeV incident electrons can readily penetrate the thick passive Al and W shields, but due to fluctuations in path length and angular scattering, few can reach the detector stack. Meanwhile, those originating from the FOV can penetrate through all four detectors, and some can even go through the W-Al back shields. In short, the passive shielding on REPTile-2 can shield off most of the $'$off-axis$'$ energetic electrons ($E \leq 10$ MeV), especially those coming from the side and the back.

Unlike electrons, protons maintain a relatively straight trajectory most of the time, as

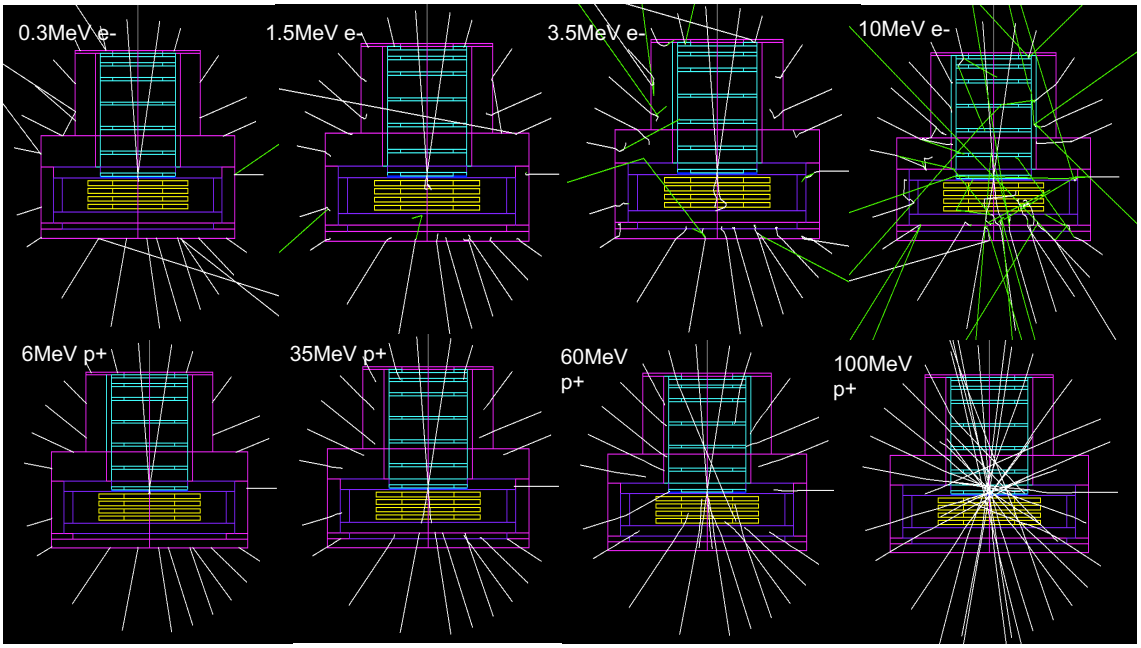

Figure 6.2: (top) Sample trajectories of incident electrons through REPTile-2, indicated as white lines, are modeled using Geant4 and visualized using HepRep visuals at four distinct incident energy. The green lines represented paths of the photon generated by the incident electrons. (bottom) Same as the top panels but for incident protons

shown in the bottom panel of Figure 6.2. Under the current REPTile-2 design, only >6 MeV incident protons entering from FOV can pass through the Be window and reach the first detector. For 35 MeV incident protons, those entering from the FOV can penetrate through the detector stack while others can only penetrate the Al shield, but none of the ′off-axis′ 35 MeV protons can reach the detector stack. For 60 MeV incident protons, some of the non-FOV protons coming from the back can reach the last two detectors but are not energetic enough to penetrate the entire detector stack. For 100 MeV incident protons, both FOV and non-FOV from all directions are capable of passing all passive shields and based on their initial angular directions, some can even pass through the entire detector stack and come out from the other side of the instrument. This underlines the potential contamination by these high-energy protons, where no passive shielding can stop these protons from reaching the detectors.

6.4.2 Monoenergetic simulation results

Figure 6.3 shows the distribution of the total energy deposited on the detector stacks by monoenergetic electrons and protons, shooting from the boresight. Incident protons deposit a narrow range of energy in the detector stack. The total energy deposit by lower energy (<∼33 MeV) protons, are generally close to its incident energy. In other words, they are likely to lose all of their energy in the detector stack. Meanwhile, the more energetic protons (≥35 MeV) from FOV deposit less than their incident energy and are likely to penetrate through the entire detector stack. The more energetic these high-energy protons are, the less energy they deposit on the detector stack. Their energy deposition distributions are also more wide-spread than those that deposit all their energy in the detectors.

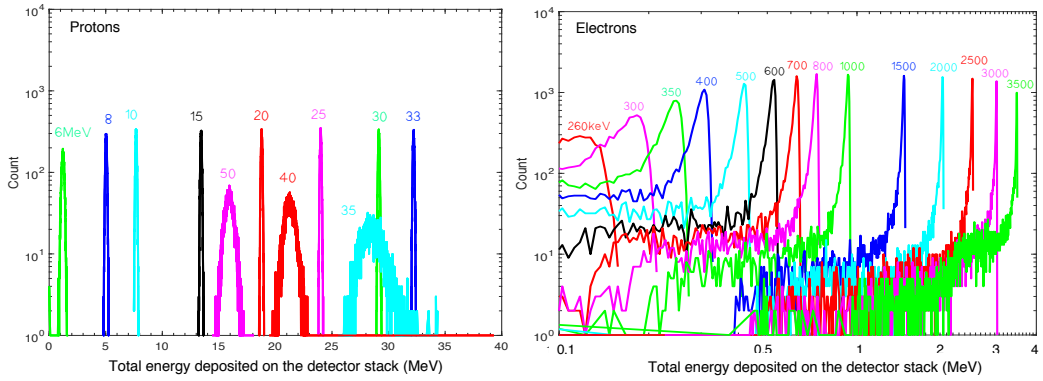

Figure 6.3: Distributions of the total energy deposited on the detector stacks by the boresight-shooting, monoenergetic electrons and protons. The x-axis for incident electrons and y axes for both incident particles are in logarithmic scale.

Unlike incident protons, the incident electrons deposit a wider range of energy in the detector stack. Despite that, the peaks of these energy spectra suggest that a majority of incident electrons deposit most of their energy in the detector stack. It is also important to point out that by using four detectors and considering the total energy deposited on the entire detector stack (rather than a single detector), REPTile-2 mitigates the secondary peaks at lower energy caused by minimum ionizing particles, which were observed in the Instrument for Particle Detection (IDP) instrument onboard DEMETER satellite that had only one detector (Figure 6 in Sauvaud et al.

[2006]). In the case of the IDP instrument, their single detector has a thickness of 1 mm where some of the relativistic electrons (>1-MeV) can penetrate through the detector and deposit a minimum amount of energy, which is demonstrated as a secondary peak at the lower energy in Figure 6 of Sauvaud et al. [2006]. On the other hand, REPTile-2 uses four detectors with a total thickness of 6 mm which on average, only electrons >∼4 MeV can penetrate through all four detectors and deposit a minimum amount of energy on the detectors. Therefore, by considering the total energy deposit on the detector stack, REPTile-2 can measure ∼0.3 to ∼4 MeV electrons with little influence from the minimum ionizing particles.

6.4.3 Anticoincidence detectors - the guard rings

Very energetic protons can penetrate through the passive shielding and be a source of contamination for electron measurements. To mitigate this, REPTile-2 uses anticoincidence detecting for active collimation. As a critical feature of the REPTile-2 design, the guard rings are employed to detect and remove all particles that deposit higher than a specified threshold, TG, on the guard rings (also referred as the outer ring detectors). Figure 6.4a illustrates all simulated energy depositions by incident protons on the third detector, D3, and the last detector, D4. Figure 6.4b shows only events where the guard rings are not triggered. The contrast between Figures 6.4a and 6.4b (without and with anticoincidence detecting) is apparent. A vast amount of background contamination is removed with the usage of anticoincidence detecting. Above all, it reveals 'footprints' of distinct incident proton populations: range (RNG) protons (which deposit all energy in the detector stack) and penetrating (PEN) protons (which deposit little energy in the detector stack, as compared to the range protons). These 'footprints' prove to be helpful in deriving the logic equations for characterizing incident particles (See Section 6.4.4).

The bottom panel of Figure 6.4 presents a similar comparison but for incident electrons. Unlike Figures 6.4a and 6.4b, fewer 'contaminated' events are removed in Figure 6.4f. The energy deposits by incident electrons have no distinct pattern. The simulated incident electron energy range deposits lower energy (<5 MeV) than incident protons. This is not surprising because the

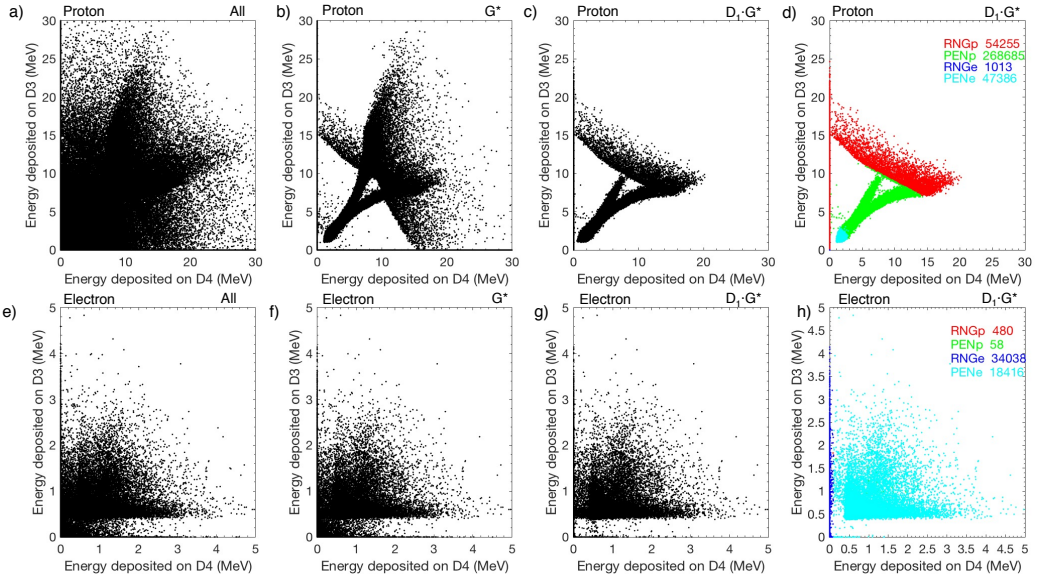

Figure 6.4: Energy deposition on the third detector (D3) against the energy deposition on the fourth detector (D4). The top and bottom panels are those by incident protons and electrons, respectively. (a & e) All events without applying the anticoincidence logic; (b & f) Only events that do not trigger the guard rings (i.e., energy deposit <= TG) (red). (c & g) Events that do not trigger the guard ring and deposit energy >T on the first detector, are considered as valid events in this study. (d & h) shows how the valid events are categorized into different particle types (red for RNGp, green for PENp, blue for RNGe, and cyan for PENe). T and TG are the threshold of the minimum energy deposit (in MeV) on a detector and guard rings, respectively. Note that a uniform incident flux spectrum is used here for both protons and electrons. The simulated electron and proton ranges are 0.1-10 MeV and 1-200 MeV, respectively.

stopping power for electrons is smaller and thus electrons deposit/lose less energy than protons when traversing through the same thickness material. It is also worth noting that the simulated results in Figure 6.4 are from the spherical Geant4 simulations based on a uniform incident energy spectrum. In reality, the incident particles more closely follow an exponential or power law energy spectrum. In other words, the number of very energetic incident particles that are removed by the anticoincidence logic will be smaller in the actual space environment.

6.4.4 Logic and binning equations

In this study, a valid event is an event that does not trigger the guard rings (i.e., energy deposit on guard rings must be less than or equal to TG) and deposit energy above a certain

threshold, T, on the first detector. T and TG are set as 0.1 MeV and 0.671 MeV based on the electronic noise analysis, where below these thresholds, electronic noise overwhelms the signal. For example, valid events from incident protons and electrons, which deposited energy on D3 and D4, are presented in Figures 6.4c and 6.4g, respectively. With the addition of D_1 requirements, the resultant valid event plot further reduces contamination from particles outside the FOV, demonstrated in comparisons between Figure 6.4b and 6.4c and between Figure 6.4f and 6.4g. The valid events are then categorized into four different particle types: range proton (RNGp), penetrating proton (PENp), range electron (RNGe), and penetrating electron (PENe) using the logic equations as described in Table 6.1. These equations were derived by the Co-PI of the CIRBE mission, Dr. Richard Selesnick, through analyzing the simulated energy deposit from Geant4 simulations. Also note that thresholds like T, TG, and the values in slant equations D_{12s} and D_{34s} can be modified during flight.

Particle types	Logic equations
Range proton (RNGp)	$D_1 \cdot D_{12s} \cdot (D_4^* + D_{34s}) \cdot G^*$
Penetrating proton (PENp)	$D_1 \cdot D_{12s} \cdot D_4 \cdot D_{34s}^* \cdot G^*$
Range electron (RNGe)	$D_1 \cdot D_{12s}^* \cdot D_4^* \cdot G^*$
Penetrating electron (PENe)	$D_1 \cdot D_{12s}^* \cdot D_4 \cdot G^*$

$\cdot$ is logical AND; + is logical OR;
* is logical complement (NOT)
E_n = measured energy deposit in detector n
$G_t = G_1 + G_2 + G_3 + G_4$
G_n = measured energy deposit in the outer ring (or the guard ring) of detector n, where n = 1, 2, 3, and 4
D_n is true if $E_n > 0.1$ MeV; G is true if $G_t > 0.67 MeV$
D_{12s} is true if $\frac{E_1}{2.8} + \frac{E_2}{4.2} > 1$; D_{34s} is true if $\frac{E_3}{13.5} + \frac{E_4}{30} > 1$

Table 6.1: Logic equations for each particle types used in REPTile-2.

To distinguish electrons from protons, we recall that the energy deposits by incident electrons are significantly lower than those by incident protons. This distinction allows the derivation of an empirical slant equation, D_{12s} (see Table 6.1 for the actual equation. Also see Figure 6.5). Particles that fulfill D_{12s} requirement deposit relatively high energy on the first two detectors and hence are most likely incident protons. The valid proton events are further binned into RNGp and

PENp using another slant equation D_{34s} and D_4 requirement (i.e., energy deposited on the last detector must be greater than T). Very energetic protons (>30 MeV) can penetrate through the instrument, including those that enter from FOV, and deposit very little energy in the detector stack. Figure 6.4c is particularly telling, where the valid events have two distinct branches and a negative-slope population. The fork is made of very energetic penetrating protons (>30 MeV): one branch is formed by those coming from the front, which deposit more energy on D_4 than D_3; the other is formed by those that enter from the back, which deposit more energy on D_3 than D_4. On top of the fork, there is a notable population with a negative slope, which is a characteristic of range protons. They distinctively deposit much higher energy in the detectors than the penetrating protons. Utilizing this characteristic difference, we derived another slant equation, D_{34s}, that is useful to distinguish the range proton that stops on the last detector from the penetrating protons, while the D_4 requirement captures the range protons that stop on the first three detectors. Together, they help differentiate range protons from penetrating protons (See Figure 6.5).

Due to electron scattering and range straggling, which cause the lack of defined characteristics in the electron's energy deposit distribution (Figure 6.4f), it is not possible to differentiate range electrons from penetrating electrons [Bichsel, 1988; Li et al., 2015]. Instead, a more simplistic approach is taken: PENe is defined as a valid event that deposits >T energy on the last detector (namely, the D_4 criteria in Table 6.1), while those that do not fulfill the D4 requirement are considered as RNGe. Figures 6.4d and 6.4h illustrate how valid events are categorized into different particle types using the logic equations. Most events are correctly categorized into their corresponding species channels. However, there are a small number of protons ($\sim$ 13% of the valid events from incident protons) that deposit very little energy and are recorded as electrons (cyan dots in Figure 6.4d). Compared to protons, most events by incident electrons are correctly identified by logic equations as electrons, and only a very small portion of incident electrons ($\sim$ 1% of the valid events from incident electrons) that deposit sufficient energy on D1 and/or D2 and fulfill D_{12s} requirements are taken as protons.

The valid events for each particle type are then binned into different energy channels

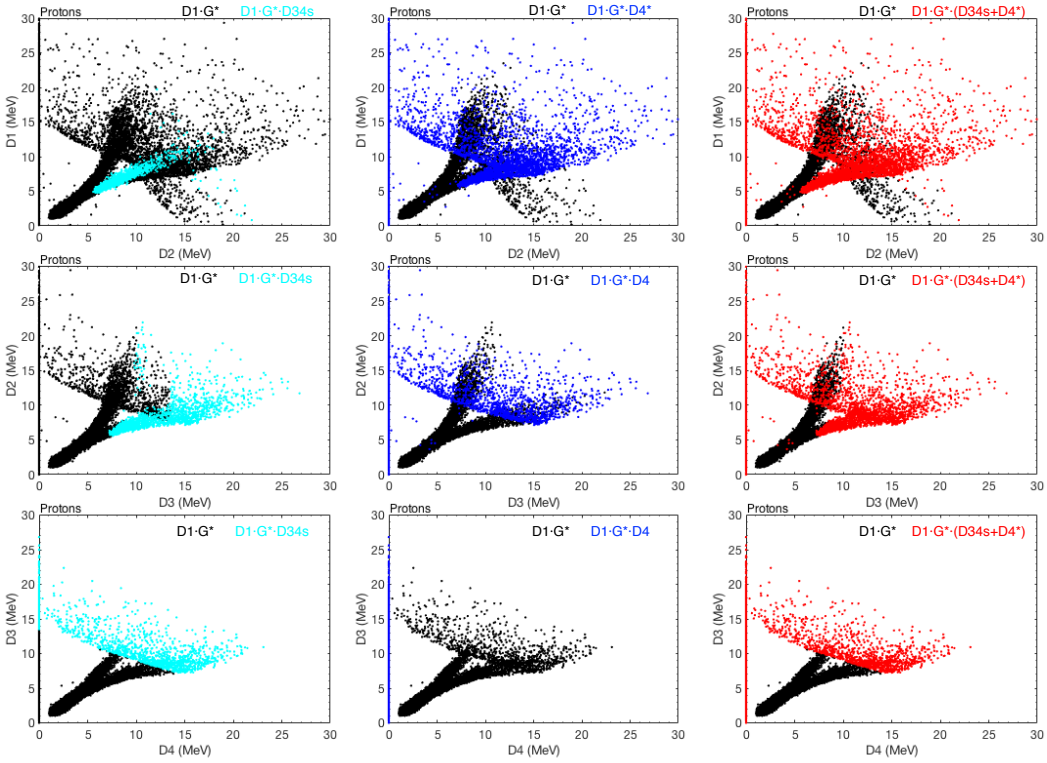

Figure 6.5: (top) Energy deposition on D1 against those on D2. (middle) Energy Deposition on D2 against those on D3. (bottom) Energy Deposition on D3 against those on D4. Events in cyan color indicate the valid events ($D_1 \cdot G^*$) that also fulfill D_{34s}; those in blue color are valid events where D_4 is not triggered; those in red color are valid events that trigger D_{34s} or do not trigger D_4.

based on their total energy deposit in all four detectors. Due to the electronic noise, only energy deposits higher than the threshold, T, on each detector are included in the computation of the total energy deposit. There are a total of 129 channels for REPTile-2. The first 120 channels are all logarithmically spaced differential channels except the last channel for each particle type (i.e., Ch 50, Ch 60, Ch 110, and Ch 120 in Tables 6.2, 6.3, and 6.4), which is an integral channel. RNGp and RNGe channels have 50 channels each, and PENp and PENe channels have ten channels each. The energy deposition width for RNGp and RNGe channels increases (decreases for PENp and PENe channels) logarithmically, dlogE = log(E2/E1)/N, where E1 and E2 are the lower/upper limit of the energy deposition for a specific particle type, and N is the number of channels for the specific particle type. The last nine channels include four channels that record counts of events

that have >T energy deposit on each detector as well as the guard rings (D_1, D_2, D_3, and D_4) and another four that record the coincidence range data ($D_1 \cdot D_2^*$, $D_1 \cdot D_2 \cdot D_3^*$, $D_1 \cdot D_2 \cdot D_3 \cdot D_4^*$, and $D_1 \cdot D_2 \cdot D_3 \cdot D_4$). The last channel, 129, records count of events on the guard rings (G). A detailed breakdown of the required total energy deposition and energy resolution for RNGp, RNGe, and both PENe/PENp are recorded in Tables 6.2, 6.3, and 6.4.

6.4.5 Instrument characterization

A careful characterization of how the instrument responds to particles is critical to ensure energetic particle data quality and verify if the instrument meets the scientific requirement. We computed instrument energy response functions from boresight-shooting particles and an isotropic flux source.

6.4.5.1 Boresight-shooting energy response function

A boresight shooting energy response function is determined by shooting particles of varying energy along the boresight of the instrument. A detector efficiency for boresight-shooting particles of specific incident energy is given by dividing number of valid events in each channel by the total number of stimulated particles within a certain energy bin. The energy response function is a product of the detector efficiency and a geometric factor of 0.52 cm^2sr. The analytical geometric factor [Equation 8 from Sullivan, 1971] is computed by assuming a two-element telescope between the aperture and the first detector,

$$G = \frac{1}{2}\pi^2[R_1^2 + R_2^2 + l^2 - ((R_1^2 + R_2^2 + l^2)^2 - 4R_1^2R_2^2)^{0.5}]$$

where R_1 is the radius of the aperture opening, R_2 is the radius of detector 1, l is the distance between the aperture and the first detector.

Figures 6.6 and 6.7 illustrate the instrument's energy response function to boresight-shooting electrons and protons, respectively. Each curve indicates the energy response function for a specific channel or in other words, the probability of incident electrons getting binned into a

Bin	Particle type	Logic equation	$E_{deposit}$ bin	G_{nom} (cm^2sr)	E_{beg} (MeV)	E_{end} (MeV)	delE (MeV)
1	RNGp	$D_1 \cdot G^* \cdot D_{12s} \cdot (D_4^* + D_{34s})$	2.800≤ Et <2.945	0.11	6.65	6.85	0.2
2	RNGp	$D_1 \cdot G^* \cdot D_{12s} \cdot (D_4^* + D_{34s})$	2.945≤ Et <3.098	0.12	6.75	6.95	0.2
3	RNGp	$D_1 \cdot G^* \cdot D_{12s} \cdot (D_4^* + D_{34s})$	3.098≤ Et <3.258	0.13	6.85	7.05	0.2
4	RNGp	$D_1 \cdot G^* \cdot D_{12s} \cdot (D_4^* + D_{34s})$	3.258≤ Et <3.427	0.10	6.85	7.15	0.3
5	RNGp	$D_1 \cdot G^* \cdot D_{12s} \cdot (D_4^* + D_{34s})$	3.427≤ Et <3.605	0.12	6.95	7.25	0.3
6	RNGp	$D_1 \cdot G^* \cdot D_{12s} \cdot (D_4^* + D_{34s})$	3.605≤ Et <3.791	0.12	7.05	7.35	0.3
7	RNGp	$D_1 \cdot G^* \cdot D_{12s} \cdot (D_4^* + D_{34s})$	3.791≤ Et <3.988	0.18	7.25	7.45	0.2
8	RNGp	$D_1 \cdot G^* \cdot D_{12s} \cdot (D_4^* + D_{34s})$	3.988≤ Et <4.194	0.20	7.35	7.55	0.2
9	RNGp	$D_1 \cdot G^* \cdot D_{12s} \cdot (D_4^* + D_{34s})$	4.194≤ Et <4.412	0.20	7.45	7.65	0.2
10	RNGp	$D_1 \cdot G^* \cdot D_{12s} \cdot (D_4^* + D_{34s})$	4.412≤ Et <4.640	0.21	7.65	7.85	0.2
11	RNGp	$D_1 \cdot G^* \cdot D_{12s} \cdot (D_4^* + D_{34s})$	4.640≤ Et <4.881	0.22	7.75	7.95	0.2
12	RNGp	$D_1 \cdot G^* \cdot D_{12s} \cdot (D_4^* + D_{34s})$	4.881≤ Et <5.134	0.24	7.95	8.15	0.2
13	RNGp	$D_1 \cdot G^* \cdot D_{12s} \cdot (D_4^* + D_{34s})$	5.134≤ Et <5.400	0.21	8.05	8.35	0.3
14	RNGp	$D_1 \cdot G^* \cdot D_{12s} \cdot (D_4^* + D_{34s})$	5.400≤ Et <5.679	0.24	8.25	8.55	0.3
15	RNGp	$D_1 \cdot G^* \cdot D_{12s} \cdot (D_4^* + D_{34s})$	5.679≤ Et <5.974	0.24	8.45	8.75	0.3
16	RNGp	$D_1 \cdot G^* \cdot D_{12s} \cdot (D_4^* + D_{34s})$	5.974≤ Et <6.283	0.33	8.75	8.95	0.2
17	RNGp	$D_1 \cdot G^* \cdot D_{12s} \cdot (D_4^* + D_{34s})$	6.283≤ Et <6.609	0.28	8.95	9.25	0.3
18	RNGp	$D_1 \cdot G^* \cdot D_{12s} \cdot (D_4^* + D_{34s})$	6.609≤ Et <6.951	0.30	9.15	9.45	0.3
19	RNGp	$D_1 \cdot G^* \cdot D_{12s} \cdot (D_4^* + D_{34s})$	6.951≤ Et <7.311	0.32	9.45	9.75	0.3
20	RNGp	$D_1 \cdot G^* \cdot D_{12s} \cdot (D_4^* + D_{34s})$	7.311≤ Et <7.690	0.34	9.75	10.05	0.3
21	RNGp	$D_1 \cdot G^* \cdot D_{12s} \cdot (D_4^* + D_{34s})$	7.690≤ Et <8.088	0.35	10.05	10.35	0.3
22	RNGp	$D_1 \cdot G^* \cdot D_{12s} \cdot (D_4^* + D_{34s})$	8.088≤ Et <8.507	0.31	10.35	10.75	0.4
23	RNGp	$D_1 \cdot G^* \cdot D_{12s} \cdot (D_4^* + D_{34s})$	8.507≤ Et <8.948	0.40	10.75	11.05	0.3
24	RNGp	$D_1 \cdot G^* \cdot D_{12s} \cdot (D_4^* + D_{34s})$	8.948≤ Et <9.412	0.34	11.05	11.45	0.4
25	RNGp	$D_1 \cdot G^* \cdot D_{12s} \cdot (D_4^* + D_{34s})$	9.412≤ Et <9.899	0.32	11.45	11.95	0.5
26	RNGp	$D_1 \cdot G^* \cdot D_{12s} \cdot (D_4^* + D_{34s})$	9.899≤ Et <10.412	0.34	11.85	12.35	0.5
27	RNGp	$D_1 \cdot G^* \cdot D_{12s} \cdot (D_4^* + D_{34s})$	10.412≤ Et <10.952	0.36	12.35	12.85	0.5
28	RNGp	$D_1 \cdot G^* \cdot D_{12s} \cdot (D_4^* + D_{34s})$	10.952≤ Et <11.519	0.39	12.85	13.35	0.5
29	RNGp	$D_1 \cdot G^* \cdot D_{12s} \cdot (D_4^* + D_{34s})$	11.519≤ Et <12.116	0.38	13.35	13.85	0.5
30	RNGp	$D_1 \cdot G^* \cdot D_{12s} \cdot (D_4^* + D_{34s})$	12.116≤ Et <12.744	0.37	13.85	14.45	0.6
31	RNGp	$D_1 \cdot G^* \cdot D_{12s} \cdot (D_4^* + D_{34s})$	12.744≤ Et <13.404	0.39	14.45	15.05	0.6
32	RNGp	$D_1 \cdot G^* \cdot D_{12s} \cdot (D_4^* + D_{34s})$	13.404≤ Et <14.099	0.40	15.05	15.65	0.6
33	RNGp	$D_1 \cdot G^* \cdot D_{12s} \cdot (D_4^* + D_{34s})$	14.099≤ Et <14.829	0.40	15.65	16.35	0.7
34	RNGp	$D_1 \cdot G^* \cdot D_{12s} \cdot (D_4^* + D_{34s})$	14.829≤ Et <15.598	0.39	16.35	17.05	0.7
35	RNGp	$D_1 \cdot G^* \cdot D_{12s} \cdot (D_4^* + D_{34s})$	15.598≤ Et <16.406	0.38	17.05	17.75	0.7
36	RNGp	$D_1 \cdot G^* \cdot D_{12s} \cdot (D_4^* + D_{34s})$	16.406≤ Et <17.256	0.36	17.75	18.55	0.8
37	RNGp	$D_1 \cdot G^* \cdot D_{12s} \cdot (D_4^* + D_{34s})$	17.256≤ Et <18.150	0.33	18.55	19.45	0.9
38	RNGp	$D_1 \cdot G^* \cdot D_{12s} \cdot (D_4^* + D_{34s})$	18.150≤ Et <19.090	0.35	19.45	20.35	0.9
39	RNGp	$D_1 \cdot G^* \cdot D_{12s} \cdot (D_4^* + D_{34s})$	19.090≤ Et <20.079	0.36	20.35	21.25	0.9
40	RNGp	$D_1 \cdot G^* \cdot D_{12s} \cdot (D_4^* + D_{34s})$	20.079≤ Et <21.120	0.35	21.25	22.25	1.0
41	RNGp	$D_1 \cdot G^* \cdot D_{12s} \cdot (D_4^* + D_{34s})$	21.120≤ Et <22.214	0.34	22.25	23.35	1.1
42	RNGp	$D_1 \cdot G^* \cdot D_{12s} \cdot (D_4^* + D_{34s})$	22.214≤ Et <23.365	0.35	23.35	24.45	1.1
43	RNGp	$D_1 \cdot G^* \cdot D_{12s} \cdot (D_4^* + D_{34s})$	23.365≤ Et <24.575	0.34	24.45	25.55	1.1
44	RNGp	$D_1 \cdot G^* \cdot D_{12s} \cdot (D_4^* + D_{34s})$	24.575≤ Et <25.849	0.30	25.55	26.85	1.3
45	RNGp	$D_1 \cdot G^* \cdot D_{12s} \cdot (D_4^* + D_{34s})$	25.849≤ Et <27.188	0.31	26.85	28.15	1.3
46	RNGp	$D_1 \cdot G^* \cdot D_{12s} \cdot (D_4^* + D_{34s})$	27.188≤ Et <28.597	0.33	28.15	29.45	1.3
47	RNGp	$D_1 \cdot G^* \cdot D_{12s} \cdot (D_4^* + D_{34s})$	28.597≤ Et <30.078	0.28	29.45	30.75	1.3
48	RNGp	$D_1 \cdot G^* \cdot D_{12s} \cdot (D_4^* + D_{34s})$	30.078≤ Et <31.637	0.23	30.95	32.45	1.5
49	RNGp	$D_1 \cdot G^* \cdot D_{12s} \cdot (D_4^* + D_{34s})$	31.637≤ Et <33.276	0.28	32.45	34.05	1.6
50	RNGp	$D_1 \cdot G^* \cdot D_{12s} \cdot (D_4^* + D_{34s})$	33.276≤ Et	0.17	34.05	34.55	0.5

Table 6.2: Logic and binning requirements for range protons, RNGp, and the nominal geometric factor, nominal incident energy and channel energy width that are obtained using the full width at half maximum (FWHM) of the energy response functions.

particular channel. In Figure 6.6, energy response functions for RNGe particles are characterized by a long tail that is caused by electron scattering and range straggling (i.e., fluctuations in path

Bin	Particle type	Logic equation	$E_{deposit}$ bin	G_{nom} (cm^2sr)	E_{beg} (MeV)	E_{end} (MeV)	delE (MeV)
61	RNGe	$D_1 \cdot G^* \cdot D_{12s}^* \cdot D_4^*$	$0.100 \leq Et < 0.109$	0.012	0.24	0.30	0.06
62	RNGe	$D_1 \cdot G^* \cdot D_{12s}^* \cdot D_4^*$	$0.109 \leq Et < 0.118$	0.011	0.24	0.35	0.11
63	RNGe	$D_1 \cdot G^* \cdot D_{12s}^* \cdot D_4^*$	$0.118 \leq Et < 0.128$	0.015	0.25	0.32	0.07
64	RNGe	$D_1 \cdot G^* \cdot D_{12s}^* \cdot D_4^*$	$0.128 \leq Et < 0.139$	0.019	0.25	0.31	0.06
65	RNGe	$D_1 \cdot G^* \cdot D_{12s}^* \cdot D_4^*$	$0.139 \leq Et < 0.151$	0.023	0.26	0.32	0.06
66	RNGe	$D_1 \cdot G^* \cdot D_{12s}^* \cdot D_4^*$	$0.151 \leq Et < 0.163$	0.025	0.27	0.33	0.06
67	RNGe	$D_1 \cdot G^* \cdot D_{12s}^* \cdot D_4^*$	$0.163 \leq Et < 0.177$	0.032	0.28	0.33	0.05
68	RNGe	$D_1 \cdot G^* \cdot D_{12s}^* \cdot D_4^*$	$0.177 \leq Et < 0.193$	0.039	0.29	0.34	0.05
69	RNGe	$D_1 \cdot G^* \cdot D_{12s}^* \cdot D_4^*$	$0.193 \leq Et < 0.209$	0.045	0.30	0.35	0.05
70	RNGe	$D_1 \cdot G^* \cdot D_{12s}^* \cdot D_4^*$	$0.209 \leq Et < 0.227$	0.060	0.32	0.36	0.04
71	RNGe	$D_1 \cdot G^* \cdot D_{12s}^* \cdot D_4^*$	$0.227 \leq Et < 0.246$	0.069	0.33	0.37	0.04
72	RNGe	$D_1 \cdot G^* \cdot D_{12s}^* \cdot D_4^*$	$0.246 \leq Et < 0.267$	0.079	0.35	0.39	0.04
73	RNGe	$D_1 \cdot G^* \cdot D_{12s}^* \cdot D_4^*$	$0.267 \leq Et < 0.290$	0.093	0.37	0.41	0.04
74	RNGe	$D_1 \cdot G^* \cdot D_{12s}^* \cdot D_4^*$	$0.290 \leq Et < 0.315$	0.103	0.39	0.43	0.04
75	RNGe	$D_1 \cdot G^* \cdot D_{12s}^* \cdot D_4^*$	$0.315 \leq Et < 0.342$	0.120	0.41	0.45	0.04
76	RNGe	$D_1 \cdot G^* \cdot D_{12s}^* \cdot D_4^*$	$0.342 \leq Et < 0.371$	0.130	0.43	0.47	0.04
77	RNGe	$D_1 \cdot G^* \cdot D_{12s}^* \cdot D_4^*$	$0.371 \leq Et < 0.402$	0.151	0.46	0.50	0.04
78	RNGe	$D_1 \cdot G^* \cdot D_{12s}^* \cdot D_4^*$	$0.402 \leq Et < 0.437$	0.169	0.49	0.53	0.04
79	RNGe	$D_1 \cdot G^* \cdot D_{12s}^* \cdot D_4^*$	$0.437 \leq Et < 0.474$	0.169	0.52	0.57	0.05
80	RNGe	$D_1 \cdot G^* \cdot D_{12s}^* \cdot D_4^*$	$0.474 \leq Et < 0.514$	0.185	0.56	0.61	0.05
81	RNGe	$D_1 \cdot G^* \cdot D_{12s}^* \cdot D_4^*$	$0.514 \leq Et < 0.558$	0.206	0.60	0.65	0.05
82	RNGe	$D_1 \cdot G^* \cdot D_{12s}^* \cdot D_4^*$	$0.558 \leq Et < 0.606$	0.223	0.64	0.69	0.05
83	RNGe	$D_1 \cdot G^* \cdot D_{12s}^* \cdot D_4^*$	$0.606 \leq Et < 0.658$	0.241	0.69	0.74	0.05
84	RNGe	$D_1 \cdot G^* \cdot D_{12s}^* \cdot D_4^*$	$0.658 \leq Et < 0.714$	0.242	0.74	0.80	0.06
85	RNGe	$D_1 \cdot G^* \cdot D_{12s}^* \cdot D_4^*$	$0.714 \leq Et < 0.775$	0.243	0.79	0.86	0.07
86	RNGe	$D_1 \cdot G^* \cdot D_{12s}^* \cdot D_4^*$	$0.775 \leq Et < 0.841$	0.254	0.85	0.92	0.07
87	RNGe	$D_1 \cdot G^* \cdot D_{12s}^* \cdot D_4^*$	$0.841 \leq Et < 0.912$	0.274	0.92	0.99	0.07
88	RNGe	$D_1 \cdot G^* \cdot D_{12s}^* \cdot D_4^*$	$0.912 \leq Et < 0.990$	0.269	0.99	1.07	0.08
89	RNGe	$D_1 \cdot G^* \cdot D_{12s}^* \cdot D_4^*$	$0.990 \leq Et < 1.075$	0.280	1.07	1.15	0.08
90	RNGe	$D_1 \cdot G^* \cdot D_{12s}^* \cdot D_4^*$	$1.075 \leq Et < 1.167$	0.256	1.15	1.25	0.10
91	RNGe	$D_1 \cdot G^* \cdot D_{12s}^* \cdot D_4^*$	$1.167 \leq Et < 1.266$	0.263	1.24	1.34	0.10
92	RNGe	$D_1 \cdot G^* \cdot D_{12s}^* \cdot D_4^*$	$1.266 \leq Et < 1.374$	0.257	1.34	1.45	0.11
93	RNGe	$D_1 \cdot G^* \cdot D_{12s}^* \cdot D_4^*$	$1.374 \leq Et < 1.491$	0.251	1.45	1.57	0.12
94	RNGe	$D_1 \cdot G^* \cdot D_{12s}^* \cdot D_4^*$	$1.491 \leq Et < 1.619$	0.255	1.57	1.69	0.12
95	RNGe	$D_1 \cdot G^* \cdot D_{12s}^* \cdot D_4^*$	$1.619 \leq Et < 1.757$	0.235	1.69	1.83	0.14
96	RNGe	$D_1 \cdot G^* \cdot D_{12s}^* \cdot D_4^*$	$1.757 \leq Et < 1.907$	0.230	1.83	1.98	0.15
97	RNGe	$D_1 \cdot G^* \cdot D_{12s}^* \cdot D_4^*$	$1.907 \leq Et < 2.069$	0.212	1.98	2.15	0.17
98	RNGe	$D_1 \cdot G^* \cdot D_{12s}^* \cdot D_4^*$	$2.069 \leq Et < 2.246$	0.199	2.14	2.32	0.18
99	RNGe	$D_1 \cdot G^* \cdot D_{12s}^* \cdot D_4^*$	$2.246 \leq Et < 2.438$	0.175	2.32	2.52	0.20
100	RNGe	$D_1 \cdot G^* \cdot D_{12s}^* \cdot D_4^*$	$2.438 \leq Et < 2.646$	0.150	2.51	2.72	0.21
101	RNGe	$D_1 \cdot G^* \cdot D_{12s}^* \cdot D_4^*$	$2.646 \leq Et < 2.871$	0.119	2.72	2.95	0.23
102	RNGe	$D_1 \cdot G^* \cdot D_{12s}^* \cdot D_4^*$	$2.871 \leq Et < 3.116$	0.085	2.94	3.20	0.26
103	RNGe	$D_1 \cdot G^* \cdot D_{12s}^* \cdot D_4^*$	$3.116 \leq Et < 3.382$	0.061	3.19	3.46	0.27
104	RNGe	$D_1 \cdot G^* \cdot D_{12s}^* \cdot D_4^*$	$3.382 \leq Et < 3.671$	0.039	3.46	3.75	0.29
105	RNGe	$D_1 \cdot G^* \cdot D_{12s}^* \cdot D_4^*$	$3.671 \leq Et < 3.984$	0.023	3.74	4.07	0.33
106	RNGe	$D_1 \cdot G^* \cdot D_{12s}^* \cdot D_4^*$	$3.984 \leq Et < 4.324$	0.012	4.06	4.46	0.40
107	RNGe	$D_1 \cdot G^* \cdot D_{12s}^* \cdot D_4^*$	$4.324 \leq Et < 4.693$	0.007	4.41	4.84	0.43
108	RNGe	$D_1 \cdot G^* \cdot D_{12s}^* \cdot D_4^*$	$4.324 \leq Et < 4.693$	0.004	4.77	5.20	0.43
109	RNGe	$D_1 \cdot G^* \cdot D_{12s}^* \cdot D_4^*$	$5.094 \leq Et < 5.528$	0.002	5.21	5.61	0.40
110	RNGe	$D_1 \cdot G^* \cdot D_{12s}^* \cdot D_4^*$	$Et \geq 5.528$	0.001	5.62	6.08	0.46

Table 6.3: Logic and binning requirements for range electrons, RNGe, and the nominal geometric factor, nominal incident energy and channel energy width that are obtained using the full width at half maximum (FWHM) of the energy response functions.

length for individual electrons. See Chapter 2 for more information). Nonetheless, the peak of each curve is well resolved from one channel to another. It also demonstrates that our instrument can

Bin	Particle Type	Logic equation	$E_{deposit}$ bin
51	PENp	$D_1 \cdot G^* \cdot D_{12s} \cdot D_4 \cdot D_{34s}^*$	$35.0 \geq Et > 32.2$
52	PENp	$D_1 \cdot G^* \cdot D_{12s} \cdot D_4 \cdot D_{34s}^*$	$32.2 \geq Et > 29.4$
53	PENp	$D_1 \cdot G^* \cdot D_{12s} \cdot D_4 \cdot D_{34s}^*$	$29.4 \geq Et > 26.6$
54	PENp	$D_1 \cdot G^* \cdot D_{12s} \cdot D_4 \cdot D_{34s}^*$	$26.6 \geq Et > 23.8$
55	PENp	$D_1 \cdot G^* \cdot D_{12s} \cdot D_4 \cdot D_{34s}^*$	$23.8 \geq Et > 21.0$
56	PENp	$D_1 \cdot G^* \cdot D_{12s} \cdot D_4 \cdot D_{34s}^*$	$21.0 \geq Et > 18.2$
57	PENp	$D_1 \cdot G^* \cdot D_{12s} \cdot D_4 \cdot D_{34s}^*$	$18.2 \geq Et > 15.4$
58	PENp	$D_1 \cdot G^* \cdot D_{12s} \cdot D_4 \cdot D_{34s}^*$	$15.4 \geq Et > 12.6$
59	PENp	$D_1 \cdot G^* \cdot D_{12s} \cdot D_4 \cdot D_{34s}^*$	$12.6 \geq Et > 9.8$
60	PENp	$D_1 \cdot G^* \cdot D_{12s} \cdot D_4 \cdot D_{34s}^*$	$Et \leq 9.8$

Bin	Particle Type	Logic equations	$E_{deposit}$ bin
111	PENe	$D_1 \cdot G^* \cdot D_{12s}^* \cdot D_4$	$6.0 \geq Et > 5.6$
112	PENe	$D_1 \cdot G^* \cdot D_{12s}^* \cdot D_4$	$5.6 \geq Et > 5.2$
113	PENe	$D_1 \cdot G^* \cdot D_{12s}^* \cdot D_4$	$5.2 \geq Et > 4.8$
114	PENe	$D_1 \cdot G^* \cdot D_{12s}^* \cdot D_4$	$4.8 \geq Et > 4.4$
115	PENe	$D_1 \cdot G^* \cdot D_{12s}^* \cdot D_4$	$4.4 \geq Et > 4.0$
116	PENe	$D_1 \cdot G^* \cdot D_{12s}^* \cdot D_4$	$4.0 \geq Et > 3.6$
117	PENe	$D_1 \cdot G^* \cdot D_{12s}^* \cdot D_4$	$3.6 \geq Et > 3.2$
118	PENe	$D_1 \cdot G^* \cdot D_{12s}^* \cdot D_4$	$3.2 \geq Et > 2.8$
119	PENe	$D_1 \cdot G^* \cdot D_{12s}^* \cdot D_4$	$2.8 \geq Et > 2.4$
120	PENe	$D_1 \cdot G^* \cdot D_{12s}^* \cdot D_4$	$Et \leq 2.4$

Table 6.4: Logic and binning requirements for penetrating protons (PENp) and penetrating electrons (PENe)

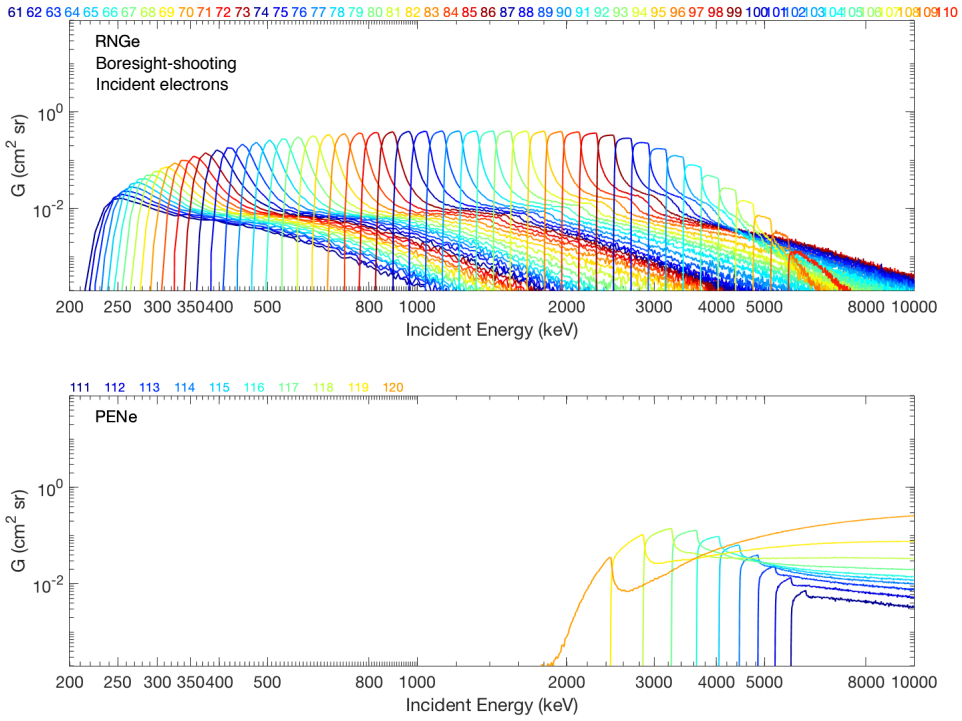

Figure 6.6: Geometric factor as a function for incident electrons that originate from the boresight. Different colors represent response function for different electron types: (top) RNGe channels, Channels 61-110, and (bottom) PENe, Channels 111-120.

measure electron from ∼300 keV to ∼3 MeV most efficiently (i.e., with a geometric factor greater than 0.1 cm^2sr). In Figure 6.7, the energy response function for incident protons for each channel is well defined without the long tail that intercepts with other channels like those in the top panel of Figure 6.6. The contrast between Figures 6.6 and 6.7 highlight the differences in how protons and electrons interact with the matter; the heavy proton is less likely to scatter and deviate from its trajectory, and hence the channels are well defined.

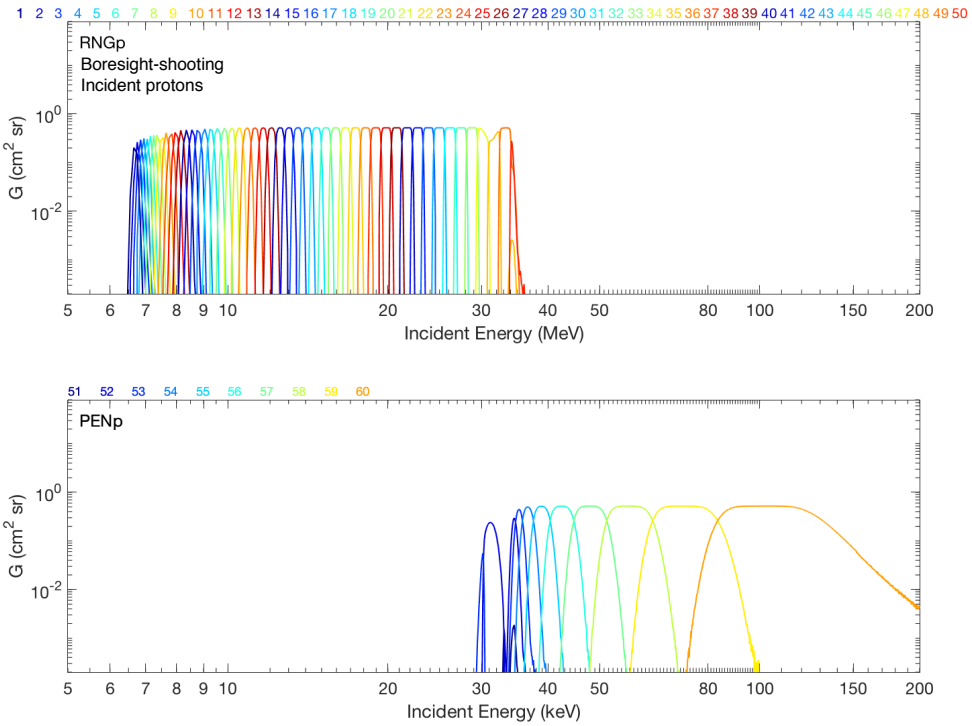

Figure 6.7: Geometric factor as a function of incident protons and electrons. Different colors represent response function for channels: (top) RNGp channels, Channels 1-50; (bottom) RNGe, Channels 61-110. The highlighted channels are Channels 10 (red), 30 (blue), 40 (green), and 50 (magenta) for RNGp; Channels 70 (red), 80 (cyan), 90 (blue), 100 (green), 105 (magenta) and 110 (yellow) for RNGe.

6.4.5.2 Full energy response function

For an isotropic flux, the energy response function is obtained by:

$$G_i(E) = \frac{n_i(E)}{N(E)} 4\pi^2 r^2$$

where n is the number of valid events for each channel, N is the total simulated events, E is the incident energy, i refers to channel i, and r is the radius of the source sphere in Geant4. This is equivalent to multiplying the geometry factor of the sphere, $4\pi^2 r^2$, by the fraction of incident particles that trigger channel i, $\frac{n_i}{N}$. Spherical simulation results based on a uniform incident flux spectrum are used in the computation. The resultant response function is independent of the choice of the source sphere size (so long as it encloses the entire detector) because an increase in the radius of the source sphere will decrease the number of valid events for each channel and, in turn, yield the same geometric factor. The full response functions for the RNGp and RNGe channels can be found in Figure 6.8, and the response functions for PENp and PENe channels are shown in Figure 6.9. The incident energy bins in these figures are 100 keV and 10 keV for protons and electrons, respectively.

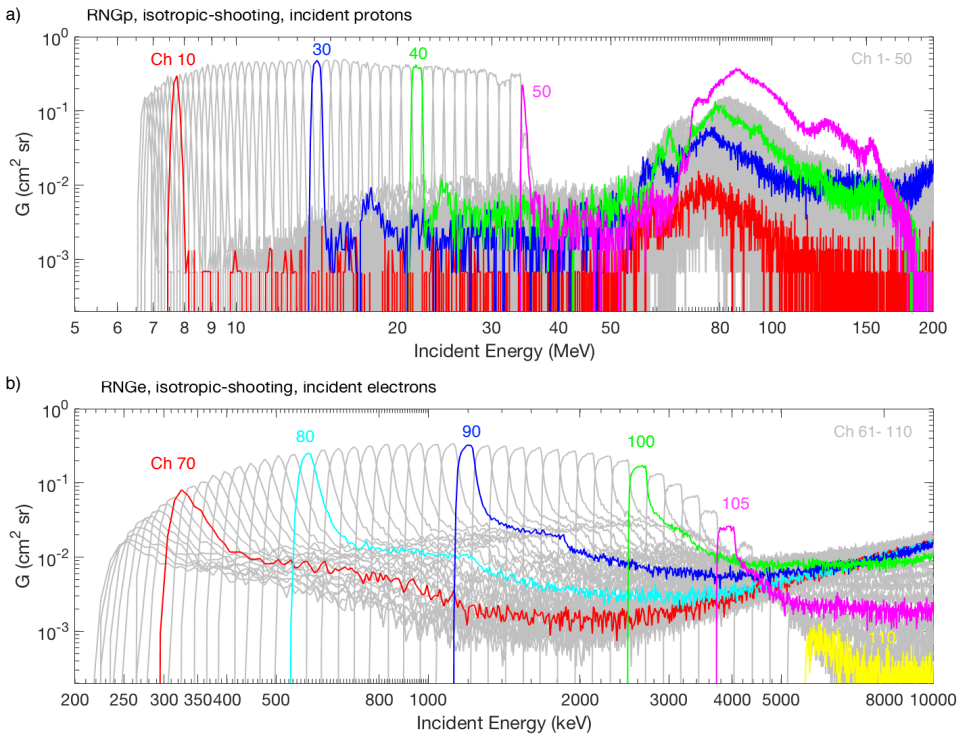

Figure 6.8: Geometric factor as a function of incident protons and electrons. Different colors represent response function for channels: (top) RNGp channels, Channels 1-50; (bottom) RNGe, Channels 61-110. The highlighted channels are Channels 10 (red), 30 (blue), 40 (green), and 50 (magenta) for RNGp; Channels 70 (red), 80 (cyan), 90 (blue), 100 (green), 105 (magenta) and 110 (yellow) for RNGe.

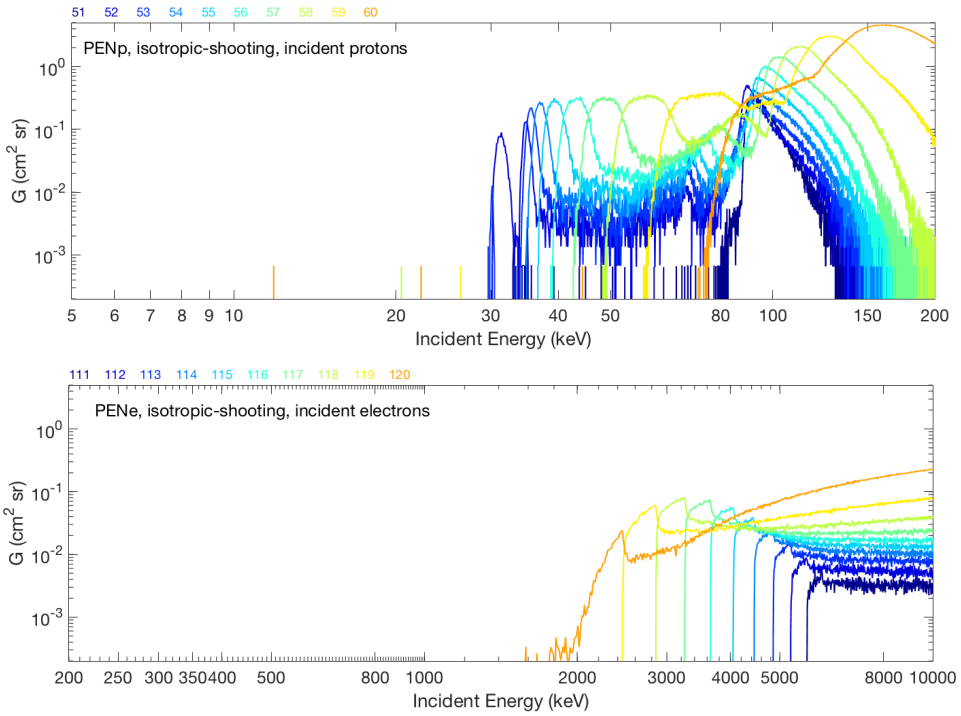

Figure 6.9: Geometric factor as a function of incident protons and electrons. Different colors represent response function for channels: (top) PENp channels, Channels 51-60; (bottom) PENe, Channels 111-120.

It is notable in Figure 6.8 that each channel is generally well-resolved, suggesting that the logic and binning equations are sufficient at categorizing the particles and the simulation statistic is adequate. These figures record the contributions of particles from and outside the FOV. For example, the hump around 60-100 MeV protons (top panel of Figure 6.8) indicates that these protons are energetic enough to penetrate through the Al-W layered shielding at a specific angle that does not trigger guard rings and deposit a small amount of energy on the detectors, appearing as lower energy protons (see Appendix B.2 for more information). This population will be monitored using PENp channels and will be corrected whenever necessary. This can be done by subtracting the observed counts in the RNGp channels by the background counts that are measured by the PENp channels.

A nominal energy resolution is determined by the full width at half maximum of the response function for each channel. Quantitively, the nominal energy resolution ($\Delta E/E$) are between 7% and 38% for RNGe channels and 1.5% and 5% for RNGp channels, which is a vast improvement

from its predecessor, REPTile (with resolution between 80% and 95% for electron channels and 29% and 67% for proton channels). A nominal geometric factor is an average of corresponding geometric factors within the nominal energy width for each channel. The nominal energy for RNGp and RNGe channels corresponds to E<35 MeV for proton and E<∼5 MeV for electrons, and their nominal geometric factor ranges from 0.001 to 0.28 cm^2sr for RNGe channels and 0.10 to 0.40 cm^2sr for RNGp channels. The nominal geometric factor and energy resolution for each channel in RNGp and RNGe are summarized in Tables 6.2 and 6.3. In addition, we examine the effect of detector gap variation on the response functions and found that the changes in the detector gap have little to no impacts on lower energy electrons (< ∼1MeV electrons) and protons (< ∼30MeV), but have a higher influence on higher energy electrons, especially >3MeV electrons. For instance, an increase from 1 mm to 2.5 mm detector gap will result in a decrease of the geometric factors (from 0.22 to 0.14 cm^2sr) for 3 MeV electrons because an increase in detector gap allows the electrons to be more easily scattered out of the detector stack.

To characterize the role of very energetic protons as background contamination to electron measurements, we have computed the response function of incident protons that get binned into electron channels (Figure 6.10a). Low energy (∼ 6 - 7 MeV) protons that barely make it through the Be window have a comparable geometric factor (as high as 0.2 cm^2sr), and this could be a significant background concern for electron measurements (0.6 - 3 MeV, namely Channel 80-100). These energetic protons generally exist in the inner belt except during solar proton events when they have access to higher L (>3.5) [e.g., Filwett et al., 2020]. Since energetic electron fluxes are much greater at higher L, the effect of proton contamination on electron measurements at higher L is generally less severe (see Appendix B.1 for more discussion). In other words, the potential contamination from these low-energy protons will likely occur when the spacecraft goes through the inner belt and will be tracked accordingly. Due to the low-energy deposit requirements for RNGe channels, the contribution of high-energy protons (> 7 MeV) to RNGe channels is relatively small, compared to < 7 MeV protons that can barely penetrate the Be window and deposit a very small amount of energy (mimicking the energy deposit by electrons) in the first detector.

Also shown in Figure 6.10b are the electrons that can be taken as RNGp particles. Specifically, higher energy (E>∼3 MeV) electrons can appear as RNGp particles. We note that their geometric factor is lower than the nominal geometric factor for the corresponding RNGp protons. Besides, energetic protons generally reside at lower L-shell (L<2.5) while higher energy electrons (>3 MeV) are located at higher L-shell (L>3). Therefore, the contribution of high-energy electron on RNGp channel is likely to be small.

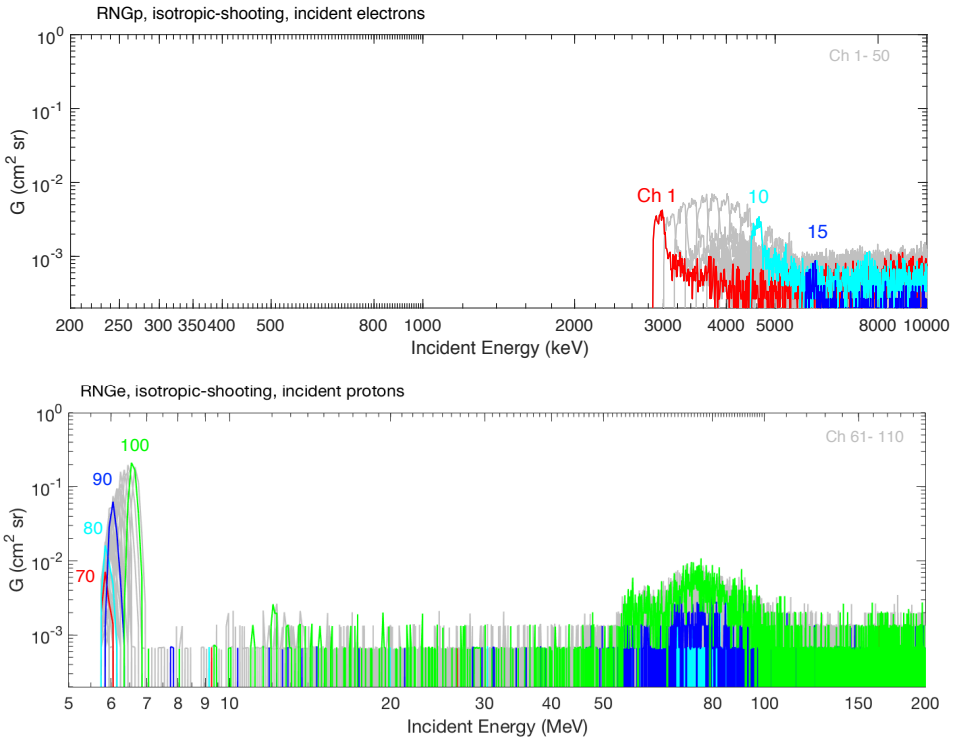

Figure 6.10: Energy response functions for incident protons and electrons. Different colors represent response functions for channels: (top) RNGp channels, Channels 1-50; (bottom) RNGe, Channels 61-110. The highlighted channels are Channels 10 (red), 30 (blue), 40 (green), and 50 (magenta) for RNGp; Channels 70 (red), 80 (cyan), 90 (blue), 100 (green), 105 (magenta) and 110 (yellow) for RNGe. A flat incident flux spectrum is used here for both protons and electrons. The simulated electron and proton energy ranges are 0.1 - 10 MeV and 1 - 200 MeV, respectively.

6.4.6 Pileup

We also examine the pileup effect on REPTile-2. The minimum time resolution between two events, τ, is 400 ns, i.e., a pileup-free count is recorded if no additional events occur within

400 ns. Before determining the pileup rate, the count rate is computed using the energy response function on the respective detector and the AE9/AP9 flux spectrum. The count rate, $r(E)$, is approximated as $r(E) = G(E)j(E)\Delta E$, where E is the incident energy, ΔE is the incident energy bin width, $G(E)$ is the energy response function, and $j(E)$ is the estimated flux from the trapped energetic electron and proton model (AE9 and AP9 model) [Ginet et al., 2013]. The mean electron and proton flux spectra as a function of geographical longitude and latitude are obtained from AE9 and AP9 models, assuming that the satellite orbits at an inclination of 97-degree and an altitude of 600 km (the highest, allowable altitude limit for a CubeSat with no active de-orbit mechanism like CIRBE, in accordance with the FCC guidelines (https://docs.fcc.gov/public/attachments/DOC-358437A1.pdf). To model the ′worst-case′ scenario, we selected energy spectra inside the South Atlantic Anomaly (SAA) region where fluxes in most energy channels are high for the pileup analysis (Figure 6.11).

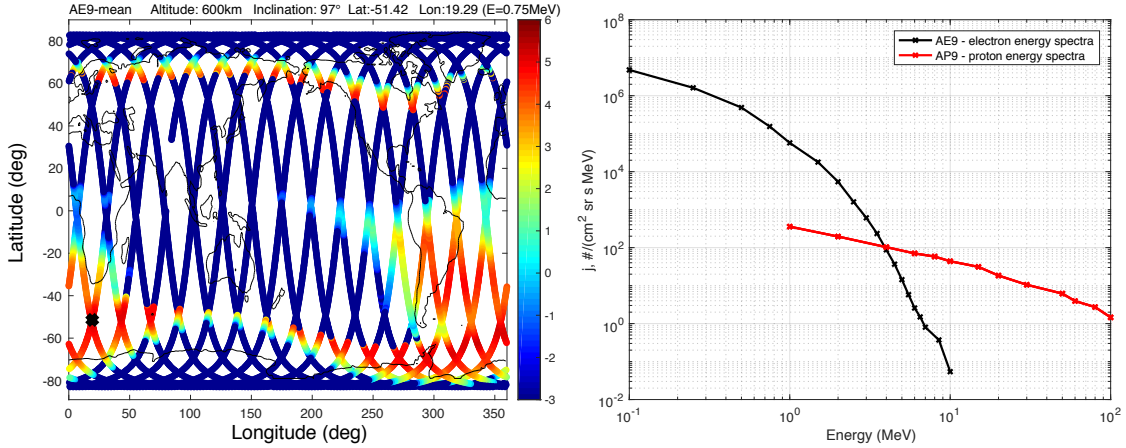

Figure 6.11: (left) Flux of 0.75 MeV electrons with a black cross that indicates the location where the electron electron spectrum is used to model the 'worst-case' scenario. (right) Energy spectrum from AE9 (black) and AP9 (red) that are used to estimate the pileup effect in the 'worst-case' scenario.

Since Geant4 simulates an ideal detector that can resolve every pulse (or event), the computed count rate from Geant-4 simulations is a pileup-free count rate, as indicated by red lines in Figure 6.12. The two-event pileup rate is computed based on the assumption that the

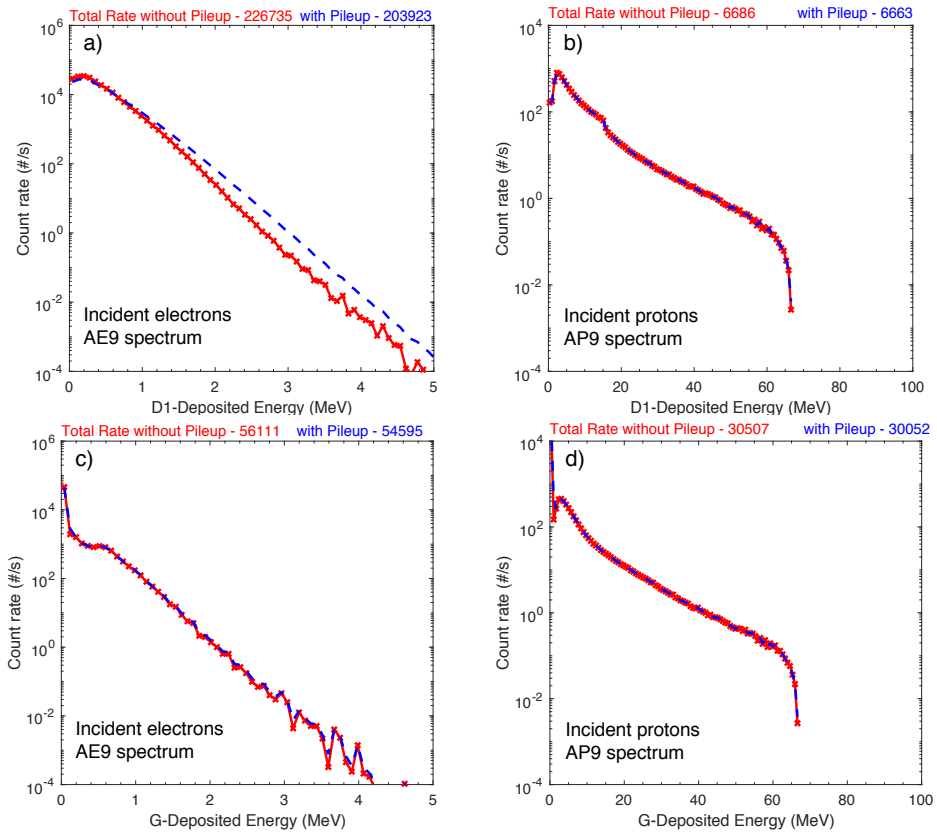

Figure 6.12: Count rate with and without two-event pileup on detector 1 (top) and guard detector (bottom) for incident electrons (left) and protons (right).

superposition only involves two pulses that occur within the instrument resolution time [Knoll, 2010; Selesnick and Stone, 1991]. It is approximated using Poisson probability distributions by adding the pileup-free count rate to events that would be in the lower energy channel but were piled up to, say, channel k and subtracting events that would be in channel k but were piled up to a higher energy channel. The results are shown as blue lines in Figure 6.12. The pileup analysis is conducted for the first detector, as it is subjected to the highest flux among all detectors and the guard detector. Figure 6.12a demonstrates that with a 0.3 mm thick Be window, the pileup count rates on detector 1 for lower-energy particles do not deviate much from the pileup-free count rate. It is noted that when the pileup occurs, multiple lower energy pulses can appear as a single high-energy pulse. Consequently, the system (incorrectly) records smaller counts for lower energy

particles and higher counts for higher energy particles. Figure 6.12 suggests that the pileup effect on Detector 1 is negligible for protons but could be a significant problem for electrons in this worst-case scenario analysis. This will likely happen when the spacecraft goes through the SAA region during which the pileup effect will be monitored, for example, one can look for any signs of flux saturation that implies a significant pileup effect, and corrected by estimating the true count rates using the theoretical pileup equation when needed. In most observations near or outside the SAA region, the pileup effect will be relatively small and negligible (e.g., see Figure 6.13 for the energy spectrum used in a nominal scenario and Figure 6.14 for the corresponding pileup analysis result). The pileup effect on the guard detectors is negligible for electrons and protons because only very energetic protons and electrons can reach the guard rings and their fluxes are generally low in space.

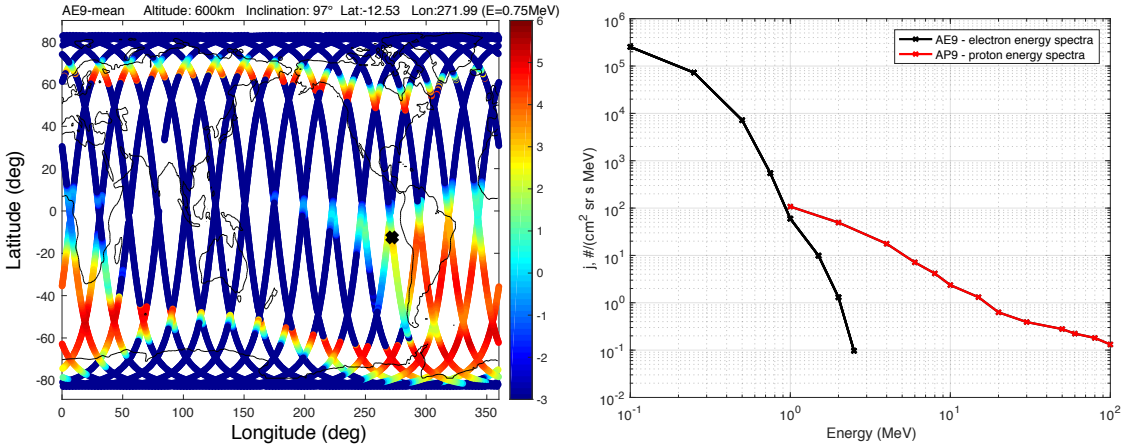

Figure 6.13: (left) Flux of 0.75 MeV electrons with a black cross that indicates the location where both the electron and proton spectrum is used to model the 'nominal' scenario. (right) Energy spectrum from AE9 (black) and AP9 (red) that are used to estimate the pileup effect in a nominal scenario.

6.5 Final remarks

This paper summarizes the comprehensive analysis involved in the design of the miniaturized solid-state charged particle instrument, REPTile-2. We would also like to emphasize the

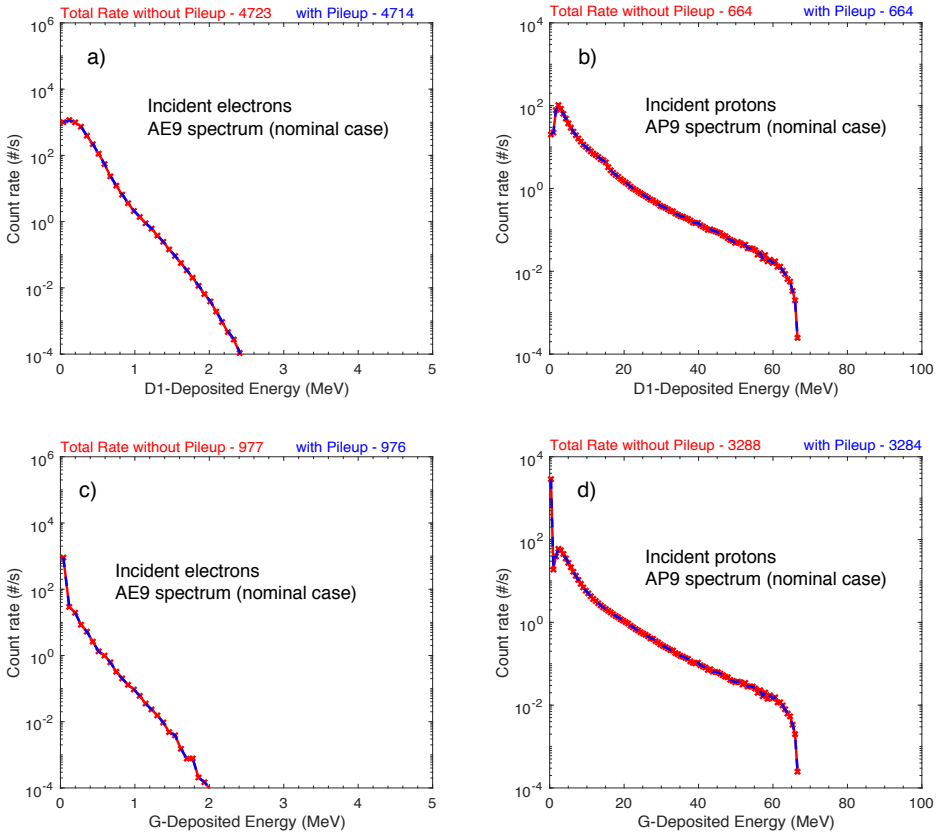

Figure 6.14: Same as Figure 6.12 but under a nominal flux condition where observations were made near the edge of the SAA region.

critical role of Geant4 simulations in informing and improving the REPTile-2 design. Most of the analysis is aided by Geant4 simulations, including the derivation of the logic and binning equations, instrument characterization, and the study of the pileup effect on REPTile-2. With the incorporation of pulse-height analysis and anticoincidence detectors, REPTile-2 has vastly improved performance relative to its predecessor instrument (REPTile), particularly in background reduction and energy resolution. Table 6.5 summarizes the differences between REPTile and REPTile-2 (as well as the requirement for REPTile-2 measurements). It demonstrates that the current REPTile-2 design meets the scientific requirements that are necessary to achieve the scientific objective of the CIRBE mission, namely to study the detailed variation of energetic particles in the inner belt.

	REPTile	REPTile-2
Electron channels	3 (2 differential channels; 1 integral channel)	60 (49 differential channels and 1 integral channel for RNGe; 9 differential channels and 1 integral channel for PENe)
Proton channels	3 (2 differential channels; 1 integral channel)	60 (49 differential channels and 1 integral channel for RNGp; 9 differential channels and 1 integral channel for PENp)
Nominal energy range for electrons	0.58 – >3.8 MeV electrons ($\Delta E/E$ < ~95 %)	~0.3 – ~4 MeV electrons ($\Delta E/E$ < ~16 %) Requirement: 0.3-3 MeV ($\Delta E/E$ < 20 %)
Nominal energy range for protons	9 – 40 MeV protons ($\Delta E/E$ < ~67 %)	~6.7 – ~35 MeV protons ($\Delta E/E$ < ~5 %) Requirement: 6.7 – 30 MeV ($\Delta E/E$ < 25 %)
Field of view	~ 51°	50°
Integration period	6 seconds	1 second (S-band) or 10 second (UHF)
Silicon detectors	Detector 1: 20 mm in diameter Detector 2 - 4: 40 mm in diameter Note: No outer rings/guard rings	Detector 1 - 4 are divided into: a) inner active area with a diameter of 20 mm b) outer active area (guard rings) with an inner and outer diameter of 20 mm and 40 mm, respectively.
Others	• Thickness of Be-window: 0.5 mm • Solid Tungsten shield • Gap between two detectors: 1 mm	• Thickness of Be-window: 0.3 mm • Tungsten shield: Tungsten-Epoxy composite cylinder (64% Tungsten and 36% Epoxy) + Tungsten sheets • Gap between two detectors: 2.5 mm • Aluminum shield was updated and reduced in thickness to meet the mass requirement

Table 6.5: Summary of the differences between REPTile and REPTile-2.

Chapter 7

Flux determination using Bowtie analysis and generalized least-square method

This chapter is based on parts of the work that is submitted to Journal of Geophysical Research: Space Physics, titled 'On the Challenges of Measuring Energetic Particles in the Inner Belt: A Geant4-based Simulation of an Energetic Particle Detector Instrument, REPTile-2', Journal of Geophysical Research: Space Physics.

7.1 Introduction

An inverse problem is a process of determining model parameters from data. A conversion of count rates to fluxes is an example of an inverse problem and is often an ill-posed inverse problem, which means that the inversion process is not alway stable and its solution is not always unique. Many techniques have been developed to efficiently convert count rates to fluxes [Van Allen et al., 1974; Sandberg et al., 2011; Cyamukungu et al., 2014; Park et al., 2021]. Among all, a bowtie method is one of the most widely used flux extraction methods for radiation belt particle measurements [Van Allen et al., 1974; Selesnick and Blake, 2000; Boudouridis et al., 2020; Lam et al., 2010; Baker et al., 2021; Claudepierre et al., 2021]. It simplifies the integral function that links count rates to fluxes to a linear conversion between a constant factor (that is independent of flux spectra) and fluxes. On the other hand, methods such as the 'multi-channel inverse methods' could provide a more accurate flux estimate [Park et al., 2021], but it also has some shortcomings such as it can sometimes produce nonphysical, negative flux.

In this chapter, we describe two major flux extraction techniques: a bowtie method and

a generalized least square method. The generalized least square method provides an elegant and robust way to estimate flux and its covariance. This approach is commonly used in geophysics to tackle inverse problems like seismology tomography [e.g., Tarantola, 1984; Charara et al., 2000]. The generalized least square method can be applied to both linear and non-linear problems. The nonlinear generalized least square solution is later proved to be useful to ensure that the solution provides only positive flux estimates. This chapter describes the derivation of each method (the bowtie analysis, the generalized least square method for linear and nonlinear problems) in detail and applies these methods under different flux spectra from both real and simulated data to examine their limitations.

In the previous chapter, we introduced the REPTile-2 instrument and characterized the instrument using the Geant4 simulations. To verify the Geant4 simulation results and the instrument performance, we conducted a Strontium-90 (Sr-90) radioactive source test and compare the estimated flux spectrum (using the bowtie analysis and the generalized least square method) with the expected Sr-90 spectrum. In addition to the Sr-90 test, we also examined the performance of each method under two extreme flux spectra to learn about the limitations of these two flux extraction techniques.

This chapter begins with a description of the bowtie method, followed by a discussion on the generalized least square method for linear and nonlinear problems. Sections 7.4 and 7.5 demonstrate the application of these flux extraction techniques on the Sr-90 test results and two extreme flux spectra. Section 7.6 summarizes our findings in this chapter.

7.2 Bowtie method

The bowtie method was first introduced by Van Allen et al. [1974] and is commonly used in space missions to determine fluxes from count rates. The relationship between count rate and flux is described as below:

$$r_i = \int G_i(E) j(E) dE \tag{7.1}$$

where r_i is the count rate in channel i, $G_i(E)$ is the channel energy response function, and $j(E)$ is the flux spectrum as a function of energy, E. The bowtie method we employed is similar to the one described in Selesnick and Blake [2000] and Claudepierre et al. [2021]. It simplifies the energy dependent response function to a constant value ($G_{eff}\Delta E_{eff}$). Eq. 7.1 is approximated as:

$$r_i = \int G_i(E)j(E)dE = G_{eff}\Delta E_{eff} j(\bar{E}_i) \tag{7.2}$$

where $\bar{E}_i$ is the 'nominal' energy. By assuming an exponential spectra, $j = j_0 e^{-E/E_0}$, we can rewrite the equation as:

$$r_i = \int G_i(E)j_0 e^{-E/E_0}dE = G_{eff}\Delta E_{eff} j_0 e^{-\bar{E}_i/E_0} \tag{7.3}$$

$$G_{eff}\Delta E_{eff} = e^{\bar{E}_i/E_0} \int G_i(E)e^{-E/E_0}dE \tag{7.4}$$

For a specific E_0, the equation above gives $G_{eff}\Delta E_{eff}$ as a function of $\bar{E}_i$. The goal is to determine a constant $G_{eff}\Delta E_{eff}$ that does not vary with flux spectra (i.e., independent of the $\bar{E}_i$ choice. Plotting lines from various E_0 yields a bowtie-like plot, as shown in Figure 7.1. The intersection point gives an approximate nominal energy $\bar{E}_i$ and $G_{eff}\Delta E_{eff}$ that is independent of flux spectra. The E_0 values in this study are 0.05, 0.1, 0.2, 0.5, 0.7, 1, 2, and 10 MeV. Once $G_{eff}\Delta E_{eff}$ for each channel is determined, the flux in each channel can be easily obtained by:

$$j_i(E) = \frac{r_i}{G_{i,eff}\Delta E_{i,eff}} \tag{7.5}$$

The bowtie method is often favored over other methods due to its simplification and the straightforward flux determination procedure once $G_{eff}\Delta E_{eff}$ for each channel is known. However, it is important to know that the solution from the bowtie analysis is not always unique (see Figure 7.1), and its resolution is limited by channel width.

7.3 Generalized least square method

A forward problem is a problem that computes what should be observed given a model. To find count rate from flux using Eq. 7.1 is an instance of forward problems. An inverse of the

forward problem is known as an inverse problem. An example of inverse problems is to determine flux from count rate using Eq. 7.1. One can solve the inverse problem using a least square method. Rather than using the simple but rather limited methods like simple least-square solution and minimum length solutions that can only solve a purely overdetermined problem and a purely underdetermined problem, respectively (see Appendices C.2 and C.3 for more discussions), we introduce the generalized least square method that is more versatile and describe its application on linear and non-linear problems. We note that the same technique was previously applied to solar proton events by Selesnick et al. [2018].

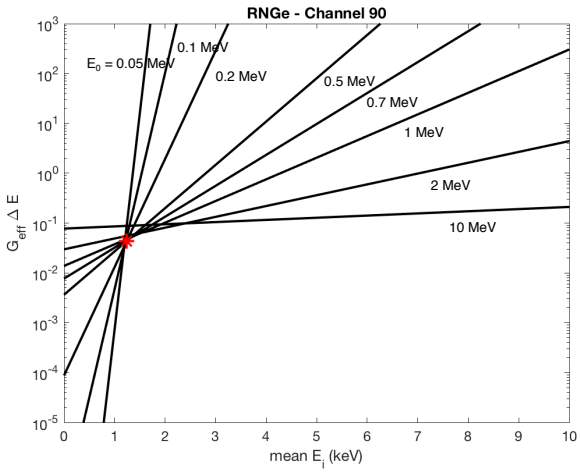

Figure 7.1: Example of bowtie analysis on RNGe channel 90. Each line represent results from different E_0. The E_0 values are 0.05, 0.1, 0.2, 0.5, 0.7, 1, 2, and 10 MeV. The red asterisk indicates the intersection point.

7.3.1 Linear problem

A generalized least square method is commonly applied in geophysics. A brief discussion on the derivation of generalized least square solution for a linear problem is provided below. Readers are referred to Tarantola [2005] for more in-depth discussions. Other helpful references include Menke [2012] and Tarantola and Valette [1982b,a].

By describing data and model parameters using probability density functions, the least square method arises when the input probability densities are assumed to be 'Gaussian'. ρ_d rep-

resents the Gaussian probability density for observable parameters (data) whose mean is $\boldsymbol{d_{obs}}$ and whose covariance matrix is $\boldsymbol{C_d}$, while ρ_m is the *a priori* information that is represented as Gaussian probability density whose mean is *a priori* estimate ($\boldsymbol{m_0}$) and whose covariance matrix is $\boldsymbol{C_m}$.

$$\rho_d(\boldsymbol{d}) = const \cdot exp(-\frac{1}{2}(\boldsymbol{d}-\boldsymbol{d_{obs}})^T C_d^{-1}(\boldsymbol{d}-\boldsymbol{d_{obs}})) \tag{7.6}$$

$$\rho_m(\boldsymbol{m}) = const \cdot exp(-\frac{1}{2}(\boldsymbol{m}-\boldsymbol{m_0})^T C_m^{-1}(\boldsymbol{m}-\boldsymbol{m_0})) \tag{7.7}$$

As elaborated in Tarantola [2005], the *a posteriori* probability density, $\sigma_m(m)$, can be described by the joint probability density between ρ_m and ρ_d divided by a normalization constant:

$$\sigma_m(\boldsymbol{m}) = \frac{\rho_m(\boldsymbol{m})\rho_d \boldsymbol{g(m)}}{\int_M \rho_m(\boldsymbol{m'})\rho_d \boldsymbol{g(m')} d\boldsymbol{m'}} \tag{7.8}$$

$$\sigma_m(\boldsymbol{m}) = const \cdot exp(-S(\boldsymbol{m})) \tag{7.9}$$

$$S(\boldsymbol{m}) = ||\boldsymbol{d}-\boldsymbol{d_{obs}}||^2 + ||\boldsymbol{m}-\boldsymbol{m_0}||^2 \tag{7.10}$$

$$= (\boldsymbol{d}-\boldsymbol{d_{obs}})^T \boldsymbol{C_d^{-1}}(\boldsymbol{d}-\boldsymbol{d_{obs}}) + (\boldsymbol{m}-\boldsymbol{m_0})^T \boldsymbol{C_m^{-1}}(\boldsymbol{m}-\boldsymbol{m_0}) \tag{7.11}$$

The goal is therefore to maximize the joint probability density or in other words, minimize S(m). Therefore, S(m) in Eq. 7.11 is known as the objective function, also referred to as the cost function or misfit function. Assume a linear problem, $\boldsymbol{d} = \boldsymbol{g(m)} = \boldsymbol{G} \cdot \boldsymbol{m}$, where $\boldsymbol{G}$ is the linear operator that relates the data and model. We can rewrite Eq. 7.11 as:

$$S(\boldsymbol{m}) = (\boldsymbol{Gm}-\boldsymbol{d_{obs}})^T \boldsymbol{C_d^{-1}}(\boldsymbol{Gm}-\boldsymbol{d_{obs}}) + (\boldsymbol{m}-\boldsymbol{m_0})^T \boldsymbol{C_m^{-1}}(\boldsymbol{m}-\boldsymbol{m_0}) \tag{7.12}$$

Minimizing Eq. 7.12 gives

$$\frac{\delta(S(\boldsymbol{m}))}{\delta \boldsymbol{m}} = 2\boldsymbol{G}^T \boldsymbol{C_d^{-1}}(\boldsymbol{Gm}-\boldsymbol{d_{obs}}) + 2\boldsymbol{C_m^{-1}}(\boldsymbol{m}-\boldsymbol{m_0}) = 0 \tag{7.13}$$

$$\boldsymbol{G}^T \boldsymbol{C_d^{-1}}(\boldsymbol{Gm}-\boldsymbol{d_{obs}}) = -\boldsymbol{C_m^{-1}}(\boldsymbol{m}-\boldsymbol{m_0}) \tag{7.14}$$

$$\boldsymbol{G}^T \boldsymbol{C_d^{-1}} \boldsymbol{Gm} + \boldsymbol{C_m^{-1}} \boldsymbol{m} = \boldsymbol{G}^T \boldsymbol{C_d^{-1}} \boldsymbol{d_{obs}} + \boldsymbol{C_m^{-1}} \boldsymbol{m_0} \tag{7.15}$$

$$(\boldsymbol{G}^T \boldsymbol{C_d^{-1}} \boldsymbol{G} + \boldsymbol{C_m^{-1}}) \boldsymbol{m} = \boldsymbol{G}^T \boldsymbol{C_d^{-1}} \boldsymbol{d_{obs}} + \boldsymbol{C_m^{-1}} \boldsymbol{m_0} \tag{7.16}$$

$$\tilde{\boldsymbol{m}} = (\boldsymbol{G}^T \boldsymbol{C_d^{-1}} \boldsymbol{G} + \boldsymbol{C_m^{-1}})^{-1} (\boldsymbol{G}^T \boldsymbol{C_d^{-1}} \boldsymbol{d_{obs}} + \boldsymbol{C_m^{-1}} \boldsymbol{m_0}) \tag{7.17}$$

Eq. 7.17 can also be written as (interested readers can find the derivation in Appendix C.4):

$$\tilde{\boldsymbol{m}} = \boldsymbol{m_0} + (\boldsymbol{G}^T\boldsymbol{C_d}^{-1}\boldsymbol{G} + \boldsymbol{C_m}^{-1})^{-1}\boldsymbol{G}^T\boldsymbol{C_d}^{-1}(\boldsymbol{d_{obs}} - \boldsymbol{G}\boldsymbol{m_0}) \tag{7.18}$$

$$= \boldsymbol{m_0} + \boldsymbol{C_m}\boldsymbol{G}^T(\boldsymbol{G}\boldsymbol{C_m}\boldsymbol{G}^T + \boldsymbol{C_d})^{-1}(\boldsymbol{d_{obs}} - \boldsymbol{G}\boldsymbol{m_0}) \tag{7.19}$$

$$\tilde{\boldsymbol{C_m}} = (\boldsymbol{G}^T\boldsymbol{C_d}^{-1}\boldsymbol{G} + \boldsymbol{C_m}^{-1})^{-1} \tag{7.20}$$

$$= \boldsymbol{C_m} - \boldsymbol{C_m}\boldsymbol{G}^T(\boldsymbol{G}\boldsymbol{C_m}\boldsymbol{G}^T + \boldsymbol{C_d})^{-1}\boldsymbol{G}\boldsymbol{C_m} \tag{7.21}$$

$\tilde{\boldsymbol{m}}$ gives us the point that realizes the minimum of the least square misfit function. It is the best solution in the sense that it is close to the 'prior estimate', m_0 and the predicted data $\boldsymbol{G}\tilde{\boldsymbol{m}}$ is close to the observed data $\boldsymbol{d_{obs}}$. $\tilde{\boldsymbol{m}}$ and $\tilde{\boldsymbol{C_m}}$ are the mean and the covariance of the posterior Gaussian distribution. Derivation of the posterior covariance is in Appendix C.5.

We can use Eq. 7.17 to estimate flux and in which case, $\boldsymbol{d_{obs}}$ is the observed count rate and $\tilde{\boldsymbol{m}}$ is the optimal flux solution. Since the covariance between channels is generally small and is hard to estimate, we can generally assume the data variance in one channel is uncorrelated to one another, i.e., the off-diagonal terms in $\boldsymbol{C_d}$ are zero. The count rate is assumed to follow a Poisson distribution. The standard deviation of counts σ_d that follows a Poisson distribution is $sqrt(n)$, where n is counts. The variance of count rates can then be estimated by propagating the statistical error from counts [see Bevington and Robinson, 2003; Knoll, 2010]:

$$\sigma_d^2 = (\frac{sqrt(r_i \times t + 1)}{t})^2 \tag{7.22}$$

where t is the measurement time and the value 1 is added to take care of instances where the count rate is zero.

On the other hand, $\boldsymbol{m_0}$ is our initial flux guess and can be set to any arbitrary value (assume we know nothing about the flux spectra) with a Gaussian covariance function, $C_m(E_i, E_j) = \sigma^2 e^{\frac{-(E_i - E_j)^2}{2\Delta^2}}$. Here σ is related to the confidence level on the initial flux guess; the larger σ is, the less confidence we have in the initial guess. The choice of σ varies from case to case. If the choice of σ is too small, the estimated $\tilde{\boldsymbol{m}}$ will barely change from the initial guess $\boldsymbol{m_0}$. Therefore

if we arbitrarily set $\boldsymbol{m_0}$ to be zero, we should set σ to be a large value so that the solution is not forced to be zero. On the other hand, Δ describes how smooth a function is; the smaller Δ is, the less dispersed a Gaussian function is, and the more quickly (or disconnected) a function value changes from one location to another. Finally, $\boldsymbol{G}$ is the energy response function, $G_i(E)dE$, that is determined from Geant4 simulations and is an NxM matrix, where N is a total number of channels and M is a total number of flux estimates. Applications of the linear least square method on a flux determination problem are demonstrated in Sections 7.4 and 7.5.

7.3.2 Generalized least square method - nonlinear problem

For our application, one disadvantage of using the generalized least square solution for linear problem (Eq. 7.17) is that the estimate can be a negative value (e.g., when converting from a low count rate), which is not physical for flux. To ensure the solution only yields positive flux estimate, it is helpful to change variables to $m = lnj$, $d_i = lnr_i$, and $x = lnE$. However, this comes at the expense of changing the linear relationship between d_i and m into a nonlinear relationship:

$$d_i = g_i(m) = lnr_i = ln \int G_i(E) j(E) dE \tag{7.23}$$

$$= ln \int G_i(x) e^{m(x)+x} dx \tag{7.24}$$

where $j(E)$ is $e^{m(x)}$ and dE is $e^x dx$.

For a (weakly) nonlinear problem, we can linearize the problem and find an estimate for $\tilde{\boldsymbol{m}}$. We do so by first expanding Eq 7.24 about $m = m_{prior}$ using Taylor expansion

$$d_i = g_i(m_{prior}) + \frac{\delta g_i(m)}{\delta m}|_{m=m_{prior}} \cdot \Delta m + \frac{1}{2} \frac{\delta^2 g_i(m)}{\Delta^2 m}|_{m=m_{prior}} \cdot \Delta m^2 + 0(\Delta m^3) \tag{7.25}$$

where $\Delta m = m - m_{prior}$. Assume contribution from high order terms is small, i.e., Δm_j^n, where n ≥ 2, is small with respect to Δm, then

$$d_i = g_i(m_{prior}) + \frac{\delta g_i(m)}{\delta m}|_{m=m_{prior}} \cdot \Delta m \tag{7.26}$$

$$d_i = g_i(m_{prior}) + \frac{1}{r_{ni}} \int G_i(x) e^{m_{prior}(x)+x} dx \Delta m \tag{7.27}$$

$$\boldsymbol{d = g(m)} \approx \boldsymbol{g(m_{prior}) + G_n[m - m_{prior}]} \tag{7.28}$$

where $\boldsymbol{G_n} = \frac{1}{r_{ni}} \int G_i(x) e^{m_{prior}(x)+x} dx$ is the linearized response. Hereafter, we use m_n in place of m_{prior}.

Now that we have the linearized relation, we can determine the objective function for $\boldsymbol{d = g(m)}$, which is similar to Eq. 7.11:

$$S(\boldsymbol{m}) = (\boldsymbol{d_n} - \boldsymbol{d_0})^T \boldsymbol{C_d^{-1}} (\boldsymbol{d_n} - \boldsymbol{d_0}) + (\boldsymbol{m_n} - \boldsymbol{m_0})^T \boldsymbol{C_m^{-1}} (\boldsymbol{m_n} - \boldsymbol{m_0}) \tag{7.29}$$

Like the solution for a linear problem, the least square solution for a weakly nonlinear problem can be obtained by minimizing the least square misfit equation Eq. 7.29, which gives

$$\begin{aligned} \boldsymbol{m_{n+1}} &= \boldsymbol{m_n} + (\boldsymbol{G^T C_d^{-1} G} + \boldsymbol{C_m^{-1}})^{-1} \boldsymbol{G^T C_d^{-1}} (\boldsymbol{d_{obs}} - \boldsymbol{g(m_{prior})}) & (7.30) \\ &= \boldsymbol{m_n} + \boldsymbol{C_m G^t} (\boldsymbol{G C_m G^T} + \boldsymbol{C_d})^{-1} (\boldsymbol{d_{obs}} - \boldsymbol{g(m_{prior})}) & (7.31) \end{aligned}$$

From Eq. 7.28, we know that $\boldsymbol{g(m_{prior})} = \boldsymbol{g(m)} - \boldsymbol{G_n}[\boldsymbol{m} - \boldsymbol{m_{prior}}]$. Hence, Eq. 7.30 and 7.31 can be rewritten as:

$$\begin{aligned} \boldsymbol{m_{n+1}} &= \boldsymbol{m_n} + (\boldsymbol{G^T C_d^{-1} G} + \boldsymbol{C_m^{-1}})^{-1} \boldsymbol{G^T C_d^{-1}} (\boldsymbol{d_{obs}} - \boldsymbol{g(m_n)} + \boldsymbol{G_n}[\boldsymbol{m_n} - \boldsymbol{m_0}]) & (7.32) \\ &= \boldsymbol{m_n} + \boldsymbol{C_m G^t} (\boldsymbol{G C_m G^T} + \boldsymbol{C_d})^{-1} (\boldsymbol{d_{obs}} - \boldsymbol{g(m_n)} + \boldsymbol{G_n}[\boldsymbol{m_n} - \boldsymbol{m_0}]) & (7.33) \end{aligned}$$

In the instances where higher order terms in Eq. 7.25 is no longer negligible and the function $\boldsymbol{g(m)}$ is quasilinear in a certain region, rather than using Eq. 7.30 or 7.31, iterative algorithms like quasi-Newton and steepest gradients can be used to find the optimal solution. Interested readers are referred to Tarantola [2002] for more discussion.

In summary, the general procedure to solve a nonlinear problem using the generalized least square method includes:

(1) Select an initial $\boldsymbol{m_0}$ and take $\boldsymbol{m_n} = \boldsymbol{m_0}$.

(2) Compute $\boldsymbol{G_n}$ and $\boldsymbol{d_n}$

(3) Solve for $\boldsymbol{m_{n+1}}$ using Eq. 7.32 or Eq. 7.33

(4) Repeat Step 1-3 until $\Delta \boldsymbol{m} = \boldsymbol{m_{n+1}} - \boldsymbol{m_0}$ or $\boldsymbol{d_{obs}} - \boldsymbol{d_{n+1}}$ is small enough (the exact value to decide whether it is small enough depends on the situation. In this case, the difference is set to be less than 1). A more systematic approach is to use a χ^2 goodness of fit test. χ^2 is the squared sum of the ratio between prediction errors and data uncertainties (see also Riley et al., 1999, equation 31.129):

$$\chi^2 = \sum_N [\frac{\boldsymbol{d} - \boldsymbol{G m_{estimate}}}{\sigma_d}]^2 \tag{7.34}$$

where $\boldsymbol{d} - \boldsymbol{G m_{estimate}}$ is the prediction error and σ_d is the data uncertainty. It is a common practice to compare the computed χ^2 from Eq. 7.34 to a χ^2 value of a chosen significance level and the degree of freedom. If χ^2 is smaller than $\chi^2_{sl,dof}$, then the fit is acceptable. But if χ^2 is significantly smaller than $\chi^2_{sl,dof}$, there is a risk of overfitting. For the generalized least square method, χ^2 is the misfit function (Eq. 7.12), and the degree of freedom is the dimension of $\boldsymbol{d}$, N. More discussions on the χ^2 goodness of fit test can be found in Tarantola [2005, Appendix 6.8].

7.4 Instrument validation: Sr-90 radioactive source test

We have performed a Sr-90 radioactive source test to verify instrument performance. The source was placed directly in front of the REPTile-2 aperture. Sr-90 has a half-life of 28.8 years and undergoes beta decay into Y-90, resulting in maximum electron energy of 546 keV. Y-90 has a half-life of 64 hours and decays into the stable Zr-90 that produces a maximum energy of 2.3 MeV [National Nuclear Data Center, 2008; Also see the grey curve in Figure 7.2b].

The black asterisks in Figure 7.2a show the count rates for these events. The relationship between count rate and flux is:

$$r_i = \int G_i(E) j(E) dE$$

where r_i is the count rate at channel i, $G_i(E)$ is the channel energy response, and $j(E)$ is flux spectrum as a function of energy, E.

Figure 7.2b presents the estimated fluxes from both bowtie and linear least square methods using Eq. 7.5 and 7.18, respectively. We converted estimated fluxes from the generalized least square method back to count rates using Eq. 7.1 and compared estimated count rates to observed count rates to verify that our least square solution is reasonable (Figure 7.2a). Compared to the solutions from the bowtie method, the least square solution yields a better-resolved energy spectrum. It provides an uncertainty estimate, as indicated by the red dotted curve in Figure 7.2b. Higher uncertainty is associated with estimated fluxes for <300 keV electrons, suggesting that this instrument measures these low-energy electrons poorly (due to the presence of the 0.3 mm Beryllium window as described in Chapter 6). In addition, the uncertainty increases near the end of the Sr-90 spectrum at E > 2.1 MeV, and flux estimates become negative for electrons with energy greater than 2.3 MeV. We also noted that count rates are not exactly zero at higher energy (where the nominal energy, $\bar{E}$ is greater than 2.3 MeV) channels, i.e., Channel 38 and above. This explains why the bowtie analysis provides a very low flux (rather than zero) at E $\sim$ 2.4 MeV.

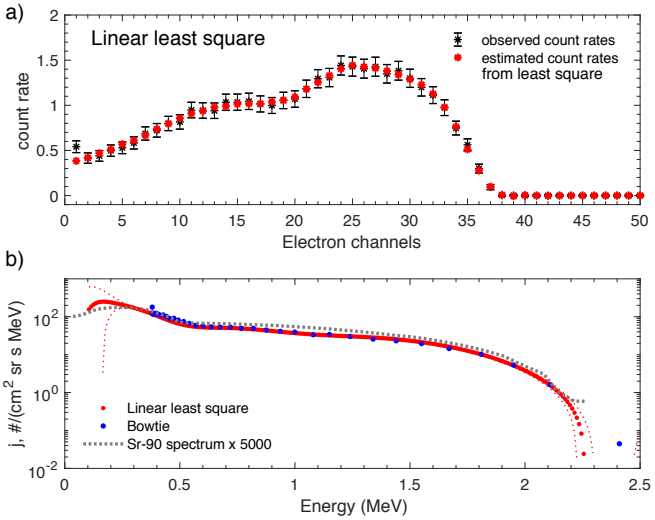

Figure 7.2: (a) Observed (black) and estimated (red) count rate from the Sr-90 source test. (b) Estimated flux from the bowtie method (blue) and linear least square method (red), in comparison with the expected Sr-90 spectrum (dotted gray curve). The red dotted curve shows uncertainties of estimated fluxes from the least square method.

Figure 7.3 shows results from the bowtie and nonlinear least square methods (Eq. 7.32 in

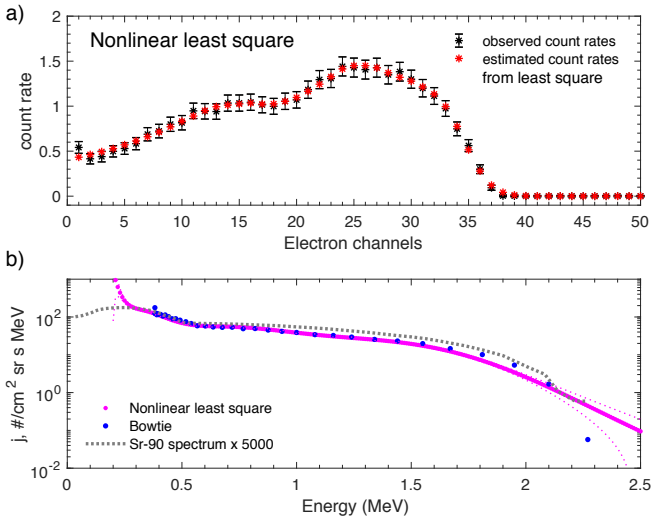

Figure 7.3: (a) Observed (black) and estimated (red) count rate from the Sr-90 source test. (b) Estimated flux from the bowtie method (blue) and nonlinear least square method (magenta), in comparison with the expected Sr-90 spectrum (dotted gray curve). The magenta dotted curve shows uncertainties of estimated fluxes from the nonlinear least square method.

Section 7.3.2). The variables in Eq. 7.1 are transformed to *log* in the nonlinear method to ensure positive flux solutions. Figure 7.3a demonstrates that estimated count rates from the nonlinear least square solution is in good agreement with observed count rates, providing confidence to the estimated flux spectrum. Magenta curves in Figure 7.3b shows that flux from nonlinear least square method has a higher uncertainty at E $<$ 0.3 MeV and E $>$ 2.1 MeV, which is consistent with the linear solution. But unlike the linear solution that contains negative fluxes at higher energy electron channels where count rates are low, the nonlinear least square method produces positive-only flux estimates. In short, solutions from bowtie analysis, linear and nonlinear least square methods are in good agreement with the expected spectrum [Euramet, 2019]. This certifies the validity of Geant4 simulations and verifies our instrument ability at measuring electrons from 300 keV to 2 MeV with fine energy resolution.

7.5 Performances under extreme scenarios

In addition to the Sr-90 test, we also examine the performances of the two flux determination methods under two extreme flux spectra: a spiky flux spectrum and a flat flux spectrum. For instance, multiple peaks in the energy spectrum [e.g., Datlowe et al., 1985; Sauvaud et al., 2013; Ukhorskiy et al., 2014] have been observed in the inner radiation belt, but how well these flux determination methods handle such spectra is not clear and is the subject of interest.

We generated an artificial spiky flux spectrum that peaks between 0.84 - 0.91 MeV electrons and is zero at other energies. Count rates are computed using the spiky flux spectrum and the energy response function from Section 6.4.5.2. To simulate sampling fluctuations, a final count rate is a random number generated from a Poisson distribution specified as the rate parameter by the computed count rate. We then use the bowtie and linear least square methods to convert the count rate back to flux and compare the estimated flux to the spikey flux spectrum. The χ^2 goodness of fit test is utilized to determine the optimal estimate from the linear least square method. Figure 7.4 shows the comparison of the estimated fluxes from the bowtie and linear least square methods. The bowtie solution misses the peak slightly, while the linear least square method captures the peak well, but there are also some (non-physical) wiggles outside the peak (see the zoom-in plot in Figure 7.4.

Another extreme spectrum test case is a flat electron flux spectrum with a constant flux of $5 \times 10^6\ cm^{-2}sr^{-1}s^{-1}MeV^{-1}$ across a wide range of energy, 0.1 to 10 MeV. Figure 7.5 illustrates that the solution from the bowtie analysis does not work well for a flat spectrum and still exhibits an exponential-like spectrum. The same observation was made by Claudepierre et al. [2021] when they calibrated measurements from MagEIS. Meanwhile, the linear least square solution reproduces the flat spectrum very well. In summary, the bowtie method can handle a spiky flux spectrum reasonably well but does not handle the flat spectra well, which is likely due to the initial exponential flux assumption used in the bowtie derivation. On the other hand, the least square method is capable of handling various types of flux spectra.

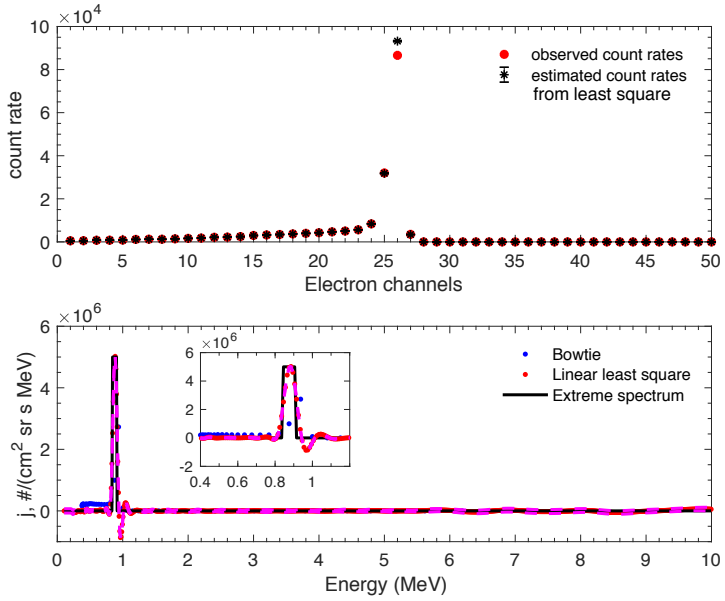

Figure 7.4: Flux comparison from bowtie (blue) and least square methods (red) under a spiky flux spectrum (black). The spiky flux spectrum only has flux peaks around 0.84-0.91 MeV electrons and the rest of the spectrum is zero.

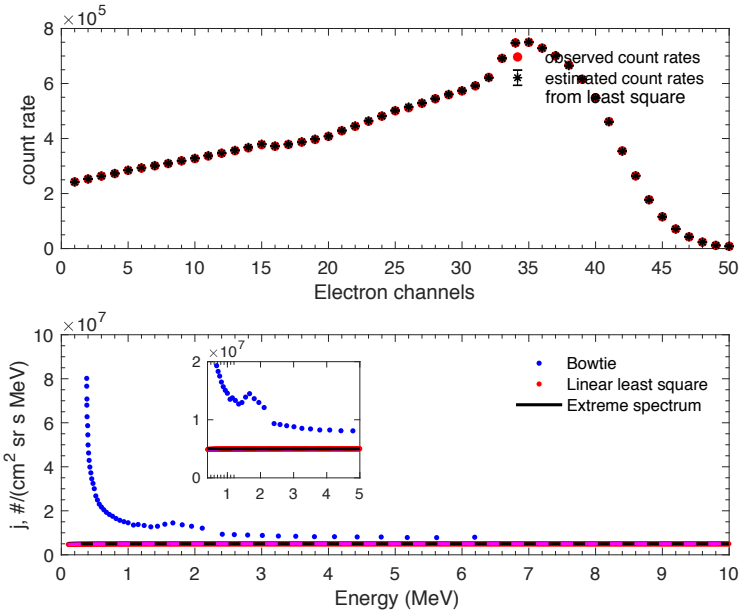

Figure 7.5: Flux comparison from bowtie (blue) and least square methods (red) under a flat flux spectrum (black) where flux of 0.1 to 10 MeV electrons are at 5×10^6.

7.6 Summary and discussion

This chapter describes two flux determination methods and examines their performance under different flux spectra. Solutions from both techniques agree with the expected Sr-90 spectrum and validates the performance of the REPTile2 instrument and the Geant4 simulation results. We further examined their capability at estimating extreme flux spectra, including a spiky flux spectrum and a flat flux spectrum that are not uncommon in space [Claudepierre et al., 2021]. Both approaches handle extreme flux spectra reasonably well, with one cautionary observation that instead of a flat spectrum, a bowtie solution yields an exponential-like spectrum at low-energy channels.

In summary, the bowtie method is easy to implement and is widely used in the calibration of radiation belt particle measurements. However, its resolution is limited by channel width, and it does not handle flat spectra well. On the other hand, the generalized least square method can yield a more well-resolved flux spectrum and handle various types of flux spectra well, but it runs the risk of 'overfitting' or 'underfitting' (depending on the choice of σ and Δ in the model covariance term, C_m) and requires careful implementation to provide optimal solutions. In other words, the bowtie method is suitable for first-order flux estimates, while the generalized least square method can provide a better-resolved solution for a variety of flux spectra.

Chapter 8

Summary and Suggestions for Future Work

8.1 Summary

Energetic electrons in the inner magnetosphere are characterized by dynamic variations in spatial and temporal scales. Despite decades of research, many lingering questions about the dynamics of energetic electrons still need to be addressed. Therefore, the overarching goal of this dissertation is to improve our understanding of energetic electrons in the inner magnetosphere. Specifically, this work offers a new perspective on the sudden enhancement of energetic electrons by examining their dynamics not as a standalone entity but with respect to the cold plasmasphere in the inner magnetosphere. In addition, this work explores ways to improve the quality of energetic electron measurements, especially those made in and near the inner belt, that are essential to advance our understanding of energetic electrons.

Chapter 3 examined initial enhancement events during the five largest geomagnetic storms between January 2013 to June 2015. Using energetic electron (30 keV to 2.5 MeV) measurements from the Van Allen Probes, We investigate where the initial enhancement occurs with respect to the innermost plasmapause location inferred from two different plasmapause models. Chapter 3 demonstrates that the initial enhancement of energetic electrons is consistently found outside the innermost plasmapause locations. The relationship between the initial enhancement locations and the innermost plasmapause locations is also energy-dependent. Initial enhancements of relativistic electrons ($>$ 500 keV) are further from the innermost plasmapause location than the initial enhancements of tens of keV electrons, and their initial enhancements occur a few hours later than

those of tens of keV electrons.

The five geomagnetic storms examined in Chapter 3 are coronal-mass-ejection (CME)-driven storms. To investigate if the geomagnetic storm drivers or storm magnitude have any influence on the relationship between initial enhancement locations and the plasmapause locations, Chapter 4 studied all enhancement events that occurred between January 2013 to June 2015 and separated them into the storm and non-storm events. Events that occur during storm periods are categorized into CME-driven storms and corotating interaction region (CIR)-driven storms. Our analysis shows that regardless of the storm type and magnitude, the innermost plasmapause location remains the innermost limit of the initial enhancement of energetic electrons (30 keV to 2.5 MeV). The relationship between the initial enhancement location and the plasmapause locations is quantified as a function of energy and exhibited a similar trend for CME- and CIR-driven storms. This fits into the current understanding of the acceleration and loss of energetic electrons: efficient acceleration mechanisms like chorus waves reside outside the plasmapause, while loss mechanisms by hiss or EMIC waves dominate inside the plasmasphere. This could explain the important role played by the plasmasphere in shaping the wave distribution, which affects the dynamics of energetic electrons.

Chapter 5 explores what causes the outlier events where the sudden enhancements of $<$ 300 keV electrons were reported inside the innermost plasmapause location. We examined nine outlier events using measurements from the Van Allen Probes and GOES spacecraft. The enhancement locations are compared to measured in-situ plasmapause locations and simulated innermost plasmapause locations. This study reveals a local-time dependence of the relationship between observed initial enhancements and in-situ plasmapause location. Enhancements near the postmidnight sector are often found outside the in-situ Lpp, while enhancements near the noon/dusk sector are mostly inside the in-situ Lpp. This is consistent with the local-time dependence of plasmasphere dynamics: the plasmapause is closest to the Earth near the postmidnight and dawn region and furthest from the Earth near the dusk and noon sectors. Due to the localized nature of spacecraft measurements and local-time dependence of inner magnetosphere dynamics, the comparison between

sudden enhancement locations and in-situ plasmapause locations could provide a contradictory result, depending on the spacecraft location. Nonetheless, these enhancement events remain outside of the simulated innermost plasmapause location (within the plasmapause model uncertainty). The phase space density analysis supports the notion that radial transport contributes to the sudden enhancement of energetic electrons. Our study indicates that the same mechanism that causes the plasmaspheric erosion can also control the dynamics of both energetic electrons. The large-scale westward electric field is a good candidate mechanism as it can transport both energetic electrons and cold plasma inward under the ExB drift. Insights from this series of work are significant, not only revealing a consistent pattern associated with these seemingly unorganized, sudden enhancement events but also suggests what contributes to such behavior, namely large scale electric fields. The persistent relationship between energetic electron enhancements and innermost plasmapause locations also allows us to improve our current energetic electron simulations by leveraging the advance in plasmapause modeling.

Analysis in Chapters 3 to 5 highlights the importance of well-resolved energetic electron measurement to provide insights into its detailed variations. However, background contamination from relativistic electrons and protons often overwhelms energetic electron observations near the slot region and inner belt. In Chapter 6, we introduce the Relativistic Electron Proton Telescope integrated little experiment-2 (REPTile-2), an energetic electron telescope that aims to provide clean and well-resolved measurements for energetic electrons (300 keV to 3 MeV) and protons (6.5 MeV to 33 MeV), especially in or near the inner belt. Geant4 simulations are used extensively to inform the design and performance of REPTile-2. With the addition of guard ring detectors and pulse-height analysis, REPTile-2 has demonstrated a promising capability for reducing background contamination and improving energy resolution (from six channels in its predecessor instrument to 120 channels).

To validate the REPTile-2 performance, we need to compare the flux spectrum to the expected Sr-90 spectrum. Chapter 7 examines two flux determination methods: a bowtie method and a generalized least square method. A detailed discussion of the derivation of these two methods

is provided. Our analysis shows that the estimated flux spectrum for the Sr-90 test from both methods is in good agreement with the expected Sr-90 spectrum, validating the performances of REPTile-2 and the Geant4 simulation results. In addition, we tested these methods under extreme flux spectra like a spiky flux spectrum (peaks in a small energy range and zero at other energies) and a flat flux spectrum (constant flux across all energies). In short, the bowtie method is simple and easy to implement, but its resolution is limited by channel width and cannot handle flat spectra very well. The generalized least square method, on the other hand, is more involved but can yield a better-resolved (in energy) flux spectrum. In short, the quality of energetic electron measurements can be improved by a detailed understanding of the instrument response and the use of rigorous inverse methods like the generalized least square method. Such measurements will enable detailed energy spectrum analysis and address lingering questions like the energy and spatial extent of a sudden enhancement event (especially a slot-filling enhancement event) and the peak energy of the bump-on-tail energy spectrum.

8.2 Future Work

In this section, I will present some ideas for potential extensions to this work, hoping to shed some light on unexplored territory.

8.2.1 Role of plasmasphere on the evolution of energetic electrons after initial enhancements

Chapters 3, 4, and 5 studied the relationship between the initial enhancement of energetic electrons and innermost plasmapause location. But, the role of the plasmasphere after initial enhancements is not fully understood. Previous studies like Thorne et al. [2013] and Pinto et al. [2020] have suggested that the plasmapause shields relativistic electrons from the dynamic process that causes the rapid enhancement of relativistic electrons in the outer belt and shapes the formation and location of the remnant belt. Recent studies like Li et al. [2021] demonstrated that the three-belt structure is also observed in sub-MeV electrons. What role does the plasmasphere play

in the evolution of energetic electrons after the initial enhancement? Is the plasmapause location crucial in the formation of a three-belt structure? A statistical study investigating the relationship between the plasmapause and the evolution of energetic electrons after initial enhancements could shed light on the underlying mechanism that controls the variations of energetic electrons. Such analysis is needed to establish a full understanding of how the plasmasphere affects energetic electron dynamics.

8.2.2 Role of large-scale electric fields on energetic particles

Chapter 5 suggests that large-scale electric fields can contribute to the sudden enhancement of energetic electrons. Previous studies like Thaller et al. [2015] and Califf et al. [2017] have demonstrated a good agreement between electric field enhancements and plasmaspheric erosion or energetic electron enhancements. It would be an interesting extension of the current work to provide observational proof that electric field enhancements are related to plasmaspheric erosion and energetic electron enhancements. In addition, the relative contribution of the large-scale convection electric field and subauroral polarization streams (SAPS) on energetic electron dynamics remains unclear. From theoretical derivations, Lejosne et al. [2018] suggest that SAPS will move energetic electrons inward and move energetic ions outward. This is different from the effect of the large-scale convection electric field that moves charged electrons and ions in the same direction. To the best of the author's knowledge, no observational study examines this theoretical prediction and demonstrates the distinct effect SAPS have on energetic electrons and protons. Such analysis could validate the SAPS influence on energetic particles and improve our understanding of the role of large-scale electric fields on energetic electrons.

8.2.3 REPTile-2 measurements and the implication of the Geant4 analysis

Chapter 6 describes the design and performance of REPTile-2. REPTile-2 is scheduled to launch no earlier than late 2022. The spacecraft bus is fully integrated with the instrument (REPTile-2) and is currently in the testing phase, as of November 2021. Tests have demonstrated

the capability of REPTile-2 at providing well-resolved and clean measurements. Once launched, the measurements near the SAA region need to be carefully tracked and corrected for inner zone proton contamination and pileup effects. Other electronic errors like deadtime and chance coincidence also need to be monitored during the operation period and corrected from the data whenever necessary.

If CIRBE is launched and operated successfully, it will be providing one of the cleanest and well-resolved measurements of energetic electrons and protons in the inner magnetosphere. Measurements from REPTile-2 can be used to address important questions like the contribution of CRAND to relativistic electrons in the inner belt. It also enables detailed energy spectrum analysis that allows the investigation of the breakpoint in terms of energy for the sudden enhancement of energetic electrons, e.g., under certain geomagnetic conditions, in which electron energy will experience enhancements. Another interesting study that could be made possible by REPTile-2 measurements is a detailed study of the bump-on-tail spectrum. Zhao et al. [2019] have demonstrated the prevalence of the bump-on-tail spectrum in the radiation belts. Due to instrument limitations, it is still unclear at which energy the bump peaks. Such studies can shed light on the energy-dependence of wave-particle interactions.

It is important to note that the analysis demonstrated in Chapters 6 and 7 can be applied to existing measurements like REPTile. For instance, the instrument response function in REPTile only involves boresight-shooting particles. One can recalibrate the instrument response function using the spherical shooting Geant4 simulations and determine flux using the generalized least square method for a better-resolved flux spectrum. Due to limited instrument channels (only three channels each for electron and proton measurements), REPTile will not give an energy spectrum as well-resolved as one from REPTile-2. However, since its operating period overlaps with the Van Allen Probes, a better characterization of the REPTile instrument and a recalibration of the REPTile data could provide valuable low-earth orbit measurements during the early Van Allen Probes era and enables detailed conjunctive studies with the Van Allen Probes. A detailed instrument response function can also be combined with radiation belt simulations to better compare the simulated energetic electrons and the observations. This could improve our understanding of

the effect of different loss and acceleration mechanisms on energetic electrons. In short, analysis in Chapters 6 and 7 is helpful for instrument calibration and/or the inter-calibration between different instruments and could help improve the quality of energetic particle measurements, advancing our understanding of energetic electron dynamics in the inner magnetosphere.

Bibliography

Abel, B. and R. M. Thorne (1998). Electron scattering loss in earth's inner magnetosphere: 1. dominant physical processes. Journal of Geophysical Research: Space Physics 103(A2), 2385–2396.

Agostinelli, S., J. Allison, K. a. Amako, J. Apostolakis, H. Araujo, P. Arce, M. Asai, D. Axen, S. Banerjee, G. Barrand, et al. (2003). Geant4—a simulation toolkit. Nuclear instruments and methods in physics research section A: Accelerators, Spectrometers, Detectors and Associated Equipment 506(3), 250–303.

Alfvén, H. (1963). Cosmical electrodynamics.

Allison, J., K. Amako, J. Apostolakis, H. Araujo, P. A. Dubois, M. Asai, G. Barrand, R. Capra, S. Chauvie, R. Chytracek, et al. (2006). Geant4 developments and applications. IEEE Transactions on nuclear science 53(1), 270–278.

Allison, J., K. Amako, J. Apostolakis, P. Arce, M. Asai, T. Aso, E. Bagli, A. Bagulya, S. Banerjee, G. Barrand, et al. (2016). Recent developments in geant4. Nuclear instruments and methods in physics research section A: Accelerators, Spectrometers, Detectors and Associated Equipment 835, 186–225.

Anderson, B., R. Millan, G. Reeves, and R. Friedel (2015). Acceleration and loss of relativistic electrons during small geomagnetic storms. Geophysical Research Letters 42(23), 10–113.

Artemyev, A., A. Neishtadt, and A. Vasiliev (2020). Mapping for nonlinear electron interaction with whistler-mode waves. Physics of Plasmas 27(4), 042902.

Baker, D., P. Erickson, J. Fennell, J. Foster, A. Jaynes, and P. Verronen (2018). Space weather effects in the earth's radiation belts. Space Science Reviews 214(1), 1–60.

Baker, D., A. Jaynes, V. Hoxie, R. Thorne, J. Foster, X. Li, J. Fennell, J. Wygant, S. Kanekal, P. Erickson, et al. (2014). An impenetrable barrier to ultrarelativistic electrons in the van allen radiation belts. Nature 515(7528), 531–534.

Baker, D., S. Kanekal, V. Hoxie, M. Henderson, X. Li, H. E. Spence, S. Elkington, R. Friedel, J. Goldstein, M. Hudson, et al. (2013). A long-lived relativistic electron storage ring embedded in earth's outer van allen belt. Science 340(6129), 186–190.

Baker, D., S. Kanekal, X. Li, S. Monk, J. Goldstein, and J. Burch (2004). An extreme distortion of the van allen belt arising from the 'hallowe'en'solar storm in 2003. Nature 432(7019), 878–881.

Baker, D., T. Pulkkinen, X. Li, S. Kanekal, K. Ogilvie, R. Lepping, J. Blake, L. Callis, G. Rostoker, H. Singer, et al. (1998). A strong cme-related magnetic cloud interaction with the earth's magnetosphere: Istp observations of rapid relativistic electron acceleration on may 15, 1997. Geophysical Research Letters 25(15), 2975–2978.

Baker, D. N., A. Jaynes, S. Kanekal, J. Foster, P. Erickson, J. Fennell, J. Blake, H. Zhao, X. Li, S. Elkington, et al. (2016). Highly relativistic radiation belt electron acceleration, transport, and loss: Large solar storm events of march and june 2015. Journal of Geophysical Research: Space Physics 121(7), 6647–6660.

Baker, D. N., S. Kanekal, V. Hoxie, S. Batiste, M. Bolton, X. Li, S. Elkington, S. Monk, R. Reukauf, S. Steg, et al. (2012). The relativistic electron-proton telescope (rept) instrument on board the radiation belt storm probes (rbsp) spacecraft: Characterization of earth's radiation belt high-energy particle populations. The Van Allen Probes Mission, 337–381.

Baker, D. N., S. G. Kanekal, V. Hoxie, X. Li, A. N. Jaynes, H. Zhao, S. R. Elkington, J. C. Foster, R. Selesnick, B. Ni, et al. (2021). The relativistic electron-proton telescope (rept) investigation: Design, operational properties, and science highlights. Space Science Reviews 217(5), 1–75.

Baker, D. N., T. Pulkkinen, V. Angelopoulos, W. Baumjohann, and R. McPherron (1996). Neutral line model of substorms: Past results and present view. Journal of Geophysical Research: Space Physics 101(A6), 12975–13010.

Baumjohann, W. and R. A. Treumann (1996). Basic space plasma physics. World Scientific.

Bevington, P. R. and D. K. Robinson (2003). Data reduction and error analysis. McGraw-Hill, New York.

Bichsel, H. (1988). Straggling in thin silicon detectors. Reviews of Modern Physics 60(3), 663.

Bingham, S., C. G. Mouikis, L. M. Kistler, A. Boyd, K. Paulson, C. J. Farrugia, C. Huang, H. E. Spence, S. Claudepierre, and C. Kletzing (2018). The outer radiation belt response to the storm time development of seed electrons and chorus wave activity during cme and cir driven storms. Journal of Geophysical Research: Space Physics 123(12), 10–139.

Blake, J., P. Carranza, S. Claudepierre, J. Clemmons, W. Crain, Y. Dotan, J. Fennell, F. Fuentes, R. Galvan, J. George, et al. (2013). The magnetic electron ion spectrometer (mageis) instruments aboard the radiation belt storm probes (rbsp) spacecraft. The Van Allen Probes Mission, 383–421.

Blum, L., A. Halford, R. Millan, J. Bonnell, J. Goldstein, M. Usanova, M. Engebretson, M. Ohnsted, G. Reeves, H. Singer, et al. (2015). Observations of coincident emic wave activity and duskside energetic electron precipitation on 18–19 january 2013. Geophysical Research Letters 42(14), 5727–5735.

Borovsky, J. E. and M. H. Denton (2006). Differences between cme-driven storms and cir-driven storms. Journal of Geophysical Research: Space Physics 111(A7).

Borovsky, J. E. and M. H. Denton (2008). A statistical look at plasmaspheric drainage plumes. Journal of Geophysical Research: Space Physics 113(A9).

Bortnik, J., U. S. Inan, and T. F. Bell (2002). L dependence of energetic electron precipitation driven by magnetospherically reflecting whistler waves. Journal of Geophysical Research: Space Physics 107(A8), SMP–1.

Bortnik, J., U. S. Inan, and T. F. Bell (2006). Temporal signatures of radiation belt electron precipitation induced by lightning-generated mr whistler waves: 1. methodology. Journal of Geophysical Research: Space Physics 111(A2).

Bortnik, J., R. M. Thorne, and N. P. Meredith (2009). Plasmaspheric hiss overview and relation to chorus. Journal of Atmospheric and Solar-Terrestrial Physics 71(16), 1636–1646.

Boudouridis, A., J. Rodriguez, B. Kress, B. Dichter, and T. Onsager (2020). Development of a bowtie inversion technique for real-time processing of the goes-16/-17 seiss mps-hi electron channels. Space Weather 18(4), e2019SW002403.

Boyd, A. J., H. E. Spence, S. Claudepierre, J. F. Fennell, J. Blake, D. Baker, G. Reeves, and D. Turner (2014). Quantifying the radiation belt seed population in the 17 march 2013 electron acceleration event. Geophysical Research Letters 41(7), 2275–2281.

Boyd, A. J., D. Turner, G. D. Reeves, H. Spence, D. Baker, and J. Blake (2018). What causes radiation belt enhancements: A survey of the van allen probes era. Geophysical Research Letters 45(11), 5253–5259.

Breneman, A., A. Crew, J. Sample, D. Klumpar, A. Johnson, O. Agapitov, M. Shumko, D. Turner, O. Santolik, J. R. Wygant, et al. (2017). Observations directly linking relativistic electron microbursts to whistler mode chorus: Van allen probes and firebird ii. Geophysical Research Letters 44(22), 11–265.

Burch, J., J. Goldstein, and B. Sandel (2004). Cause of plasmasphere corotation lag. Geophysical Research Letters 31(5).

Burtis, W. and R. Helliwell (1969). Banded chorus—a new type of vlf radiation observed in the magnetosphere by ogo 1 and ogo 3. Journal of Geophysical Research 74(11), 3002–3010.

Califf, S., X. Li, R. Wolf, H. Zhao, A. Jaynes, F. Wilder, D. Malaspina, and R. Redmon (2016). Large-amplitude electric fields in the inner magnetosphere: Van allen probes observations of subauroral polarization streams. Journal of Geophysical Research: Space Physics 121(6), 5294–5306.

Califf, S., X. Li, H. Zhao, A. Kellerman, T. Sarris, A. Jaynes, and D. Malaspina (2017). The role of the convection electric field in filling the slot region between the inner and outer radiation belts. Journal of Geophysical Research: Space Physics 122(2), 2051–2068.

Cao, X., B. Ni, D. Summers, Y. Y. Shprits, X. Gu, S. Fu, Y. Lou, Y. Zhang, X. Ma, W. Zhang, et al. (2019). Sensitivity of emic wave-driven scattering loss of ring current protons to wave normal angle distribution. Geophysical Research Letters 46(2), 590–598.

Carpenter, D. and R. Anderson (1992). An isee/whistler model of equatorial electron density in the magnetosphere. Journal of Geophysical Research: Space Physics 97(A2), 1097–1108.

Carpenter, D. L. (1963). Whistler evidence of a 'knee'in the magnetospheric ionization density profile. Journal of Geophysical Research 68(6), 1675–1682.

Carpenter, D. L. and J. Lemaire (1997). Erosion and recovery of the plasmasphere in the plasmapause region. Space Science Reviews 80(1), 153–179.

Chapman, S. and V. C. Ferraro (1930). A new theory of magnetic storms. Nature 126(3169), 129–130.

Chappell, C. (1972). Recent satellite measurements of the morphology and dynamics of the plasmasphere. Reviews of Geophysics 10(4), 951–979.

Chappell, C., K. Harris, and G. Sharp (1970). A study of the influence of magnetic activity on the location of the plasmapause as measured by ogo 5. Journal of Geophysical Research 75(1), 50–56.

Charara, M., C. Barnes, and A. Tarantola (2000). Full waveform inversion of seismic data for a viscoelastic medium. In Methods and applications of inversion, pp. 68–81. Springer.

Chen, F. F. et al. (1984). Introduction to plasma physics and controlled fusion, Volume 1. Springer.

Chen, L., R. M. Thorne, J. Bortnik, W. Li, R. B. Horne, G. Reeves, C. Kletzing, W. Kurth, G. Hospodarsky, H. E. Spence, et al. (2014). Generation of unusually low frequency plasmaspheric hiss. Geophysical Research Letters 41(16), 5702–5709.

Chen, L., R. M. Thorne, V. K. Jordanova, M. F. Thomsen, and R. B. Horne (2011). Magnetosonic wave instability analysis for proton ring distributions observed by the lanl magnetospheric plasma analyzer. Journal of Geophysical Research: Space Physics 116(A3).

Chen, Y., R. Friedel, and G. Reeves (2006). Phase space density distributions of energetic electrons in the outer radiation belt during two geospace environment modeling inner magnetosphere/storms selected storms. Journal of Geophysical Research: Space Physics 111(A11).

Claudepierre, S., J. Blake, A. Boyd, J. Clemmons, J. Fennell, C. Gabrielse, M. Looper, J. Mazur, T. O'Brien, G. Reeves, et al. (2021). The magnetic electron ion spectrometer: A review of on-orbit sensor performance, data, operations, and science. Space science reviews 217(8), 1–67.

Claudepierre, S., T. O'Brien, J. Blake, J. Fennell, J. Roeder, J. Clemmons, M. Looper, J. Mazur, T. Mulligan, H. Spence, et al. (2015). A background correction algorithm for van allen probes mageis electron flux measurements. Journal of Geophysical Research: Space Physics 120(7), 5703–5727.

Claudepierre, S., T. O'Brien, M. Looper, J. Blake, J. Fennell, J. Roeder, J. Clemmons, J. Mazur, D. Turner, G. Reeves, et al. (2019). A revised look at relativistic electrons in the earth's inner radiation zone and slot region. Journal of Geophysical Research: Space Physics 124(2), 934–951.

Claudepierre, S. G., T. P. O'Brien, J. Fennell, J. Blake, J. Clemmons, M. Looper, J. Mazur, J. Roeder, D. L. Turner, G. D. Reeves, et al. (2017). The hidden dynamics of relativistic electrons (0.7–1.5 mev) in the inner zone and slot region. Journal of Geophysical Research: Space Physics 122(3), 3127–3144.

Cohen, J. (2013). Statistical power analysis for the behavioral sciences. Academic press.

Cyamukungu, M., S. Benck, S. Borisov, G. Grégoire, J. Cabrera, J.-L. Bonnet, B. Desoete, F. Preud'homme, C. Semaille, G. Creve, et al. (2014). The energetic particle telescope (ept) on board proba-v: description of a new science-class instrument for particle detection in space. IEEE Transactions on Nuclear Science 61(6), 3667–3681.

Daglis, I. A., R. M. Thorne, W. Baumjohann, and S. Orsini (1999). The terrestrial ring current: Origin, formation, and decay. Reviews of Geophysics 37(4), 407–438.

Datlowe, D., W. Imhof, E. Gaines, and H. Voss (1985). Multiple peaks in the spectrum of inner belt electrons. Journal of Geophysical Research: Space Physics 90(A9), 8333–8342.

Denton, M. H., J. E. Borovsky, R. Skoug, M. Thomsen, B. Lavraud, M. Henderson, R. McPherron, J.-C. Zhang, and M. Liemohn (2006). Geomagnetic storms driven by icme-and cir-dominated solar wind. Journal of Geophysical Research: Space Physics 111(A7).

Ebihara, Y. and Y. Miyoshi (2011). Dynamic inner magnetosphere: A tutorial and recent advances. The dynamic magnetosphere, 145–187.

Elkington, S. R., M. K. Hudson, and A. A. Chan (2003). Resonant acceleration and diffusion of outer zone electrons in an asymmetric geomagnetic field. Journal of Geophysical Research: Space Physics 108(A3).

Elphic, R., M. Thomsen, and J. Borovsky (1997). The fate of the outer plasmasphere. Geophysical research letters 24(4), 365–368.

Escoubet, C., A. Pedersen, R. Schmidt, and P.-A. Lindqvist (1997). Density in the magnetosphere inferred from isee 1 spacecraft potential. Journal of Geophysical Research: Space Physics 102(A8), 17595–17609.

Euramet (2019). Radionuclide beta spectra metrology. http://metrobetaempir.eu/wp-content/uploads/2019/11/15SIB10_MetroBeta_Final_Publishable_Report.pdf.

Fennell, J., S. Claudepierre, J. Blake, T. O'Brien, J. Clemmons, D. Baker, H. E. Spence, and G. Reeves (2015). Van allen probes show that the inner radiation zone contains no mev electrons: Ect/mageis data. Geophysical Research Letters 42(5), 1283–1289.

Filwett, R. J., A. N. Jaynes, D. N. Baker, S. G. Kanekal, B. Kress, and J. B. Blake (2020). Solar energetic proton access to the near-equatorial inner magnetosphere. Journal of Geophysical Research: Space Physics 125(6), e2019JA027584.

Finlay, C. C., S. Maus, C. Beggan, T. Bondar, A. Chambodut, T. Chernova, A. Chulliat, V. Golovkov, B. Hamilton, M. Hamoudi, et al. (2010). International geomagnetic reference field: the eleventh generation. Geophysical Journal International 183(3), 1216–1230.

Foster, J., P. Erickson, D. Baker, S. Claudepierre, C. Kletzing, W. Kurth, G. Reeves, S. Thaller, H. E. Spence, Y. Shprits, et al. (2014). Prompt energization of relativistic and highly relativistic electrons during a substorm interval: Van allen probes observations. Geophysical Research Letters 41(1), 20–25.

Foster, J., P. Erickson, D. Baker, A. Jaynes, E. Mishin, J. Fennel, X. Li, M. Henderson, and S. Kanekal (2016). Observations of the impenetrable barrier, the plasmapause, and the vlf bubble during the 17 march 2015 storm. Journal of Geophysical Research: Space Physics 121(6), 5537–5548.

Frank, L. A. (1971). Relationship of the plasma sheet, ring current, trapping boundary, and plasmapause near the magnetic equator and local midnight. Journal of Geophysical Research 76(10), 2265–2275.

Frey, H. U. (2007). Localized aurora beyond the auroral oval. Reviews of Geophysics 45(1).

Friedel, R., H. Korth, M. Henderson, M. Thomsen, and J. Scudder (2001). Plasma sheet access to the inner magnetosphere. Journal of Geophysical Research: Space Physics 106(A4), 5845–5858.

Ghamry, E., A. Lethy, T. Arafa-Hamed, and E. Abd Elaal (2016). A comprehensive analysis of the geomagnetic storms occurred during 18 february and 2 march 2014. NRIAG Journal of Astronomy and Geophysics 5(1), 263–268.

Ginet, G., T. O'Brien, S. Huston, W. Johnston, T. Guild, R. Friedel, C. Lindstrom, C. Roth, P. Whelan, R. Quinn, et al. (2013). Ae9, ap9 and spm: New models for specifying the trapped energetic particle and space plasma environment. Space science reviews 179(1-4), 579–615.

Gold, T. (1959). Motions in the magnetosphere of the earth. Journal of Geophysical Research 64(9), 1219–1224.

Goldstein, J. (2006). Plasmasphere response: Tutorial and review of recent imaging results. Solar dynamics and its effects on the heliosphere and earth, 203–216.

Goldstein, J., D. Baker, J. Blake, S. De Pascuale, H. Funsten, A. Jaynes, J.-M. Jahn, C. Kletzing, W. Kurth, W. Li, et al. (2016). The relationship between the plasmapause and outer belt electrons. Journal of Geophysical Research: Space Physics 121(9), 8392–8416.

Goldstein, J., J. Burch, and B. Sandel (2005). Magnetospheric model of subauroral polarization stream. Journal of Geophysical Research: Space Physics 110(A9).

Goldstein, J., S. Kanekal, D. Baker, and B. Sandel (2005). Dynamic relationship between the outer radiation belt and the plasmapause during march–may 2001. Geophysical Research Letters 32(15).

Goldstein, J., S. Pascuale, and W. Kurth (2019). Epoch-based model for stormtime plasmapause location. Journal of Geophysical Research: Space Physics 124(6), 4462–4491.

Goldstein, J., S. D. Pascuale, C. Kletzing, W. Kurth, K. Genestreti, R. Skoug, B. Larsen, L. M. Kistler, C. Mouikis, and H. Spence (2014). Simulation of van allen probes plasmapause encounters. Journal of Geophysical Research: Space Physics 119(9), 7464–7484.

Goldstein, J. and B. Sandel (2005). The global pattern of evolution of plasmaspheric drainage plumes. Inner magnetosphere interactions: New perspectives from imaging 159, 1–22.

Goldstein, J., B. Sandel, W. Forrester, M. Thomsen, and M. Hairston (2005). Global plasmasphere evolution 22–23 april 2001. Journal of Geophysical Research: Space Physics 110(A12).

Goldstein, J., B. Sandel, M. Hairston, and P. Reiff (2003). Control of plasmaspheric dynamics by both convection and sub-auroral polarization stream. Geophysical Research Letters 30(24).

Goldstein, J., B. Sandel, M. Thomsen, M. Spasojević, and P. Reiff (2004). Simultaneous remote sensing and in situ observations of plasmaspheric drainage plumes. Journal of Geophysical Research: Space Physics 109(A3).

Goldstein, J., M. Thomsen, and A. DeJong (2014). In situ signatures of residual plasmaspheric plumes: Observations and simulation. Journal of Geophysical Research: Space Physics 119(6), 4706–4722.

Grebowsky, J. (1970). Model study of plasmapause motion. Journal of Geophysical Research 75(22), 4329–4333.

Hanser, F. (2011). Eps/hepad calibration and data handbook. Assurance Technology Corporation, Carlisle, Mass.

Horne, R. B., R. M. Thorne, S. A. Glauert, J. M. Albert, N. P. Meredith, and R. R. Anderson (2005a). Timescale for radiation belt electron acceleration by whistler mode chorus waves. Journal of Geophysical Research: Space Physics 110(A3).

Horne, R. B., R. M. Thorne, S. A. Glauert, N. P. Meredith, D. Pokhotelov, and O. Santolík (2007). Electron acceleration in the van allen radiation belts by fast magnetosonic waves. Geophysical Research Letters 34(17).

Horne, R. B., R. M. Thorne, Y. Y. Shprits, N. P. Meredith, S. A. Glauert, A. J. Smith, S. G. Kanekal, D. N. Baker, M. J. Engebretson, J. L. Posch, et al. (2005b). Wave acceleration of electrons in the van allen radiation belts. Nature 437(7056), 227–230.

Hudson, M., R. Denton, M. Lessard, E. Miftakhova, and R. Anderson (2004). A study of pc-5 ulf oscillations. In Annales Geophysicae, Volume 22, pp. 289–302. Copernicus GmbH.

Hudson, M., S. Elkington, J. Lyon, and C. Goodrich (2000). Increase in relativistic electron flux in the inner magnetosphere: Ulf wave mode structure. Advances in Space Research 25(12), 2327–2337.

Hudson, M., A. Kotelnikov, X. Li, I. Roth, M. Temerin, J. Wygant, J. Blake, and M. Gussenhoven (1995). Simulation of proton radiation belt formation during the march 24, 1991 ssc. Geophysical research letters 22(3), 291–294.

Inan, U., D. Carpenter, R. Helliwell, and J. Katsufrakis (1985). Subionospheric vlf/lf phase perturbations produced by lightning-whistler induced particle precipitation. Journal of Geophysical Research: Space Physics 90(A8), 7457–7469.

Jahn, J.-M., J. Goldstein, W. Kurth, S. Thaller, S. De Pascuale, J. Wygant, G. Reeves, and H. Spence (2020). Determining plasmaspheric density from the upper hybrid resonance and from the spacecraft potential: How do they compare? Journal of Geophysical Research: Space Physics 125(3), no–no.

Jaynes, A. N., D. N. Baker, H. J. Singer, J. V. Rodriguez, T. Loto'aniu, A. Ali, S. R. Elkington, X. Li, S. G. Kanekal, S. G. Claudepierre, et al. (2015). Source and seed populations for relativistic electrons: Their roles in radiation belt changes. Journal of Geophysical Research: Space Physics 120(9), 7240–7254.

Kamide, Y., W. Baumjohann, I. Daglis, W. Gonzalez, M. Grande, J. Joselyn, R. McPherron, J. Phillips, E. Reeves, G. Rostoker, et al. (1998). Current understanding of magnetic storms: Storm-substorm relationships. Journal of Geophysical Research: Space Physics 103(A8), 17705–17728.

Kasahara, S., Y. Miyoshi, S. Yokota, T. Mitani, Y. Kasahara, S. Matsuda, A. Kumamoto, A. Matsuoka, Y. Kazama, H. U. Frey, et al. (2018). Pulsating aurora from electron scattering by chorus waves. Nature 554(7692), 337–340.

Kataoka, R. and Y. Miyoshi (2006). Flux enhancement of radiation belt electrons during geomagnetic storms driven by coronal mass ejections and corotating interaction regions. Space Weather 4(9).

Kavanagh, L., J. Freeman Jr, and A. Chen (1968). Plasma flow in the magnetosphere. Journal of Geophysical Research 73(17), 5511–5519.

Khoo, L.-Y., X. Li, H. Zhao, X. Chu, Z. Xiang, and K. Zhang (2019). How sudden, intense energetic electron enhancements correlate with the innermost plasmapause locations under various solar wind drivers and geomagnetic conditions. Journal of Geophysical Research: Space Physics 124(11), 8992–9002.

Khoo, L. Y., X. Li, H. Zhao, T. E. Sarris, Z. Xiang, K. Zhang, A. C. Kellerman, and J. B. Blake (2018). On the initial enhancement of energetic electrons and the innermost plasmapause locations: Coronal mass ejection-driven storm periods. Journal of Geophysical Research: Space Physics 123(11), 9252–9264.

Khoo, L.-Y., X. Li, H. Zhao, S. Thaller, and B. Hogan (2021). Multi-event studies of sudden energetic electron enhancements in the inner magnetosphere and its association with plasmapause positions. Journal of Geophysical Research: Space Physics 126(11), e2021JA029769.

Kilpua, E., H. Hietala, D. Turner, H. Koskinen, T. I. Pulkkinen, J. Rodriguez, G. Reeves, S. Claudepierre, and H. E. Spence (2015). Unraveling the drivers of the storm time radiation belt response. Geophysical Research Letters 42(9), 3076–3084.

Kivelson, M. G. and C. T. Russell (1995). Introduction to space physics. Cambridge university press.

Kletzing, C., W. Kurth, M. Acuna, R. MacDowall, R. Torbert, T. Averkamp, D. Bodet, S. Bounds, M. Chutter, J. Connerney, et al. (2013). The electric and magnetic field instrument suite and integrated science (emfisis) on rbsp. Space Science Reviews 179(1-4), 127–181.

Knoll, G. F. (2010). Radiation detection and measurement. John Wiley & Sons.

Korth, H., M. Thomsen, J. Borovsky, and D. McComas (1999). Plasma sheet access to geosynchronous orbit. Journal of Geophysical Research: Space Physics 104(A11), 25047–25061.

Kurth, W., S. De Pascuale, J. Faden, C. Kletzing, G. Hospodarsky, S. Thaller, and J. Wygant (2015). Electron densities inferred from plasma wave spectra obtained by the waves instrument on van allen probes. Journal of Geophysical Research: Space Physics 120(2), 904–914.

Lam, M. M., R. B. Horne, N. P. Meredith, S. A. Glauert, T. Moffat-Griffin, and J. C. Green (2010). Origin of energetic electron precipitation >30 kev into the atmosphere. Journal of Geophysical Research: Space Physics 115(A4).

Lei, M., L. Xie, J. Li, Z. Pu, S. Fu, B. Ni, M. Hua, L. Chen, and W. Li (2017). The radiation belt electron scattering by magnetosonic wave: Dependence on key parameters. Journal of Geophysical Research: Space Physics 122(12), 12–338.

Lejosne, S., B. S. Kunduri, F. S. Mozer, and D. Turner (2018). Energetic electron injections deep into the inner magnetosphere: A result of the subauroral polarization stream (saps) potential drop. Geophysical Research Letters 45(9), 3811–3819.

Lemaire, J. F. and K. I. Gringauz (1998). The Earth's plasmasphere.

Li, J., J. Bortnik, X. An, W. Li, V. Angelopoulos, R. M. Thorne, C. T. Russell, B. Ni, X. Shen, W. S. Kurth, et al. (2019). Origin of two-band chorus in the radiation belt of earth. Nature communications 10(1), 1–9.

Li, W. and M. Hudson (2019). Earth's van allen radiation belts: From discovery to the van allen probes era. Journal of Geophysical Research: Space Physics 124(11), 8319–8351.

Li, W., Q. Ma, R. Thorne, J. Bortnik, C. Kletzing, W. Kurth, G. Hospodarsky, and Y. Nishimura (2015). Statistical properties of plasmaspheric hiss derived from van allen probes data and their effects on radiation belt electron dynamics. Journal of Geophysical Research: Space Physics 120(5), 3393–3405.

Li, W., Y. Shprits, and R. Thorne (2007). Dynamic evolution of energetic outer zone electrons due to wave-particle interactions during storms. Journal of Geophysical Research: Space Physics 112(A10).

Li, W., R. Thorne, Q. Ma, B. Ni, J. Bortnik, D. Baker, H. E. Spence, G. Reeves, S. Kanekal, J. Green, et al. (2014). Radiation belt electron acceleration by chorus waves during the 17 march 2013 storm. Journal of Geophysical Research: Space Physics 119(6), 4681–4693.

Li, X., D. Baker, S. Kanekal, M. Looper, and M. Temerin (2001). Long term measurements of radiation belts by sampex and their variations. Geophysical Research Letters 28(20), 3827–3830.

Li, X., D. Baker, T. O'Brien, L. Xie, and Q. Zong (2006). Correlation between the inner edge of outer radiation belt electrons and the innermost plasmapause location. Geophysical research letters 33(14).

Li, X., D. Baker, M. Temerin, T. Cayton, E. Reeves, R. Christensen, J. Blake, M. Looper, R. Nakamura, and S. Kanekal (1997). Multisatellite observations of the outer zone electron variation during the november 3–4, 1993, magnetic storm. Journal of Geophysical Research: Space Physics 102(A7), 14123–14140.

Li, X., D. Baker, H. Zhao, K. Zhang, A. Jaynes, Q. Schiller, S. Kanekal, J. Blake, and M. Temerin (2017). Radiation belt electron dynamics at low l (<4): Van allen probes era versus previous two solar cycles. Journal of Geophysical Research: Space Physics 122(5), 5224–5234.

Li, X., A. B. Barker, D. Baker, W. Tu, T. Sarris, R. Selesnick, R. Friedel, and C. Shen (2009). Modeling the deep penetration of outer belt electrons during the "halloween" magnetic storm in 2003. Space Weather 7(2).

Li, X., S. Palo, R. Kohnert, L. Blum, D. Gerhardt, Q. Schiller, and S. Califf (2013b). Small mission accomplished by students—big impact on space weather research. Space Weather 11(2), 55–56.

Li, X., S. Palo, R. Kohnert, D. Gerhardt, L. Blum, Q. Schiller, D. Turner, W. Tu, N. Sheiko, and C. S. Cooper (2012). Colorado student space weather experiment: Differential flux measurements of energetic particles in a highly inclined low earth orbit. Dynamics of the Earth's Radiation Belts and Inner Magnetosphere, Geophys. Monogr. Ser 199, 385–404.

Li, X., I. Roth, M. Temerin, J. Wygant, M. Hudson, and J. Blake (1993). Simulation of the prompt energization and transport of radiation belt particles during the march 24, 1991 ssc. Geophysical Research Letters 20(22), 2423–2426.

Li, X., Q. Schiller, L. Blum, S. Califf, H. Zhao, W. Tu, D. Turner, D. Gerhardt, S. Palo, S. Kanekal, et al. (2013a). First results from csswe cubesat: Characteristics of relativistic electrons in the near-earth environment during the october 2012 magnetic storms. Journal of Geophysical Research: Space Physics 118(10), 6489–6499.

Li, X., R. Selesnick, D. Baker, A. Jaynes, S. Kanekal, Q. Schiller, L. Blum, J. Fennell, and J. Blake (2015). Upper limit on the inner radiation belt mev electron intensity. Journal of Geophysical Research: Space Physics 120(2), 1215–1228.

Li, Y.-X., C. Yue, Y.-X. Hao, Q.-G. Zong, X.-Z. Zhou, S.-Y. Fu, X.-R. Chen, and X.-X. Zhao (2021). The characteristics of three-belt structure of sub-mev electrons in the radiation belts. Journal of Geophysical Research: Space Physics 126(7), e2021JA029385.

Liu, S., M. Chen, L. Lyons, H. Korth, J. Albert, J. Roeder, P. Anderson, and M. Thomsen (2003). Contribution of convective transport to stormtime ring current electron injection. Journal of Geophysical Research: Space Physics 108(A10).

Liu, S., F. Xiao, C. Yang, Y. He, Q. Zhou, C. Kletzing, W. Kurth, G. Hospodarsky, H. E. Spence, G. Reeves, et al. (2015). Van allen probes observations linking radiation belt electrons to chorus waves during 2014 multiple storms. Journal of Geophysical Research: Space Physics 120(2), 938–948.

Liu, X., W. Liu, J. Cao, H. Fu, J. Yu, and X. Li (2015). Dynamic plasmapause model based on themis measurements. Journal of Geophysical Research: Space Physics 120(12), 10–543.

Loto'Aniu, T., H. Singer, C. Waters, V. Angelopoulos, I. Mann, S. Elkington, and J. Bonnell (2010). Relativistic electron loss due to ultralow frequency waves and enhanced outward radial diffusion. Journal of Geophysical Research: Space Physics 115(A12).

Lyons, L. R. and R. M. Thorne (1973). Equilibrium structure of radiation belt electrons. Journal of Geophysical Research 78(13), 2142–2149.

Lyons, L. R. and D. J. Williams (2013). Quantitative aspects of magnetospheric physics, Volume 23. Springer Science & Business Media.

Malaspina, D. M., A. N. Jaynes, C. Boulé, J. Bortnik, S. A. Thaller, R. E. Ergun, C. A. Kletzing, and J. R. Wygant (2016). The distribution of plasmaspheric hiss wave power with respect to plasmapause location. Geophysical Research Letters 43(15), 7878–7886.

Mann, I. R., L. Ozeke, K. R. Murphy, S. G. Claudepierre, D. L. Turner, D. N. Baker, I. Rae, A. Kale, D. K. Milling, A. J. Boyd, et al. (2016). Explaining the dynamics of the ultra-relativistic third van allen radiation belt. Nature Physics 12(10), 978–983.

Mauk, B., N. J. Fox, S. Kanekal, R. Kessel, D. Sibeck, and a. A. Ukhorskiy (2012). Science objectives and rationale for the radiation belt storm probes mission. The Van Allen Probes Mission, 3–27.

Menke, W. (2012). Geophysical data analysis: discrete inverse theory: MATLAB edition, Volume 45. Academic press.

Meredith, N. P., R. B. Horne, S. A. Glauert, and R. R. Anderson (2007). Slot region electron loss timescales due to plasmaspheric hiss and lightning-generated whistlers. Journal of Geophysical Research: Space Physics 112(A8).

Miyoshi, Y., K. Sakaguchi, K. Shiokawa, D. Evans, J. Albert, M. Connors, and V. Jordanova (2008). Precipitation of radiation belt electrons by emic waves, observed from ground and space. Geophysical Research Letters 35(23).

Moldwin, M. B., L. Downward, H. Rassoul, R. Amin, and R. Anderson (2002). A new model of the location of the plasmapause: Crres results. Journal of Geophysical Research: Space Physics 107(A11), SMP–2.

Mozer, F., O. Agapitov, J. Blake, and I. Vasko (2018). Simultaneous observations of lower band chorus emissions at the equator and microburst precipitating electrons in the ionosphere. Geophysical Research Letters 45(2), 511–516.

Nakamura, R., M. Isowa, Y. Kamide, D. Baker, J. Blake, and M. Looper (2000). Sampex observations of precipitation bursts in the outer radiation belt. Journal of Geophysical Research: Space Physics 105(A7), 15875–15885.

National Nuclear Data Center, B. N. L. (2008, March). Nudat2. Accessed November 2021. https://www.nndc.bnl.gov/nudat2/

Ni, B., H. Huang, W. Zhang, X. Gu, H. Zhao, X. Li, D. Baker, S. Fu, Z. Xiang, and X. Cao (2019). Parametric sensitivity of the formation of reversed electron energy spectrum caused by plasmaspheric hiss. Geophysical Research Letters 46(8), 4134–4143.

Obara, T., T. Nagatsuma, M. Den, Y. Miyoshi, and A. Morioka (2000). Main-phase creation of "seed" electrons in the outer radiation belt. Earth, planets and space 52(1), 41–47.

O'Brien, T. and M. Moldwin (2003). Empirical plasmapause models from magnetic indices. Geophysical Research Letters 30(4).

Olson, W. and K. Pfitzer (1979). Magnetospheric magnetic field modeling. Technical report, MCDONNELL DOUGLAS ASTRONAUTICS CO-WEST HUNTINGTON BEACH CALIF.

Park, I., Y. Miyoshi, T. Mitani, T. Hori, T. Takashima, S. Kurita, I. Shinohara, S. Kasahara, S. Yokota, K. Keika, et al. (2021). Characterization and calibration of high-energy electron instruments onboard the arase satellite. Journal of Geophysical Research: Space Physics 126(7), e2021JA029110.

Pinto, V., X.-J. Zhang, D. Mourenas, J. Bortnik, A. Artemyev, L. Lyons, and P. Moya (2020). On the confinement of ultrarelativistic electron remnant belts to low shells. Journal of Geophysical Research: Space Physics 125(3), e2019JA027469.

Pinto, V. A., J. Bortnik, P. S. Moya, L. R. Lyons, D. G. Sibeck, S. G. Kanekal, H. E. Spence, and D. N. Baker (2018). Characteristics, occurrence, and decay rates of remnant belts associated with three-belt events in the earth's radiation belts. Geophysical Research Letters 45(22), 12–099.

Pokhotelov, D., I. Rae, K. Murphy, I. Mann, and L. Ozeke (2016). Effects of ulf wave power on relativistic radiation belt electrons: 8–9 october 2012 geomagnetic storm. Journal of Geophysical Research: Space Physics 121(12), 11–766.

Reeves, G., K. McAdams, R. Friedel, and T. O'brien (2003). Acceleration and loss of relativistic electrons during geomagnetic storms. Geophysical Research Letters 30(10).

Reeves, G., H. E. Spence, M. Henderson, S. Morley, R. Friedel, H. Funsten, D. Baker, S. Kanekal, J. Blake, J. Fennell, et al. (2013). Electron acceleration in the heart of the van allen radiation belts. Science 341(6149), 991–994.

Reeves, G. D., R. H. Friedel, B. A. Larsen, R. M. Skoug, H. O. Funsten, S. G. Claudepierre, J. F. Fennell, D. L. Turner, M. H. Denton, H. E. Spence, et al. (2016). Energy-dependent dynamics of kev to mev electrons in the inner zone, outer zone, and slot regions. Journal of Geophysical Research: Space Physics 121(1), 397–412.

Ripoll, J.-F., S. Claudepierre, A. Ukhorskiy, C. Colpitts, X. Li, J. Fennell, and C. Crabtree (2020). Particle dynamics in the earth's radiation belts: Review of current research and open questions. Journal of Geophysical Research: Space Physics 125(5), e2019JA026735.

Roederer, J. G. (1970). Dynamics of geomagnetically trapped radiation, Volume 2. Springer Science & Business Media.

Russell, C. (2003). Solar system, magnetic and electric fields.

Sandberg, I., I. Daglis, A. Anastasiadis, P. Bühler, P. Nieminen, and H. Evans (2011). Unfolding and validation of srem fluxes. In 2011 12th European Conference on Radiation and Its Effects on Components and Systems, pp. 599–606. IEEE.

Sandel, B., J. Goldstein, D. Gallagher, and M. Spasojevic (2003). Extreme ultraviolet imager observations of the structure and dynamics of the plasmasphere. Magnetospheric imaging—The image prime mission, 25–46.

Santolík, O., D. Gurnett, J. Pickett, S. Grimald, P. Decreau, M. Parrot, N. Cornilleau-Wehrlin, F. El-Lemdani Mazouz, D. Schriver, N. P. Meredith, et al. (2010). Wave-particle interactions in the equatorial source region of whistler-mode emissions. Journal of Geophysical Research: Space Physics 115(A8).

Sauvaud, J., T. Moreau, R. Maggiolo, J.-P. Treilhou, C. Jacquey, A. Cros, J. Coutelier, J. Rouzaud, E. Penou, and M. Gangloff (2006). High-energy electron detection onboard demeter: The idp spectrometer, description and first results on the inner belt. Planetary and space Science 54(5), 502–511.

Sauvaud, J.-A., M. Walt, D. Delcourt, C. Benoist, E. Penou, Y. Chen, and C. Russell (2013). Inner radiation belt particle acceleration and energy structuring by drift resonance with ulf waves during geomagnetic storms. Journal of Geophysical Research: Space Physics 118(4), 1723–1736.

Schiller, Q., S. Kanekal, L. Jian, X. Li, A. Jones, D. Baker, A. Jaynes, and H. Spence (2016). Prompt injections of highly relativistic electrons induced by interplanetary shocks: A statistical study of van allen probes observations. Geophysical Research Letters 43(24), 12–317.

Schiller, Q., X. Li, L. Blum, W. Tu, D. L. Turner, and J. Blake (2014). A nonstorm time enhancement of relativistic electrons in the outer radiation belt. Geophysical Research Letters 41(1), 7–12.

Schiller, Q. and A. Mahendrakumar (2010). Reptile: A miniaturized detector for a cubesat mission to measure relativistic particles in near-earth space. SSC10-VIII-1.

Schriver, D., M. Ashour-Abdalla, F. Coroniti, J. LeBoeuf, V. Decyk, P. Travnicek, O. Santolík, D. Winningham, J. Pickett, M. Goldstein, et al. (2010). Generation of whistler mode emissions in the inner magnetosphere: An event study. Journal of Geophysical Research: Space Physics 115(A8).

Schulz, M. and L. J. Lanzerotti (2012). Particle diffusion in the radiation belts, Volume 7. Springer Science & Business Media.

Schutz, B., B. Tapley, and G. H. Born (2004). Statistical orbit determination. Elsevier.

Selesnick, R. (2015a). High-energy radiation belt electrons from crand. Journal of Geophysical Research: Space Physics 120(4), 2912–2917.

Selesnick, R. (2015b). Measurement of inner radiation belt electrons with kinetic energy above 1 mev. Journal of Geophysical Research: Space Physics 120(10), 8339–8349.

Selesnick, R., D. Baker, A. Jaynes, X. Li, S. Kanekal, M. Hudson, and B. Kress (2014). Observations of the inner radiation belt: Crand and trapped solar protons. Journal of Geophysical Research: Space Physics 119(8), 6541–6552.

Selesnick, R., D. Baker, A. Jaynes, X. Li, S. Kanekal, M. Hudson, and B. Kress (2016). Inward diffusion and loss of radiation belt protons. Journal of Geophysical Research: Space Physics 121(3), 1969–1978.

Selesnick, R., D. Baker, S. Kanekal, V. Hoxie, and X. Li (2018). Modeling the proton radiation belt with van allen probes relativistic electron-proton telescope data. Journal of Geophysical Research: Space Physics 123(1), 685–697.

Selesnick, R. and J. Blake (2000). On the source location of radiation belt relativistic electrons. Journal of Geophysical Research: Space Physics 105(A2), 2607–2624.

Selesnick, R. and E. Stone (1991). Energetic electrons at uranus: Bimodal diffusion in a satellite limited radiation belt. Journal of Geophysical Research: Space Physics 96(A4), 5651–5665.

Selesnick, R., Y.-J. Su, and J.-A. Sauvaud (2019). Energetic electrons below the inner radiation belt. Journal of Geophysical Research: Space Physics 124(7), 5421–5440.

Selesnick, R., W. Tu, K. Yando, R. Millan, and R. Redmon (2020). Poes/meped angular response functions and the precipitating radiation belt electron flux. Journal of Geophysical Research: Space Physics 125(9), e2020JA028240.

Sergeev, V., M. Shukhtina, R. Rasinkangas, A. Korth, G. Reeves, H. Singer, M. Thomsen, and L. Vagina (1998). Event study of deep energetic particle injections during substorm. Journal of Geophysical Research: Space Physics 103(A5), 9217–9234.

Shen, X.-C., M. K. Hudson, A. N. Jaynes, Q. Shi, A. Tian, S. G. Claudepierre, M.-R. Qin, Q.-G. Zong, and W.-J. Sun (2017). Statistical study of the storm time radiation belt evolution during van allen probes era: Cme-versus cir-driven storms. Journal of Geophysical Research: Space Physics 122(8), 8327–8339.

Shprits, Y. Y., D. A. Subbotin, N. P. Meredith, and S. R. Elkington (2008). Review of modeling of losses and sources of relativistic electrons in the outer radiation belt ii: Local acceleration and loss. Journal of atmospheric and solar-terrestrial physics 70(14), 1694–1713.

Shue, J.-H., P. Song, C. Russell, J. Steinberg, J. Chao, G. Zastenker, O. Vaisberg, S. Kokubun, H. Singer, T. Detman, et al. (1998). Magnetopause location under extreme solar wind conditions. Journal of Geophysical Research: Space Physics 103(A8), 17691–17700.

Sibeck, D. and R.-Q. Lin (2014). Size and shape of the distant magnetotail. Journal of Geophysical Research: Space Physics 119(2), 1028–1043.

Smith, P. H. and R. Hoffman (1974). Direct observations in the dusk hours of the characteristics of the storm time ring current particles during the beginning of magnetic storms. Journal of Geophysical Research 79(7), 966–971.

Stern, D. P. (1975). The motion of a proton in the equatorial magnetosphere. Journal of Geophysical Research 80(4), 595–599.

Su, Y.-J., R. S. Selesnick, and J. Blake (2016). Formation of the inner electron radiation belt by enhanced large-scale electric fields. Journal of Geophysical Research: Space Physics 121(9), 8508–8522.

Su, Z., F. Xiao, H. Zheng, Z. He, H. Zhu, M. Zhang, C. Shen, Y. Wang, S. Wang, C. Kletzing, et al. (2014). Nonstorm time dynamics of electron radiation belts observed by the van allen probes. Geophysical Research Letters 41(2), 229–235.

Sugiura, M. (1991). Equatorial dst index 1957-1986. IAGA bulletin 40, 17–38.

Sullivan, J. (1971). Geometric factor and directional response of single and multi-element particle telescopes. Nuclear Instruments and methods 95(1), 5–11.

Summers, D., B. Ni, and N. P. Meredith (2007). Timescales for radiation belt electron acceleration and loss due to resonant wave-particle interactions: 2. evaluation for vlf chorus, elf hiss, and electromagnetic ion cyclotron waves. Journal of Geophysical Research: Space Physics 112(A4).

Summers, D. and R. M. Thorne (2003). Relativistic electron pitch-angle scattering by electromagnetic ion cyclotron waves during geomagnetic storms. Journal of Geophysical Research: Space Physics 108(A4).

Summers, D., R. M. Thorne, and F. Xiao (1998). Relativistic theory of wave-particle resonant diffusion with application to electron acceleration in the magnetosphere. Journal of Geophysical Research: Space Physics 103(A9), 20487–20500.

Tarantola, A. (1984). Linearized inversion of seismic reflection data. Geophysical prospecting 32(6), 998–1015.

Tarantola, A. (2005). Inverse problem theory and methods for model parameter estimation. SIAM.

Tarantola, A. and B. Valette (1982a). Generalized nonlinear inverse problems solved using the least squares criterion. Reviews of Geophysics 20(2), 219–232.

Tarantola, A. and B. Valette (1982b). Inverse problems= quest for information. Journal of geophysics 50(1), 159–170.

Tetrick, S., M. Engebretson, J. Posch, C. Olson, C. Smith, R. Denton, S. Thaller, J. Wygant, G. D. Reeves, E. MacDonald, et al. (2017). Location of intense electromagnetic ion cyclotron (emic) wave events relative to the plasmapause: Van allen probes observations. Journal of Geophysical Research: Space Physics 122(4), 4064–4088.

Thaller, S., J. Wygant, C. Cattell, A. Breneman, E. Tyler, S. Tian, A. Engel, S. De Pascuale, W. Kurth, C. Kletzing, et al. (2019). Solar rotation period driven modulations of plasmaspheric density and convective electric field in the inner magnetosphere. Journal of Geophysical Research: Space Physics 124(3), 1726–1737.

Thaller, S., J. Wygant, L. Dai, A. Breneman, K. Kersten, C. Cattell, J. Bonnell, J. Fennell, M. Gkioulidou, C. Kletzing, et al. (2015). Van allen probes investigation of the large-scale duskward electric field and its role in ring current formation and plasmasphere erosion in the 1 june 2013 storm. Journal of Geophysical Research: Space Physics 120(6), 4531–4543.

Thorne, R., W. Li, B. Ni, Q. Ma, J. Bortnik, D. Baker, H. E. Spence, G. Reeves, M. Henderson, C. Kletzing, et al. (2013). Evolution and slow decay of an unusual narrow ring of relativistic electrons near l˜ 3.2 following the september 2012 magnetic storm. Geophysical Research Letters 40(14), 3507–3511.

Thorne, R. e., W. Li, B. Ni, Q. Ma, J. Bortnik, L. Chen, D. Baker, H. E. Spence, G. Reeves, M. Henderson, et al. (2013). Rapid local acceleration of relativistic radiation-belt electrons by magnetospheric chorus. Nature 504(7480), 411–414.

Thorne, R. M. (2010). Radiation belt dynamics: The importance of wave-particle interactions. Geophysical Research Letters 37(22).

Thorne, R. M., T. O'Brien, Y. Shprits, D. Summers, and R. B. Horne (2005). Timescale for mev electron microburst loss during geomagnetic storms. Journal of Geophysical Research: Space Physics 110(A9).

Thorne, R. M., Y. Shprits, N. Meredith, R. Horne, W. Li, and L. Lyons (2007). Refilling of the slot region between the inner and outer electron radiation belts during geomagnetic storms. Journal of Geophysical Research: Space Physics 112(A6).

Tsurutani, B. T. and G. S. Lakhina (1997). Some basic concepts of wave-particle interactions in collisionless plasmas. Reviews of Geophysics 35(4), 491–501.

Tsurutani, B. T. and E. J. Smith (1974). Postmidnight chorus: A substorm phenomenon. Journal of Geophysical Research 79(1), 118–127.

Tsyganenko, N. and M. Sitnov (2005). Modeling the dynamics of the inner magnetosphere during strong geomagnetic storms. Journal of Geophysical Research: Space Physics 110(A3).

Tsyganenko, N. A. (1989). A magnetospheric magnetic field model with a warped tail current sheet. Planetary and Space Science 37(1), 5–20.

Turner, D., S. Claudepierre, J. Fennell, T. O'Brien, J. Blake, C. Lemon, M. Gkioulidou, K. Takahashi, G. Reeves, S. Thaller, et al. (2015). Energetic electron injections deep into the inner magnetosphere associated with substorm activity. Geophysical Research Letters 42(7), 2079–2087.

Turner, D., E. Kilpua, H. Hietala, S. Claudepierre, T. O'Brien, J. Fennell, J. Blake, A. Jaynes, S. Kanekal, D. Baker, et al. (2019). The response of earth's electron radiation belts to geomagnetic storms: Statistics from the van allen probes era including effects from different storm drivers. Journal of Geophysical Research: Space Physics 124(2), 1013–1034.

Turner, D. L., T. O'Brien, J. Fennell, S. Claudepierre, J. Blake, A. Jaynes, D. Baker, S. Kanekal, M. Gkioulidou, M. G. Henderson, et al. (2017). Investigating the source of near-relativistic and relativistic electrons in earth's inner radiation belt. Journal of Geophysical Research: Space Physics 122(1), 695–710.

Turner, D. L., Y. Shprits, M. Hartinger, and V. Angelopoulos (2012). Explaining sudden losses of outer radiation belt electrons during geomagnetic storms. Nature Physics 8(3), 208–212.

Ukhorskiy, A., B. Anderson, P. Brandt, and N. Tsyganenko (2006). Storm time evolution of the outer radiation belt: Transport and losses. Journal of Geophysical Research: Space Physics 111(A11).

Ukhorskiy, A. and M. Sitnov (2012). Dynamics of radiation belt particles. The van allen probes mission, 545–578.

Ukhorskiy, A., M. Sitnov, D. Mitchell, K. Takahashi, L. Lanzerotti, and B. Mauk (2014). Rotationally driven 'zebra stripes' in earth's inner radiation belt. Nature 507(7492), 338–340.

Usanova, M., A. Drozdov, K. Orlova, I. Mann, Y. Shprits, M. Robertson, D. Turner, D. Milling, A. Kale, D. Baker, et al. (2014). Effect of emic waves on relativistic and ultrarelativistic electron populations: Ground-based and van allen probes observations. Geophysical Research Letters 41(5), 1375–1381.

Usanova, M., I. Mann, Z. Kale, I. Rae, R. Sydora, M. Sandanger, F. Søraas, K.-H. Glassmeier, K.-H. Fornacon, H. Matsui, et al. (2010). Conjugate ground and multisatellite observations of compression-related emic pc1 waves and associated proton precipitation. Journal of Geophysical Research: Space Physics 115(A7).

Vampola, A. (1998). Measuring energetic electrons-what works and what doesn't. GEOPHYSICAL MONOGRAPH-AMERICAN GEOPHYSICAL UNION 102, 339–355.

Van Allen, J., D. Baker, B. Randall, and D. Sentman (1974). The magnetosphere of jupiter as observed with pioneer 10: 1. instrument and principal findings. Journal of Geophysical Research 79(25), 3559–3577.

Van Allen, J. A., G. H. Ludwig, E. C. Ray, and C. E. McIlwain (1958). Observation of high intensity radiation by satellites 1958 alpha and gamma. Journal of Jet Propulsion 28(9), 588–592.

Volland, H. (1973). A semiempirical model of large-scale magnetospheric electric fields. Journal of Geophysical Research 78(1), 171–180.

Wang, D., Y. Y. Shprits, I. S. Zhelavskaya, F. Effenberger, A. M. Castillo, A. Y. Drozdov, N. A. Aseev, and S. Cervantes (2020). The effect of plasma boundaries on the dynamic evolution of relativistic radiation belt electrons. Journal of Geophysical Research: Space Physics 125(5), e2019JA027422.

Wolf, R., R. Spiro, S. Sazykin, and F. Toffoletto (2007). How the earth's inner magnetosphere works: An evolving picture. Journal of Atmospheric and Solar-Terrestrial Physics 69(3), 288–302.

Wygant, J., J. Bonnell, K. Goetz, R. Ergun, F. Mozer, S. D. Bale, M. Ludlam, P. Turin, P. R. Harvey, R. Hochmann, et al. (2013). The electric field and waves instruments on the radiation belt storm probes mission. The Van Allen Probes Mission, 183–220.

Xiang, Z., W. Tu, X. Li, B. Ni, S. K. Morley, and D. Baker (2017). Understanding the mechanisms of radiation belt dropouts observed by van allen probes. Journal of Geophysical Research: Space Physics 122(10), 9858–9879.

Xiang, Z., W. Tu, B. Ni, M. Henderson, and X. Cao (2018). A statistical survey of radiation belt dropouts observed by van allen probes. Geophysical Research Letters 45(16), 8035–8043.

Xiao, F., C. Yang, Z. He, Z. Su, Q. Zhou, Y. He, C. Kletzing, W. Kurth, G. Hospodarsky, H. E. Spence, et al. (2014). Chorus acceleration of radiation belt relativistic electrons during march 2013 geomagnetic storm. Journal of Geophysical Research: Space Physics 119(5), 3325–3332.

Yuan, C. and Q. Zong (2013). The double-belt outer radiation belt during cme-and cir-driven geomagnetic storms. Journal of Geophysical Research: Space Physics 118(10), 6291–6301.

Zhao, H., D. Baker, S. Califf, X. Li, A. Jaynes, T. Leonard, S. Kanekal, J. Blake, J. Fennell, S. Claudepierre, et al. (2017). Van allen probes measurements of energetic particle deep penetration into the low l region (l<4) during the storm on 8 april 2016. Journal of Geophysical Research: Space Physics 122(12), 12–140.

Zhao, H., X. Li, D. Baker, S. Claudepierre, J. Fennell, J. Blake, B. A. Larsen, R. M. Skoug, H. O. Funsten, R. H. W. Friedel, et al. (2016). Ring current electron dynamics during geomagnetic storms based on the van allen probes measurements. Journal of Geophysical Research: Space Physics 121(4), 3333–3346.

Zhao, H., B. Ni, X. Li, D. Baker, W. Johnston, W. Zhang, Z. Xiang, X. Gu, A. Jaynes, S. Kanekal, et al. (2019). Plasmaspheric hiss waves generate a reversed energy spectrum of radiation belt electrons. Nature Physics 15(4), 367–372.

Zhao, X.-Y., H.-Y. Wang, F. Wu, X.-C. Meng, Y.-Q. Ma, H. Lu, H. Wang, P. Wang, X.-Q. Li, Y.-B. Xu, et al. (2013). A geometric factor calculation method based on the isotropic flux assumption. Chinese Physics C 37(12), 126201.

Zheng, Y., A. T. Lui, X. Li, and M.-C. Fok (2006). Characteristics of 2–6 mev electrons in the slot region and inner radiation belt. Journal of Geophysical Research: Space Physics 111(A10).

Zyla, P., R. Barnett, J. Beringer, O. Dahl, D. Dwyer, D. Groom, C.-J. Lin, K. Lugovsky, E. Pianori, et al. (2020). Review of particle physics. Progress of Theoretical and Experimental Physics 2020(8), 083C01.

Appendix A

Additional information for Chapter 4, "On the Initial Enhancement of Energetic Electrons and the Innermost Plasmapause Locations: CME vs CIR-Driven Storm Periods and Non-Storm Periods"

Event	CME (yyyy/mm/dd)	Dst_{min} (nT)	Event	CIR (yyyy/mm/dd)	Dst_{min} (nT)
1	2013/03/17	-132	1	2013/03/01	-55
2	2013/04/30	-67	2	2013/04/24	-50
3	2013/05/18	-57	3	2013/08/04	-44
4	2013/05/24	-54	4	2013/08/27	-54
5	2013/06/01	-119	5	2013/10/08	-62
6	2013/06/06	-73	6	2013/12/08	-66
7	2013/06/27	-98	7	2014/01/01	-40
8	2013/07/09	-47	8	2014/10/14	-43
9	2013/08/22	-34	9	2015/02/02	-46
10	2013/10/02	-67	10	2015/02/17	-64
11	2013/10/29	-50	11	2015/02.24	-56
12	2013/12/13	-37	12	2015/05/12	-76
13	2014/02/18	-116	13	2015/06/08	-73
14	2014/02/27	-94			
15	2014/05/03	-44			
16	2014/05/07	-44			
17	2014/09/12	-75			
18	2014/12/21	-51			
19	2015/01/07	-99			
20	2015/03/17	-223			
21	2015/06/21	-204			

Table A.1: List of storm events with the corresponding start date (starting from 00UT) and minimum Dst values.

Non-storm period	Start date yyyy/mm/dd (UT)	End date yyyy/mm/dd (UT)
1	2013/01/01 (00)	2013/01/12 (09)
2	2013/02/01(11)	2013/02/11 (10)
3	2013/03/09 (03)	2013/03/16 (12)
4	2013/04/05 (00)	2013/04/22 (13)
5	2013/05/07 (11)	2013/05/16 (22)
6	2013/06/12 (19)	2013/06/18 (21)
7	2013/07/20 (19)	2013/08/04 (00)
8	2013/09/06 (23)	2013/10/02 (00)
9	2013/10/20 (08)	2013/10/30 (00)
10	2013/11/21 (07)	2013/12/06 (00)
11	2013/12/19 (20)	2013/12/25 (11)
12	2014/01/08 (21)	2014/02/08 (00)
13	2014/03/06 (17)	2014/03/12 (00)
14	2014/03/18 (07)	2014/04/11 (00)
15	2014/04/19 (00)	2014/04/28 (21)
16	2014/05/26 (00)	2014/06/07 (00)
17	2014/06/23 (23)	2014/07/07 (00)
18	2014/07/17 (14)	2014/07/31 (00)
19	2014/08/11 (06)	2014/08/17 (00)
20	2014/09/06 (00)	2014/09/11 (16)
21	2014/09/18 (13)	2014/09/30 (23)
22	2014/11/27 (06)	2014/12/12 (00)
23	2015/01/17 (14)	2015/01/26 (00)
24	2015/04/03 (12)	2015/04/09 (00)
25	2015/05/03 (01)	2015/05/10 (00)
26	2015/05/24 (07)	2015/06/05 (00)

Table A.2: List of non-storm periods that include the corresponding start and end date/time.

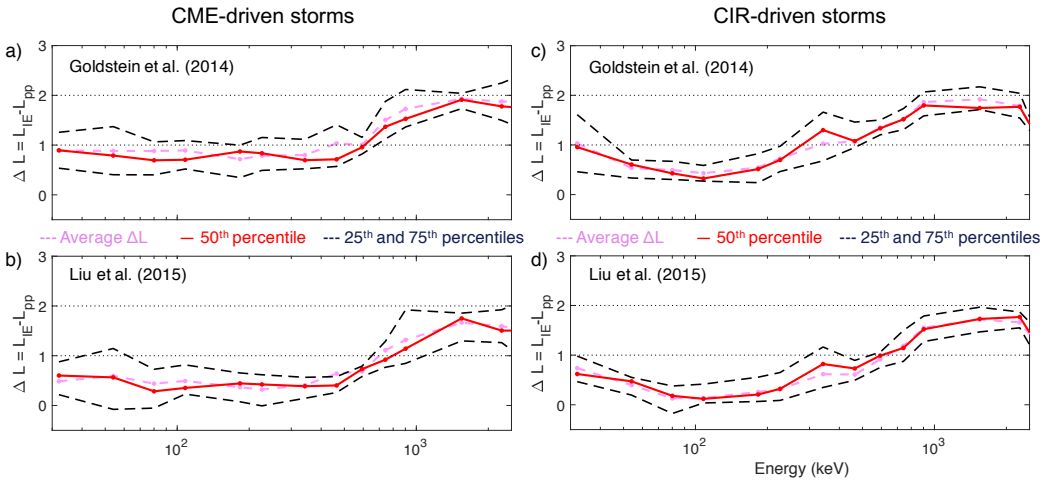

Figure A.1: Quantification of the median (50th percentiles) and average distance between L_{IE} and L_{pp} using background-corrected data are indicated by solid red and pink lines, respectively. The top panels are ΔL using Goldstein et al. (2014) model and the bottom panels are ΔL using Liu et al. (2015) model. The left (and right) panel is the results obtained for CME- (and CIR-) driven storms. The dashed black lines indicate the 25th and 50th percentiles of ΔL.

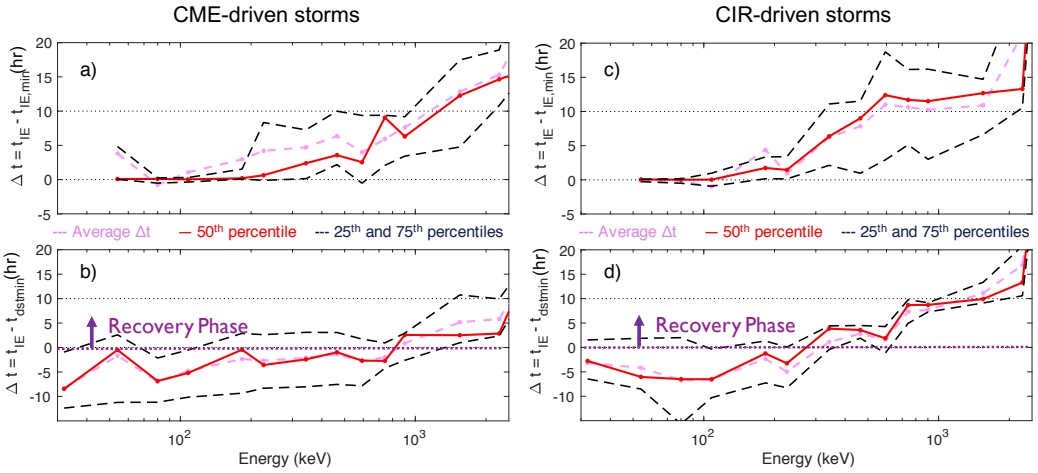

Figure A.2: Quantification of the median (50th percentile) and average temporal difference for two different references across different energy channels using background-corrected data are indicated by solid red lines and dashed pink lines, respectively. The top panels are the time-lag of initial enhancements of higher energy electrons as compared to the initial enhancements of the lowest available energy electrons. The bottom panels are the time difference between the initial electron enhancements and the time where the minimum Dst value occurs. The left (and right) panel is the results obtained for CME- (and CIR-) driven storms. The dashed black lines indicate the 25th and 75th percentiles of Δt from non-background-corrected data. The unit of the Δt is hour. The two horizontal dashed lines mark Δt = 0 and Δt = 10-hour, respectively.

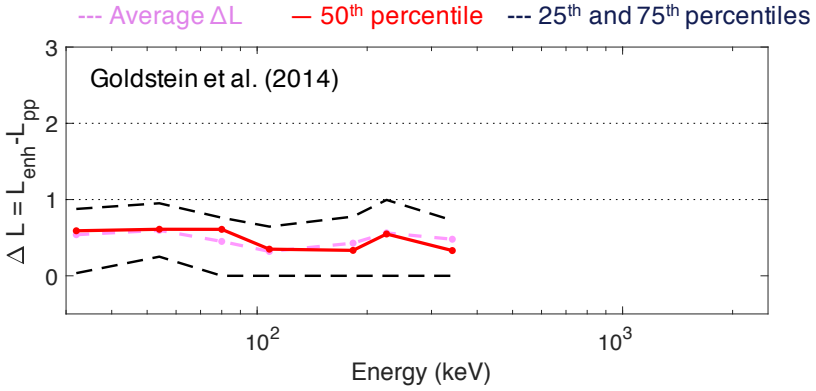

Figure A.3: Quantification of the median (50th percentiles) and average distance between L_{IE} and L_{pp} are indicated by solid red and pink lines using the Goldstein et al. (2014) plasmapause model during non-storm periods using background-corrected data.

Appendix B

Additional information on REPTile-2

B.1 Estimated count rate per energy using AE9 and AP9

We have estimated the expected count rate per energy ($\#/s/MeV$) in each channel by multiplying the computed energy response function in each channel, incident energy width, and flux model spectrum from AE9 and/or AP9

$$r_{i,E} = G_i(E) j_{model}(E) \Delta E$$

.

Figures B.1 and B.2 show the count rate (per energy) for RNG and PEN channels using the estimated 'worst-case scenario' from AE9 and AP9 models (Figure 6.11). As expected, the contribution of 60-100 MeV protons on RNGp channels is smaller compared to those from < 35 MeV. Likewise, the contribution of > 5 MeV electrons on RNGe channels is significantly lower than lower-energy electrons. Besides, we have assessed the relative contribution of incident proton on RNGe channels, as shown in Figure B.3. In certain channels like Ch 40, the count rate from low-energy protons can be comparable to those from incident electrons. Therefore, cautions are required when analyzing those data. It is important to note that to characterize or quantify the expected count rate, we need to integrate the count rate for different populations. For instance, one can sum all count rates per energy in the low-energy particles and compare them with count rates of high-energy particles. Such an analysis is left for future data calibration.

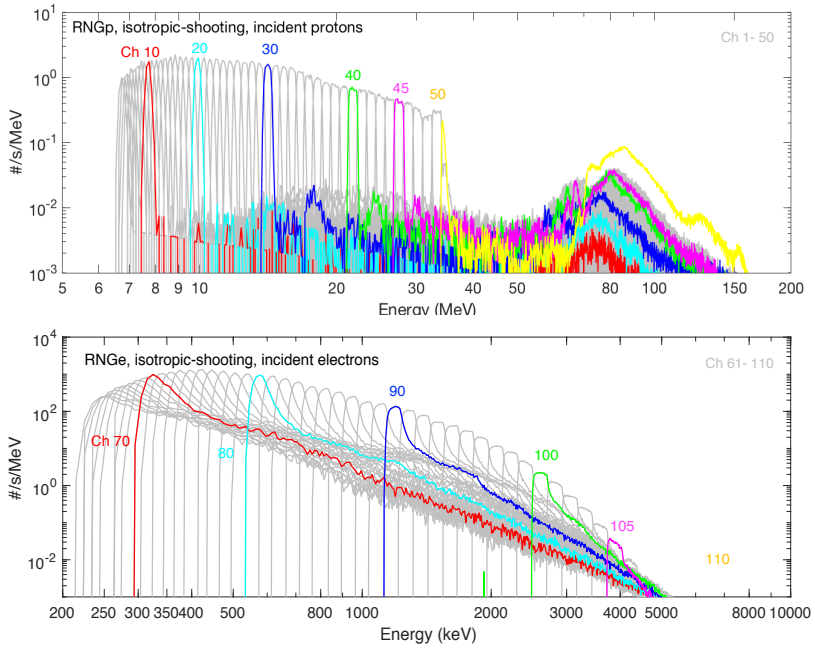

Figure B.1: Count rate as a function of incident energy. Different colors represent response function for channels: (top) RNGp channels, Channels 1-50; (bottom) RNGe, Channels 61-110. The highlighted channels are Channels 10 (red), 20(cyan), 30 (blue), 40 (green), 45(magenta), and 50 (yellow) for RNGp; Channels 70 (red), 80 (cyan), 90 (blue), 100 (green), 105 (magenta), and 110 (yellow) for RNGe.

B.2 Angular response function

From the spherical simulations, we know the incident energy and incident angle (with respect to the telescope axis) of each simulated event. Using these information, we can compute angular response functions, following the procedure described in Selesnick et al. [2020]. Using the same nomenclature in Selesnick et al. [2020], the angular response is determined by:

$$a_{ik}(\theta_{tl}) = \frac{1}{2\pi sin\theta_{tl}\Delta\theta_{tl}} \frac{\sum_m n_{iml}}{\sum_m n_{im}}$$

where θ_{tl} is the incident angle bin l with respect to the telescope, $\Delta\theta_t$ is the bin width in incident angle θ_t, n_{iml} is the number of simulated counts in channel i from incident energy bin m and incident angle bin l and the summations over m include all incident energies, E_m within range k. Incident angle of zero means that particles enter along the boresight, and 90 degree means particles come in at an angle perpendicular to the detector stack.

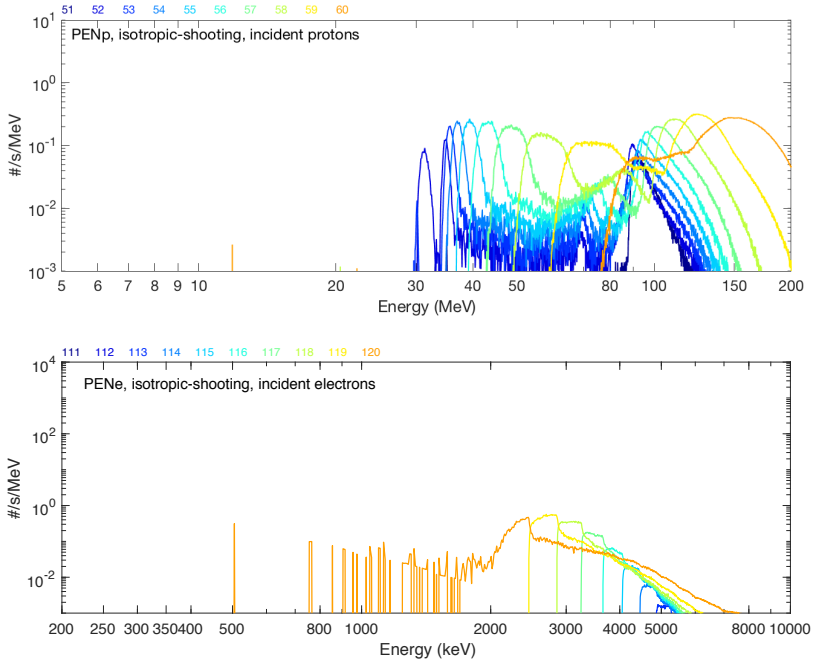

Figure B.2: Count rate as a function of incident energy. Different colors represent response function for channels: (top) RNGp channels, Channels 1-50; (bottom) RNGe, Channels 61-110. The highlighted channels are Channels 10 (red), 20(cyan), 30 (blue), 40 (green), 45(magenta), and 50 (yellow) for RNGp; Channels 70 (red), 80 (cyan), 90 (blue), 100 (green), 105 (magenta), and 110 (yellow) for RNGe.

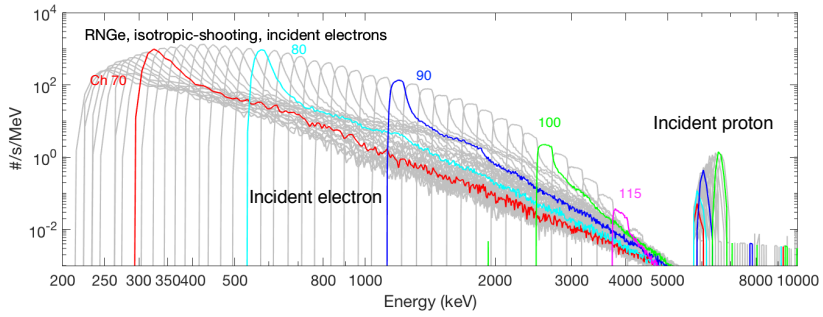

Figure B.3: Count rate as a function of incident energy by incident electrons and protons on RNGe channels: Channels 70 (red), 80 (cyan), 90 (blue), 100 (green), 105 (magenta), and 110 (yellow).

Figure B.4 shows angular response function for RNGe channels at two energy intervals (<4 MeV) and (>4 MeV) against incident angle with respect to the telescope axis. Most events in RNGe channels (whether it is < 4 MeV or > 4 MeV electrons) are coming from the field of view (indicated by the dashed black line). This is consistent with the analysis in Figure 6.2 that < 10

MeV electrons are mostly stop by the layered shield and hence entered mostly from the field of view.

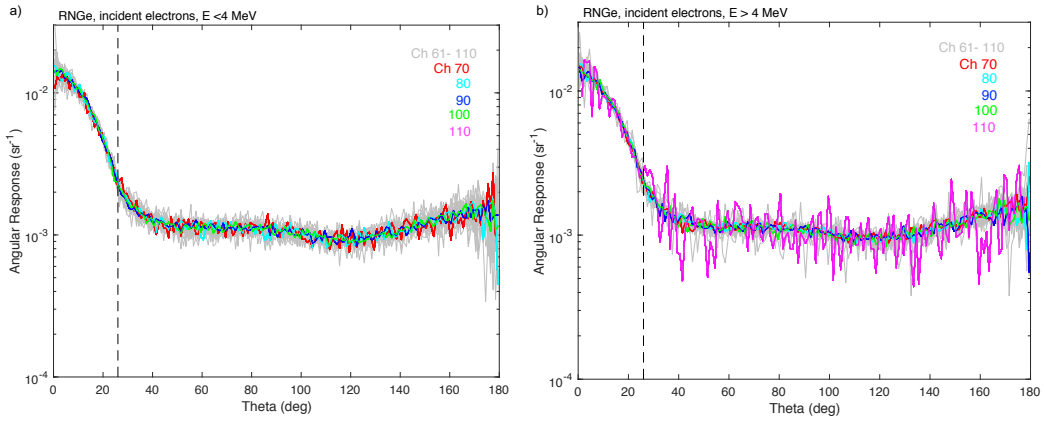

Figure B.4: Angular response function for RNGe channels as a function of incident angle with respect to the telescope axis at two energy intervals ($<$ 4 MeV and $>$ 4 MeV). The highlighted color-coded channels are channels 70 (red), 80 (cyan), 90 (blue), 100 (green), and 110 (magenta).

For RNGp channels, we are interested in two specific populations: <40 MeV protons and 60-100 MeV protons. From Figure B.5, low energy protons ($<$ 40 MeV) are mostly from the field of view, consistent with our observation in Figure 6.2. The angular response for 60-100 MeV protons are informative. It shows that most particles come in at angle slightly outside of FOV. We know from Figure 6.2 that these protons can penetrate through Aluminum shielding and Tantalum teeth and reach the detector(s). Since they have a wider angle access to the detector, it explains the appearance of a hump between 80-100 MeV protons in Figure 6.8. In summary, the angular response analysis complements the energy response function to provide a full understanding of how particles interact with the instrument. It can be a powerful analysis tool when combined with radiation belt simulation.

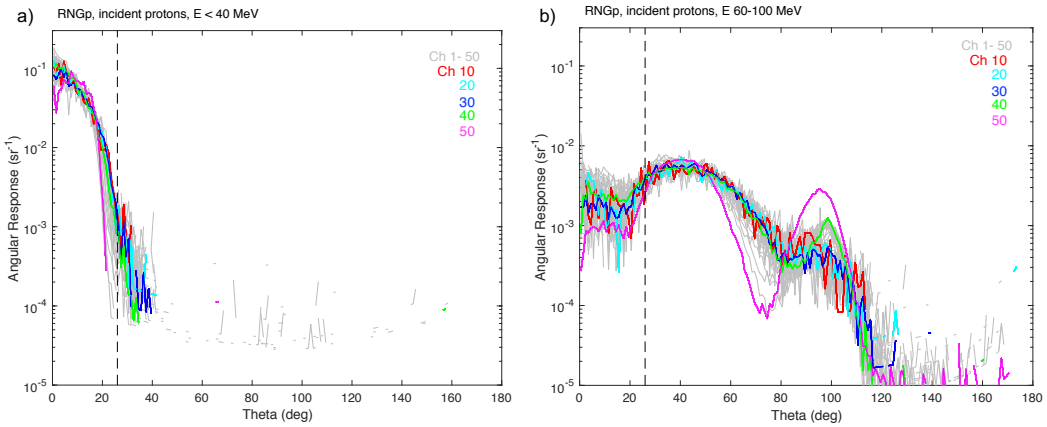

Figure B.5: Angular response function for RNGp channels as a function of incident angle with respect to the telescope axis at two energy intervals (< 40 MeV and 60-100 MeV). The highlighted color-coded channels are channels 10 (red), 20 (cyan), 30 (blue), 40 (green), and 50 (magenta).

Appendix C

Review for Chapter 7: solving inverse problem using the length method

This appendix reviews some fundamental concepts that are used in Chapter 7. Interested readers are referred to Schutz et al. [2004], Tarantola [2005], and Menke [2012] for more detailed discussion.

C.1 Derivation of matrix

Let $\boldsymbol{X}$ be an $n \times 1$ vector and $\boldsymbol{A}$ and $\boldsymbol{B}$ are $m \times 1$ vector as a function of vector $\boldsymbol{X}$.

$$\frac{\delta(\boldsymbol{A^T B})}{\delta \boldsymbol{X}} = \boldsymbol{B}^T \frac{\delta \boldsymbol{A}}{\delta \boldsymbol{X}} + \boldsymbol{A}^T \frac{\delta \boldsymbol{B}}{\delta \boldsymbol{X}} \tag{C.1}$$

where $\frac{\delta \boldsymbol{A}}{\delta \boldsymbol{X}}$ is a $m \times n$ matrix and $\frac{\delta(\boldsymbol{A^T B})}{\delta \boldsymbol{X}}$ is a $1 \times n$ row vector. Likewise,

$$\frac{\delta(\boldsymbol{A^T} W \boldsymbol{A})}{\delta \boldsymbol{X}} \tag{C.2}$$

where W is an $m \times m$ matrix. Let $\boldsymbol{B} = W^{1/2}\boldsymbol{A}$, then

$$\frac{\delta(\boldsymbol{A^T} W \boldsymbol{A})}{\delta \boldsymbol{X}} = \frac{\delta(\boldsymbol{B^T B})}{\delta \boldsymbol{X}} = \boldsymbol{B}^T \frac{\delta \boldsymbol{B}}{\delta \boldsymbol{X}} + \boldsymbol{B}^T \frac{\delta \boldsymbol{B}}{\delta \boldsymbol{X}} \tag{C.3}$$

$$\frac{\delta(\boldsymbol{A^T} W \boldsymbol{A})}{\delta \boldsymbol{X}} = 2\boldsymbol{B}^T \frac{\delta \boldsymbol{B}}{\delta \boldsymbol{X}} \tag{C.4}$$

where $\frac{\delta \boldsymbol{B}}{\delta \boldsymbol{X}} = W^{1/2} \frac{\delta \boldsymbol{A}}{\delta \boldsymbol{X}}$ and $\boldsymbol{B}^T$ is $\boldsymbol{A}^T W^{1/2}$. Eq. C.4 can therefore be rewritten as:

$$\frac{\delta(\boldsymbol{A^T} W \boldsymbol{A})}{\delta \boldsymbol{X}} = 2\boldsymbol{A}^T W \frac{\delta \boldsymbol{A}}{\delta \boldsymbol{X}} \tag{C.5}$$

C.2 Simple least square solution

The goal of the least square solution is to find an estimate that minimize the squared sum of the observation residual or data misfit [Menke, 2012; Schutz et al., 2004] By taking d as observations, m as model parameters, and G as the relationship between d and m, we can represent Eq. 7.1 as $\boldsymbol{d} = \boldsymbol{g(m)}$. Since integral is a linear operator, Eq. 7.1 is therefore a linear problem and we can rewritten $\boldsymbol{d} = \boldsymbol{g(m)}$ as $\boldsymbol{d} = \boldsymbol{Gm}$, where $\boldsymbol{d}$ is a $n \times 1$ matrix, $\boldsymbol{m}$ is a $m \times 1$ matrix and $\boldsymbol{G}$ is a $n \times m$ matrix. Data misfit or observation residual refers to $\boldsymbol{d_{obs}} - \boldsymbol{d_{pred}} = \boldsymbol{d_{obs}} - \boldsymbol{Gm}$. The task is therefore to determine a solution that minimizes the objective function, also known as cost function, misfit function, or performance index:

$$J_{LS} = ||\boldsymbol{d_{obs}} - \boldsymbol{d_{pred}}||^2 = ||\boldsymbol{d_{obs}} - \boldsymbol{Gm}||^2 = (\boldsymbol{d_{obs}} - \boldsymbol{Gm})^T(\boldsymbol{d_{obs}} - \boldsymbol{Gm}) \tag{C.6}$$

The observations and the corresponding observation residuals in Eq. C.6 are equal-weighted, which is not the best way to approach the problem since the accuracy of observations may differ. Alternatively, we can introduce a weighting matrix using the inverse of the covariance matrix of the data, $\boldsymbol{C_d}$, which is a $n \times n$ matrix. With this choice of weighting matrix, data with large variances will weigh less in the objective function than data with small variances. We can rewrite Eq. C.6 as:

$$J_{LS} = (\boldsymbol{d_{obs}} - \boldsymbol{Gm})^T\boldsymbol{C_d^{-1}}(\boldsymbol{d_{obs}} - \boldsymbol{Gm}) \tag{C.7}$$

To minimize Eq. C.7 means that the derivative of Eq. C.7 must be zero, $\frac{\delta J}{\delta m} = 0$. The derivative of Eq. C.7, and it can be written as:

$$\frac{\delta J_{LS}}{\delta m} = \frac{\delta((\boldsymbol{d_{obs}} - \boldsymbol{Gm})^T\boldsymbol{C_d^{-1}}(\boldsymbol{d_{obs}} - \boldsymbol{Gm}))}{\delta m} = 0 \tag{C.8}$$

Using Eq. C.5, we get:

$$\frac{\delta J_{LS}}{\delta m} = 2(\boldsymbol{d_{obs}} - \boldsymbol{Gm})^T\boldsymbol{C_d^{-1}}\frac{\delta(\boldsymbol{d_{obs}} - \boldsymbol{Gm})}{\delta \boldsymbol{m}} = 0 \tag{C.9}$$

$$\frac{\delta J_{LS}}{\delta m} = -2(\boldsymbol{d_{obs}} - \boldsymbol{Gm})^T\boldsymbol{C_d^{-1}}\boldsymbol{G} = 0 \tag{C.10}$$

Taking a transpose of the entire equation gives:

$$\frac{\delta J_{LS}}{\delta m} = -2\boldsymbol{G}^T\boldsymbol{C}_{\boldsymbol{d}}^{-1}(\boldsymbol{d_{obs}} - \boldsymbol{Gm}) = 0 \tag{C.11}$$

$$\boldsymbol{G}^T\boldsymbol{C}_{\boldsymbol{d}}^{-1}\boldsymbol{d_{obs}} = \boldsymbol{G}^T\boldsymbol{C}_{\boldsymbol{d}}^{-1}\boldsymbol{Gm} \tag{C.12}$$

$$\tilde{\boldsymbol{m}} = [\boldsymbol{G}^T\boldsymbol{C}_{\boldsymbol{d}}^{-1}\boldsymbol{G}]^{-1}\boldsymbol{G}^T\boldsymbol{C}_{\boldsymbol{d}}^{-1}\boldsymbol{d_{obs}} \tag{C.13}$$

Eq. C.13 gives the optimal estimate of m that minimizes the objective function. However, we note that this solution only exists when the inverse of $\boldsymbol{G}^T\boldsymbol{C}_{\boldsymbol{d}}^{-1}\boldsymbol{G}$ exists. $\boldsymbol{G}^T\boldsymbol{C}_{\boldsymbol{d}}^{-1}\boldsymbol{G}$ is a matrix of $m \times m$. $\boldsymbol{G}^T\boldsymbol{C}_{\boldsymbol{d}}^{-1}\boldsymbol{G}$ exists when $\boldsymbol{G}^T\boldsymbol{C}_{\boldsymbol{d}}^{-1}\boldsymbol{G} > 0$, i.e. it must be positive definite. $\boldsymbol{G}^T\boldsymbol{C}_{\boldsymbol{d}}^{-1}\boldsymbol{G}$ is positive definite in an overdetermined and even-determined system. An overdetermined system describes a system that has more observations (n) than unknown parameters (m), while an underdetermined system is a system that has more unknown parameters than observations ($n < m$). An even-determined system is when the number of observations is equal to the number of unknown parameters ($n = m$). Therefore, the least square solution can only solve overdetermined and even-determined problem, but cannot solve underdetermined problem.

C.3 Minimum length solution

In an underdetermined system where there are more unknowns than observations, we can use the minimum length or minimum norm criterion and add *a priori* information in the system to obtain a unique solution. The minimum length criterion is an analogy to the least square method. But instead of minimizing the data misfit, we minimize the total length of the model parameter vector, $\boldsymbol{m} - \boldsymbol{m_0}$, where $\boldsymbol{m_0}$ is the *a priori* information. We note that the problem is also subjected to a constraint that is the data misfit must be zero. We use Lagrange multiplier to solve a problem that is subjected to some constraints. The objective function is then

$$J_{ML} = (\boldsymbol{m} - \boldsymbol{m_0}^T)(\boldsymbol{m} - \boldsymbol{m_0}) + \lambda^T[\boldsymbol{d} - \boldsymbol{Gm}] \tag{C.14}$$

Like Eq. C.7, a weighting matrix can be added to optimize the solution. We choose the inverse of the *a priori* model covariance ($\boldsymbol{C_m^{-1}}$) as our weighting matrix and rewrite Eq. C.14:

$$J_{ML} = (\boldsymbol{m} - \boldsymbol{m_0^T})\boldsymbol{C_m^{-1}}(\boldsymbol{m} - \boldsymbol{m_0}) + \lambda^T[\boldsymbol{d} - \boldsymbol{Gm}] \tag{C.15}$$

Similar to the derivation of least square solution, we can set the derivative of J_{ML} as 0:

$$\frac{\delta(J_{ML(\boldsymbol{m},\boldsymbol{\lambda})})}{\delta \boldsymbol{m}} = \frac{\delta((\boldsymbol{m} - \boldsymbol{m_0^T})\boldsymbol{C_m^{-1}}(\boldsymbol{m} - \boldsymbol{m_0}) + \boldsymbol{\lambda}^T[\boldsymbol{d} - \boldsymbol{Gm}])}{\delta \boldsymbol{m}} = 0 \tag{C.16}$$

$$\frac{\delta(J_{ML(\boldsymbol{m},\boldsymbol{\lambda})})}{\delta \boldsymbol{m}} = 2(\boldsymbol{m} - \boldsymbol{m_0})^T\boldsymbol{C_m^{-1}} - \boldsymbol{\lambda}^T\boldsymbol{G} = 0 \tag{C.17}$$

$$= 2\boldsymbol{C_m^{-1}}(\boldsymbol{m} - \boldsymbol{m_0}) - \boldsymbol{G}^T\boldsymbol{\lambda} = 0 \tag{C.18}$$

$$\boldsymbol{m} = \boldsymbol{C_m}(\frac{1}{2}\boldsymbol{G}^T\boldsymbol{\lambda}) + \boldsymbol{m_0} \tag{C.19}$$

$$\frac{\delta(J_{ML(\boldsymbol{m},\boldsymbol{\lambda})})}{\delta \boldsymbol{\lambda}} = \frac{\delta((\boldsymbol{m} - \boldsymbol{m_0^T})\boldsymbol{C_m^{-1}}(\boldsymbol{m} - \boldsymbol{m_0}) + \boldsymbol{\lambda}^T[\boldsymbol{d} - \boldsymbol{Gm}])}{\delta \boldsymbol{m}} = 0 \tag{C.20}$$

$$\frac{\delta(J_{ML(\boldsymbol{m},\boldsymbol{\lambda})})}{\delta \boldsymbol{\lambda}} = \boldsymbol{d} - \boldsymbol{Gm} = 0 \tag{C.21}$$

$$\boldsymbol{d} = \boldsymbol{Gm} \tag{C.22}$$

Put Eq. C.19 into Eq. C.22 to get $\boldsymbol{\lambda}$:

$$\boldsymbol{d} = \boldsymbol{Gm} \tag{C.23}$$

$$\boldsymbol{d} = \boldsymbol{GC_m}(\frac{1}{2}\boldsymbol{G}^T\boldsymbol{\lambda}) + \boldsymbol{Gm_0} \tag{C.24}$$

$$\boldsymbol{\lambda} = 2(\boldsymbol{GC_mG}^T)^{-1}(\boldsymbol{d} - \boldsymbol{Gm_0}) \tag{C.25}$$

Plug Eq. C.25 into Eq. C.19 to get the solution $\boldsymbol{m}$

$$\boldsymbol{m} = \boldsymbol{C_m}(\frac{1}{2}\boldsymbol{G}^T(2(\boldsymbol{GC_mG}^T)^{-1}(\boldsymbol{d} - \boldsymbol{Gm_0}))) + \boldsymbol{m_0} \tag{C.26}$$

$$\boldsymbol{m} = \boldsymbol{m_0} + \boldsymbol{C_mG}^T(\boldsymbol{GC_mG}^T)^{-1}(\boldsymbol{d} - \boldsymbol{Gm_0}) \tag{C.27}$$

Eq. C.27 gives the minimum length solution for a purely underdetermined problem, where the data misfit equals zero. The underdetermined problem that has non-zero prediction error or data misfit is known as a mixed-determined problem [Menke, 2012]. We can use generalized least square method to solve for mixed-determined problem.

C.4 Derivation of different forms of the generalized least square solution for linear problems

To get Eq. 7.18 from Eq. 7.17, we first replace $\tilde{\boldsymbol{C_m}} = (\boldsymbol{G}^T\boldsymbol{C_d}^{-1}\boldsymbol{G} + \boldsymbol{C_m}^{-1})^{-1}$

$$\tilde{\boldsymbol{m}} = \tilde{\boldsymbol{C_m}}(\boldsymbol{G}^T\boldsymbol{C_d}^{-1}\boldsymbol{d_{obs}} + \boldsymbol{C_m}^{-1}\boldsymbol{m_0}) \tag{C.28}$$

$$\tilde{\boldsymbol{m}} = \tilde{\boldsymbol{C_m}}(\boldsymbol{G}^T\boldsymbol{C_d}^{-1}\boldsymbol{d_{obs}}) + \tilde{\boldsymbol{C_m}}(\boldsymbol{C_m}^{-1}\boldsymbol{m_0}) \tag{C.29}$$

$$\tilde{\boldsymbol{m}} = \tilde{\boldsymbol{C_m}}(\boldsymbol{G}^T\boldsymbol{C_d}^{-1}\boldsymbol{d_{obs}}) + \tilde{\boldsymbol{C_m}}(\boldsymbol{G}^T\boldsymbol{C_d}^{-1}\boldsymbol{G} - \boldsymbol{G}^T\boldsymbol{C_d}^{-1}\boldsymbol{G} + \boldsymbol{C_m}^{-1})\boldsymbol{m_0} \tag{C.30}$$

$$\tilde{\boldsymbol{m}} = \tilde{\boldsymbol{C_m}}(\boldsymbol{G}^T\boldsymbol{C_d}^{-1}\boldsymbol{d_{obs}}) + \tilde{\boldsymbol{C_m}}(\tilde{\boldsymbol{C_m}}^{-1} - \boldsymbol{G}^T\boldsymbol{C_d}^{-1}\boldsymbol{G})\boldsymbol{m_0} \tag{C.31}$$

$$\tilde{\boldsymbol{m}} = \tilde{\boldsymbol{C_m}}(\boldsymbol{G}^T\boldsymbol{C_d}^{-1}\boldsymbol{d_{obs}}) + (\boldsymbol{I} - \tilde{\boldsymbol{C_m}}\boldsymbol{G}^T\boldsymbol{C_d}^{-1}\boldsymbol{G})\boldsymbol{m_0} \tag{C.32}$$

$$\tilde{\boldsymbol{m}} = \boldsymbol{m_0} + \tilde{\boldsymbol{C_m}}\boldsymbol{G}^T\boldsymbol{C_d}^{-1}(\boldsymbol{d_{obs}} - \boldsymbol{G}\boldsymbol{m_0}) \tag{C.33}$$

$$\tilde{\boldsymbol{m}} = \boldsymbol{m_0} + (\boldsymbol{G}^T\boldsymbol{C_d}^{-1}\boldsymbol{G} + \boldsymbol{C_m}^{-1})^{-1}\boldsymbol{G}^T\boldsymbol{C_d}^{-1}(\boldsymbol{d_{obs}} - \boldsymbol{G}\boldsymbol{m_0}) \tag{C.34}$$

Eq. C.39 is the same as E. 7.18. To derive Eq. 7.19 from Eq. 7.18, we demonstrate a matrix identity.

$$(\boldsymbol{G}^T\boldsymbol{C_d}^{-1}\boldsymbol{G} + \boldsymbol{C_m}^{-1})^{-1}\boldsymbol{G}^T\boldsymbol{C_d}^{-1} = \boldsymbol{C_m}\boldsymbol{G}^{\boldsymbol{T}}(\boldsymbol{C_d} + \boldsymbol{G}\boldsymbol{C_M}\boldsymbol{G}^T)^{-1} \tag{C.35}$$

This matrix identity can be derived from:

$$\boldsymbol{G}^T + \boldsymbol{G}^T\boldsymbol{C_d}^{-1}\boldsymbol{G}\boldsymbol{C_m}\boldsymbol{G}^T = \boldsymbol{G}^T\boldsymbol{C_d}^{-1}(\boldsymbol{C_d} + \boldsymbol{G}\boldsymbol{C_m}\boldsymbol{G}^T) \tag{C.36}$$

$$\boldsymbol{G}^T\boldsymbol{C_d}^{-1}(\boldsymbol{C_d} + \boldsymbol{G}\boldsymbol{C_m}\boldsymbol{G}^T) = (\boldsymbol{G}^T\boldsymbol{C_d}^{-1}\boldsymbol{G} + \boldsymbol{C_m}^{-1})\boldsymbol{C_m}\boldsymbol{G}^T \tag{C.37}$$

$$(\boldsymbol{G}^T\boldsymbol{C_d}^{-1}\boldsymbol{G} + \boldsymbol{C_m}^{-1})^{-1}\boldsymbol{G}^T\boldsymbol{C_d}^{-1} = \boldsymbol{C_m}\boldsymbol{G}^T(\boldsymbol{C_d} + \boldsymbol{G}\boldsymbol{C_m}\boldsymbol{G}^T)^{-1} \tag{C.38}$$

$$\tilde{\boldsymbol{m}} = \boldsymbol{m_0} + (\boldsymbol{G}^T\boldsymbol{C_d}^{-1}\boldsymbol{G} + \boldsymbol{C_m}^{-1})^{-1}\boldsymbol{G}^T\boldsymbol{C_d}^{-1}(\boldsymbol{d_{obs}} - \boldsymbol{G}\boldsymbol{m_0}) \tag{C.39}$$

$$\tilde{\boldsymbol{m}} = \boldsymbol{m_0} + \boldsymbol{C_m}\boldsymbol{G}^T(\boldsymbol{C_d} + \boldsymbol{G}\boldsymbol{C_m}\boldsymbol{G}^T)^{-1}(\boldsymbol{d_{obs}} - \boldsymbol{G}\boldsymbol{m_0}) \tag{C.40}$$

C.5 Covariance for posterior model

The definition of covariance is the expected value (or mean) of the product of the deviations from the expected value.

$$Cov[X,Y] = E[(X - E(X))(Y - E(Y))]$$

The covariance matrix for generalized least square posterior model is:

$$\tilde{\boldsymbol{m}} = (\boldsymbol{G}^T\boldsymbol{C}_{\boldsymbol{d}}^{-1}\boldsymbol{G} + \boldsymbol{C}_{\boldsymbol{m}}^{-1})^{-1}(\boldsymbol{G}^T\boldsymbol{C}_{\boldsymbol{d}}^{-1}\boldsymbol{d}_{\boldsymbol{obs}} + \boldsymbol{C}_{\boldsymbol{m}}^{-1}\boldsymbol{m}_{\boldsymbol{0}}) \tag{C.41}$$

$$\tilde{\boldsymbol{m}} = (\boldsymbol{G}^T\boldsymbol{C}_{\boldsymbol{d}}^{-1}\boldsymbol{G} + \boldsymbol{C}_{\boldsymbol{m}}^{-1})^{-1}\boldsymbol{G}^T\boldsymbol{C}_{\boldsymbol{d}}^{-1}\boldsymbol{d}_{\boldsymbol{obs}} + (\boldsymbol{G}^T\boldsymbol{C}_{\boldsymbol{d}}^{-1}\boldsymbol{G} + \boldsymbol{C}_{\boldsymbol{m}}^{-1})^{-1}\boldsymbol{C}_{\boldsymbol{m}}^{-1}\boldsymbol{m}_{\boldsymbol{0}} \tag{C.42}$$

$$\tilde{\boldsymbol{m}} = \boldsymbol{A}^{-1}\boldsymbol{G}^T\boldsymbol{C}_{\boldsymbol{d}}^{-1}\boldsymbol{d}_{\boldsymbol{obs}} + \boldsymbol{A}^{-1}\boldsymbol{C}_{\boldsymbol{m}}^{-1}\boldsymbol{m}_{\boldsymbol{0}} \tag{C.43}$$

$$\tilde{\boldsymbol{m}} = \boldsymbol{G}^{-g}\boldsymbol{d}_{\boldsymbol{obs}} + \boldsymbol{G}^{-g}\boldsymbol{m}_{\boldsymbol{0}} \tag{C.44}$$

where $\boldsymbol{A}$ is $\boldsymbol{G}^T\boldsymbol{C}_{\boldsymbol{d}}^{-1}\boldsymbol{G} + \boldsymbol{C}_{\boldsymbol{m}}^{-1}$, $\boldsymbol{G}^{-g}$ is $\boldsymbol{A}^{-1}\boldsymbol{G}^T\boldsymbol{C}_{\boldsymbol{d}}^{-1}$, and $\boldsymbol{H}^{-g}$ is $\boldsymbol{A}^{-1}\boldsymbol{C}_{\boldsymbol{m}}^{-1}$. We also note that $\boldsymbol{A}$ is a symmetric and the inverse $\boldsymbol{A}^{-1}$ is also symmetric (i.e., $(\boldsymbol{A}^{-1})^T = \boldsymbol{A}^{-1}$).

$$\tilde{\boldsymbol{C}_{\boldsymbol{m}}} = \boldsymbol{G}^{-g}\boldsymbol{C}_{\boldsymbol{d}}^{-1}\boldsymbol{G}^{-gT} + \boldsymbol{H}^{-g}\boldsymbol{C}_{\boldsymbol{m}}\boldsymbol{H}^{-gT} \tag{C.45}$$

$$\tilde{\boldsymbol{C}_{\boldsymbol{m}}} = \boldsymbol{A}^{-1}\boldsymbol{G}^T\boldsymbol{C}_{\boldsymbol{d}}^{-1}\boldsymbol{C}_{\boldsymbol{d}}^{-1}(\boldsymbol{A}^{-1}\boldsymbol{G}^T\boldsymbol{C}_{\boldsymbol{d}}^{-1})^T + \boldsymbol{A}^{-1}\boldsymbol{C}_{\boldsymbol{m}}^{-1}\boldsymbol{C}_{\boldsymbol{m}}(\boldsymbol{A}^{-1}\boldsymbol{C}_{\boldsymbol{m}}^{-1})^T \tag{C.46}$$

$$\tilde{\boldsymbol{C}_{\boldsymbol{m}}} = \boldsymbol{A}^{-1}\boldsymbol{G}^T\boldsymbol{C}_{\boldsymbol{d}}^{-1}\boldsymbol{C}_{\boldsymbol{d}}^{-1}\boldsymbol{C}_{\boldsymbol{d}}^{-1}\boldsymbol{G}\boldsymbol{A}^{-1} + \boldsymbol{A}^{-1}\boldsymbol{C}_{\boldsymbol{m}}^{-1}\boldsymbol{C}_{\boldsymbol{m}}\boldsymbol{C}_{\boldsymbol{m}}^{-1}\boldsymbol{A}^{-1} \tag{C.47}$$

$$\tilde{\boldsymbol{C}_{\boldsymbol{m}}} = \boldsymbol{A}^{-1}(\boldsymbol{G}^T\boldsymbol{C}_{\boldsymbol{d}}^{-1}\boldsymbol{C}_{\boldsymbol{d}}^{-1}\boldsymbol{C}_{\boldsymbol{d}}^{-1}\boldsymbol{G} + \boldsymbol{C}_{\boldsymbol{m}}^{-1})\boldsymbol{A}^{-1} \tag{C.48}$$

$$\tilde{\boldsymbol{C}_{\boldsymbol{m}}} = \boldsymbol{A}^{-1}(\boldsymbol{A}^{-1})\boldsymbol{A}^{-1} \tag{C.49}$$

$$\tilde{\boldsymbol{C}_{\boldsymbol{m}}} = \boldsymbol{A}^{-1} \tag{C.50}$$

$$\tilde{\boldsymbol{C}_{\boldsymbol{m}}} = (\boldsymbol{G}^T\boldsymbol{C}_{\boldsymbol{d}}^{-1}\boldsymbol{G} + \boldsymbol{C}_{\boldsymbol{m}}^{-1})^{-1} \tag{C.51}$$